The Synthesis of a Cobalt(I) σ-alkane Complex and Pincer Complex Catalysts for the Generation of Polyaminoborane on Scale.

Timothy Morgan Boyd

A thesis submitted in partial fulfilment of the requirements for the degree of Doctor of Philosophy at the University of Oxford





Magdalen College

October 2021

Declaration

The work presented in this thesis was carried out between October 2017 and June 2021 under the supervision of Professor Andrew S. Weller. All of the work is my own, unless otherwise stated, and has not been submitted previously for any degree at this, or any other, university.

Timothy Morgan Boyd

September 2021

Acknowledgements

First and foremost, I must thank Professor Andrew Weller. The move to York will always prompt the memory of you chasing after us to sit us down on the top floor of a double-decker bus to tell us that we were all moving halfway across the country. One thing the pandemic will remind me of is watching over zoom throughout the first lockdown, as you gradually grew the beard you told us Katie would leave you if you grew. You then reminded us that when we were back, you wanted ‘to be able to look an ICU nurse in the eyes and tell them our work is worth it.’. I feel privileged to have worked for some hilarious merger of David Brent and Alan Partridge. But like David Brent, you are a boss who genuinely cares for their workers. Throughout my PhD, the support, advice, and life lessons that have been in constant supply have been invaluable and sincerely appreciated.

I must thank Andy again for hiring all the fantastic people I have had the joy of knowing during my time in the group. Annie, Gemma, James Silk, Alasdair, Anna, Max, Tom, Hollie and Alice, you all deserve a specific mention, but thankfully you have all long since left the group, so shall hopefully not read this. I must thank Antonio for the advice and guidance at the start of my PhD and specifically for almost falling out a window dressed only in a towel just to remind me (and the rest of Looe) in a thick Spanish accent that ‘cobalt sucks’. Alex, I will never forget Andy looking you straight in the eye, saying, ‘we have never had a group member from Devon, have we?’ and your quiet reply of ‘I’m from Devon.’. Olie, I miss your one-person breakaways on our snail-paced social rides. The Firestarter Danny, you had an admirable affinity to both ice and fire. Katie, thanks for being the smashiest of Part II students and for the hard work on team Cobalt AB. Matt Webster deserves thanks for being quite literally 18 and letting us take him out for his first drink. Kori requires a thank you for keeping David and me sane

through the summer of 2019. Sam, your motherly care is beyond reproach, and we were all exceptionally fortunate to have you shepherd us through the move to York. Laurence ‘deadbeat dad’ thank you for the frequency with which Neil Young appeared on the lab speakers. Claire, I enjoyed our Rh AB teamwork – I think we made quite the pair! Thank you for keeping me motivated through the last project of my PhD. Joe, good luck with the crystals; I hope they are kind to you. Helena, please listen to something that is not the 1975s.

An extra special mention must go to Cameron, David and James, the ladz of 72 Alcuin Avenue. It is a shame our time in 72 was cruelly cut short by the COVID, but I hope we always find time to meet up for a documentary and a Ryan cooked feast. David, from the day you joined the group, I think the Weller group became a more supportive and friendly place – your willingness to drop everything and help someone else with any problem is a steadfast commitment to procrastination that I admire. Cameron, your intense interest in literally everything has always impressed me, and I hope to use you as a source of pretentious films and music for many years to come. James Race, on the day you visited Andy for an interview, I knew you would be an excellent fit for the group; what I didn’t realise is that you would become one of my very closest friends. A selection of my favourite Racey memories includes a wonderful week in Montréal, a dreamlike night of launching fireworks across a misty flood plain and running a silly marathon for no real reason.

Lots of this work lent itself to collaboration, and so I must thank all my collaborators. Professor Mike Hayward collected the SQUID magnetometry data and provided invaluable help with the analysis and processing. This work was guided by the computational work of collaborators in the Macgregor group, specifically Dr Bengt

Tenger, Dr Lia Sotorrios, Dr Sam Neale, and Professor Stuart Macgregor. All of them influenced this thesis directly and deserve thanks. I must thank the National Crystallography Service for their help with Chapter 2, specifically Dr Graham Tizzard, for his never-ending patience with my terrible crystals, the exquisite trousers, and for being present for the discovery of Robalt. I must also thank all the technical staff without whom none of this work would have been possible, let alone the move. Specific mentions must go to Dr Amber Thompson for the comprehensive X-ray training, Dr Adrian Whitwood for the valuable help and advice both with X-ray and more generally, and Dr Heather Fish and Dr Alex Heyam both for how helpful they have been with our many strange NMR requests. Teri deserves a thank you for the purpose-built SQUID tubes. Ronald Tarry and Dr Graham McAllister are both excessively accommodating, and the time they put into ensuring us a smooth move to York is hugely appreciated.

Outside of the lab, my housemates at 18 London Place (Alex, Alida, Bea, and Louise) deserve a special mention. The countless evenings of contentless chat, spontaneous trips in the Nissan Micra, and lack of judgement for my dairy milk/nuggies/dumplings addiction collectively form some of my favourite memories from my PhD. Thank you, Mum and Dad, for realising when my reception teacher said, ‘it is alright if he can’t read and write, he can always become a builder’ that I would have made a terrible builder. I have learnt a lot from you both and aspire to be a mix of Mum’s fair and rational logic, Dad’s creative tendencies and both of your caring natures. Joe and Daisy, thank you both for getting jobs before me just to highlight just how long I have been in school. Granny B, I know you would have been very proud of me for finally completing education. Lastly, Caitilín, thank you for not just tolerating but enjoying my voluble nature and helping me in more ways than you know; míle buíochas ort a Chaitilín, mo ghrá thú.

Abbreviations

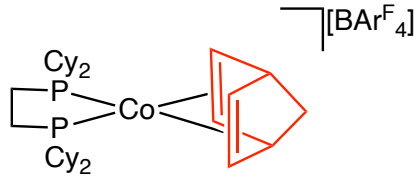
$[Al(O^tBu^F)_4]^-$	$[Al(OC(CF_3)_3)_4]^-$
$[BAr^{Cl}{}_4]^-$	$[B(3,5\text{-}C_6H_3Cl_2)_4]^-$
$[BAr^F{}_4]^-$	$[B(3,5\text{-}C_6H_3(CF_3)_2)_4]^-$
Cat	Catalyst
3c-2e	Three centre two electron
Å	Angstroms
au	Atomic units
B	Bohr Magnetrons
BIAN	Bisaryl-(imino)acenaphthene
Bz	Benzyl
C	Curie constant
COD	Cyclooctadiene
Cp	Cyclopentadienyl
CTA	Chain transfer agent
Cy	Cyclohexyl
Δ	Crystal field splitting energy
Đ	Dispersity
DFT	Density functional theory
ΔH	Change in enthalpy
Dipp	2,6-diisopropylphenyl
DPEPhos-Ph	Bis[(2-diphenylphosphino)phenyl]ether
$\Delta\Sigma$	Change in entropy
R,R$^{i\text{Pr}}$DuPhos	1,2-bis((2*R*,5*R*)-2,5-diisopropylphospholano)benzene
E_a	Activation energy
EPR	Electron paramagnetic resonance
eq	Equivalents
ESI-MS	Electrospray ionisation mass spectrometry
FC	Field cooled
FR	Flexibility range
GC	Gas chromatography
GC/MS	Gas chromatography / Mass spectrometry
GPC	Gel permutation chromatography
h	Hour
HOMO	Highest occupied molecular orbital
Hz	Hertz - s^{-1}
IR	Infra-red
I^{t}Bu	1,3-di-*tert*-butylimidazol-2-ylidene
I^{t}Bu′	Cyclometalated I^{t}Bu ligand
J	Coupling constant in Hz
K	Kelvin

KIE	Kinetic isotope effect
λ	Wavelength
LUMO	Lowest unoccupied molecular orbital
M	Molar - $moldm^{-3}$
MesCCC	Bis(2,4,6-trimethylphenyl-benzimidazol-2-ylidene)phenyl
M_n	Number average molecular weight of the polymer
NBA	Norbornane
NBD	Norbornadiene
NBO	Natural Bond Orbitals
NCI	Non-covalent interaction
NMR	Nuclear magnetic resonance
NOESY	Nuclear Overhauser Effect Spectroscopy
°	Degrees
Ph	Phenyl
POCOP-*i*Pr	κ^3-1,3-$(OP^iPr_2)_2C_6H_3$
POCOP-*t*Bu	κ^3-1,3-$(OP^tBu_2)_2C_6H_3$
PONOP	κ^3-2,6-$(^tBu_2PO)_2C_5H_3N$
ppm	Parts per million
QTAIM	Quantum Theory of Atoms in Molecules
rg	Receiver gain
RI	RI
S	Spin
SC-SC	Single-crystal to single-crystal
SMOM	Solid-state molecular organometallics
SQUID	Superconducting quantum interference device
SSNMR	Solid-State NMR
*t*Bu	Tertiary butyl
THF	Tetrahydrofuran
TIP	Temperature-independent paramagnetism
ToF	Turnover frequency
ToN	Turnover number
TRIR	Time-resolved infrared
UV	Ultra violet
UV-Vis	Ultra violet / visable light
Xantphos-Ph	4,5-bis(diphenylphosphino)-9,9-dimethylxanthene
XRD	X-ray diffraction
β	Bite angle
θ	Tolman cone angle
θ	Weiss constant
μ	Magnetic moment
ρ(r)	Electron density
$\tau_{1/2}$	Half life

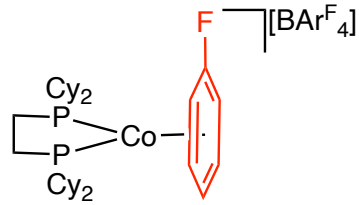
χ	Magnetic susceptibility
χ_n	Number average degree of polymerisation
k	Rate constant
m/z	Mass to charge ratio
kV	Kilovolt
ZFC	Zero field cooled

Complexes

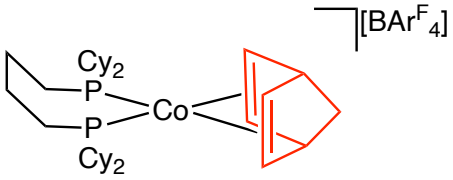
Chapter 2:



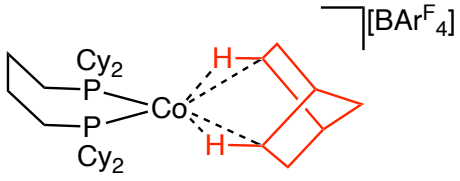
[Co(L1)NBD][BAr$^F_4$]



[Co(L1)(η-FC$_6$H$_5$)][BAr$^F_4$]

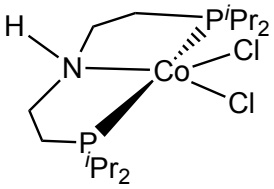


[Co(L2)NBD][BAr$^F_4$]

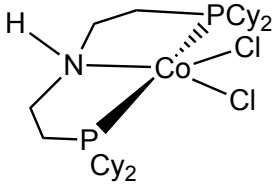


[Co(L2)NBA][BAr$^F_4$]

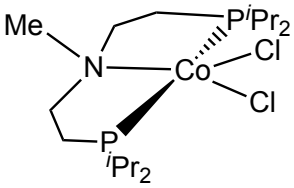
Chapter 3:



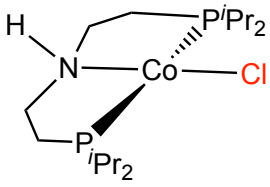
CoCl$_2$(L3)



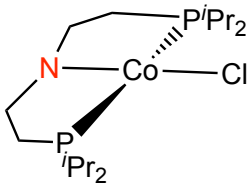
CoCl$_2$(L4)



CoCl$_2$(^{i}Pr$_2$PCH$_2$CH$_2$)$_2$NMe

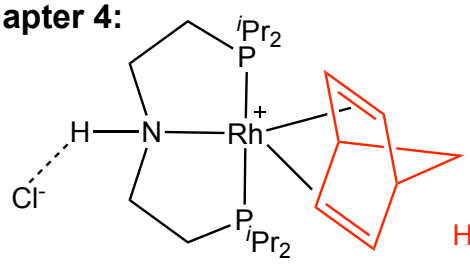


CoCl(^{i}Pr$_2$PCH$_2$CH$_2$)$_2$N

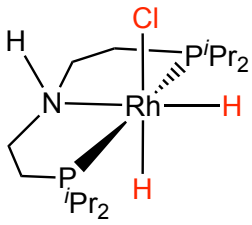


CoCl(^{i}Pr$_2$PCH$_2$CH$_2$)$_2$N

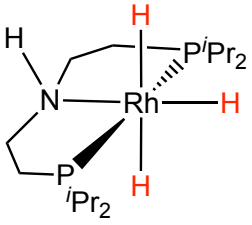
Chapter 4:



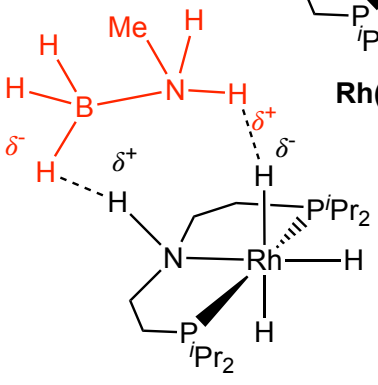
[Rh(L3)NBD]Cl



Rh(L3)H$_2$Cl



Rh(L3)H$_3$



Rh(L3)H$_3$(H$_3$B·NMeH$_2$)

Abstract

This thesis at looks the synthesis of a Co(I) σ-alkane complex and the development of cobalt and rhodium catalysts for the dehydropolymerisation of amine-boranes. Chapter 1 provides a brief introduction to the organometallic chemistry of cobalt and rhodium.

Chapter 2 describes the synthesis of an X-ray crystallographically characterised cobalt σ-alkane complex, **[Co(Cy$_2$P(CH$_2$)$_4$PCy$_2$)(norbornane)][BAr$^F{}_4$]**. This complex was prepared by a solid/gas route from a norbornadiene precursor *via* a single-crystal to single-crystal hydrogenation. SQUID magnetometry data show this complex to be in a triplet electronic state, suggesting this is a relatively unstable σ-alkane complex. Periodic DFT and electronic structure calculations demonstrated the importance of dispersive interactions between the alkane ligand and the anion framework in stabilising weak C-H→Co σ-interactions.

In Chapter 3, the simple Co(II) catalyst, **Co(NH((CH$_2$)$_2$P^{i}Pr$_2$)$_2$)Cl$_2$**, was used in amine-borane dehydropolymerisation. This pre-catalyst operates at low loadings to selectively give $(H_2B{\cdot}NMeH)_n$ polymer on a 10 g scale. Increasing catalyst loading decreased the M_n of isolated polymer, while maintaining narrow dispersities. A Mayo analysis of the polymer formed and chain transfer agents enabled the speciation of catalysis to be probed.

Chapter 4 reports on a bench stable pre-catalyst, [**Rh(NH((CH$_2$)$_2$P^{i}Pr$_2$)$_2$)NBD]Cl**, for the selective dehydropolymerisation of $H_3B{\cdot}NMeH_2$ on 10 g scale. Detailed speciation studies showed an amine-borane adduct **Rh(NH((CH$_2$)$_2$P^{i}Pr$_2$)$_2$)H$_3$(H$_3$B·NMeH$_2$)** was the on-cycle resting state. Kinetic profiles of dehydrogenation were determined from eudiometer data and the rate law found to be rate = $k[\text{Catalyst}]^1[H_3B{\cdot}NMeH_2]^0$. Kinetic isotope effects were determined using $D_3B{\cdot}NMeH_2$ and $H_3B{\cdot}NMeD_2$. All these data together with computational studies enabled a catalytic cycle to be determined. M_n could be selectively decreased by doping with $[(H_2NMe)_2BH_2]Cl$ allowing chain control as described by a Mayo analysis. Chapter 3 and 4 have enabled the preparation of polyaminoboranes on scale with chain length control.

Contents

Declaration i
Acknowledgements ii
Abbreviations v
Complexes viii
Abstract ix
Contents x
Chapter 1: Introduction 1
1.1 Catalysis 1
1.2 Rhodium organometallic catalysis 2
1.3 Weakly coordinating anions 5
1.4 Cobalt organometallic catalysis 6
1.5 Environmental considerations 11
1.6 Phosphines 12
1.7 σ-complexes 15
1.8 References 19
Chapter 2: A structurally characterised cobalt(I) σ-alkane complex 22
2.1 Introduction 22
2.1.1 In-situ photolysis generation of σ-alkane complexes in matrixes 23
2.1.2 In-situ photolysis generation of σ-alkane complexes in solution 24
2.1.3 In-situ protonation generation of σ-alkane complexes in solution 25
2.1.4 Solid-state synthesis of σ-alkane complexes 26
2.1.5 Solid-state reactivity of σ-alkane complexes with D_2 28
2.1.6 Room temperature solid-state dehydrogenation of σ-alkane complexes 29
2.1.7 Catalytic solid-gas 1-butene isomerisation by SMOM systems. 30
2.1.8 Solid-state reactivity of cationic iridium diene complexes with H_2 32
2.1.9 Previous attempts to synthesises σ-alkane complexes of cobalt 32
2.2 Results and Discussion 35
2.2.1 Synthesis and characterisation of [Co(L1)NBD][BAr^F_4] 35
2.2.2 Synthesis and characterisation of [Co(L1)(η-FC_6H_5)][BAr^F_4] 38
2.2.3 Solution state reactivity of [Co(L1)(η-FC_6H_5)][BAr^F_4] 39
2.2.4 Magnetic studies of [Co(L1)NBD][BAr^F_4] and [Co(L1)(η-FC_6H_5)][BAr^F_4] 40
2.2.5 Solid-state reactivity of [Co(L1)NBD][BAr^F_4] with H_2. 43
2.2.6 Synthesis and characterisation of [Co(L2)NBD][BAr^F_4] 44
2.2.7 Synthesis and characterisation of [Co(L2)NBA][BAr^F_4] 46
2.2.8 Magnetic studies of [Co(L2)NBD][BAr^F_4] and [Co(L2)NBA][BAr^F_4] 50
2.2.9 Bound volatile trapping experiments of [Co(L2)NBA][BAr^F_4] 52
2.2.10 Solid-state reactivity of [Co(L2)NBA][BAr^F_4] with D_2 53
2.2.11 Solid-state reactivity of [Co(L2)NBA][BAr^F_4] with 1-butene 54

2.2.12 Computational characterisation of [Co(L2)NBD][BAr^F_4] 55
2.3 Conclusions 59
2.4 References 60
Chapter 3: A simple cobalt-based catalyst system for the controlled dehydropolymerisation of $H_3B{\cdot}NMeH_2$ on the gram-scale 63
3.1 Introduction 63
3.1.1 Dehydropolymerisation of amine-boranes 63
3.1.2 Polymer characterisation 65
3.1.3 Catalyst-free routes to polyaminoboranes 66
3.1.4 Catalysed routes to polyaminoboranes 67
3.1.5 {Rh(chelating diphosphine)} catalysts for dehydropolymerisation. 68
3.1.6 Further late transition metal catalysts for dehydropolymerisation 72
3.1.7 Iron based catalysts for dehydropolymerisation 73
3.1.8 Early and mid-transition metal catalysts for dehydropolymerisation 74
3.1.9 Summary of representative dehydropolymerisation catalysts 74
3.1.10 Cobalt catalysed routes to polyaminoboranes 76
3.1.11 Mechanism for the dehydrogenation of amine-boranes 78
3.1.12 Mechanism for the polymerisation of amino-borane ($H_2B{=}NMeH$) 81
3.1.13 Aims of this chapter 84
3.2 Results and discussion 85
3.2.1 Initial Screening of cationic Co(I) catalysts for dehydropolymerisation. 85
3.2.2 Screening of Co(ligand)Cl_2 type catalysts for dehydropolymerisation 86
3.2.3 Optimisation using Co(L3)Cl_2 and Co(L4)Cl_2 pre-catalysts 87
3.2.4 THF as a solvent for dehydropolymerisation of $H_3B{\cdot}NMeH_2$ 90
3.2.5 10 g scale dehydropolymerisation of $H_3B{\cdot}NMeH_2$ using Co(L4)Cl_2 pre-catalyst 93
3.2.6 Processing the $(H_2B{\cdot}NMeH)_n$ produced 93
3.2.7 Mechanistic investigations 94
3.2.8 Testing for homogeneous vs heterogeneous catalysis 94
3.2.9 Suggested mechanism for amine-borane dehydrogenation 95
3.2.10 Pre-catalyst activation pathways 98
3.2.11 Mayo plots – understanding chain transfer agent 100
3.2.12 Role of chain transfer agent - CoCl($^i Pr_2PCH_2CH_2)_2N$ as a probe 101
3.2.13 Role of chain transfer agent - CoCl(L3) as a probe 104
3.3 Conclusions 108
3.4 References 109
Chapter 4: A simple robust rhodium-based catalyst system for the controlled dehydropolymerisation of $H_3B{\cdot}NMeH_2$ on the gram-scale 112
4.1 Introduction 112
4.2 Results and discussion 113
4.2.1 Attempted synthesis of Rh(L3)Cl 113
4.2.2 Synthesis and characterisation of [Rh(L3)NBD]Cl 113
4.2.3 Synthesis and characterisation of [Rh(L3)NBD][BAr^F_4] 115
4.2.4 Synthesis and characterisation of [Rh(L3)$H_2(H_3B{\cdot}NMe_3)$][BAr^F_4] 116

4.2.5 Use of [Rh(L3)NBD]Cl, [Rh(L3)H_2(H_3B·NMe_3)][BAr^F_4] and [Rh(L3)NBD][BAr^F_4] for the dehydropolymerisation of H_3B·$NMeH_2$ in 1,2-$C_6H_4F_2$ 119
4.2.6 Use of [Rh(L3)NBD]Cl for dehydropolymerisation of H_3B·$NMeH_2$ in THF 122
4.2.7 Varying the concentration of H_3B·$NMeH_2$ for dehydropolymerisation 125
4.2.8 Effect on kinetic profile of varying catalyst loading using [Rh(L3)NBD]Cl 127
4.2.9 Synthesis and characterisation of [Rh(HN((CH_2)$_2$$PPh_2$)$_2$)NBD]Cl 129
4.2.10 Dehydropolymerisation of H_3B·$NMeH_2$ using Rh(HN((CH_2)$_2$$PPh_2$)$_2$)NBD]Cl 130
4.2.11 Testing for homogeneous vs heterogeneous catalysis 131
4.2.12 Investigating sensitivity to hydrogen and water 133
4.2.13 Attempted synthesis of [Rh(MeN((CH_2)$_2$)P^iPr_2)NBD]Cl 136
4.2.14 Effect on kinetic profile of varying temperature using [Rh(L3)NBD]Cl 136
4.2.15 Speciation study on [Rh(L3)NBD]Cl 138
4.2.16 Activation pathway for [Rh(L3)NBD]Cl to Rh(L3)H_3(H_3B·$NMeH_2$) ... 142
4.2.17 Activation pathway for Rh(L3)H_2Cl to Rh(L3)H_3 142
4.2.18 Formation of Rh(L3)H_2Cl at the end of catalysis 143
4.2.19 Synthesis of Rh(L3)H_2Cl 144
4.2.20 In-situ generation of Rh(L3)H_3 147
4.2.21 Formation of Rh(L3)H_2Cl by reaction of Rh(L3)H_3 with boronium .. 148
4.2.22 Kinetic profile of dehydropolymerisation of H_3B·$NMeH_2$ using Rh(L3)H_2Cl 149
4.2.23 Effect on kinetic profile of varying catalyst loading using Rh(L3)H_2Cl 150
4.2.24 Effect on kinetic profile of varying temperature using Rh(L3)H_2Cl 153
4.2.25 Speciation Study on Rh(L3)H_2Cl 154
4.2.26 Computational studies 156
4.2.27 Determination of kinetic isotope effects using [Rh(L3)NBD]Cl 159
4.2.28 Determination of kinetic isotope effects using Rh(L3)H_2Cl 159
4.2.29 Alternative mechanism 165
4.2.30 Variation of M_n with catalyst loading 166
4.2.31 Further mechanistic consideration of the $CoCl_2$(L3) pre-catalyst .. 167
4.2.32 Molecular weight control of (H_2B·NMeH)$_n$ with boronium doping .. 169
4.2.33 10 g H_3B·$NMeH_2$ scale dehydropolymerisation reaction 172
4.3 Conclusions 173
4.4 References 174
Chapter 5: Experimental methods 176
5.1 General methods and chemicals 176
5.1.1 General methods and chemicals – Chapter 2 and 3 176
5.1.2 General methods and chemicals – Chapter 4 177
5.1.3 NMR spectroscopic data – Chapter 2 and 3 178
5.1.4 NMR spectroscopic data – Chapter 4 179
5.1.5 Mass spectrometry data 179
5.1.6 Gel permeation chromatography data 180

5.2 Chapter 2 experimental data 181
5.2.1 Synthetic procedures and characterisation data 181
5.2.1.1 Preparation and characterisation of [Co(L1)NBD][BAr^F_4] 181
5.2.1.2 Preparation and characterisation of [Co(L1)(η-FC_6H_5)][BAr^F_4] ... 183
5.2.1.3 Preparation and characterisation of [Co(L2)NBD][BAr^F_4] 186
5.2.1.4 Preparation and characterisation of [Co(L2)NBA][BAr^F_4] 188
5.2.2 Crystallographic and refinement data 190
5.2.2.1 Crystal structure determinations 190
5.2.2.2 Additional comments crystal structures and refinement data ... 190
5.2.2.3 Single crystal X-ray diffraction structures 194
5.2.3 Magnetic characterisation 197

5.3 Chapter 3 experimental data 198
5.3.1 Synthesis of $CoCl_2(^iPr_2PCH_2CH_2)_2NMe$ 198
5.3.2 Dehydropolymerization under open conditions 198
5.3.3 Dehydropolymerization under hydrogen evolution measurement conditions 199
5.3.4 Scale-up dehydropolymerization and metal-removal procedure 199
5.3.5 10 g scale dehydropolymerization of $H_3B{\cdot}NMeH_2$ catalysed by $Co(L4)Cl_2$ 200
5.3.6 In situ formation of $Co(L3)Cl_2$ for the catalytic dehydropolymerisation of $H_3B{\cdot}NMeH_2$ 203
5.3.7 In situ formation of colloidal cobalt nanoparticles for the dehydropolymerisation of $H_3B{\cdot}NMeH_2$ 203

5.4 Chapter 4: Experimental data 204
5.4.1 Synthesis of complexes 204
5.4.1.1 Synthesis of [Rh(L3)NBD]Cl 204
5.4.1.2 Synthesis of [Rh(L3)NBD][BAr^F_4] 207
5.4.1.3 Synthesis of [Rh(L3)H_2($H_3B{\cdot}NMe_3$)][BAr^F_4] 209
5.4.1.5 Synthesis of Rh(L3)H_3 in an NMR tube 217
5.4.1.6 Synthesis of [Rh(HN($(CH_2)_2PPh_2)_2$)NBD]Cl 220
5.4.2 Catalytic dehydropolymerisation of $H_3B{\cdot}NMeH_2$ 222
5.4.2.1 Typical dehydropolymerisation procedure under hydrogen evolution measurement conditions 222
5.4.2.2 Dehydropolymerisation procedure under open conditions in air in a vial 223
5.4.2.3 10g scale dehydropolymerisation of $H_3B{\cdot}NMeH_2$ 223
5.4.2.4 Dehydropolymerisation using boronium as a chain-transfer agent 224
5.4.2.5 General procedure for NMR speciation experiments 224
5.4.4 Crystallographic data 225
5.4.4.1 Crystal structure determinations 225
5.4.4.2 Crystallographic tables 226
5.4.4.3 Single crystal X-ray diffraction structures 228

5.5 References 230

Chapter 1: Introduction

1.1 Catalysis

This thesis will look at the organometallic chemistry of rhodium and cobalt and their use in both the dehydropolymerisation of amine-boranes and the synthesis of a Co(I) σ-alkane complex. A specific introduction to the synthesis of σ-alkane complexes will be presented at the start of Chapter 2 and an introduction to the dehydropolymerisation of amine-boranes at the start of Chapter 3. This introduction chapter is a more general introduction to Rh and Co chemistry.

The global market for catalysis was worth $34.1 bn in 2019, with the value created from this market in downstream sectors (e.g. sales of chemicals, polymers, fuels and vehicles) estimated at $15 trillion.[1] This amounts to some ~20% of global GDP.[2] Additionally, the catalysis market is a sector growing faster than GDP and forecast to reach a net value of $44 bn by 2025.[1] This value is not without reason. All of our lives have been improved by catalytic processes, with benefits including new polymers, pharmaceuticals, cheaper more efficient fuels and a range of commodity chemicals.[3] In the transition towards net-zero, catalysis has an essential role in many areas including the production of biofuels, H_2 and in the batteries of electric cars.[1,4] While 75% of these catalytic processes are heterogeneous, homogeneous catalysis offers advantages when it comes to atomic level understanding and control.[3] Homogeneous catalysts have well-defined active sites which when combined with the ability to interrogate structure by NMR spectroscopy and single-crystal X-ray diffraction make them more easily studied than their heterogeneous counterparts.[5] The ability to readily modify homogeneous catalysts by metal/ligand modification only adds to this relative ease of investigation. This enables the often relatively straight forward determination

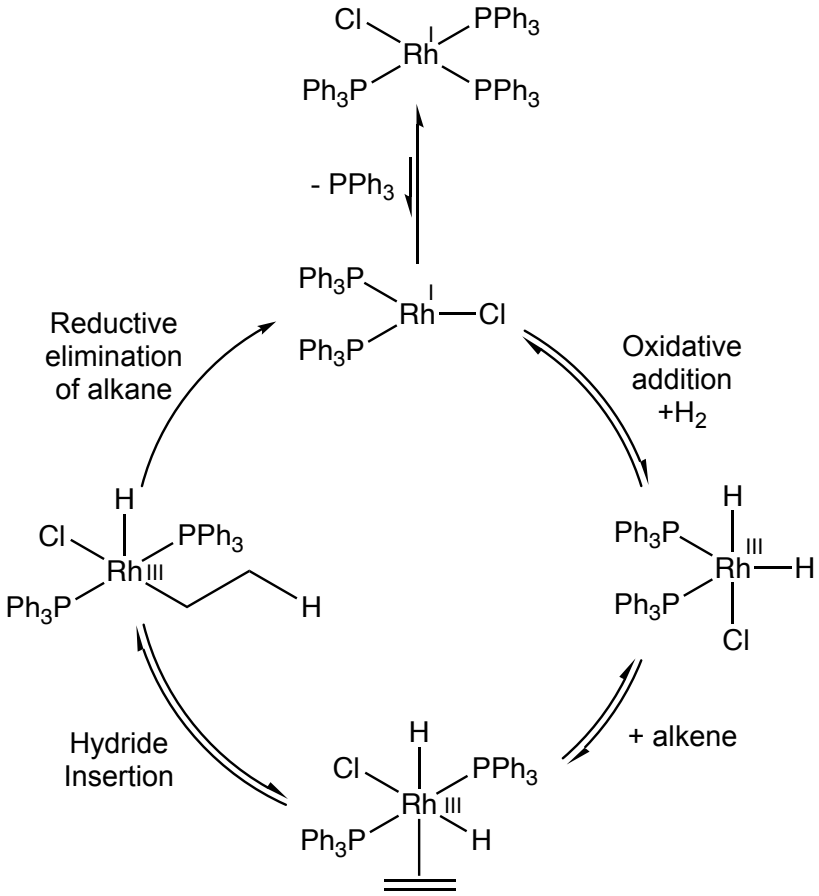
of reaction mechanisms and energetics; this understanding can be applied to iteratively improve and refine catalytic systems more generally.[3]

1.2 Rhodium organometallic catalysis

As already stated this thesis shall focus on rhodium and cobalt organometallics. Rhodium is a late (group 9), second row (4d) transition metal. With rhodium complexes two electron chemistry is almost always observed. For rhodium the most common oxidation states are Rh(I) and Rh(III), and the ability to switch between the two enables rhodium to support key bond activation processes such as oxidative addition and reductive elimination.[5] These regular two electron processes and the relatively large ligand field splitting from a 4d metal result in low spin electronic configurations and thus diamagnetic NMR spectra. Together, these benefits have enabled rhodium catalysts with high activity and predictable selectivity to be developed. Rhodium complexes have been used in a wide range of synthetic processes, and examples include catalytic hydroformylation,[6,7] hydrogenation,[8,9] hydroacylation,[10,11] and hydroboration.[12]

Wilkinson's catalyst, **$Rh(PPh_3)_3Cl$**, is perhaps the best known and prototypical example. **$Rh(PPh_3)_3Cl$** is an effective hydrogenation catalyst that demonstrates many of the features typical to late transition metal catalysis.[13] A simplified catalytic cycle showing only the main operative pathway is shown in Scheme 1.1.[5,14] Initial endergonic loss of PPh_3 is required to form a low-coordinate 14 e^- Rh(I) complex - **$Rh(PPh_3)_2Cl$**. This is followed by rapid oxidative addition of H_2 to form a 16 e^- Rh(III) dihydride - **$Rh(PPh_3)_2H_2Cl$**. Subsequent coordination of an alkene follows which then inserts into the Rh-H bond to give an intermediate Rh(III) alkyl. This alkyl then undergoes irreversible reductive elimination of an alkane to complete the cycle. This is a cycle

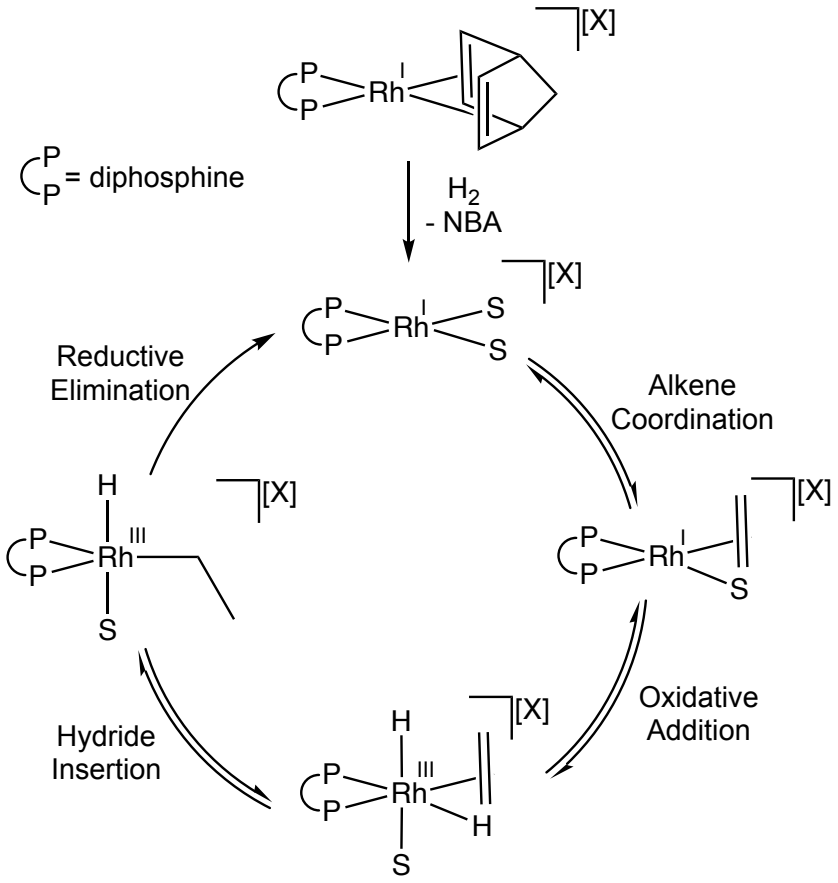
comprised of regular two electron steps, such as oxidative addition and reductive elimination, cycling between Rh(I) and Rh(III). Catalytic performance is essentially limited by the initial unfavourable dissociation of phosphine.



Scheme 1.1 The main operative catalytic pathway for hydrogenation using Wilkinson's catalyst. It is comprised of regular two electron steps like oxidative addition and reductive elimination, cycling between Rh(I) and Rh(III).

Overcoming the unfavourable pre-equilibria has been the focus of much research. One methodology is through use of cationic rhodium(I) complexes with two phosphines and a diene bound, these are known as Shrock-Osborn-type catalysts.[15,16] Commonly these complexes use bisphosphines and so take the form, **[Rh(bisphosphine)(diene)][X]** (X = anion) and are shown in Scheme 1.2. Hydrogenation of the bound diene ligand creates open highly reactive coordination

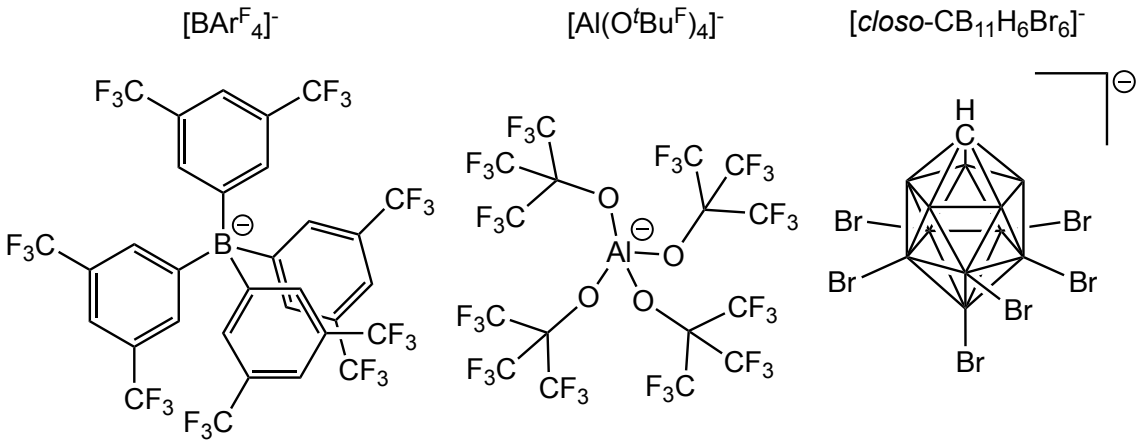
sites which first coordinate weakly bound solvent ligands, such as methanol or acetone. Therefore, these catalysts are no longer limited by the initial unfavourable dissociation of phosphine. When used for hydrogenations, these systems differ mechanistically from Wilkinson's catalyst in that the alkene binds prior to the oxidative addition of hydrogen.[14] However, the mechanism is still proceeds through two electron steps, cycling between Rh(I) and Rh(III). In order to prevent competitive binding of the anion, it is necessary to use weakly coordinating anions.



Scheme 1.2 Schrock-Osborn-type catalysts are frequently used to overcome the problem of unfavourable phosphine dissociation. Hydrogenation of the bound diene ligand creates open highly reactive coordination sites which first coordinate weakly bound solvent ligands. Alkene coordination occurs prior to oxidative addition of hydrogen.

1.3 Weakly coordinating anions

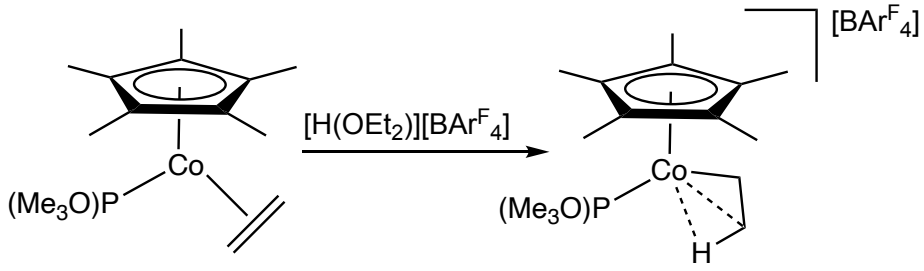
These Schrock-Obsborn-type catalysts have been used to prepare cationic complexes with weakly coordinating ligands (i.e. alkanes), therefore the anion system must be weakly coordinating so that it will not displace an already weakly bound ligand. Additionally the anion must be robust and not undergo competitive side reactions such as hydrolysis or fluoride abstraction as seen with $[PF_6]^-$ and $[BF_4]^-$.[17,18] Borate, carborane and alkoxy anions are common and some examples ($[BAr^F{}_4]^-$, $[Al(O^tBu^F)_4]^-$ and [*closo*-$CB_{11}H_6Br_6]^-$) are shown in Scheme 1.3.[19]



Scheme 1.3 Examples of weakly coordinating anions - $[BAr^F{}_4]^-$, $[Al(O^tBu^F)_4]^-$ and [*closo*-$CB_{11}H_6Br_6]^-$.

$[BAr^F{}_4]^-$ ($[B(3,5\text{-}C_6H_3(CF_3)_2)_4]^-$) is a very weakly coordinating anion and is used within this thesis. $[BAr^F{}_4]^-$ has been integral to the isolation of a number of latent low coordinate complexes. Latent low coordinate complexes are those in which agostic or solvent interactions "mask" a vacant site and the agostic complex **$[Co(Cp^*)P(OMe_3)(CH_2CH_3)][BAr^F{}_4]$** is an example. This complex was isolated as an analytically pure solid by protonation of the ethylene complex **$Co(Cp^*)P(OMe_3)(H_2C{=}CH_2)$** with $[H(OEt_2)][BAr^F{}_4]$.[20] Previous attempts with $[BF_4]^-$ had

all been unsuccessful, so the stability of **[Co(Cp*)P(OMe$_3$)(CH$_2$CH$_3$)][BAr$^F_4$]** was assigned in part to the weakly coordinating anion. This complex was used to catalyse the living polymerisation of ethylene to synthesis polyethylene.

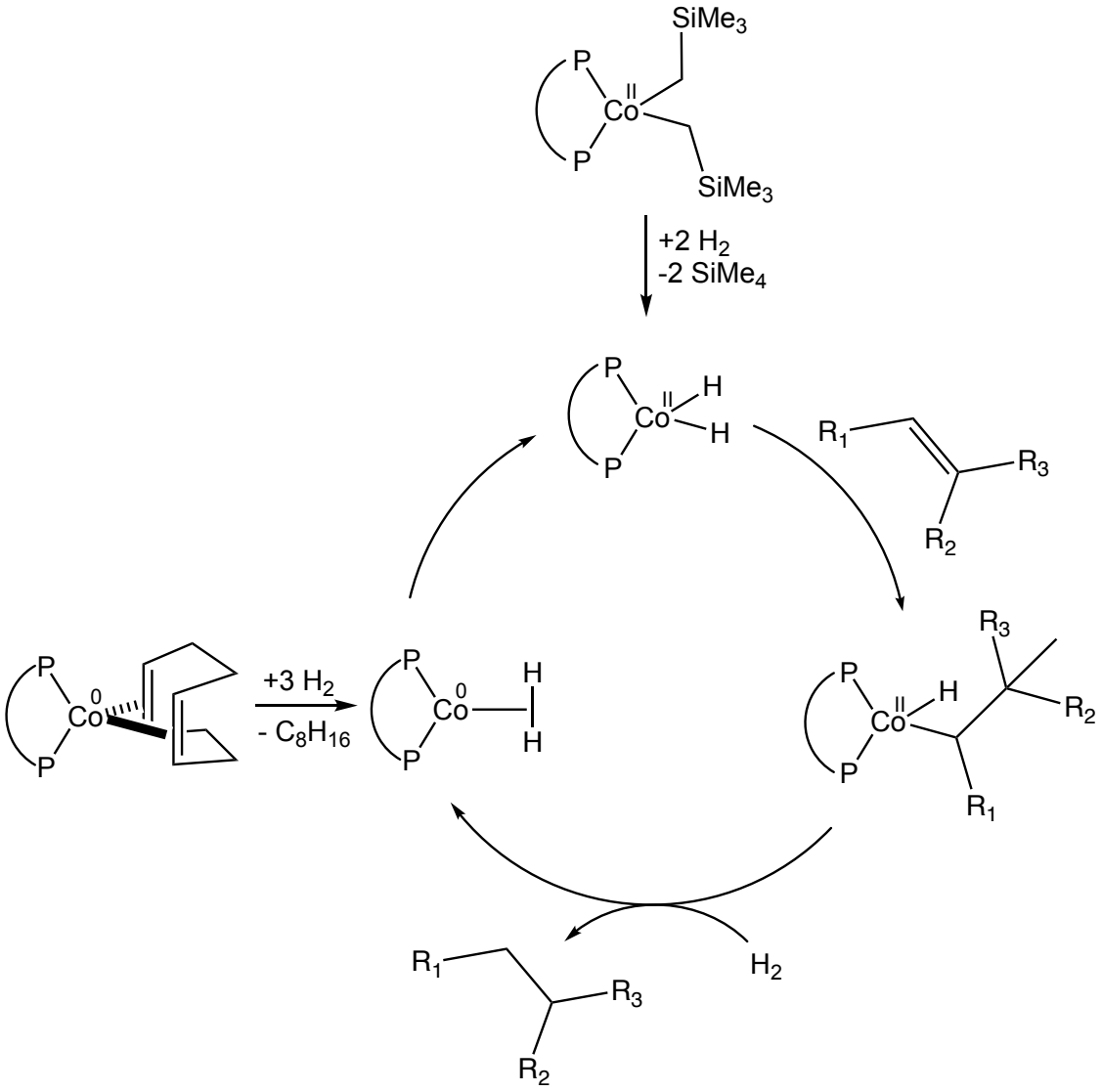


Scheme 1.4 [BAr$^F_4$]$^-$ anion enables the isolation by protonation of the ethylene precursor **[Co(Cp*)P(OMe$_3$)(CH$_2$CH$_3$)][BAr$^F_4$]**.

1.4 Cobalt organometallic catalysis

Cobalt is a first row group 9 transition metal. While historically the organometallic systems developed have focused upon precious metals, in the last two decades there has been a renewed focus on 3d metals such as cobalt. Co complexes have been developed in a wide range of oxidation states from Co(III) to Co(-I).[21] This wide range of oxidation states and smaller ligand field splitting from the 3d metal give the associated complication of open shell electronic configurations and thus paramagnetism. Furthermore, the accessibility of multiple spin states, variable coordination geometries (e.g. tetrahedral and square planar) and relative substitutional lability of 3d metals may give access to new reactivity and a different range of substrates compared to those typical with precious metals.[5] Paramagnetic nuclei result in broad NMR spectra which are dispersed across a wide range of chemical shifts and are more difficult to interpret as a result. Despite this, great progress has been made in synthesis, structural characterisation, reactivity and mechanism. This has allowed

access to catalysis including hydrogenations,[22,23] hydrosilylations,[24,25] and a range of C-C bond forming reactions.[26–28]

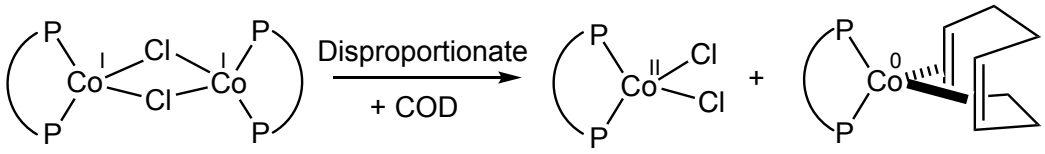


Scheme 1.5 Proposed catalytic cycle for hydrogenation using **(PP)Co(CH$_2$SiMe$_3$)$_2$** and **(PP)Co(COD)** as pre-catalysts for hydrogenation of simple dienes.

The use of **{Co(bisphosphine)}** type complexes for hydrogenation illustrates these properties (Scheme 1.5). The Chirik group have shown that bisphosphine cobalt(II) dialkyl precursor (**(PP)Co(CH$_2$SiMe$_3$)$_2$** where PP = bisphosphine) complexes are effective pre-catalysts for hydrogenation reactions.[23,29,30] It was proposed that these are first activated to the bisphosphine cobalt(II) dihydride - **(PP)Co(H)$_2$**.[31–33]

Subsequent insertion of an alkene into a Co-H bond yields the alkyl hydride intermediate, which then coordinates a dihydrogen molecule and reductively eliminates an alkane to yield the Co(0) σ-dihydrogen complex - **(PP)CoH$_2$**. This σ-dihydrogen complex undergoes oxidative cleavage to close the cycle. Bisphosphine cobalt(0) cyclooctadiene (COD) complexes, **(PP)Co(COD)**, were shown by EPR studies to activate to the same cycle, which was suggested to occur by hydrogenation of the bound diene.[23,29] This mechanism is very similar to that found with Wilkson's catalyst consisting of regular two electron steps, but instead cycling between Co(0) and Co(II).

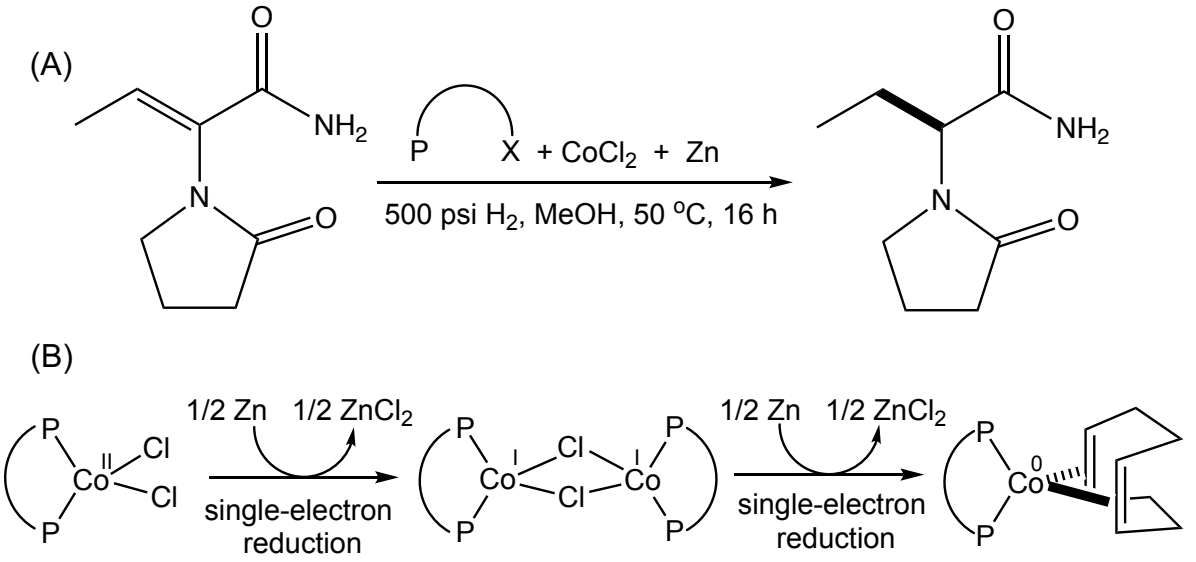
Bisphosphine cobalt(I) bridging dichloride complexes, **((PP)Co)$_2$(μ$_2$-Cl)$_2$**, were shown to give similar selectivity and reactivity to the **(PP)Co(CH$_2$SiMe$_3$)$_2$** and **(PP)Co(COD)** complexes.[29] EPR studies showed that **((PP)Co)$_2$(μ$_2$-Cl)$_2$** was activated by a one electron process in the form of a disproportionation reaction (Scheme 1.7). This reaction led to one equivalent of the bisphosphine cobalt(II) dichloride (**(PP)CoCl$_2$**) and another equivalent of substrate bound complex, such as **(PP)Co(COD)**.



Scheme 1.7 ((PP)Co)$_2$(μ$_2$-Cl)$_2$ undergoes disproportionates to give **(PP)CoCl$_2$** and substrate bound species which can then hydrogenate onto the catalytic cycle.

All of **(PP)Co(CH$_2$SiMe$_3$)$_2$**, **(PP)Co(COD)** and **((PP)Co)$_2$(μ$_2$-Cl)$_2$** are synthetically challenging complexes to prepare, requiring multiple steps and rigorously air and moisture free conditions. However, by making use of one electron reductions, the Chirik group were able to generate the catalyst in-situ. In the presence of a Zn activator, mixtures of asymmetric phosphine and **CoCl$_2$** were found to catalyse the asymmetric hydrogenation of alkenes (Scheme 1.8 (A)).[29] A wide range of phosphines (> 200) were

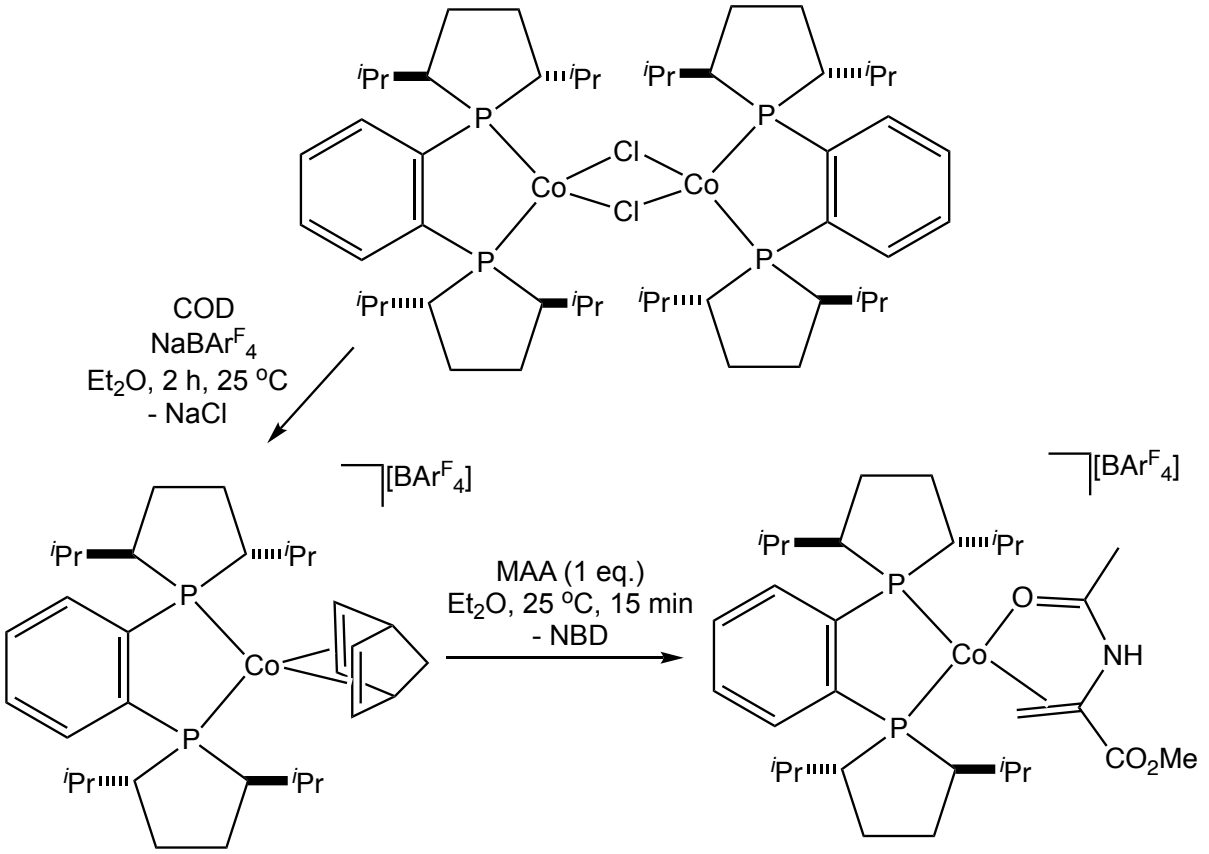
trialled through high-throughput screening. The catalytic cycle was suggested to be as proposed in Scheme 1.8 (B), with the catalyst getting onto cycle by two sequential single electron reductions to form a Co(0) species.



Scheme 1.8 (A) Reaction conditions for enantioselective hydrogenation. **(B)** Activation pathway for **(PP)CoCl₂** in the enantioselective hydrogenations.

Halide abstraction from **((R,R)-(*iPr*DuPhos)Co)₂(μ₂-Cl)₂** with Na[BAr$^F_4$] led to the first literature reported examples of cobalt analogues to Schrock-Osborn type complexes in the form **[(R,R)-(*iPr*DuPhos)Co(COD)][BAr$^F_4$]** and **[(R,R)-(*iPr*DuPhos)Co(NBD)][BAr$^F_4$]** (Scheme 1.9, NBD = norbornadiene).[34] Which were reported at the same time as the work in this thesis was being carried out. These complexes were effective pre-catalysts for the hydrogenation of methyl 2-acetamidoacrylate (MAA) at 50 °C in 12 h under 4 atm H_2. The enantioselectivity for this hydrogenation was greater than that observed with **(PP)Co(CH₂SiMe₃)₂**, **(PP)Co(COD)** and **((PP)Co)₂(μ₂-Cl)₂** suggesting a different mechanism occurs. By stoichiometric reaction with methyl 2-acetamidoacrylate (MAA) the substrate bound complex **[(R,R)-(*iPr*DuPhos)Co(MAA)][BAr$^F_4$]** was isolated in quantitative yield and

suggested to be an intermediate on a Co(I)/Co(III) catalytic cycle. Such a mechanism would be analogous to those reported with the classical rhodium based Schrock-Osborn complexes (Section 1.2).



Scheme 1.9 Synthesis of the first literature reported example of a cobalt equivalent of the ubiquitous Schrock-Osborn-type complexes. Stoichiometric reactivity with MAA yields the substrate bound complex in quantitative yield.

Within these complexes a wide range of spin states and geometries have been reported. **(PP)CoCl$_2$** and **((PP)Co)$_2$(μ_2-Cl)$_2$** are both in high spin states and as a result generally have tetrahedral coordination geometries.[29,35] While both **[(R,R)-(*iPr*DuPhos)Co(COD)][BAr$^F_4$]** and **[(R,R)-(*iPr*DuPhos)Co(NBD)][BAr$^F_4$]** have d^8 low spin electronic structures and have resultant pseudo square planar coordination geometries.[34] Furthermore, the Co(II) **(PP)Co(CH$_2$SiMe$_3$)$_2$** complexes are also low spin and square planar.[23]

In summary, **{Co(bisphosphine)}** type complexes used as pre-catalysts for hydrogenations have been suggested to proceed via a range of catalytic pathways that involve Co(0) through to Co(III) oxidation states. While many of these catalytic steps are based on regular two electron chemistry, single electron processes are also important. With zinc as an initiator single-electron reduction enable in-situ catalyst generation. Additionally, in the absence of Zn single electron disproportionation reactions are also shown to be relevant to catalytic activation. Additionally, both high spin and low spin states were observed, alongside variable coordination geometries (e.g. tetrahedral and square planar) all of which may give access to new reactivity and a different range of substrates to those typical with precious metals. This wider range of reactivity available to cobalt than rhodium presents an additional challenge, but through understanding these processes it should be possible to use them to develop new efficient catalytic pathways.

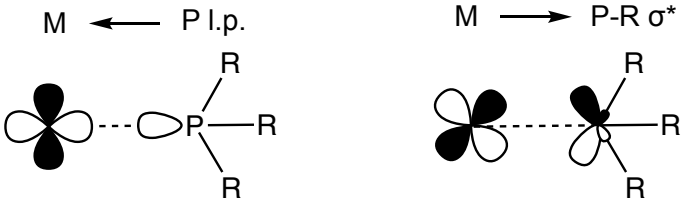
1.5 Environmental considerations

With the current global transition to net-zero it is worth considering the larger impact of the metal identity in a catalytic system. Rhodium is one of the least abundant metals and as a result is one of the most valuable metals in the Earth's lithosphere. Cost is not the only limitation for rhodium - the environmental impact of extracting this scarce element from the earth's crust is significant.[36] Relative to rhodium the environmental impact of cobalt extraction is small, for example, the following cradle-to-gate data are strikingly lower for cobalt than rhodium: global warming potential (35,100 vs 8.3 kg CO_2-eq/kg), cumulative energy demand (683,000 vs 128 MJ-eq/kg), terrestrial acidification (5,200 vs 0.089 kg SO_2-eq/kg), freshwater eutrophication(150 vs 0.004 kg P-eq/kg), and human toxicity (2.7×10^{-1} vs 3.8×10^{-6} CTUh/kg).[36] These data together

with the current global emphasis on sustainable chemistry provide significant motivation for research into cobalt and earth abundant metals generally.

1.6 Phosphines

All of the complexes discussed within this thesis use phosphine ligands (prototypically PR_3) which are one of the most widely used ligands in organometallic chemistry. This popularity is due to their ability to support a wide range of transition metal complexes and oxidation states with an ability to stabilise both electron rich and electron poor metals, over the course of a reaction. Phosphines are readily modified both sterically and electronically enabling them to be easily optimised for specific purposes. In addition, the ^{31}P nucleus with nuclear spin ½ (Abundance = 100 %) provides a useful handle for NMR spectroscopic studies, and this is an important advantage of phosphines over other N and O donors. Phosphine metal bonding can be described as consisting of both σ donation from the phosphorus lone pair to a vacant metal d-orbital and backdonation from filled metal d-orbitals into the P-R σ* antibonding orbital (Scheme 1.10).[5] The extent of these interactions can be modified by varying the R groups.[37]

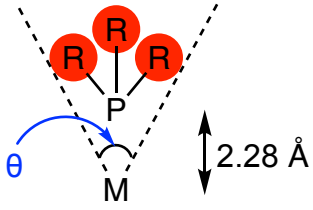


Scheme 1.10 Left, phosphorus lone pair donating into a vacant d-orbital to from a sigma bond. Right, metal d-orbital π back donating into the vacant P-R σ* orbitals.

These interactions can be influenced by the oxidation state of the metal. For example, Chirik's **(PP)$CoCl_2$** complexes were shown to be labile to phosphine substitution with methanol, however reduction to the Co(I) (**((PP)$Co)_2(\mu_2$-$Cl)_2$**) and Co(0) (**(PP)Co(COD)**) complexes reinforced the binding of the phosphine ligand and stopped substitution.[29] This decrease in lability is likely due to increased backdonation from the more electron rich metal centre that increases the M-P bond strength.

The electronic properties of phosphines can be compared using the Tolman electronic parameter. This parameter measures the electron donating ability of the ligand by comparing the highest frequency CO vibration in the IR spectra of **$Ni(CO)_3(PR_3)$** complexes.[38] More electron donating phosphines lead to a decrease in the C-O stretching frequency as more backdonation into the CO ligand occurs from the more electron rich metal. Notably, the more electron withdrawing a substituent (aryl < alkoxy < Cl < F) the further this lowers the energy of the P-R σ*, resulting in a greater interaction with the metal d-orbitals and removing more electron density from the metal centre.[39]

The steric properties of a phosphine can be compared using the Tolman cone angle (θ).[38] The Tolman cone angle is calculated by fixing the M-P bond length to 2.28 Å, where M lies at the vertex and θ is the angle between the outer edges of the R groups in a space filling model of the M-PR_3 (Scheme 1.11). A phosphine with bulkier substituents has a larger cone angle, as demonstrated by P(mesityl)$_3$ having θ = 212^o while PH_3 has θ = 87^o. More refined methods also exist such as buried volume calculations.[40]



Scheme 1.11 Tolman cone angle (θ).

Within this thesis bidentate and pincer 'PNP' type ligands will be used exclusively. Bidentate phosphine ligands contain two phosphorus atoms such as those based on $Ph_2P(CH_2)_xPPh_2$ (x = 2 - 5, Figure 1.1). These can be compared using bite angle (β).[41] Bite angle is a measure of the preferred chelation angle of a multidentate diphosphine and was defined by Casey and Whiteker in 1990.[42] The preferred chelation angle is determined computationally by the constraints of the ligand backbone and angles within ±3 kcal mol^{-1} of the preferred bite angle were considered to be within the flexibility range (FR) of the ligand. They have also been applied to diphosphine pincer ligands more generally.[43] 'PNP' type ligands are particularly interesting as they enable outer sphere effects, which will be discussed further in Chapters 3 and 4.[44]

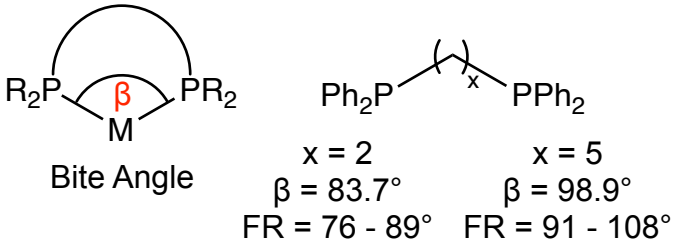
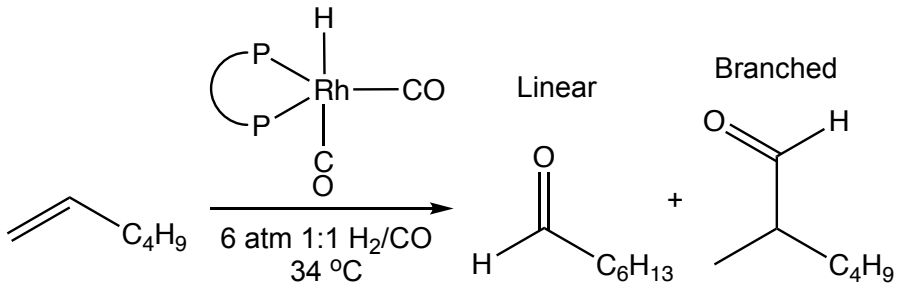
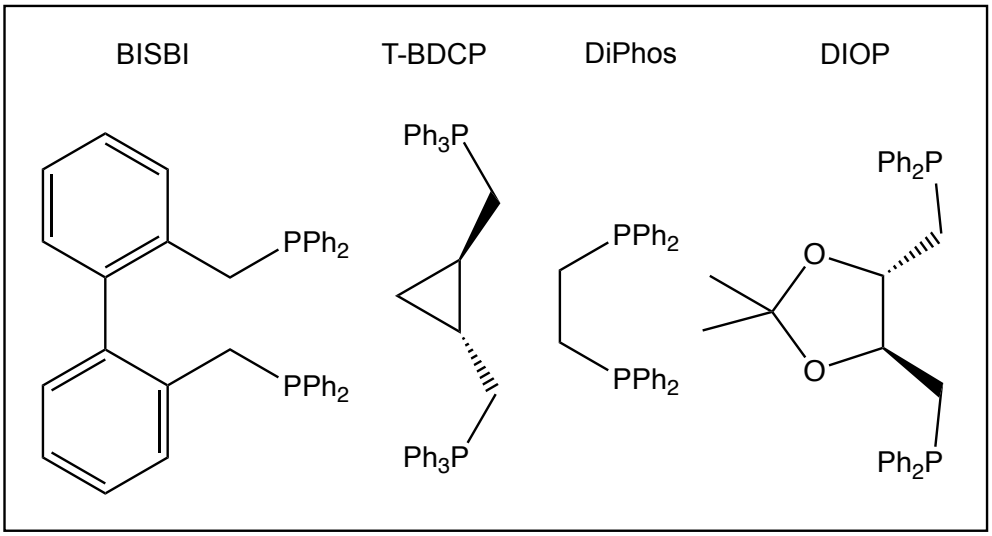


Figure 1.1 Representation of the bite angle (β) and some calculated values for bite angle and flexibility range (FR) for $Ph_2P(CH_2)_xPPh_2$.

Varying bite angle often has predictable effects on selectivity or rate of reactions. A clear example of a bite angle effect is seen for the hydroformylation of 1-hexene using **(diphosphine)$Rh(CO)_2H$** catalysts.[45] Figure 1.2 shows this and a range of phosphines used for this process. It can be seen there is a clear trend of increasing selectivity for

the linear product (heptanal) with increasing bite angle, due to the increased steric bulk at the metal centre favouring a terminal alkyl intermediate.





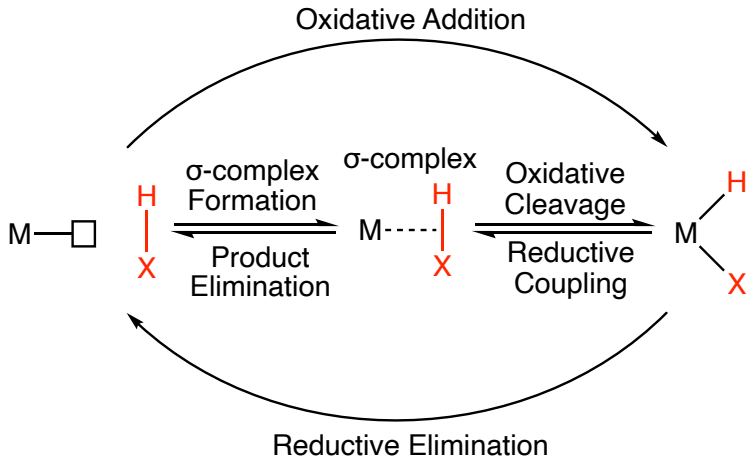
Diphophine	B (°)	Linear:branched ratio
BISBI	112.6	66.5
T-BDCP	106.6	12.1
DIOP	102.2	8.5
DiPhos	84.5	2.1

Figure 1.2 Hydroformylation of 1-hexene using **(Diphosphine)Rh(CO)$_2$H** catalysts. Increasing bite angle correlates to increasing selectivity for heptanal.

1.7 σ-complexes

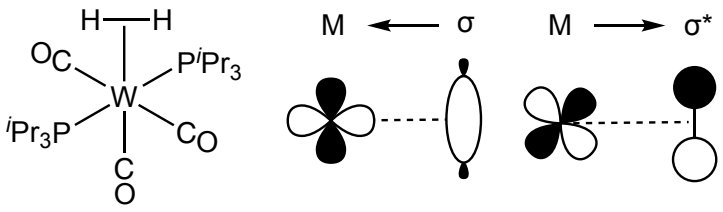
σ-complexes are suggested intermediates in many catalytic cycles for example the hydrogenations using bisphosphine cobalt(II) dialkyl pre-catalysts described in Section 1.4. Metal σ-complex are complexes where an intermolecular X-H σ-bond acts as a donor to a metal centre forming a three centre two electron bond. σ-complexes are

frequently suggested to be key intermediates in oxidative cleavage and reductive bond forming events during catalysis (Scheme 1.12). Understanding the bonding, structure and reactivity of σ-complexes is important to explain bond activation processes and develop new or further refine existing catalytic processes. σ-interactions are distinct from agostic interactions, which occur when there is an intramolecular X-H σ-bond acting as a donor to a metal centre.



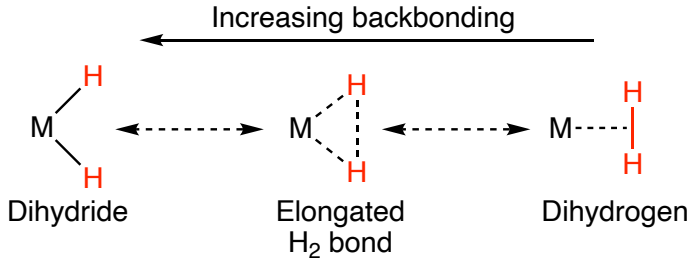
Scheme 1.12 The role of σ-complexes in oxidative addition and reductive elimination.

The archetypal σ-complex is a dihydrogen complex. The first example of a σ-dihydrogen complex was characterised by Kubas in 1984, in the complex **$W(CO)_3(P^iPr_3)_2(\eta^2\text{-}H_2)$** (Scheme 1.13) a σ-complex of H_2.[46] Since then many σ-complexes of H_2 have been reported.[47] This complex exemplifies the bonding in σ-complexes. Two electrons are donated from the H-H σ bonding molecular orbital into a vacant metal d-orbital, and there is a back-donation component from an occupied metal d-orbital into the vacant H-H σ* antibonding orbital (Scheme 1.13). The combination of these bonding interactions leads to side on binding of H_2 through a three centre, two electron bond. This bonding can be studied by single crystal X-ray and neutron diffraction studies, NMR, and IR spectroscopy.



Scheme 1.13 (Left) Kubas's σ-dihydrogen complex. (Right) bonding model for σ-complex.

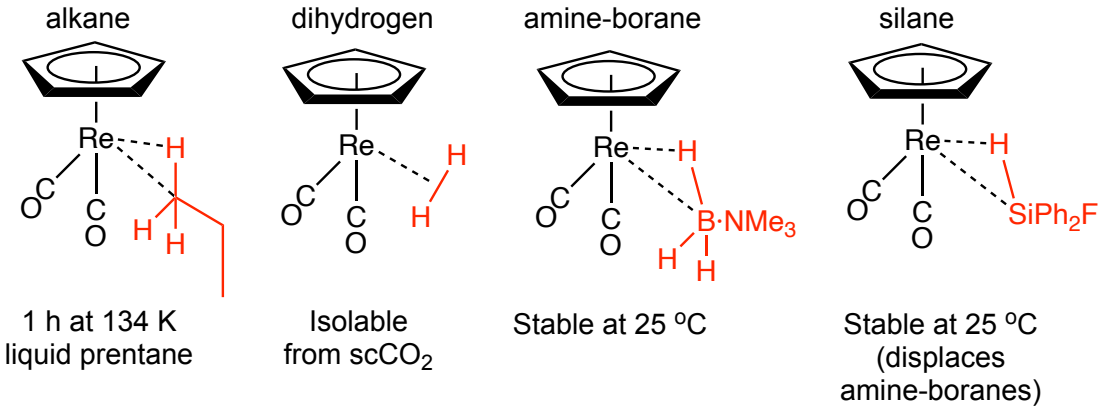
A greater extent of backbonding from the metal will result in a lengthening of the H-H bond and eventually cleavage to the dihydride species (Scheme 1.14). Metals with greater radial extension of the d-orbitals will result in more backbonding and favour dihydrides. Therefore dihydride species are less favoured across a period but more favoured descending a group. The co-ligands on the metal also matter – more strongly accepting π accepting co-ligands will lead to less back donation to H_2 and the σ-complex will be more favoured. Complex charge also matters; cationic metal centres are less electron rich and less prone to back-donation favouring the formation σ-complexes.



Scheme 1.14 More dihydride character favoured by increased backbonding.

While dihydrogen σ-complexes are the archetype they are by no means the only. Silanes and boranes often bind more strongly to metal centres than dihydrogen.[48–50] This bonding is favourable due to the polarisation of the $^{\delta-}$H-E$^{\delta+}$ bond. It has been suggested the borane B-H σ* is too high in energy for effective back-donation but that

the low-lying Si-H σ* are accessible for backbonding.[51,52] Alkanes bind more weakly to metal centres than dihydrogen, boranes or silanes. The C-H bond is essentially non-polar and steric interactions further disfavour the alkanes approach to the metal.[48,53,54] Furthermore, the C-H σ* is relatively high in energy and a poor energy match for back-donation. Scheme 1.15 highlights these general observations for σ-complexes using solution based methods with the same metal fragment.[51,54–56] To summarise, σ-dihydrogen, silane and borane complexes can be relatively stable and are often characterised using NMR spectroscopy and even single-crystals can be grown for single-crystal X-ray diffraction studies. σ-alkanes, on the other hand, are only marginally stable in solution even at low temperatures.[48] This thesis reports on the synthesis of a cobalt(I) σ-alkane complex and also the dehydrocoupling of amine-boranes – where both σ-amine-borane and σ-amino-borane complexes have been suggested as important to catalytic activity.[57,58] The next chapter shall report on the synthesis of a structurally characterised cobalt(I) σ-alkane complex; starting with an introduction the prior literature on the synthesis of these complexes.



Scheme 1.15 Comparing the stability σ-complexes of **Mn(η^5-C$_5$H$_4$R)(CO)$_2$L**. Where L = propane,[59] H_2,[55] $H_3B{\cdot}NMe_3$,[52] $HSiPh_2F$.[56] $scCO_2$ = super critical CO_2.

1.8 References

(1) Lynch, M. K.; Frsc, C. **2020**.

(2) GDP (current US$) | Data https://data.worldbank.org/indicator/NY.GDP.MKTP.CD (accessed Sep 24, 2021).

(3) *Metal-catalysis in Industrial Organic Processes*; Royal Society of Chemistry, 2007.

(4) Wittcoff, H. A.; Reuben, B. G.; Plotkin, J. S. *Industrial Organic Chemicals: Third Edition*; John Wiley & Sons, 2013.

(5) Crabtree, R. H. *Organomet. Chem. Transit. Met. Sixth Ed.* **2014**, *9781118138076*, 1–504.

(6) Franke, R.; Selent, D.; Börner, A. *Chem. Rev.* **2012**, *112* (11), 5675–5732.

(7) Evans, D.; Osborn, J. A.; Wilkinson, G. *J. Chem. Soc. A Inorganic, Phys. Theor.* **1968**, *62* (0), 3133–3142.

(8) Osborn, J. A.; Jardine, F. H.; Young, J. F.; Wilkinson, G. *J. Chem. Soc. A Inorganic, Phys. Theor.* **1966**, *I* (0), 1711–1732.

(9) Etayo, P.; Vidal-Ferran, A. *Chem. Soc. Rev.* **2012**, *42* (2), 728–754.

(10) Barwick-Silk, J.; Hardy, S.; Willis, M. C.; Weller, A. S. *J. Am. Chem. Soc.* **2018**, *140* (23), 7347–7357.

(11) Willis, M. C. *Chem. Rev.* **2009**, *110* (2), 725–748.

(12) Brown, J. M.; Lloyd-Jones, G. C. *Tetrahedron: Asymmetry* **1990**, *1* (12), 869–872.

(13) Osborn, J. A.; Jardine, F. H.; Young, J. F.; Wilkinson, G. *J. Chem. Soc. A Inorganic, Phys. Theor.* **1966**, No. 0, 1711–1732.

(14) Halpern, J. *Inorganica Chim. Acta* **1981**, *50* (C), 11–19.

(15) Schrock, R. R.; Osborn, J. A. *J. Am. Chem. Soc.* **1976**, *98* (15), 4450–4455.

(16) Shapley, J. R.; Schrock, R. R.; Osborn, J. A. *Journal of the American Chemical Society*. American Chemical Society May 1969, pp 2816–2817.

(17) Shanmugaperumal Kannan; Morgan A. Moody; Charles L. Barnes, and; Duval*, P. B. *Inorg. Chem.* **2006**, *45* (23), 9206–9212.

(18) Paul, R. L.; Amoroso, A. J.; Jones, P. L.; Couchman, S. M.; Reeves, Z. R.; Rees, L. H.; Jeffery, J. C.; McCleverty, J. A.; Ward, M. D. *J. Chem. Soc. Dalt. Trans.* **1999**, *0* (10), 1563–1568.

(19) Krossing, I.; Raabe, I. *Angew. Chemie Int. Ed.* **2004**, *43* (16), 2066–2090.

(20) Brookhart, M.; Grant, B.; Jr., A. F. V. *Organometallics* **2002**, *11* (11), 3920–3922.

(21) Hapke, M.; Hilt, G. *Cobalt Catal. Org. Synth. Methods React.* **2019**, 1–462.

(22) Chirik, P. J. *Acc. Chem. Res.* **2015**, *48* (6), 1687–1695.

(23) Friedfeld, M. R.; Margulieux, G. W.; Schaefer, B. A.; Chirik, P. J. *J. Am. Chem. Soc.* **2014**, *136* (38), 13178–13181.

(24) Sun, J.; Deng, L. *ACS Catal.* **2015**, *6* (1), 290–300.

(25) Chen, C.; Hecht, M. B.; Kavara, A.; Brennessel, W. W.; Mercado, B. Q.; Weix, D. J.; Holland, P. L. *J. Am. Chem. Soc.* **2015**, *137* (41), 13244–13247.

(26) Moselage, M.; Li, J.; Ackermann, L. *ACS Catal.* **2016**, *6* (2), 498–525.

(27) Gao, K.; Yoshikai, N. *Acc. Chem. Res.* **2014**, *47* (4), 1208–1219.

(28) Vinogradov, M. G.; Tuzikov, A. B.; Nikishin, G. I.; Shelimov, B. N.; Kazansky, V. B. *J. Organomet. Chem.* **1988**, *348* (1), 123–134.

(29) Friedfeld, M. R.; Zhong, H.; Ruck, R. T.; Shevlin, M.; Chirik, P. J. *Science* **2018**, *360* (6391), 888–893.

(30) Friedfeld, M. R.; Shevlin, M.; Hoyt, J. M.; Krska, S. W.; Tudge, M. T.; Chirik, P. J. *Science (80-.).* **2013**, *342* (6162), 1076–1080.

(31) Zhong, H.; Shevlin, M.; Chirik, P. J. *J. Am. Chem. Soc.* **2020**, *142* (11), 5272–5281.

(32) Zhong, H.; Friedfeld, M. R.; Camacho-Bunquin, J.; Sohn, H.; Yang, C.; Delferro, M.; Chirik, P. J. *Organometallics* **2018**, *38* (1), 149–156.

(33) Ma, X.; Lei, M. *J. Org. Chem.* **2017**, *82* (5), 2703–2712.

(34) Chirik, P. J.; Zhong, H.; Friedfeld, M. R. *Angew. Chemie Int. Ed.* **2019**, ange.201903766.

(35) Rösler, S.; Obenauf, J.; Kempe, R. *J. Am. Chem. Soc.* **2015**, *137 VN*- (25), 7998–8001.

(36) Nuss, P.; Eckelman, M. J. *PLoS One* **2014**, *9* (7), e101298.

(37) Orpen, A. G.; Connelly, N. G. *J. Chem. Soc. Chem. Commun.* **1985**, No. 19, 1310–1311.

(38) Tolman, C. A. *Chem. Rev.* **2002**, *77* (3), 313–348.

(39) Dias, P. B.; de Piedade, M. E. M.; Simões, J. A. M. *Coord. Chem. Rev.* **1994**, *135–136* (C), 737–807.

(40) Herve´clavier, H.; Nolan, S. P. .

(41) Achord, P. D.; Kiprof, P.; Barker, B. *J. Mol. Struct. THEOCHEM* **2008**, *849* (1–3), 103–111.

(42) Casey, C. P.; Whiteker, G. T. *Isr. J. Chem.* **1990**, *30* (4), 299–304.

(43) Adams, G. M.; Weller, A. S. *Coord. Chem. Rev.* **2018**, *355*, 150–172.

(44) Peris, E.; Crabtree, R. H. *Chem. Soc. Rev.* **2018**, *47* (6), 1959–1968.

(45) Casey, C. P.; Whiteker, G. T.; Melville, M. G.; Petrovich, L. M.; Jr., J. A. G.; Powell, D. R. *J. Am. Chem. Soc.* **2002**, *114* (14), 5535–5543.

(46) Kubas, G. J.; Ryan, R. R.; Swanson, B. I.; Vergamini, P. J.; Wasserman, H. J. *J. Am. Chem. Soc.* **2002**, *106* (2), 451–452.

(47) Kubas, G. J. *Chem. Rev.* **2007**, *107* (10), 4152–4205.

(48) Weller, A. S.; Chadwick, F. M.; McKay, A. I. *Adv. Organomet. Chem.* **2016**, *66*, 223–276.

(49) Kubas, G. J. *J. Organomet. Chem.* **2014**, *751*, 33–49.

(50) Kubas, G. J. *Met. Dihydrogen σ-Bond Complexes* **2001**.

(51) Alcaraz, G.; Sabo-Etienne, S. *Coord. Chem. Rev.* **2008**, *252* (21–22), 2395–2409.

(52) Kawano, Y.; Yamaguchi, K.; Miyake, S.; Kakizawa, T.; Shimoi, M. *Chem. – A Eur. J.* **2007**, *13* (24), 6920–6931.

(53) Hall, C.; Perutz, R. N. *Chem. Rev.* **1996**, *96* (8), 3125–3146.

(54) Calladine, J. A.; Duckett, S. B.; George, M. W.; Matthews, S. L.; Perutz, R. N.; Torres, O.; Vuong, K. Q. *J. Am. Chem. Soc.* **2011**, *133* (7), 2303–2310.

(55) Banister, J. A.; Lee, P. D.; Poliakoff, M. *Organometallics* **1995**, *14*, 3876–3885.

(56) Schubert, U.; Ackermann, K.; Woerle, B. *J. Am. Chem. Soc.* **2002**, *104* (25), 7378–7380.

(57) Kumar, A.; Beattie, N. A.; Pike, S. D.; Macgregor, S. A.; Weller, A. S. *Angew. Chemie Int. Ed.* **2016**, *55* (23), 6651–6656.

(58) Dallanegra, R.; Robertson, A. P. M.; Chaplin, A. B.; Manners, I.; Weller, A. S. *Chem. Commun.* **2011**, *47* (13), 3763–3765.

(59) Calladine, J. A.; Duckett, S. B.; George, M. W.; Matthews, S. L.; Perutz, R. N.; Torres, O.; Vuong, K. Q. *J. Am. Chem. Soc.* **2011**, *133* (7), 2303–2310.

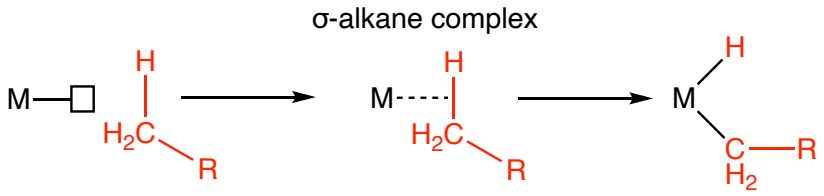
Chapter 2: A structurally characterised cobalt(I) σ-alkane complex

2.1 Introduction

Natural gas and petroleum are both near exclusively burnt as fuel sources. Meanwhile, petrochemicals have the potential for use as vast and inexpensive chemical feedstocks. There is currently a lack of practical, convenient and low energy methods to convert these hydrocarbons efficiently and selectively into synthetically valuable chemicals.[1,2] There are 200 Tm^3 of natural gas reserves, with 97% of this burnt for calorimetric value or flared.[3,4] Flaring is a process whereby at locations where natural gas cannot be economically stored or transported, it is burnt. Flaring accounts for enough energy to power 74 million automobiles.[5] Clearly, converting this gas (mainly methane) to a liquid that could be used as a chemical feedstock or fuel has significant potential economic and environmental benefits.

A potential route for converting hydrocarbons into synthetically useful chemicals is through use of transition metal catalysts to carry out C-H activation reactions where functional groups are installed into the hydrocarbon.[6] The key intermediates in these reactions would be σ-alkane complexes (Scheme 2.1). The C-H alkane bond is nonpolar; the HOMO (C-H σ) is too low in energy to be effective at electron donation, and the LUMO (C-H σ*) is too high to effectively accept electron density.[7] Bonding is further disadvantaged by the directional and sterically crowded nature of the alkane. The combination of this poor orbital energy match and steric repulsion make the alkane a terrible ligand, resulting in weak metal alkane bonding. In solution, the alkane is likely to be rapidly displaced from the metal by solvent or ligand. Therefore, in principle, the coordination of an alkane to a metal should be challenging to observe. Despite these

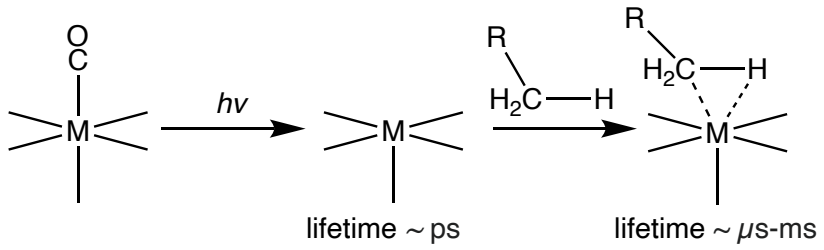
difficulties, a range of methods have been developed to monitor and characterise these complexes.[7]



Scheme 2.1 Showing σ-alkane complexes as key intermediates in transition metal catalysed C-H activations - here an oxidative addition.

2.1.1 In-situ photolysis generation of σ-alkane complexes in matrixes

The first reported examples of σ-alkane complexes came from the photochemistry of metal carbonyl complexes. UV photolysis of these complexes led to the loss of a CO ligand to yield an unsaturated intermediate. If this photolysis was carried out in the presence of an alkane, it was possible to form **ML(CO)$_n$(alkane)** complexes (Scheme 2.2).[7,8] Initially, the experiments were carried out in matrices (Ar or Ar/alkane mixes) and were characterised using in-situ IR and UV-Vis spectroscopy. These experiments have been carried out with various metal complexes, giving evidence for alkane complexes of chromium, molybdenum and tungsten.[9–12] All of these alkane complexes had short lifetimes, on the order of μs to ms, even at low temperatures.

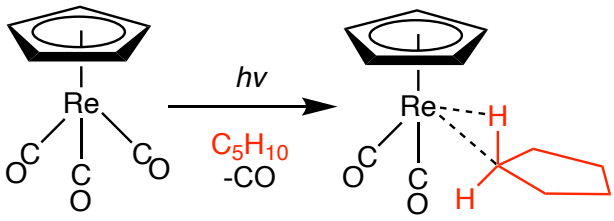


Scheme 2.2 Removal of a carbonyl ligand via photolysis leads to in-situ generation of σ-alkane complexes.

One example is the photolysis of **$Cr(CO)_6$**, which was carried out in mixed matrices (Ar, CH_4 at 20 K). By comparing the UV-Vis spectra and IR spectra between different matrix hosts (Ar vs Ar/CH_4 mix at 20 K), it was proposed that the methane bound to form **$Cr(CO)_5(CH_4)$**.[9] This complex was unstable with respect to both recombination with the carbonyl ligand and other decomposition products.

2.1.2 In-situ photolysis generation of σ-alkane complexes in solution

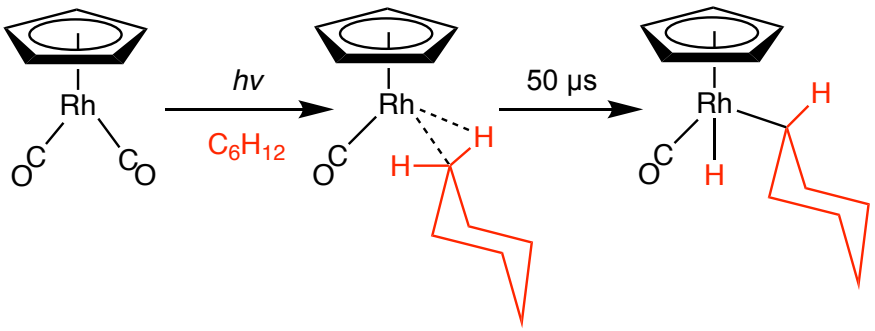
Photolysis is also possible in solution, allowing the use of in-situ NMR spectroscopy, in addition to the IR and UV-vis spectroscopies already mentioned. For example, when **$CpRe(CO)_3$** was photolysed in cyclopentane, it led to the alkane complex **CpRh(CO)(cyclopentane)** (Scheme 2.3), which could be characterised by NMR spectroscopy at -80 °C.[11] In the ^1H NMR spectrum, upon irradiation, a new peak was observed for the Cp ligand at 4.92 ppm (5.23 ppm without irradiation), and a new highly shielded resonance is seen at -2.32 ppm due to the bound alkane. This complex is unstable with a $\tau_{1/2}$ = 22.5 min at -80 °C, forming the insoluble dimer **$Cp_2Re_2(CO)_5$**.



Scheme 2.3 The photolysis of **$CpRe(CO)_3$** at -80 °C in cyclopentane yields **CpRh(CO)(cyclopentane)** with a $\tau_{1/2}$ = 22.5 min.

Additional complexity is present when the alkane is thermodynamically unstable with respect to the C-H activated product. In these cases, the alkane product is only a transient intermediate on the pathway to the C-H activated product. These can be studied by fast time-resolved infrared (TRIR) studies, which can probe the formation of

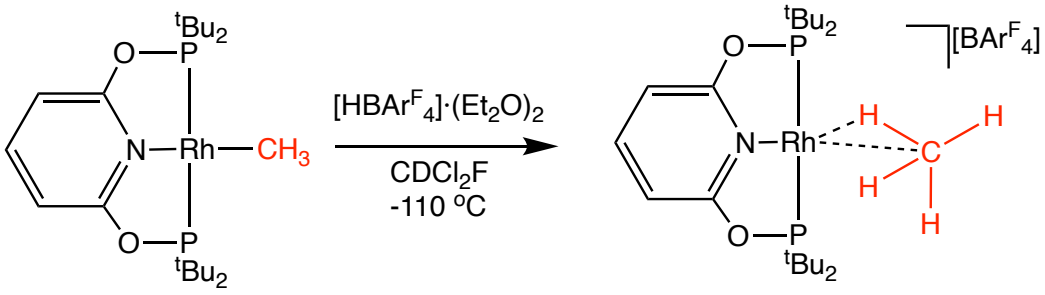
the alkane product and its onwards reactivity. An example of this is **$CpRh(CO)_2$**, shown in Scheme 2.4, which, when photolysed in cyclohexane, generates **CpRh(CO)(H)(Cy)** via a transient intermediate **CpRh(CO)(cyclohexane)**.[12,13] **CpRh(CO)(cyclohexane)** has a 50 μs lifetime at -100 °C in $Kr_{(l)}$.



Scheme 2.4 The photolysis of **$CpRh(CO)_2$** generates **CpRh(CO)(cyclohexane)**, which undergoes rapid C-H activation to **CpRh(CO)(H)(Cy)** at -100 °C.

2.1.3 In-situ protonation generation of σ-alkane complexes in solution

An alternative route to generate a σ-alkane complex is via protonation in solution at low temperature. The rhodium(I) σ-methane complex, **[(PONOP-^{t}Bu)Rh(CH_4)][BAr^F_4]** (PONOP-^{t}Bu = 2,6-(^{t}Bu$_2$PO)$_2$C$_5$H$_3$N) was prepared from the rhodium methyl complex **(PONOP-^{t}Bu)RhCH$_3$** using H[B(Ar^F)$_4$]·(Et_2O)$_2$ in $CDFCl_2$ solvent at -110 °C (Scheme 2.5). The deuterium and ^{13}C labelled equivalents were also prepared to enable complete NMR spectroscopic characterisation.[14] It is important to note that like all σ-alkane complexes so far reported, this complex is unstable with $\tau_{1/2}$ = 83 min at -87 °C. On warming the **[(PONOP-tBu)Rh($CDFCl_2$)][BAr^F_4]** complex forms.[15]



Scheme 2.5 Protonation of **(PONOP)RhCH₃** at -110 °C generates the σ-alkane complex **[(PONOP)Rh(CH₄)][BArᶠ₄]**.

2.1.4 Solid-state synthesis of σ-alkane complexes

A recent focus within the Weller group has been on the isolation of σ-alkane complexes of group 9 metals. To remove the obstacle of solvent coordination, the group has carried out single-crystal to single-crystal (SC-SC) solid-gas reactions, which have led to the isolation of numerous rhodium based σ-alkane complexes, some of which are remarkably stable when isolated in the solid-state.[16,17] For example, addition of H_2 to crystals of the diene precursor **[Rh(L1)NBD][BArᶠ₄]** (Ar^F = 3,5-$(CF_3)_2C_6H_3$, NBD = norbornadiene, L1 = $Cy_2P(CH_2)_2PCy_2$) in the solid-state yields single-crystalline **[Rh(L1)NBA][BArᶠ₄]** (NBA = norbornane) in near quantitative yield on the gram scale (Figure 2.1). This complex can be crystallographically characterised, and the solid-state structure is shown in Figure 2.1 (B). The Rh centre interacts with the C-H bonds of the NBA via 3c-2e σ-bonds. The complex is stable in the solid-state, not degrading even after months.[18] The stability is proposed to come from an octahedral packing environment of the $[BAr^F_4]^-$ anions, with six anions around a cationic fragment. This packing provides stabilising dispersive non-covalent interactions, which allow the hydrogenation to occur without loss of crystallinity (Figure 2.1 (C)).[19] Therefore, key to these systems is both the absence of solvent and the enhanced stability from the

single-crystal microenvironment. We refer to these systems as solid-state molecular organometallics (SMOM), and they are known to support transformations such as alkane C-H activation and catalysis, e.g., solid/gas alkene isomerization.[20]

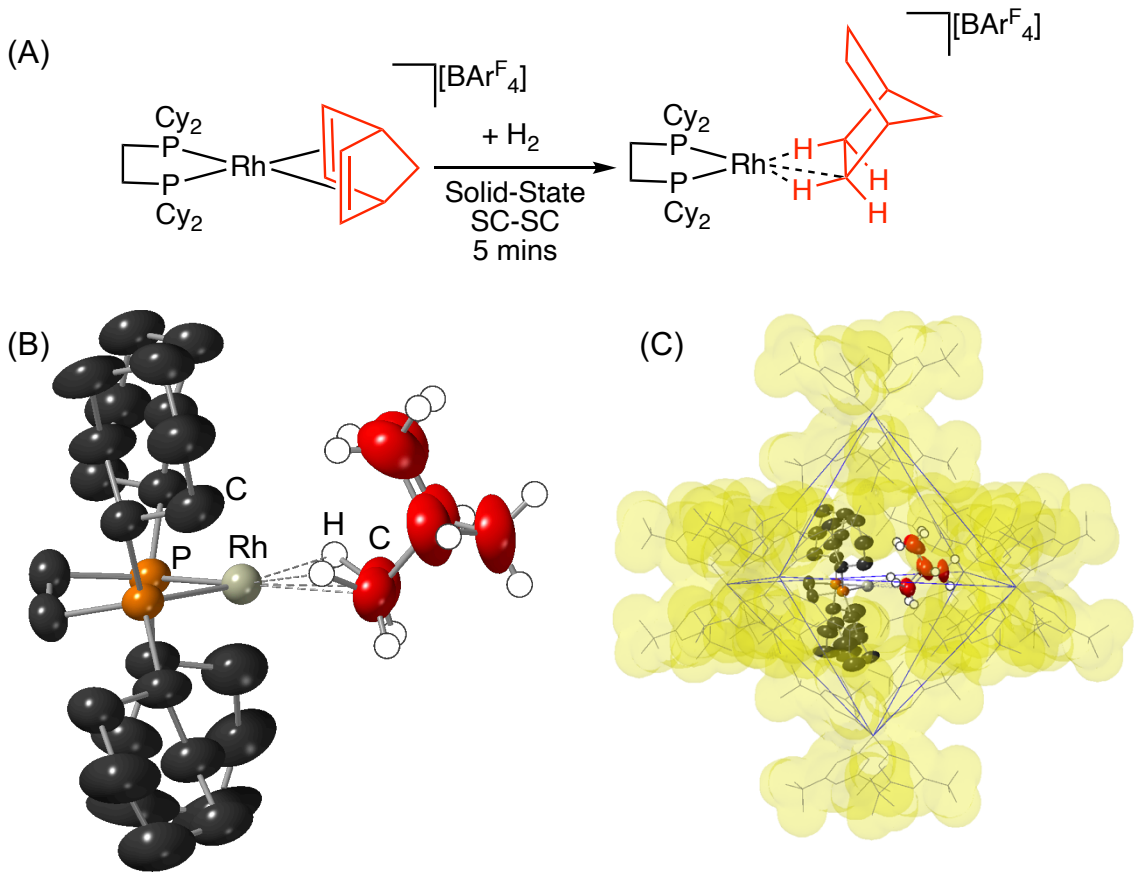
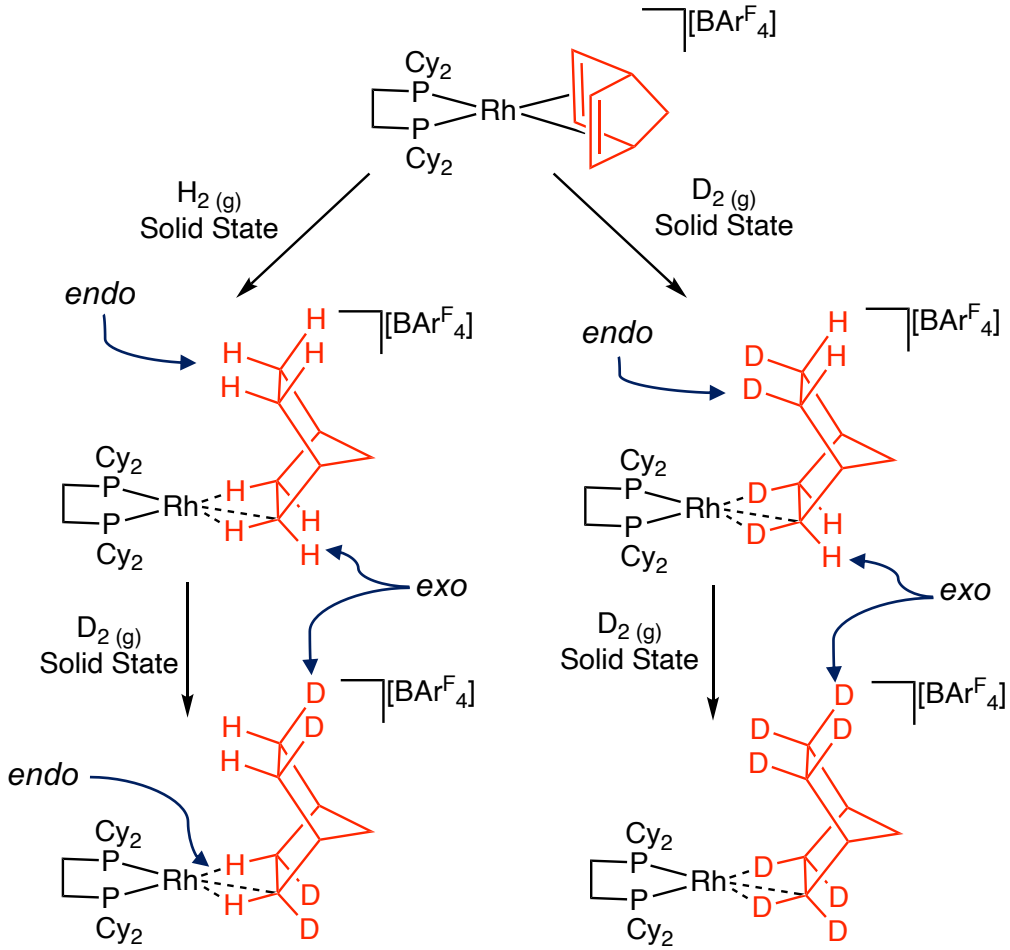


Figure 2.1 (A) The solid-state hydrogenation of **[Rh(L1)NBD][BAr$^F_4$]** yields the quantitative formation of **[Rh(L1)NBA][BAr$^F_4$]**. **(B)** The solid-state structure of the cation; 50% displacement ellipsoids, anion and most H atoms not shown. (**C)** Approximate octahedral packing of six anions around a cationic fragment. Cation displayed at 50% displacement ellipsoids and the anion as a wireframe with a surface plotted at the van der Waals radii.

2.1.5 Solid-state reactivity of σ-alkane complexes with D_2

The σ-bound NBA ligand is known to undergo H/D exchange in the solid-state on exposure to D_2, and the selectivity of deuterium incorporation enables this C-H activation to be probed. For example, when single-crystals of **[Rh(L1)NBA][BAr$^F_4$]** were placed under an atmosphere of D_2 in the solid-state for an extended time, it was determined that deuterium was incorporated only at the *exo* positions of the NBA (Scheme 2.6 left).[16] This incorporation was determined through ^{1}H NMR of vacuum transferred volatiles. When single-crystals of **[Rh(L1)NBD][BAr$^F_4$]** were placed under an atmosphere of D_2 in the solid-state, deuterium was fully incorporated at both the *exo* and *endo* positions (Scheme 2.6 right). Together these data suggest that, in the initial hydrogenation, the deuterium was incorporated at the *endo* position and then in the subsequent H/D exchange the addition occurred at the *exo* positions. All of these transformations occur by SC-SC reactions and deuterium atom placements were confirmed by neutron diffraction studies.

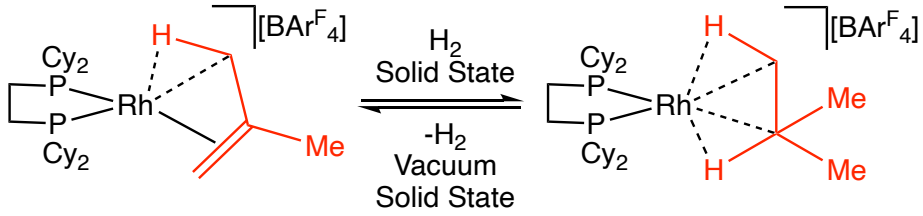


Scheme 2.6 Selective H/D exchange at the *exo* positions of the NBA on **[Rh(L1)NBA][BAr$^F_4$]** by SC-SC reactions in the solid-state.

2.1.6 Room temperature solid-state dehydrogenation of σ-alkane complexes

When single crystals of the complexes **[Rh(L1)(isobutene)][BAr$^F_4$]** and **[Rh(L1)(cyclohexadiene][BAr$^F_4$]** were exposed to a H_2 atmosphere they underwent a SC-SC reaction to form the well-defined isobutane and cyclohexane σ-complexes, **[Rh(L1)(isobutane)][BAr$^F_4$]** and **[Rh(L1)(cyclohexane][BAr$^F_4$].**[21] These complexes could be characterised by single-crystal X-ray diffraction studies and solid-state NMR spectroscopy. Subsequently, exposing crystals of the alkane complexes, **[Rh(L1)(isobutane)][BAr$^F_4$]** and **[Rh(L1)(cyclohexane][BAr$^F_4$],** to either vacuum or

a flow of argon lead to dehydrogenation of the σ-bound alkane to reform the alkene complexes (Scheme 2.7), **[Rh(L1)(isobutene][BAr$^F_4$]** and **[Rh(L1)(cyclohexadiene][BAr$^F_4$]**. This dehydrogenation occurred at room temperature without a hydrogen acceptor and provided insight into the energetics of such alkane dehydrogenation processes when bound at metal centres.[22]

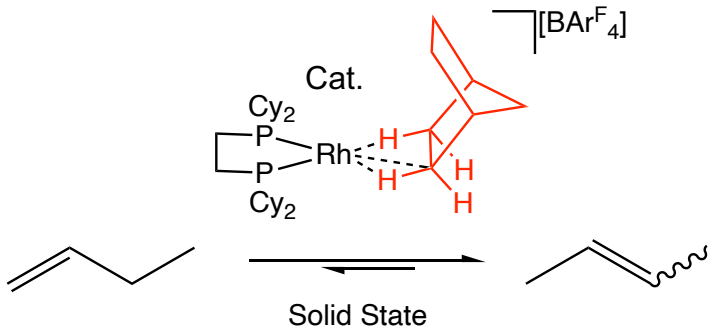


Scheme 2.7 Reversible SC-SC hydrogenation and dehydrogenation of a σ-bound isobutane molecule in the solid-state at room temperature.

2.1.7 Catalytic solid-gas 1-butene isomerisation by SMOM systems.

A reaction supported by these systems is the solid/gas isomerisation of 1-butene to 2-butene shown in Scheme 2.8.[23] Initially, this isomerisation was carried out under batch conditions, where a measured amount of finely divided crystals of σ-alkane complexes such as **[Rh(L1)NBA][BAr$^F_4$]** (~2.5 mg) were placed into a regular J. Youngs NMR tube, the NMR tube was evacuated and refilled with 1-butene and the reaction monitored by gas-phase ^{1}H NMR spectroscopy. Assuming all sites in the crystalline material have equal activity,[18] this catalytic system obtains a turn over number (ToN) of ~50 and a turn over frequency (ToF) of ~30 h^{-1}. These are a minimum ToN and ToF, as sites at the surface of crystals will likely kinetically dominate. The catalytic system reached the thermodynamic equilibrium mixture of 1-butene:2-butene of ~3:97 and a cis:trans ratio of 1:2. The diene bound complexes such as **[Rh(L1)NBA][BAr$^F_4$]** do not

catalyse the isomerisation as 1-butene cannot displace the diene from the metal centre.

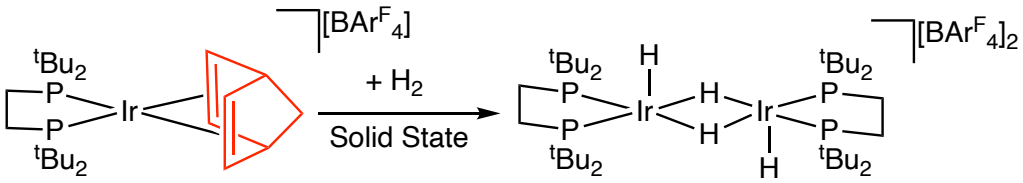


Scheme 2.8 Pre-hydrogenated SMOM systems support catalytic conversion of 1-butene to 2-butene.

More recently, this isomerisation has been carried out under flow conditions by passing a stream of 1-butene over **[Rh(L1)NBA][BArF4]** supported on glass wool and conversion to 2-butene was measured in the outflow of a solid-gas flow reactor via gas chromatography (GC). The catalyst activity was attenuated over time dropping below ~10% conversion to 2-butenes after 3 hours. However, changing ligand, catalyst loading, or other variables were shown to affect this. Changing the R groups on the ligand from Cy to ^{t}Bu increased the on-stream lifetime to 90 h.[20] This represents a significant step towards using these SMOM systems for catalytic processes with real commercial value. The isomerisation of 1-butene potentially has industrial uses. Subsequent metathesis of the 2-butenes produced with ethene, produces propene. After ethene, propene is the alkene in second highest demand.[24] A 100 million tonnes of propene are produced annually and this number is forecasted only to increase. So low energy room temperature routes for the production of propene are of importance.

2.1.8 Solid-state reactivity of cationic iridium diene complexes with H_2

Applying this metal/ligand fragment (key to templating the anion framework) broadly within group 9 was hypothesised to allow isolation of isostructural σ-alkane complexes with the same oxidation state and solid-state packing. Attempts were made to form an analogous iridium σ-alkane complex. Exposing the complex **[Ir(^{t}Bu$_2$PCH$_2$CH$_2$P^{t}Bu$_2$)NBD][BAr$^F_4$]** to a hydrogen atmosphere resulted in a solid/gas reaction occurring to give the bridging hydride product **[Ir(^{t}Bu$_2$PCH$_2$CH$_2$P^{t}Bu$_2$)(H)(μ-H)]$_2$[BAr$^F_4$]$_2$** (Scheme 2.9) without retention of crystallinity. For iridium, the σ-alkane complex is thermodynamically unstable with respect to the bridging hydride; this is due to a strong preference for Ir(III) over Ir(I) and strong bonds from Ir to hydrides.[25] Therefore, a σ-alkane complex of iridium cannot be isolated using SMOM methodology.[26]

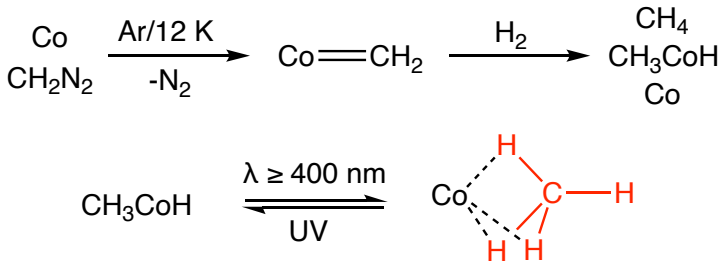


Scheme 2.9 Solid-state hydrogenation of **[Ir(^{t}Bu$_2$PCH$_2$CH$_2$P^{t}Bu$_2$)NBD][BAr^{F}4]** yields the hydride complex **[Ir(^{t}Bu$_2$PCH$_2$CH$_2$P^{t}Bu$_2$)(H)(μ-H)]$_2$[BAr$^F_4$]$_2$**.

2.1.9 Previous attempts to synthesises σ-alkane complexes of cobalt

This chapter shall look up group 9, to the SMOM chemistry of Co organometallics. Remarkably, **Co(CH$_4$)** is the only example of a σ-alkane complex reported in the literature. **CH$_3$CoH** is observed by co-condensation of cobalt atoms, diazomethane, and dihydrogen with argon onto a rhodium-plated copper surface at 12 K (Scheme 2.10). Subsequent photolysis using λ ≥ 400 nm radiation initiated reductive elimination

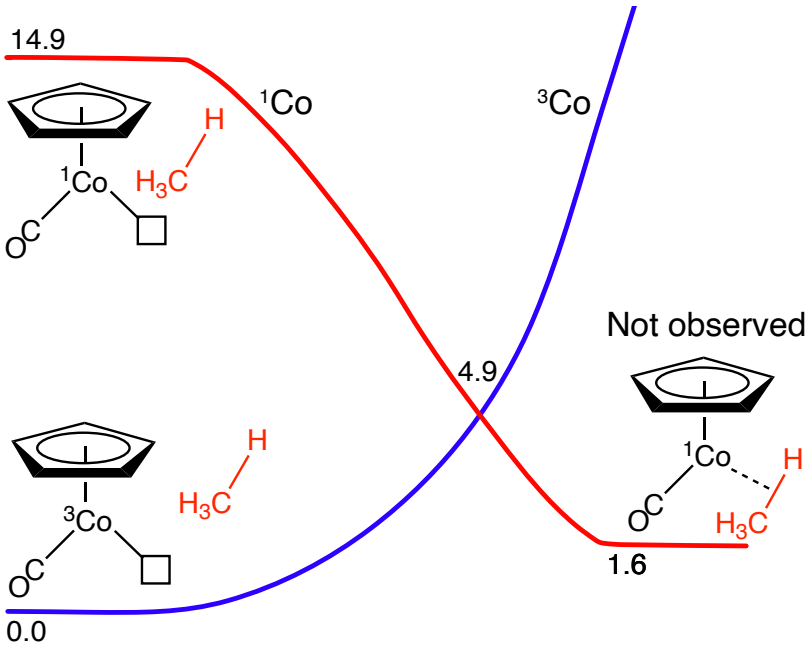
to form the **Co(CH$_4$)** complex, with the reverse upon irradiation with UV. Characterisation with FTIR suggested that the **Co(CH$_4$)** complex had C_{3v} symmetry, indicating the cobalt was bound to three of the C-H bonds as shown in Scheme 2.10.[27]



Scheme 2.10 Co-condensation of Co atoms, CH_2N_2 and H_2 in an Ar matrix at 12 K allowing the synthesis of **CH$_3$CoH**. Subsequent photolysis gives the complex **Co(CH$_4$),** which was characterised by FTIR spectroscopy.

3d metal centres are expected to form weaker σ-bonds with an alkane compared to the 4d/5d metals due to poor metal-alkane orbital overlap resulting from the more contracted metal d-orbitals. For cobalt, these σ-bonds are further disadvantaged by the ^{3}Co(I) triplet electronic state being accessible, with the d^8 electronic structure leading to the partial occupation of all five of the d-orbitals and a significant reduction of the amount of σ-donation possible into the d-orbitals from the C-H bonds of the alkane, due to electron-electron repulsion. As described above, **CpRh(CO)(Alkane)** is observed as a transient intermediate on the way to the C-H activated product.[28] The photolysis of **CpCo(CO)$_2$** leads to **^{3}Co(CO)Cp** generation, but no interaction with alkanes is observed.[29,30] Consistent with this, calculations show that the **Cp(CO)^{1}Co···HCH$_3$** interaction is attractive but has higher energy than the separate ^{3}Co reactants. No significant bounding minimum on the triplet surface could be located. Therefore, the **^{3}Co(CO)Cp···HCH$_3$** interaction would be repulsive, and this complex is not accessible even as a transition state (Scheme 2.11).[31] The triplet σ-alkane complex, **^{3}Mn(CO)$_2$Cp(heptane)**, has been suggested as a transient intermediate on

the pathway to C-H activation, which is feasible due to a vacant d-orbital available for σ-donation into, due to the d^6 electronic structure.[32] Manganese has provided rare examples of σ-alkane complexes of 3d metals characterised, **^{1}Mn(CO)$_2$Cp(propane)** has been observable at very low temperature by photolysis of **Mn(CO)$_3$Cp** in liquid propane.[10,33]



Scheme 2.11 Potential energy profile (kcalmol^{-1}) for the insertion of CH_4 to CpCoCO.[31] The **^{3}Co(CO)Cp···HCH$_3$** interaction would be repulsive, and while **^{1}Co(CO)Cp···HCH$_3$** interaction is net-attractive (lower in energy than **^{1}Co(CO)Cp** and CH_4), it is unstable with respect to separate ^{3}Co reactants and hence not observed.

This chapter reports the synthesis of a cobalt(I) σ-alkane complex **[Co(L2)NBA][BAr$^F_4$]**, by a single-crystal to single-crystal solid/gas hydrogenation from a norbornadiene precursor and its structural determination by X-ray crystallography.

2.2 Results and Discussion

2.2.1 Synthesis and characterisation of [Co(L1)NBD][BAr$^F_4$]

As previously described, SMOM methodology has enabled the isolation of numerous σ-alkane complexes. The lack of solvent and the stabilising environment provided by the anion microenvironment offers the optimum conditions to isolate a σ-alkane complex. To achieve a SMOM synthesis of a cobalt σ-alkane complex, a route to a cationic cobalt diene complex needed to be developed. The most developed SMOM system is **[Rh(L1)NBD][BAr$^F_4$]**, so the Co equivalent was the most rational initial target compound. A synthetic route to **[Co(L1)NBD][BAr$^F_4$]** was developed (Figure 2.2 (A)). This route added the ligand (L1, $Cy_2P(CH_2)_2PCy_2$) in THF to $CoCl_2$, followed by Na[BAr$^F_4$], then a KC_8 reduction and finally a CH_2Cl_2 extraction. The product was isolated as a purple crystalline solid in moderate yield (45 %). Extensive optimisation of this synthesis was carried out mainly through trial and error due to the paramagnetic nature of the cobalt metal, making NMR spectroscopic studies challenging. While the conditions for this synthesis were being optimised, the Chirik group reported the synthesis of the similar compound **[Co(R,R^{iPr}DuPhos)COD][BAr$^F_4$]** (R,R^{iPr}DuPhos = 1,2-bis((2*R*,5*R*)-2,5-diisopropylphospholano)benzene).[34]

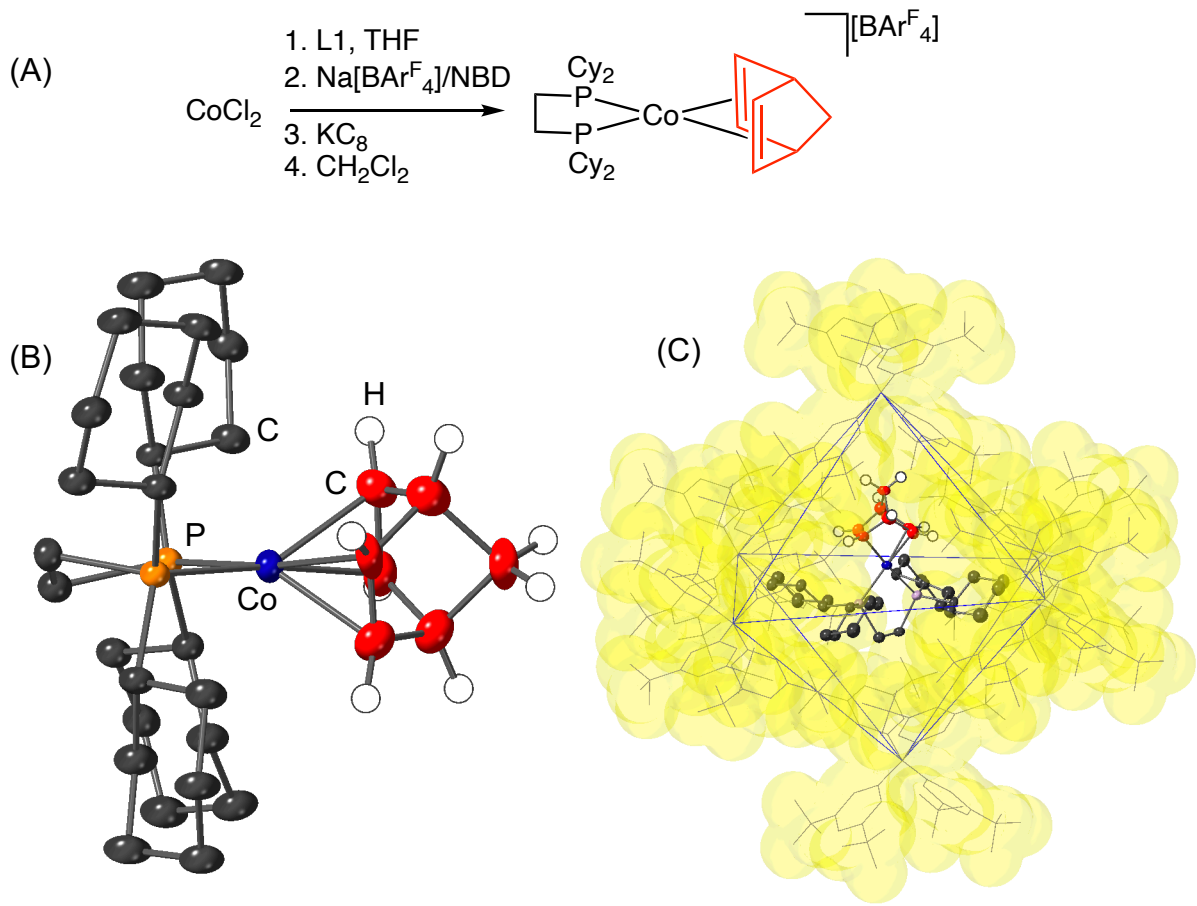


Figure 2.2 (A) Synthesis of **[Co(L1)NBD][BAr$^F_4$]**. **(B)** The solid-state structure of the cation; 30% displacement ellipsoids, anion and most H atoms not shown. **(C)** Approximate octahedral packing of anions. Cation plotted at 30% displacement ellipsoids and anion as a wireframe with a surface displayed at the van der Waals radii.

The solid-state structure of **[Co(L1)NBD][BAr$^F_4$]** is present in Figure 2.2 (B). A useful metric to describe the coordination geometry around the metal centre is the dihedral angle between the P-M-P and the (centC=C)-M-(centC=C) planes, where centC=C is the centres of the respective alkene bonds. For a perfect tetrahedral geometry the dihedral angle would be 90° and the τ parameter 1.[16] While for square planer the diehedral angle would be 0° and the τ parameter 0. For **[Co(L1)NBD][BAr$^F_4$]** the dihedral angle is 22.0(2)° and τ is 0.229(3), which is more twisted than for **[Rh(L1)-NBD][BAr$^F_4$]** (13.1(2)° and 0.159(2) but less twisted than

[Co(R,R^{iPr}DuPhos)COD][BAr$^F_4$] (29.6(4)^o and 0.229(3)). The average Co-P (2.228 Å), Co-C (2.085 Å) and C=C (1.407 Å) distances are similar to those reported for **[Co(R,R^{iPr}DuPhos)COD][BAr$^F_4$]** (Table 2.1). **[Co(L1)NBD][BAr$^F_4$]** has similar Co-P and C=C (1.407(12) Å vs 1.380(10) Å) distances to **[Rh(L1)NBD][BAr$^F_4$]** (2.228(2) Å vs 2.289(2) Å) but shorter M-C (2.085(8) Å vs 2.217(13) Å). These structural data are summarised in Table 2.1. The [BAr$^F_4$]$^-$ anions form an approximate octahedral coordination environment (Figure 2.2 (C)) around the cation, as seen in **[Rh(L1)NBD][BAr$^F_4$]** and **[Co(R,R^{iPr}DuPhos)COD][BAr$^F_4$]**.[18,34]

Compound	**[Co(R,R^{iPr}DuPhos) COD][BAr$^F_4$]**	**[Co(L1) NBD][BAr$^F_4$]**	**[Rh(L1) NBD][BAr$^F_4$]**
Dihedral angle / ^{o}	29.6(4)	22.0(2)	13.1(2)
τ	0.299(3)	0.229(3)	0.159(2)
M-P$_{ave}$ / Å	2.232(3)	2.228(2)	2.289(2)
M-C$_{ave}$ / Å	2.103(5)	2.085(8)	2.217(13)
C=C$_{ave}$ / Å	1.39(2)	1.407(12)	1.380(10)

Table 2.1 Comparison of the bonding metrics of **[Co(R,R^{iPr}DuPhos)COD][BAr$^F_4$]**,[34] **[Co(L1)NBD][BAr$^F_4$]**, and **[Rh(L1)NBD][BAr$^F_4$]**.[18] Average bond distances used. dihedral angle between the P-M-P and the (centC=C)-M-(centC=C) planes. Where centC=C is the centres of the respective alkene bonds.

The ^{31}P{^{1}H} NMR spectrum in solution displays a broad singlet at 61.0 ppm at 298 K, which is unchanged by lowering the temperature to 183 K. In the ^{1}H NMR spectrum, all peaks appear sharp, are readily assigned, and fall within the range expected for a diamagnetic compound (0-8 ppm). The ^{1}H NMR chemical shifts did not vary significantly with temperature which is unexpected for a paramagnetic system where chemical shifts are predicted to follow a Curie (1/T) relationship.[35] Interestingly, the magnetic moment was measured using the Evans method to be μ_{eff}(298 K) = 1.5(1) μB.[36] This magnetic moment is intermediate to what is expected for a ^{1}Co spin-state

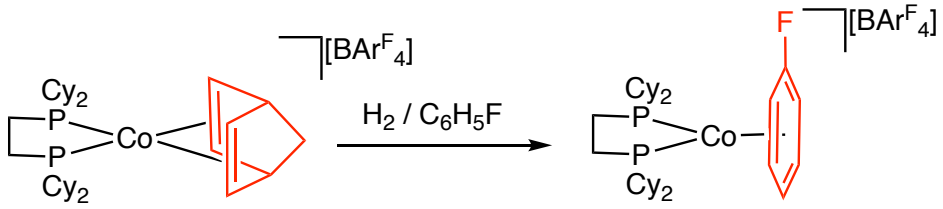
(S = 0, μ_{eff} = 0 μ_B) and a ^{3}Co spin-state (S = 1, μ_{eff} = 2.82 μ_B) and is discussed further in Section 2.2.4.

Schrock and Osborn first prepared cationic bis(phosphine) rhodium(I) complexes over forty years ago.[37] The first examples they reported were **[Rh(PPh$_3$)$_2$COD]$^+$** and **[Rh(PPh$_3$)$_2$NBD]$^+$** with both $[BPh_4]^-$ and $[ClO_4]^-$ anions. This class of complexes have been used as pre-catalysts for various applications from alkene hydrogenation,[38] hydroacylation,[39–41] hydroformylation[42] and C-C bond forming reactions.[43] The equivalent cobalt complexes are essentially unexplored, with Chirik's **[Co(R,R^{iPr}DuPhos)COD][BAr$^F_4$]** the only reported example.[34] On dissolving **[Co(R,R^{iPr}DuPhos)COD][BAr$^F_4$]** in C_6H_5F the complex **[Co(R,R^{iPr}DuPhos)(η-FC$_6$H$_5$)][BAr$^F_4$]** was formed. **[Co(L1)NBD][BAr$^F_4$]** was unchanged on dissolving in C_6H_5F, so solution state reactivity with H_2 was investigated.

2.2.2 Synthesis and characterisation of [Co(L1)(η-FC$_6$H$_5$)][BAr$^F_4$]

Exposing FC_6H_5 solutions of **[Co(L1)NBD][BAr$^F_4$]** to H_2 (1 atm, 298 K) led to a colour change from purple to brown upon mixing and the quantitative formation of **[Co(L1)(η-FC$_6$H$_5$)][BAr$^F_4$]**. Diffusion of *n*-pentane into the C_6H_5F solution led to the isolation of **[Co(L1)(η-FC$_6$H$_5$)][BAr$^F_4$]** as highly air-sensitive brown crystals in 90% yield (Scheme 2.12). The solid-state structure is presented in Figure 2.3. The ^{31}P{^{1}H} NMR spectrum displays a singlet at 95.5 ppm at 298 K. In the ^{1}H NMR spectrum, all signals appear sharp, are readily assigned, and fall within the range expected for a diamagnetic compound (0-8 ppm). The magnetic moment was measured using the Evans method to be μ_{eff}(298 K) = 1.1(1) μB. As with **[Co(L1)NBD][BAr$^F_4$]** this value is intermediate to

what is expected for a ^{1}Co spin-state and a ^{3}Co spin-state and is discussed in more detail later (Section 2.2.4).



Scheme 2.12 Solution-phase synthesis of **[Co(L1)(η-FC$_6$H$_5$)][BAr$^F_4$]**.

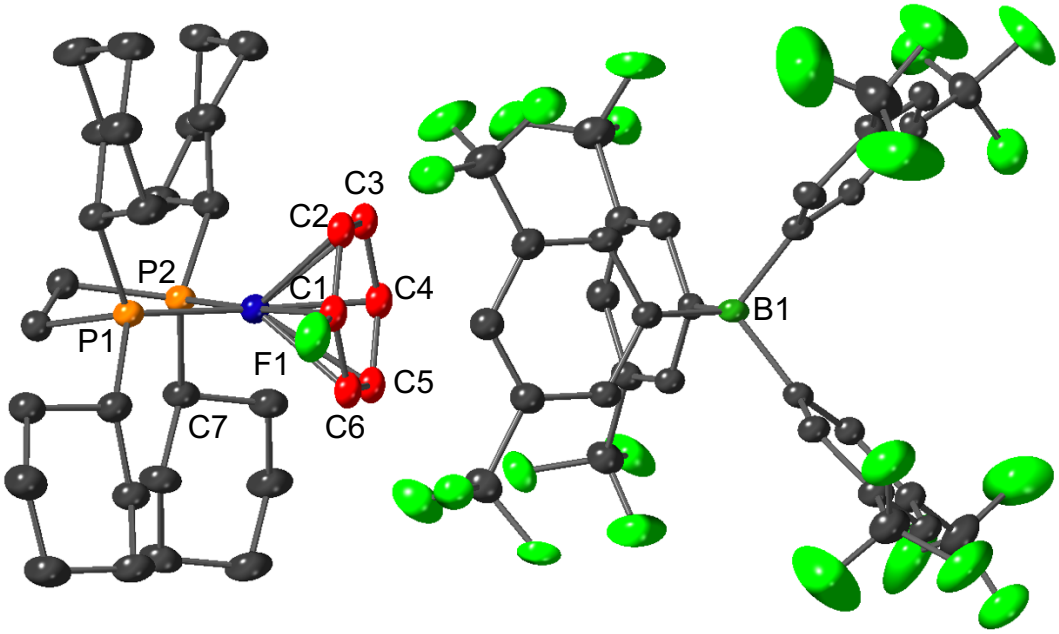
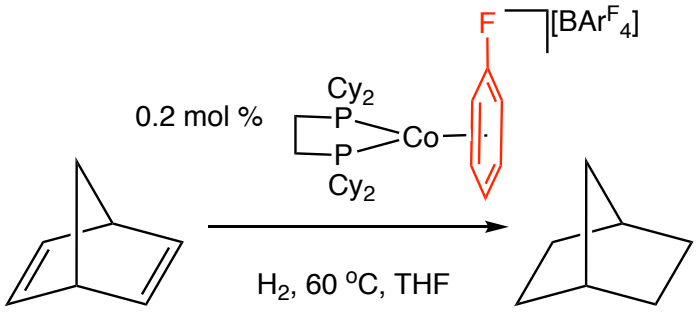


Figure 2.3 Solid-state structure of **[Co(L1)(η-FC$_6$H$_5$)][BAr$^F_4$]**; 30% displacement ellipsoids and H atoms not shown for clarity. Selected bond lengths (Å) and angles (°): Co1-P1 2.1839(16), Co1-P2 2.1803(17), Co-centC1C2C3C4C5C6 1.601(5), P1-Co-P2 86.69(6).

2.2.3 Solution state reactivity of [Co(L1)(η-FC$_6$H$_5$)][BAr$^F_4$]

The solution state reactivity of **[Co(L1)(η-FC$_6$H$_5$)][BAr$^F_4$]** was probed by using it as a pre-catalyst for the hydrogenation of NBD to NBA, which proceeded at 0.2 mol % catalyst loading at 60 °C in THF and went to completion after 12 hours (Scheme 2.13). This is a lower catalyst loading (1 mol% vs 0.2 mol%), comparable hydrogenation

temperature (60 °C vs 50 °C) and same time to completion (12 hours) to that previously reported with **[Co(R,R$^{i\text{Pr}}$DuPhos)COD][BAr$^{F}_{4}$]**.[34] For both systems, these are relatively unoptimised conditions but compare unfavourably to cationic rhodium complexes, which are known to operate at low catalyst loadings (0.05 mol%), at room temperature and with ToFs as high as ~20,000 h^{-1} (which would reach completion in ~2 minutes for the catalyst loading used for **[Co(L1)(η-FC$_6$H$_5$)][BAr$^{F}_{4}$]**).[38] The resting state of catalysis was observed to be **[Co(L1)NBD][BAr$^{F}_{4}$]** by ^{1}H and ^{31}P NMR spectroscopy; pre-hydrogenation was not necessary for effective catalysis. During catalysis, NBD was first hydrogenated to largely norbornene (~80%) which was then hydrogenated to NBA.



Scheme 2.13 Catalytic hydrogenation of NBD to NBA using **[Co(L1)(η-FC$_6$H$_5$)][BAr$^{F}_{4}$]** as a drop-in catalyst.

2.2.4 Magnetic studies of [Co(L1)NBD][BAr$^{F}_{4}$] and [Co(L1)(η-FC$_6$H$_5$)][BAr$^{F}_{4}$]

Earlier in this thesis it was reported that both **[Co(L1)NBD][BAr$^{F}_{4}$]** and **[Co(L1)(η-FC$_6$H$_5$)][BAr$^{F}_{4}$]** possessed magnetic moments intermediate between what would be expected for a singlet (S=0, μ_{eff} = 0 μ_B) and a triplet (S=1, μ_{eff} = 2.82 μ_B) electronic spin state, while displaying NMR spectra suggesting diamagnetism. In order to further investigate the intermediate magnetic moments of **[Co(L1)NBD][BAr$^{F}_{4}$]** and **[Co(L1)(η-FC$_6$H$_5$)][BAr$^{F}_{4}$]**, SQUID (superconducting quantum interference device) magnetometry measurements were performed.

SQUID magnetometry measurements are typically performed on solid state samples and are able to accurately measure the magnetic susceptibility (χ) of a sample.[44] χ = M/H where M is the magnetisation and H is the magnetic field strength. For a paramagnetic sample the susceptibility should follow the Curie-Weiss law $\chi = C/(T-\theta) + K$.[44] In this equation C is the Curie constant, T the absolute temperature, θ the Weiss constant and K a diamagnetic correction term. The magnetic moment of a sample can be calculated from the Curie constant and compared to the spin only formula. In this work magnetic susceptibility was measured from 5 to 300 K and then fitted to the Curie-Weiss law. The magnetisation data collected from SQUID magnetometry measurements for both **[Co(L1)NBD][BAr$^F_4$]** and **[Co(L1)(η-FC$_6$H$_5$)][BAr$^F_4$]** are shown in Figure 2.4 and were collected in collaboration with Professor Hayward. These data can be fitted to the Curie-Weiss law over the temperature range 75 < T/K < 300 to yield Curie constants of 0.584(2) cm^3 K mol^{-1} and 0.327(1) cm^3 K mol^{-1} respectively, giving calculated μ_{eff} values of 2.16 μ_B and 1.61 μ_B, respectively. These values are intermediate between those expected for a ^{1}Co spin-state (S = 0, C = 0 cm^3 K mol^{-1}, μ_{eff} = 0 μ_B) and a ^{3}Co spin-state (S = 1, C = 1 cm^3 K mol^{-1}, μ_{eff} = 2.82 μ_B).

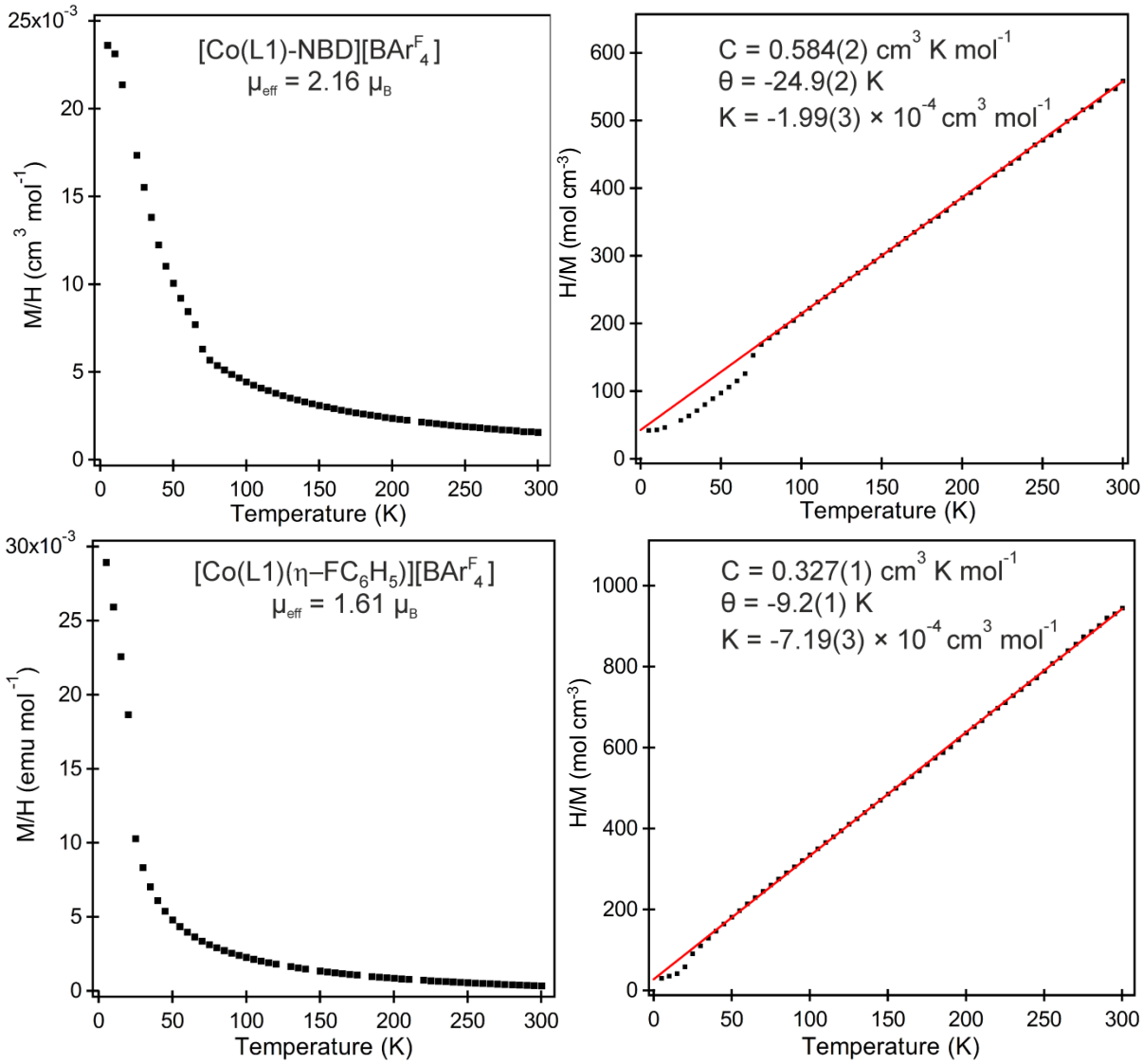


Figure 2.4 SQUID magnetometry data (left) from **[Co(L1)NBD][BAr$^F_4$]** (top) and **[Co(L1)(η-FC$_6$H$_5$)][BAr$^F_4$]** (bottom) and Curie-Weiss fit (right) to these data over the temperature range 75 < T/K < 300.

The Evans method is a way to determine magnetic moments of paramagnetic complexes in solution.[45] In this method NMR spectroscopy is used to observe the difference in chemical shift of a signal from an inert reference (often the residual solvent peaks) in the presence and absence of a paramagnetic sample.[36] This is typically performed using a capillary inset of diamagnetic reference sample, and comparing this to the paramagnetic NMR sample. From this difference in chemical shifts the magnetic moment can be calculated. For both **[Co(L1)NBD][BAr$^F_4$]** and **[Co(L1)(η-**

FC_6H_5)][BAr^F_4] the solid state SQUID magnetometry give higher values for μ_{eff} than the solution Evans method values. For **[Co(L1)NBD][BAr^F_4]** were μ_{eff} = 2.16 μ_B and μ_{eff} = 1.5(1) μ_B for SQUID and Evans measurements respectively. While for **[Co(L1)(η-FC_6H_5)][BAr^F_4]** these values were μ_{eff} = 1.61 μ_B and μ_{eff} = 1.1(1) μ_B respectively. The lower solution magnetic moments are likely due to slight differences in the coordination environment around cobalt when in solution compared to in the solid-state. Low-temperature deviations from Curie–Weiss behaviour below 50 K are attributed to intermolecular magnetic couplings.

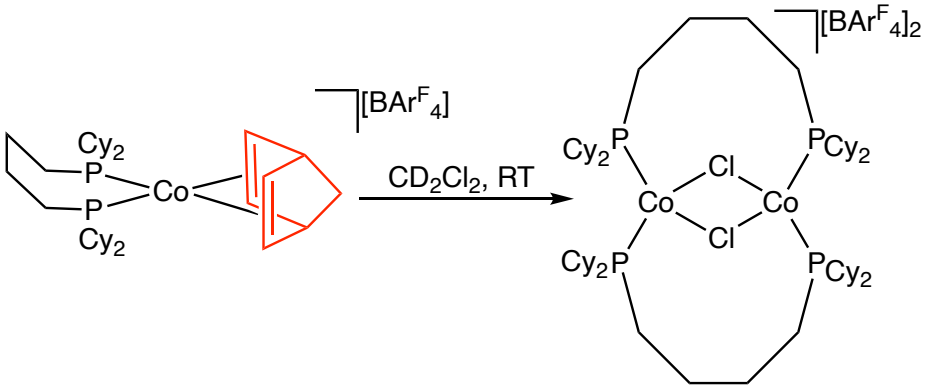
These intermediate magnetic moments are consistent with temperature-independent paramagnetism (TIP) reported for some Co(III) complexes and numerous Re(III) complexes.[46,47] TIP is explained by a second-order Zeeman effect caused by a diamagnetic ground spin state (^{1}Co) having significant mixing with an excited paramagnetic spin state (^{3}Co). TIP has been known to give rise to sharp ^{1}H NMR spectra for complexes that possess an intermediate magnetic moment. TIP chemical shifts are predicted not to vary significantly with temperature as observed for **[Co(L1)NBD][BAr^F_4]** and **[Co(L1)(η-FC_6H_5)][BAr^F_4]**.[35]

2.2.5 Solid-state reactivity of [Co(L1)NBD][BAr^F_4] with H_2.

Hydrogenation of **[Co(L1)NBD][BAr^F_4]** in the solid-state lead to rapid loss of crystallinity and complete loss of diffraction, which meant this system was unsuitable for the investigation of the solid-state structure of a Co(I) σ-alkane complex. Calculations have shown dispersive interactions key to the stabilisation of σ-alkane complexes.[48,49] It was hypothesised that increasing the steric bulk of the ligand would increase the stabilising dispersive interactions with the anion framework and hopefully help retain crystallinity upon hydrogenation. To achieve this, the number of carbons in

the backbone of the ligand was increased. It was reasoned that this would widen the P-Co-P bite angle and resultantly increase steric bulk within the cobalt coordination sphere.

2.2.6 Synthesis and characterisation of [Co(L2)NBD][BAr$^F_4$]



Scheme 2.14 (Co(μ$_2$-L2)(μ$_2$-Cl))$_2$ forms rapidly on exposure of **[Co(L2)-NBD][BAr$^F_4$]** to CH_2Cl_2.

Attempting to prepare **[Co(L2)NBD][BAr$^F_4$]** (L2 = $Cy_2P(CH_2)_4PCy_2$), using the same protocol as for **[Co(L1)NBD][BAr$^F_4$]**, lead to the isolation of **(Co(μ$_2$-L2)(μ$_2$-Cl))$_2$** (Scheme 2.14), which was formed by activation of the CH_2Cl_2 and characterised by X-ray diffraction. This solvent activation was prevented by carrying out the extraction into CH_2Cl_2 at -78 °C, which enabled the isolation of **[Co(L2)NBD][BAr$^F_4$]** as a powder (Figure 2.5 (A)). Dissolving **[Co(L2)NBD][BAr$^F_4$]** in CH_2Cl_2 at room temperature led to the formation of **(Co(μ$_2$-L2(μ$_2$-Cl))$_2$** on time of mixing. Instead, subsequent recrystallisation of **[Co(L2)NBD][BAr$^F_4$]** powder from 1,2-$C_6H_4F_2$/*n*-pentane enabled a solid-state structure to be determined (Figure 2.5 (B)). The complex displayed silent NMR spectra, and a solution magnetic moment of μ_{eff}(298 K) = 3.2(2) μB was measured using the Evans method, consistent with a ^{3}Co spin state and with the silent NMR spectra. This magnetic moment is higher than for **[Co(L1)NBD][BAr$^F_4$]** which

was determined to be μ_{eff}(298 K) = 1.5(1) μB. High spin, S=1, electronic states are more favoured for tetrahedral geometries than square planar (due to a smaller crystal field splitting energy, Δ)[25] and **[Co(L2)NBD][BAr$^F_4$]** has both a larger dihedral angle (28.0(3)° vs 22.0(2)°), higher τ parameter (0.371(2) vs 0.229(2)), and wider P-Co-P bite angle (103.09(4)° vs 87.48(7)°) than for **[Co(L1)NBD][BAr$^F_4$].** Therefore, **[Co(L2)NBD][BAr$^F_4$]** has a more tetrahedral geometry around cobalt consistent with the larger measured magnetic moment. For **[Co(L2)NBD][BAr$^F_4$]** the C=C bond is similar (1.394(6) Å vs 1.407(12) Å), the Co-P distances are longer (2.2717(8) Å vs 2.228(2) Å), and the Co-C distances are longer (2.161(5) Å vs 2.085(8) Å) than for **[Co(L1)NBD][BAr$^F_4$]**. These data are summarised in Table 2.2 and are consistent with weaker bonding to the ^{3}Co centre due to fewer vacant orbitals available for electron donation. The approximate octahedral packing of the [BAr$^F_4$]$^-$ anions had been maintained (Figure 2.5 (C)).

Compound	**[Co(R,R^{iPr}DuPhos) COD][BAr$^F_4$]**	**[Co(L2) NBD][BAr$^F_4$]**	**[Co(L1) NBD][BAr$^F_4$]**
Dihedral angle / °	29.6(4)	28.0(3)	22.0(2)
τ	0.299(3)	0.371(2)	0.229(3)
M-P$_{ave}$ / Å	2.232(3)	2.2717(8)	2.228(2)
M-C$_{ave}$ / Å	2.103(5)	2.161(5)	2.085(8)
C=C$_{ave}$ / Å	1.39(2)	1.394(6)	1.407(12)

Table 2.2 Comparison of the bonding metrics of **[Co(R,R^{iPr}DuPhos)COD][BAr$^F_4$]**,[34] **[Co(L1)NBD][BAr$^F_4$]**, and **[Co(L2)NBD][BAr$^F_4$]**.[18] Average bond distances used. dihedral angle between the P-M-P and the (centC=C)-M-(centC=C) planes. Where centC=C is the centres of the respective alkene bonds.

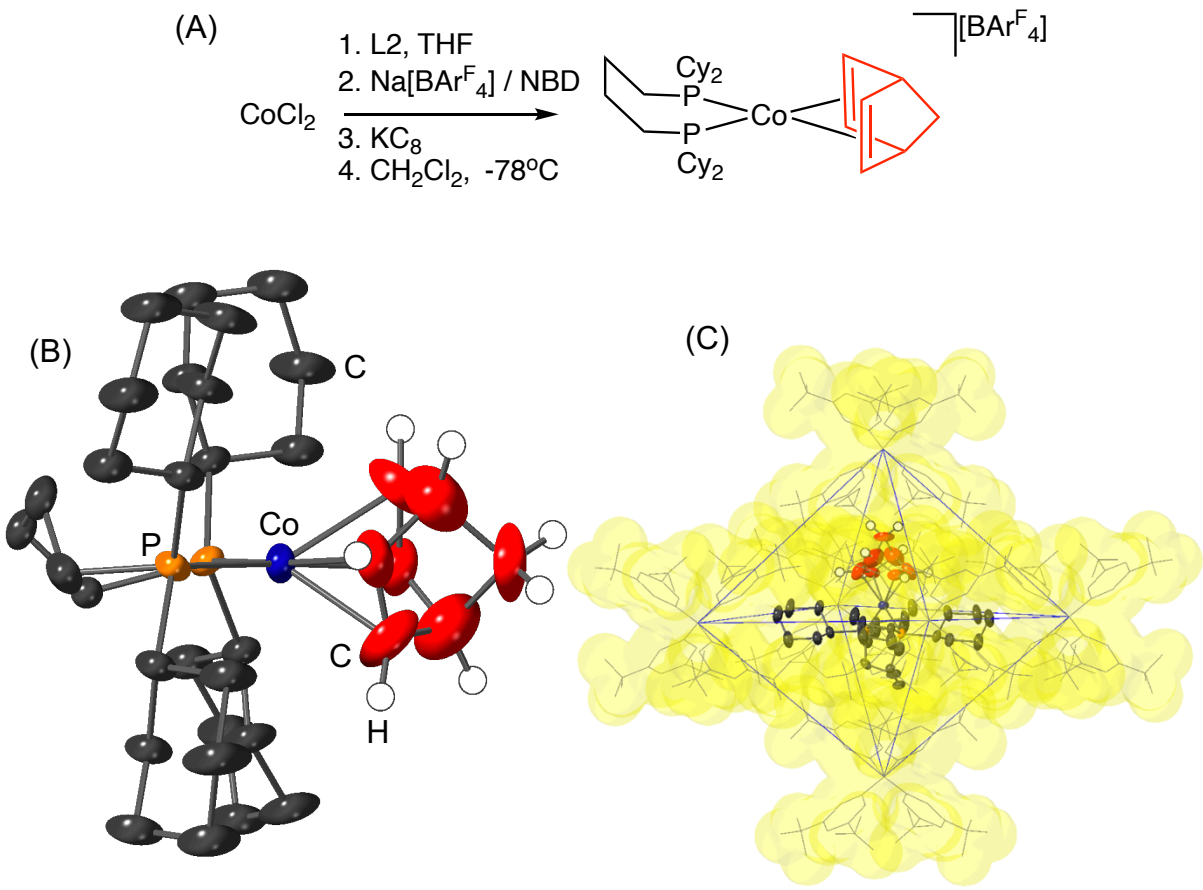


Figure 2.5 (A) Synthesis of **[Co(L2)NBD][BAr$^F_4$]**. **(B)** The solid-state structure of the cation; 30% displacement ellipsoids, anion and most H atoms not shown. **(C)** Approximate octahedral packing of anions. Cation plotted at 30% displacement ellipsoids and anion as a wireframe with a surface displayed at the van der Waals radii.

2.2.7 Synthesis and characterisation of [Co(L2)NBA][BAr$^F_4$]

Exposure of **[Co(L2)NBD][BAr$^F_4$]** to H_2 in C_6H_5F solutions leads to decomposition to a range of products, unlike for **[Co(L1)NBD][BAr$^F_4$]**. However, placing single crystals of **[Co(L2)NBD][BAr$^F_4$]** under an H_2 atmosphere resulted in a SC-SC transformation to form the σ-alkane complex **[Co(L2)NBA][BAr$^F_4$]** (Figure 2.6 (A)).

Through extensive optimisation, it was determined that single crystal X-ray diffraction experiments lasting longer than 2 hours resulted in decomposition, which caused loss of diffraction and a colour change from brown to blue. This decomposition was

assigned to oxidation from Co(I) to Co(II) due to oxygen within the mounting oil. **[Co(L2)NBA][BAr$^F_4$]** is exceptionally reactive, and this decomposition occurred even at 100 K. Through the application of an optimised data collection (2 h, 100 K, frozen oil drop), H_2 addition time (2 bar, 1 h, 289 K) and rapid transfer to the diffractometer, an unambiguous structure and acceptable refinement (R_1 = 8 %) was obtained. The H-atoms could not be located and were instead geometrically placed.

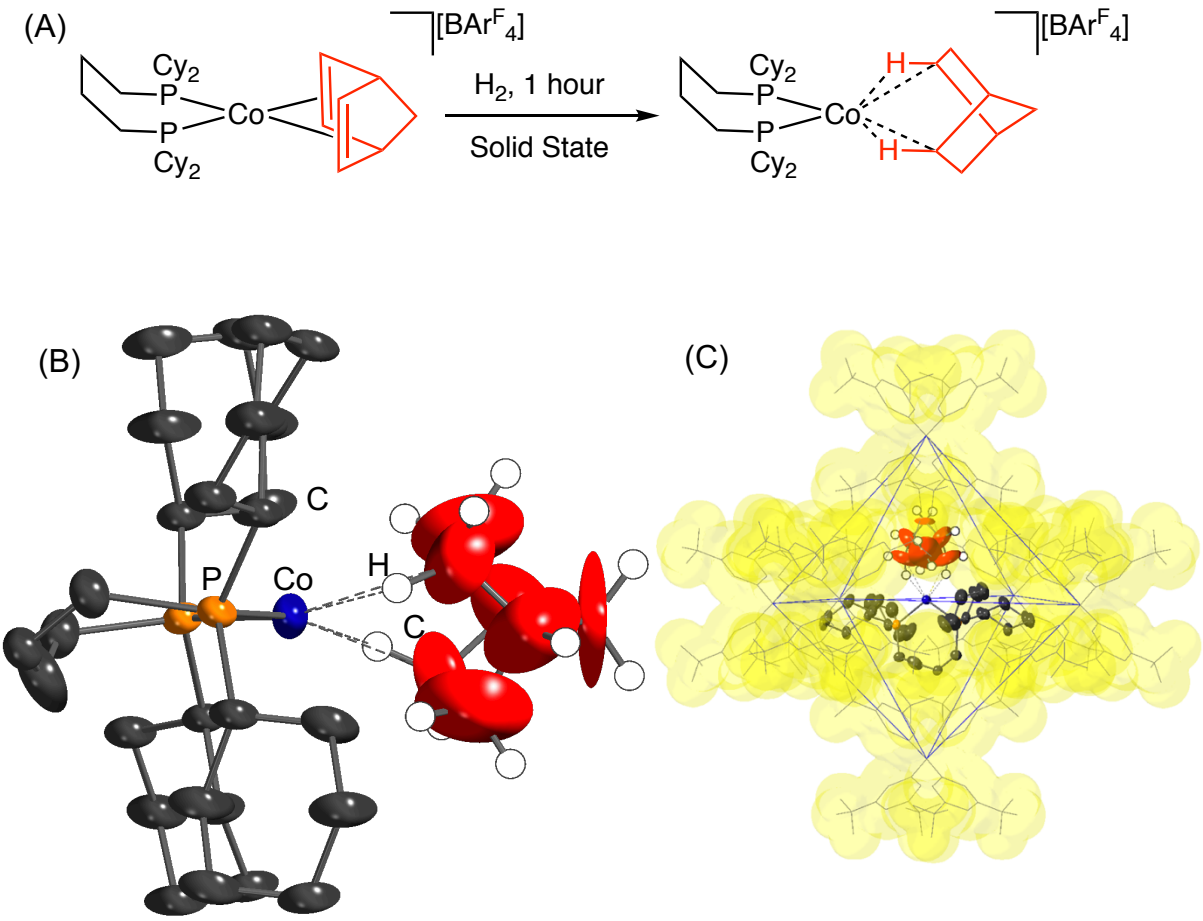


Figure 2.6 (A) Synthesis of **[Co(L2)NBA][BAr$^F_4$]**. **(B)** The solid-state structure of the cation; 30% displacement ellipsoids, anion and most H atoms not shown. **(C)** Approximate octahedral packing of anions. Cation plotted at 30% displacement ellipsoids and anion as a wireframe with a surface plotted at the van der Waals radii.

The solid-state structure of **[Co(L2)NBA][BAr$^F_4$]** is shown in Figure 2.6 (B). The approximate octahedral packing of the [BAr$^F_4$]$^-$ anions had been maintained (Figure

2.6 (C)). The crystal symmetry imposes a two-fold symmetry axis, resulting in the phosphine backbone disordered over two conformations, with only one shown. The NBA ligand sits in the pocket provided by two of the $[BAr^F{}_4]^-$ aryl rings. Notably, the displacement parameters for the NBA are significantly larger and show pronounced ellipticity, in contrast to the ordinary ellipsoids for the rest of the complex. These ellipsoids are a sign that the alkane is relatively loosely bound in the cavity.

Upon hydrogenation, several changes in structural parameters were observed (Table 2.3), with the solid-state structures before and after hydrogenation shown in Figure 2.7 comparing **[Co(L2)NBD][BAr$^F{}_4$]** with **[Co(L2)NBA][BAr$^F{}_4$]**. A shortening of the M-P bond (2.2717(8) Å to 2.232(1) Å) was observed due to a weaker trans ligand (NBA vs NBD), and a significant lengthening of the Co···C distances (2.161(5) Å to 2.612(16) Å) due to a weaker bound ligand (alkane vs alkene). Additionally, a further twist towards a tetrahedral geometry (28.0(3)° to 39.9(8)°), higher τ parameter (0.371(2) to 0.512(6)), and a wider P-M-P bite angle (103.09(4) to 108.94(7)) is more consistent with tetrahedral geometry for the **[Co(L2)NBA][BAr$^F{}_4$]**. These data are all evidence for a weaker-field ligand, an alkane rather than an alkene.[7] The Co···C distances are notably longer (0.3 Å) for **[Co(L2)NBA][BAr$^F{}_4$]** than found for intramolecular agostic complexes, further suggesting that this is a weak intermolecular interaction.[50]

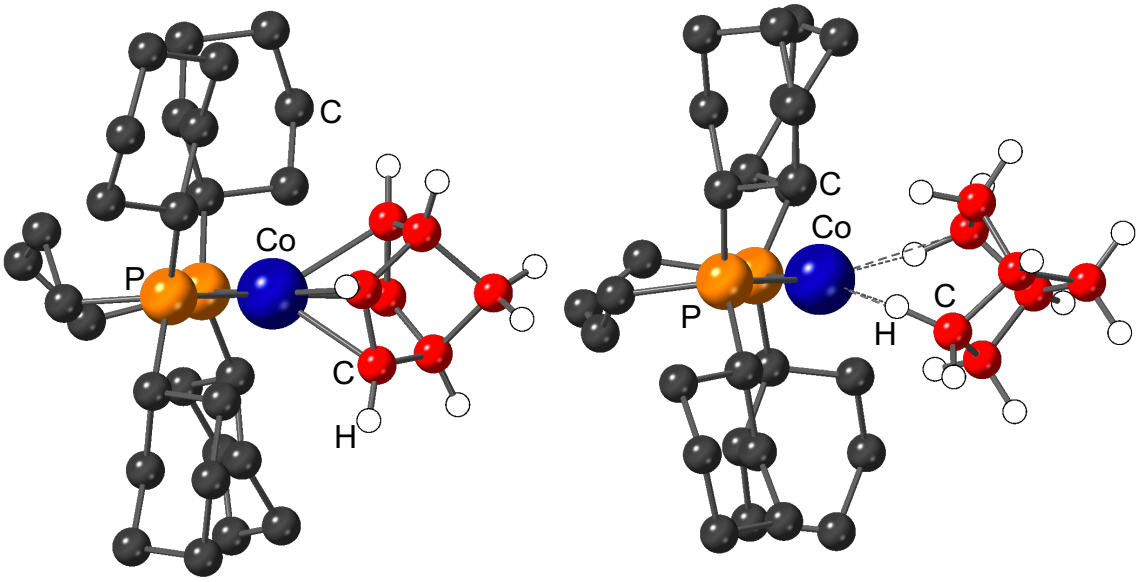


Figure 2.7 Solid-state structures of the cations of **[Co(L2)NBD][BAr$^F_4$]** (left) and **[Co(L2)NBA][BAr$^F_4$]** (right). Displayed as ball and stick models for clarity.

Compound	**[Rh(L2) NBA][BAr$^F_4$]**	**[Co(L2) NBA][BAr$^F_4$]**	**[Co(L2) NBD][BAr$^F_4$]**
Dihedral angle / °	4.62(5)	39.9(8)	28.0(3)
τ	0.079(11)	0.512(6)	0.371(2)
P-M-P bite angle / °	97.87(2)	108.94(7)	103.09(4)
M-P$_{ave}$ / Å	2.215(4)	2.232(1)	2.2717(8)
M-C$_{ave}$ / Å	2.396(2)	2.612(16)	2.161(5)

Table 2.3 Comparison of the bonding metrics of **[Rh(L2)NBA][BAr$^F_4$]**, **[Co(L2)NBA][BAr$^F_4$]**, and **[Co(L2)NBD][BAr$^F_4$]**. Average bond distances used. dihedral angle between the P-M-P and the (centC=C)-M-(centC=C) planes. Where centC=C is the centres of the respective alkene bonds.

Comparing the cobalt complex **[Co(L2)NBA][BAr$^F_4$]** to the rhodium equivalent, **[Rh(L2)NBA][BAr$^F_4$]** more notable structural differences were seen (Figure 2.8). The cobalt complex has significantly longer M-C distances, 0.22 Å longer, despite the small difference in covalent radii between Rh(I) and high-spin Co(I) (1.42 Å and 1.50 Å, respectively), suggesting a weaker bond.[51] The cobalt complex binds the alkane through two mutually opposed C-H bonds rather than two adjacent ones in a pseudo square planar geometry resulting in a smaller dihedral angle (4.62(5) vs 39.9(8)°). All

these data suggest the cobalt system is in a very different electronic environment to the rhodium.

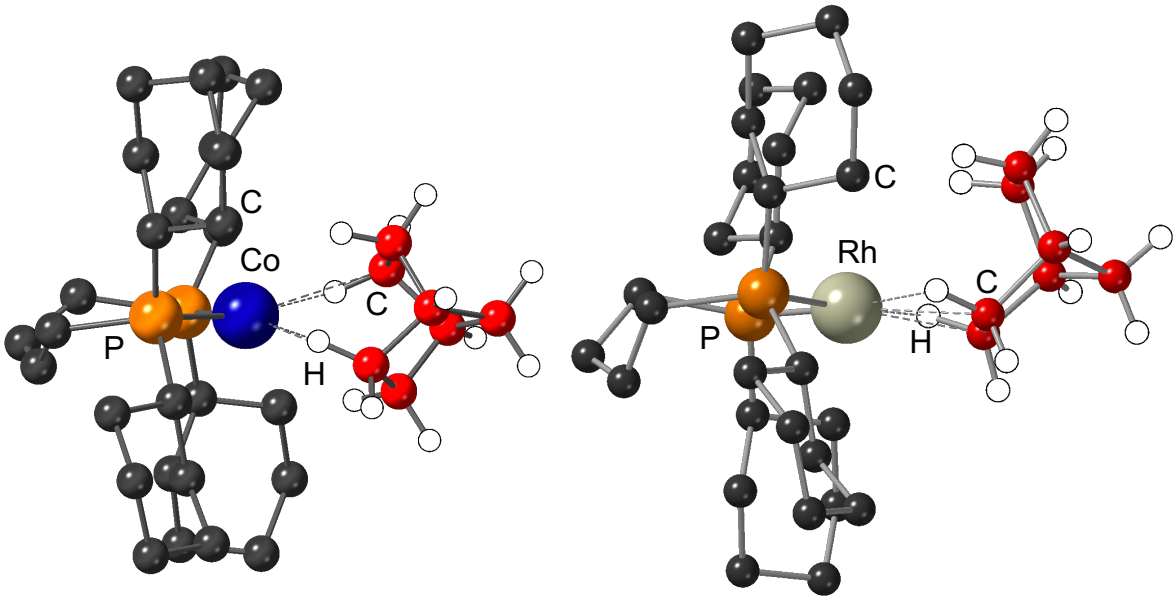


Figure 2.8 Solid-state structures of the cations of **[Co(L2)NBA][BAr$^F_4$]** (left) and **[Rh(L2)NBA][BAr$^F_4$]** (right). Displayed as ball and stick models for clarity.

2.2.8 Magnetic studies of [Co(L2)NBD][BAr$^F_4$] and [Co(L2)NBA][BAr$^F_4$]

SQUID magnetometry measurements probed the electronic structure of both **[Co(L2)NBD][BAr$^F_4$]** and **[Co(L2)NBA][BAr$^F_4$]**. The magnetisation data for both **[Co(L2)NBD][BAr$^F_4$]** and **[Co(L2)NBA][BAr$^F_4$]** were fit to the Curie–Weiss law over the temperature range 50≤T/K≤300 to yield values consistent with a ^{3}Co spin state (Figure 2.9). The observation of a temperature-independent component to the magnetic susceptibility of both compounds is indicative of a small unquenched orbital contribution to the magnetisation and is consistent with the slightly elevated moments for both compounds, compared to expected spin-only values: **[Co(L2)NBD][BAr$^F_4$]** μ_{eff} = 3.14 μ_B; **[Co(L2)NBA][BAr$^F_4$]** μ_{eff} = 3.38 μ_B; S = 1, spin-only μ_{eff} = 2.82 μ_B. The size of the orbital contribution to the moment will increase as the splitting energy decreases

and as a result the spin-orbit coupling.[52] Therefore, the greater moment for the alkane complex is consistent with the NBA being a weaker-field ligand than NBD. Low-temperature deviations from Curie–Weiss behaviour below 50 K are attributed to intermolecular magnetic couplings. These intermolecular magnetic couplings are supported by the deviation between fiel cooled (FC) and zero field cooled (ZFC) measurements below 50 K.[44]

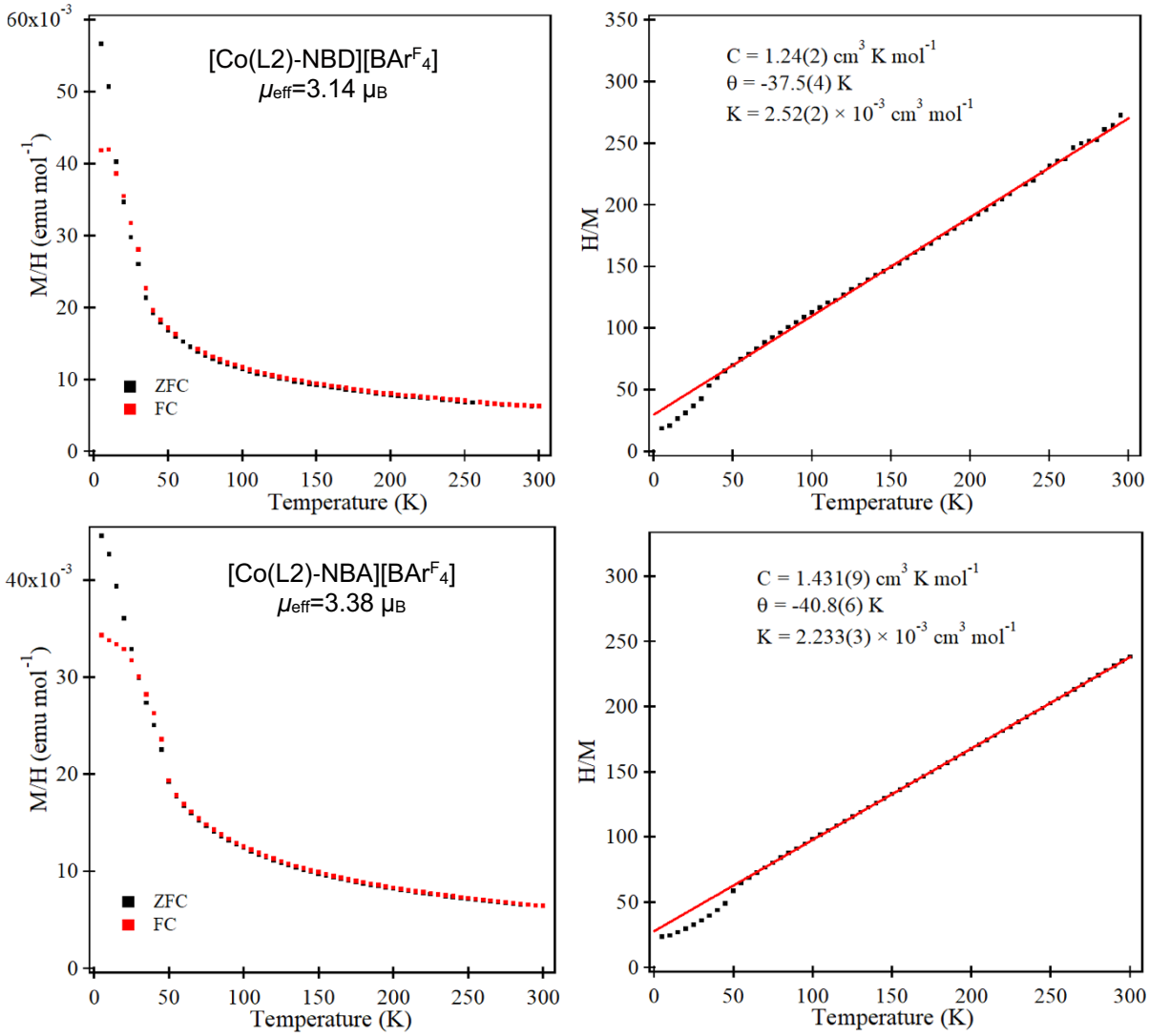
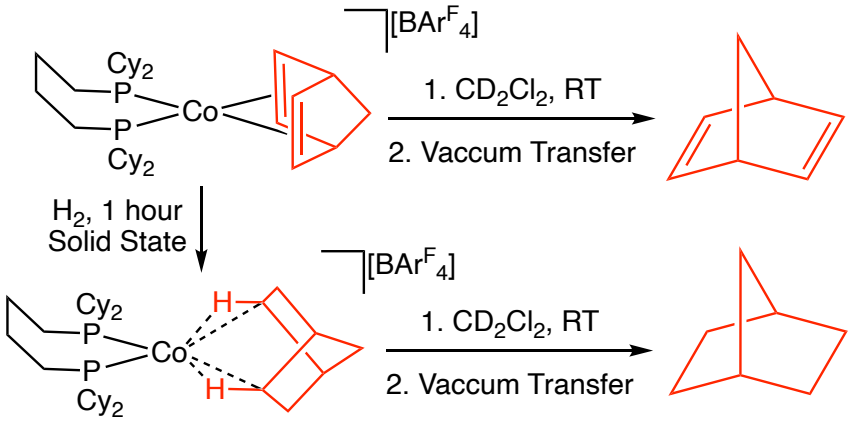


Figure 2.9 SQUID Magnetometry data (left) from **[Co(L2)NBD][BAr$^F_4$]** (top) and **[Co(2)NBA][BAr$^F_4$]** (bottom) and Curie-Weiss fit (right) to these data over the temperature range 75 < T/K < 300.

As a result of this ^{3}Co spin state, the $^{31}P\{^{1}H\}$ SSNMR spectra were silent. The EPR spectra also appeared featureless due to the sizeable zero-field splitting requiring too high energy radiofrequency pulses for X, Q or W-band EPR sepectroscopy.[53]

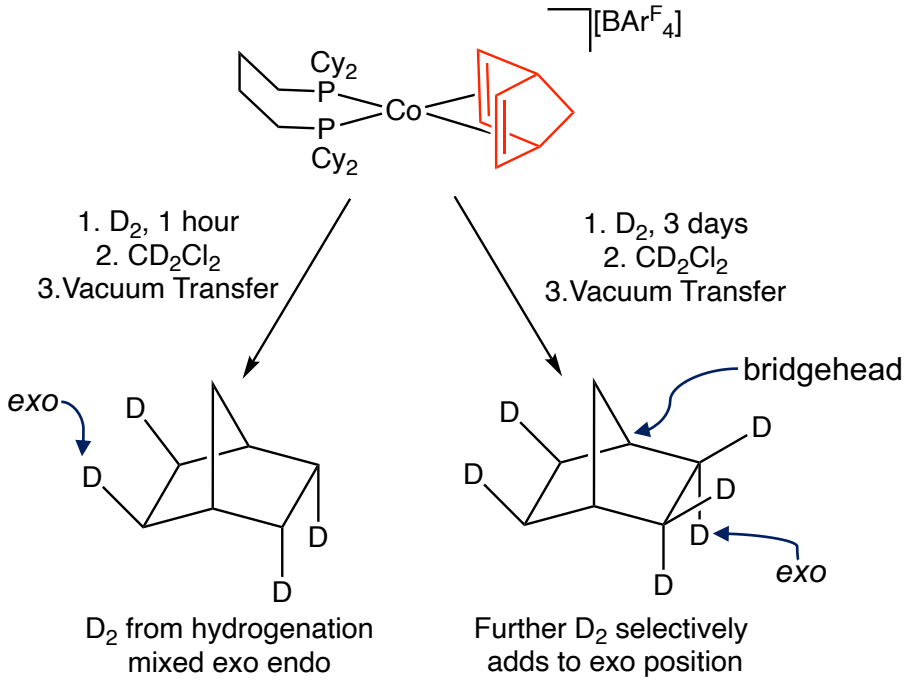
2.2.9 Bound volatile trapping experiments of [Co(L2)NBA][BAr$^{F}_{4}$]

To confirm that the reaction had gone to completion in the bulk crystalline sample, solution-phase NMR spectroscopic interrogation of the volatiles released from coordination to the metal centre provided a convenient spectroscopic handle to measure conversion and selectivity. When CD_2Cl_2 was added to **[Co(L2)NBD][BAr$^{F}_{4}$]**, **(Co(μ$_2$-L2(μ$_2$-Cl))$_2$** was formed, and NBD released into solution. Upon vacuum transfer of the volatiles, only NBD could be observed using ^{1}H NMR spectroscopy (Scheme 2.15). If CD_2Cl_2 was instead added to **[Co(L2)NBA][BAr$^{F}_{4}$]** again, **(Co(μ$_2$-L2(μ$_2$-Cl))$_2$** is formed (confirmed by XRD), but now NBA released into solution and upon vacuum transfer of the volatiles only NBA was seen (^{1}H NMR), with no residual NBD observed. These experiments confirmed that the hydrogenation had occurred in the bulk of the sample and not just the single crystal placed onto the diffractometer.



Scheme 2.15 Vacuum transfer of the volatiles released from coordination to the metal (NBD/NBA) was used to confirm that the solid-state hydrogenation had gone to completion.

2.2.10 Solid-state reactivity of [Co(L2)NBA][BAr$^F_4$] with D_2



Scheme 2.16 Deuterium incorporation from the initial hydrogenation is at a mixture of the *exo* and *endo* positions. Further deuterium is added to the *exo* position via a C-H activation process.

Inspired by the reactivity of **[Rh(L1)NBD][BAr$^F_4$]** with D_2, the reactivity of **[Co(L2)NBD][BAr$^F_4$]** with D_2 was explored. On hydrogenation of **[Co(L2)NBD][BAr$^F_4$]** under a D_2 atmosphere (for 1 h, 298 K, 1 bar), the integral of both the *exo* and *endo* positions reduced to 2H as observed in the ^{1}H NMR of trapped volatiles (Scheme 2.16). The integral was relative to the bridgehead protons, which remained equivalent at 2.20 ppm (s). The chemical shifts for both the *exo* and *endo* protons are the same as the literature values at 1.48 ppm (br) and 1.17 ppm (d, $J_{H\text{-}H}$ = 7 Hz).[16] This equal reduction in relative integrals implies the deuterium incorporation was seen equally at both the *exo* and *endo* positions. This equal incorporation at both *exo* and *endo* positions was seen with the **[Rh(^{i}Bu$_2$P(CH$_2$)$_2$P^{i}Bu$_2$)NBD][BAr$^F_4$]** system and was explained by the metal binding to the *exo* face of the norbornene in the norbornene intermediate, as

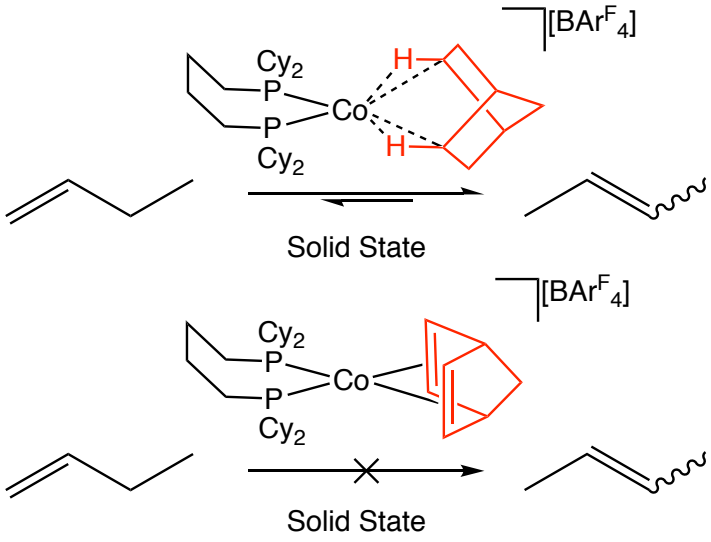
opposed to the endo in the diene starting material.[17] This selectivity is distinct from **[Rh(L1)NBD][BAr$^F_4$],** in which all deuterium from the initial hydrogenation are added to the *endo* face (Section 2.1.5), which is due to the norbornene intermediate remaining bonded through the *endo* position.[16]

If **[Co(L2)NBD][BAr$^F_4$]** was left under deuterium for longer (3 days), a further reduction in the ^{1}H NMR integral of trapped volatiles for the *exo* position (decrease from 2H to 1H) was seen with no change in the integral for the *endo* position (remaining at 2H). This data demonstrated that further incorporation was seen at the *exo* position exclusively. This selectivity for incorporation in the *exo* position has previously been reported for **[Rh(L1)NBA][BAr$^F_4$]**.[16] This further incorporation provides evidence for C-H activation of the alkane by the cobalt centre and contributes evidence for σ-bonding between the metal and alkane.

2.2.11 Solid-state reactivity of [Co(L2)NBA][BAr$^F_4$] with 1-butene

As described in Section 2.1.7, a reaction supported by SMOM systems is the solid gas isomerisation of 1-butene to 2-butene; it was thought **[Co(L2)NBA][BAr$^F_4$]** could be an effective pre-catalyst for this transformation. To investigate this **[Co(L2)NBD][BAr$^F_4$]** crystals were exposed to a hydrogen atmosphere in the solid-state for 1 h in an NMR tube, forming **[Co(L2)NBA][BAr$^F_4$]**, before being transferred into a 1-butene atmosphere. The 1-butene underwent isomerisation to 2-butene, stopping at 80% conversion as determined by gas-phase ^{1}H NMR spectroscopy (Scheme 2.17). If the NMR tube was recharged with more 1-butene, no further conversion to 2-butene was seen. With the same amount of catalyst, pressure of 1-butene and headspace of NMR tube, this isomerisation was much slower than the

equivalent Rh systems (reaching 50% conversion after 3.5 days for **[Co(L2)NBA][BAr$^F_4$]** vs 5 min **[Rh(L2)NBD][BAr$^F_4$]**).[23] This slower rate is likely due to both catalyst decomposition and the inherent nature of the more contracted Co metal d-orbitals. Exposure of crystals of **[Co(L2)NBD][BAr$^F_4$]** without pre-hydrogenation to a 1-butene atmosphere gave no isomerisation to 2-butene, suggesting 1-butene does not displace NBD from the Co. This lack of activity without pre-hydrogenation was also seen with the Rh systems; **[Rh(L2)NBD][BAr$^F_4$]** was not an active catalyst for 1-butene isomerisation.



Scheme 2.17 [Co(L2)NBA][BAr$^F_4$] was an active pre-catalyst for the solid gas isomerisation of 1-butene to 2-butene while **[Co(L2)NBD][BAr$^F_4$]** was not.

2.2.12 Computational characterisation of [Co(L2)NBD][BAr$^F_4$]

To further probe this system, computational calculations were carried out by our collaborators in the Macgregor group (Heriot-Watt University) to investigate the bonding in **[Co(L2)NBD][BAr$^F_4$]** and **[Co(L2)NBA][BAr$^F_4$]**. Periodic DFT calculations were carried out with the crystal structure providing the basis for heavy atom positions, with H and F positions optimised in the ^{3}Co spin state with the PBE-D3 functional and

the energies recomputed with the hybrid PBE0-D3 approach. With **[Co(L2)NBD][BAr$^F_4$]**, the ^{3}Co spin-state is lower in energy by only 4.1 kcal mol^{-1} than the ^{1}Co, with which state being lower in energy highly dependent on the orientation of the NBD ligand and the computational methods used. With **[Co(L2)NBA][BAr$^F_4$]**, the ^{3}Co is strongly favoured (by 32.3 kcal mol^{-1}), reflected in the experimental magnetisation data (Section 2.2.8).

A careful look at the computed structure of the **[Co(L2)NBA]$^+$** cation (Figure 2.10 (A), which contains the labelling scheme used in the computational work), the Co···H11 distance suggests an interaction at 1.82 Å, and the C1-H11 bond has been elongated to 1.12 Å, which indicates some extent of C1-H11→Co σ-interaction. For **[Rh(L1)NBA][BAr$^F_4$],** the C-H bond is elongated further to 1.16 Å so indicating a more significant σ-interaction for Rh.[18] The QTAIM molecular graph (Figure 2.10 (B)) confirms a Co···H11 bond path, implying a C1-H11→Co σ-interaction. With a bond critical point (point along the bond with least electron density (ρ(r))) of ρ(r) = 0.047 au, which is lower than for **[Rh(L1)NBA][BAr$^F_4$]** with ρ(r) = 0.060 au which indicates a weaker σ-bond for the Co complex. For the C1-H11 bond, the minimum electron density is ρ(r) = 0.252 au, which is more than for **[Rh(L1)NBA][BAr$^F_4$] of** ρ(r) = 0.231 au but less than for free NBA of ρ(r) = 0.274 au, which suggests a weaker bonding interaction for **[Co(L2)NBA][BAr$^F_4$]**. Non-covalent interaction (NCI) plots show weak (non-covalent) interactions; they are colour-coded from blue (more stabilising) through to green (weakly stabilising) to red (more destabilising). The NCI plot of **[Co(L2)NBA][BAr$^F_4$]** (Figure 2.10 (D)) shows dispersive stabilisation between the NBA ligand and i) the PCy_2 substituents, ii) the aryl groups of the $[BAr^F_4]^-$ anion, and iii) non-classical C-F···H-C H-bonding. When viewed from the metal centre (Figure 2.10 (C)), blue regions between Co···H11 and Co···H11′ are assigned to C-H→Co σ-interactions.

These data suggest both the C-H→Co σ-interactions and the stabilising dispersive interactions are significant providing stability to this complex.

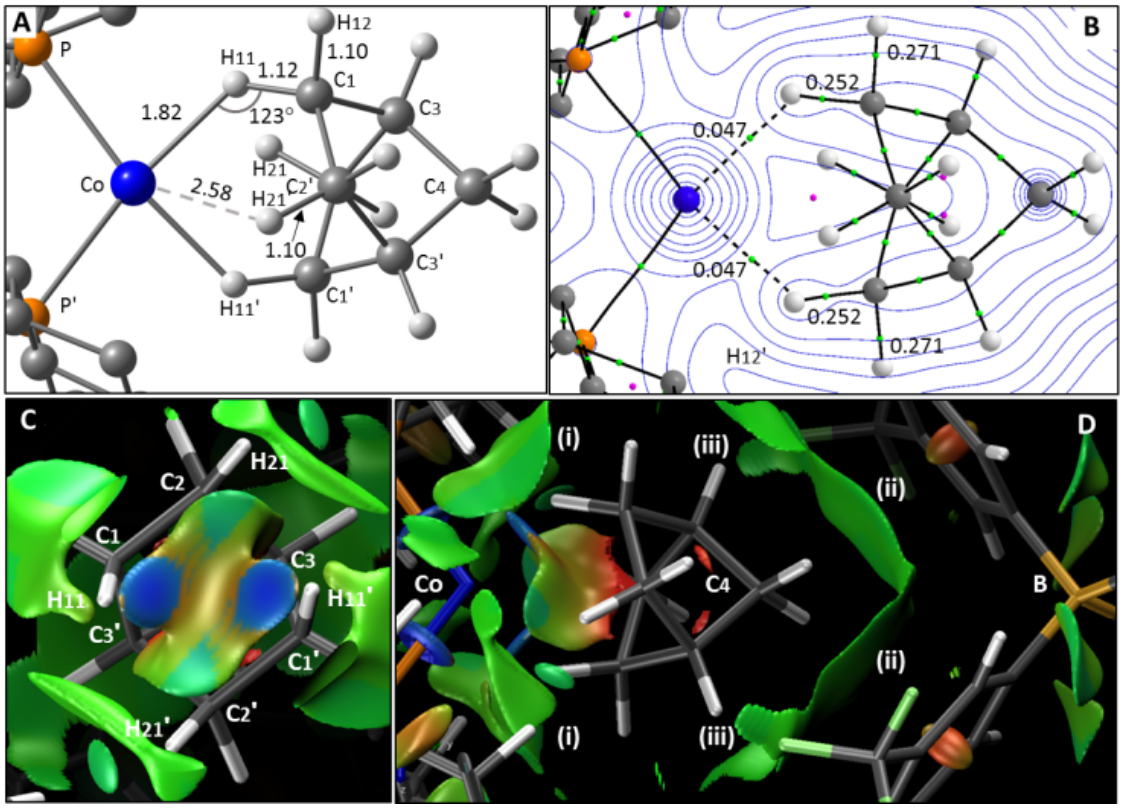


Figure 2.10 (A) Computed structure of the **[Co(L2)NBA]$^{+}$** cation viewed down the C2···C2' axis highlighting key distances (Å) and angles to H atoms. **(B)** Quantum Theory of Atoms in Molecules (QTAIM) molecular graph with bond critical bonds (BCPs) in green, ring critical points (RCPs) in pink and selected BCP electron densities, ρ(r), in eA^{-3}. **(C)** Non-Covalent Interaction (NCI) plot of the proximate **[Co(L2)NBA][BAr$^{F}_{4}$]** ion-pair viewed from the Co centre. **(D)** NCI plot perpendicular to the Co···C4···B axis highlighting the (i) the PCy_2 substituents, (ii) [BAr$^{F}_{4}$]$^{-}$ aryl groups, (iii) C-F···H-C H-bonding.

To further investigate the bonding between C-H and Co, a spin-unrestricted NBO second-order perturbation analysis was used to separate interactions into the α- and β-spins at the ^{3}Co centre (Figure 2.11). All five of the 3d-orbitals are occupied for the α-spin, so donation is only possible from $\sigma_{C\text{-}H}$ into a Co low-valent (4s) NBO (3.5 kcal mol^{-1}). For the β-spin, there are two vacant Co d-orbitals, so donation is seen from $\sigma_{C\text{-}H}$ into both a Co low-valent (4s) NBO (4.7 kcal mol^{-1}) and also into an empty d-orbital

(5.9 kcal mol^{-1}). P-lone pairs back donate into the $\sigma^*_{C\text{-}H}$ NBOs with both spins, and a further back donation from occupied Co 3d NBO is seen in the α-spin (1.7 kcal mol^{-1}).

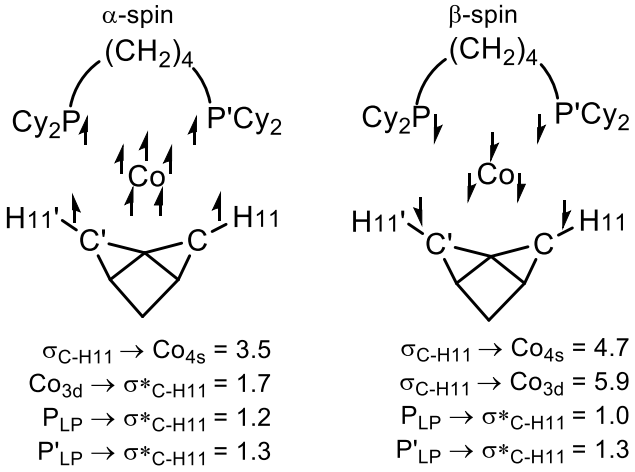


Figure 2.11 Spin unrestricted NBO 2nd order perturbation analysis highlighting key donor-acceptor interactions (kcal mol^{-1}) in **[Co(L2)NBA]$^+$**.

These NBO data give a total $\sigma_{C\text{-}H}$ donation of 14.1 kcal mol^{-1} and back donation to $\sigma^*_{C\text{-}H}$ of 6.5 kcal mol^{-1}. These suggest a weaker interaction than in **[Rh(L2)NBA]$^+$** cation with a total $\sigma_{C\text{-}H}$ donation amounting to 19.7 kcal mol^{-1} and back-donation to $\sigma^*_{C\text{-}H}$ is 8.5 kcal mol^{-1}.[16,23] This weaker bonding is consistent with all the experimental observations, from the large displacement ellipsoids to the only marginal stability of **[Co(L2)NBA][BAr$^F{}_4$]**.

From these data, it is clear that isolation of **[Co(L2)NBA][BAr$^F{}_4$]** owes a lot to the dispersive interactions provided by the [BAr$^F{}_4$]$^-$ anions. These weak interactions are fundamental in the isolation of an only marginally stable ^{3}Co σ-alkane complex.

2.3 Conclusions

In this chapter, a Co(I) σ-alkane complex was synthesised using SMOM methodology, the first of its kind and a landmark discovery in the field. The σ-alkane complex was crystallographically characterised. It was shown to be in a ^{3}Co spin state (SQUID magnetometry and DFT calculations) and dispersive interactions with the $[BAr^{F}_{4}]^{-}$ anions key to the stability. Reflecting this, the work was published in Angew. Chem. Int. Ed. and selected as a VIP paper and for an outside back cover.[54] Moving into the next chapter, the focus will shift to cobalt complexes for catalytic transformations.

2.4 References

(1) Bergman, R. G. *Nature*. Nature Publishing Group March 22, 2007, pp 391–393.
(2) Goldberg, K. I.; Goldman, A. S. *Accounts of Chemical Research*. American Chemical Society 2017, pp 620–626.
(3) Goss, R. M. **1983**.
(4) Wittcoff, H. A.; Reuben, B. G.; Plotkin, J. S. *Industrial Organic Chemicals: Third Edition*; John Wiley & Sons, 2013.
(5) Elvidge, C. D.; Zhizhin, M.; Baugh, K.; Hsu, F. C.; Ghosh, T. *Energies* **2016**, *9* (1), 14.
(6) Goldberg, K. I.; Goldman, A. S. *Accounts of Chemical Research*. American Chemical Society March 21, 2017, pp 620–626.
(7) Hall, C.; Perutz, R. N. *Chem. Rev.* **1996**, *96* (8), 3125–3146.
(8) Weller, A. S.; Chadwick, F. M.; McKay, A. I. *Adv. Organomet. Chem.* **2016**, *66*, 223–276.
(9) Perutz, R. N.; Turner, J. J. *J. Am. Chem. Soc.* **1975**, *97* (17), 4791–4800.
(10) Calladine, J. A.; Duckett, S. B.; George, M. W.; Matthews, S. L.; Perutz, R. N.; Torres, O.; Vuong, K. Q. *J. Am. Chem. Soc.* **2011**, *133* (7), 2303–2310.
(11) Geftakis, S.; Ball, G. E. *Journal of the American Chemical Society*. American Chemical Society September 30, 1998, pp 9953–9954.
(12) Pitts, A. L.; Wriglesworth, A.; Sun, X. Z.; Calladine, J. A.; Zarić, S. D.; George, M. W.; Hall, M. B. *J. Am. Chem. Soc.* **2014**, *136* (24), 8614–8625.
(13) Schultz, R. H.; Bengali, A. A.; Tauber, M. J.; Weiller, B. H.; Wasserman, E. P.; Kyle, K. R.; Moore, C. B.; Bergman, R. G. *J. Am. Chem. Soc.* **1994**, *116* (16), 7369–7377.
(14) Bernskoetter, W. H.; Schauer, C. K.; Goldberg, K. I.; Brookhart, M. *Science (80-.).* **2009**, *326* (5952), 553–556.
(15) Adams, G. M.; Chadwick, F. M.; Pike, S. D.; Weller, A. S. *Dalt. Trans.* **2015**, *44* (14), 6340–6342.
(16) Chadwick, F. M.; Krämer, T.; Gutmann, T.; Rees, N. H.; Thompson, A. L.; Edwards, A. J.; Buntkowsky, G.; Macgregor, S. A.; Weller, A. S. *J. Am. Chem. Soc.* **2016**, *138* (40), 13369–13378.
(17) Pike, S. D.; Thompson, A. L.; Algarra, A. G.; Apperley, D. C.; Macgregor, S. A.; Weller, A. S. *Science (80-.).* **2012**, *337* (6102), 1648–1651.
(18) Pike, S. D.; Chadwick, F. M.; Rees, N. H.; Scott, M. P.; Weller, A. S.; Krämer, T.; Macgregor, S. A. *J. Am. Chem. Soc.* **2015**, *137* (2), 820–833.
(19) McKay, A. I.; Martínez-Martínez, A. J.; Griffiths, H. J.; Rees, N. H.; Waters, J. B.; Weller, A. S.; Krämer, T.; MacGregor, S. A. *Organometallics* **2018**, *37* (20), 3524–3532.
(20) Martínez-Martínez, A. J.; Royle, C. G.; Furfari, S. K.; Suriye, K.; Weller, A. S. *ACS Catal.* **2020**, *10* (3), 1984–1992.
(21) McKay, A. I.; Bukvic, A. J.; Tegner, B. E.; Burnage, A. L.; Martínez-Martínez, A. J.; Rees, N. H.; Macgregor, S. A.; Weller, A. S. *J. Am. Chem. Soc.* **2019**, *141* (29), 11700–11712.
(22) Kumar, A.; Bhatti, T. M.; Goldman, A. S. *Chem. Rev.* **2017**, *117* (19), 12357–12384.
(23) Chadwick, F. M.; McKay, A. I.; Martinez-Martinez, A. J.; Rees, N. H.; Krämer, T.; Macgregor, S. A.; Weller, A. S. *Chem. Sci.* **2017**, *8* (9), 6014–6029.
(24) *IHS Chemical North American Propylene Supply Study, 2014*.
(25) Crabtree, R. H. *Organomet. Chem. Transit. Met. Sixth Ed.* **2014**, *9781118138*,

1–504.
(26) Chadwick, F. M.; Olliff, N.; Weller, A. S. *J. Organomet. Chem.* **2016**, *812*, 268–271.
(27) Billups, W. E.; Chang, S. C.; Hauge, R. H.; Margrave, J. L. *J. Am. Chem. Soc.* **1993**, *115* (5), 2039–2041.
(28) Schultz, R. H.; Bengali, A. A.; Tauber, M. J.; Weiller, B. H.; Wasserman, E. P.; Kyle, K. R.; Moore, C. B.; Bergman, R. G. *IR Flash Kinetic Spectroscopy of C-H Bond Activation of Cyclohexane-do and -d12 by Cp∗Rh(CO)2 in Liquid Rare Gases: Kinetics, Thermodynamics, and an Unusual Isotope Effect*; 1994; Vol. 116.
(29) Bengali, A. A.; Bergman, R. G.; Moore, C. B. *J. Am. Chem. Soc.* **1995**, *117* (13), 3879–3880.
(30) Lomont, J. P.; Nguyen, S. C.; Schlegel, J. P.; Zoerb, M. C.; Hill, A. D.; Harris, C. B. *J. Am. Chem. Soc.* **2012**, *134* (6), 3120–3126.
(31) Carreón-Macedo, J. L.; Harvey, J. N. *J. Am. Chem. Soc.* **2004**, *126* (18), 5789–5797.
(32) Wu, X.; Liu, Z.; Murphy, T. S.; Sun, X. Z.; Hanson-Heine, M. W. D.; Towrie, M.; Harvey, J. N.; George, M. W. *Faraday Discuss.* **2019**, *220* (0), 86–104.
(33) Torres, O.; Calladine, J. A.; Duckett, S. B.; George, M. W.; Perutz, R. N. *Chem. Sci.* **2015**, *6* (1), 418–424.
(34) Zhong, H.; Friedfeld, M. R.; Chirik, P. J. *Angew. Chemie - Int. Ed.* **2019**, *58* (27), 9194–9198.
(35) Soncini, A.; Van Den Heuvel, W. *J. Chem. Phys.* **2013**, *138* (2), 021103.
(36) Piguet, C. *J. Chem. Educ.* **1997**, *74* (7), 815–816.
(37) Schrock, R. R.; Osborn, J. A. *J. Am. Chem. Soc.* **1976**, *98* (8), 2143–2147.
(38) Etayo, P.; Vidal-Ferran, A. *Chem. Soc. Rev.* **2013**, *42* (2), 728–754.
(39) Barwick-Silk, J.; Hardy, S.; Willis, M. C.; Weller, A. S. *J. Am. Chem. Soc.* **2018**, *140* (23), 7347–7357.
(40) Willis, M. C. *Chem. Rev.* **2010**, *110* (2), 725–748.
(41) Shen, Z.; Dornan, P. K.; Khan, H. A.; Woo, T. K.; Dong, V. M. *J. Am. Chem. Soc.* **2009**, *131* (3), 1077–1091.
(42) Murphy, S. K.; Park, J. W.; Cruz, F. A.; Dong, V. M. *Science (80-.).* **2015**, *347* (6217), 56–60.
(43) Colby, D. A.; Bergman, R. G.; Ellman, J. A. *Chem. Rev.* **2010**, *110* (2), 624–655.
(44) Williams, D. *Electricity and magnetism*; 2017; Vol. 18.
(45) Evans, D. F. *J. Chem. Soc.* **1959**, *81* (0), 2003–2005.
(46) Chatt, J.; Leigh, G. J.; Mingos, D. M. P. *J. Chem. Soc. A Inorganic, Phys. Theor. Chem.* **1969**, No. 0, 1674–1680.
(47) Griffith, J. S.; Orgel, L. E. *Trans. Faraday Soc.* **1957**, *53* (0), 601–606.
(48) Lu, Q.; Neese, F.; Bistoni, G. *Phys. Chem. Chem. Phys.* **2019**, *21* (22), 11569–11577.
(49) Bukvic, A. J.; Burnage, A. L.; Tizzard, G. J.; Martínez-Martínez, A. J.; Mckay, A. I.; Rees, N. H.; Tegner, B. E.; Krämer, T.; Fish, H.; Warren, M. R.; Coles, S. J.; Macgregor, S. A.; Weller, A. S. *J. Am. Chem. Soc.* **2021**, *143* (13), 5106–5120.
(50) Murugesan, S.; Stöger, B.; Pittenauer, E.; Allmaier, G.; Veiros, L. F.; Kirchner, K. *Angew. Chemie - Int. Ed.* **2016**, *55* (9), 3045–3048.
(51) Cordero, B.; Gómez, V.; Platero-Prats, A. E.; Revés, M.; Echeverría, J.; Cremades, E.; Barragán, F.; Alvarez, S. *J. Chem. Soc. Dalt. Trans.* **2008**, No. 21, 2832–2838.

(52) Smura, C. F.; Parker, D. R.; Zbiri, M.; Johnson, M. R.; Gál, Z. A.; Clarke, S. J. *J. Am. Chem. Soc.* **2011**, *133* (8), 2691–2705.
(53) Krzystek, J.; Park, J. H.; Meisel, M. W.; Hitchma, M. A.; Stratemeier, H.; Brunel, L. C.; Telser, J. *Inorg. Chem.* **2002**, *41* (17), 4478–4487.
(54) Boyd, T. M.; Tegner, B. E.; Tizzard, G. J.; Martínez-Martínez, A. J.; Neale, S. E.; Hayward, M. A.; Coles, S. J.; Macgregor, S. A.; Weller, A. S. *Angew. Chemie - Int. Ed.* **2020**, *59* (15), 6177–6181.

Chapter 3: A simple cobalt-based catalyst system for the controlled dehydropolymerisation of $H_3B{\cdot}NMeH_2$ on the gram-scale

3.1 Introduction

The next two chapters will focus on the catalytic dehydropolymerisation of amine-boranes, initially using Co-based catalysts (Chapter 3) and then moving to Rh-based systems (Chapter 4). Before this an introduction to the most relevant literature is presented.

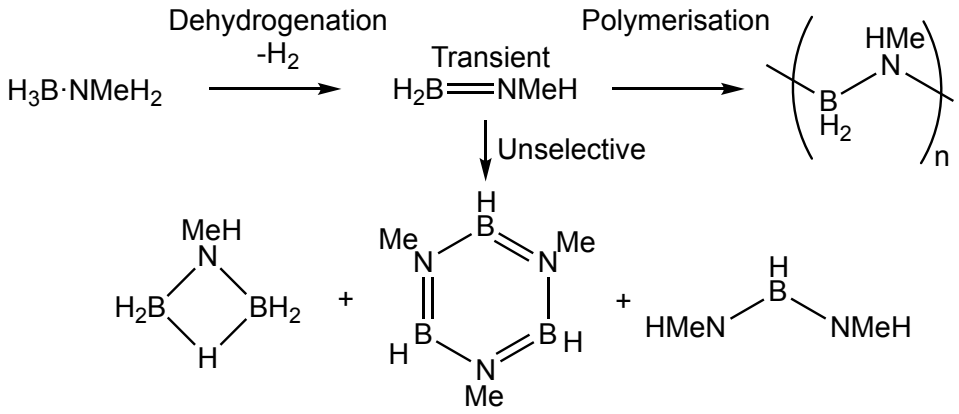
3.1.1 Dehydropolymerisation of amine-boranes

The synthesis of polyaminoboranes has been the focus of considerable work since Manners and co-workers first reported the synthesis of polyaminoborane by the dehydropolymerisation of $H_3B{\cdot}NMeH_2$ in 2008.[1] Amine-boranes take the form $R_3B{\cdot}NR_3$ (R = H, alkyl, or aryl) they are Lewis adducts of an amine with a borane and they are isoelectronic with alkanes. Alkane dehydrogenation requires both the presence of a catalyst and high reaction temperature (>150 ^oC) to overcome the endothermicity of the reaction.[2] Whereas, for amine-boranes where there are hydrogens on the nitrogen and boron (ammonia borane, 1^o or 2^o amine-boranes), dihydrogen loss is more feasible than for the alkane equivalents. This is due to the hydridic nature of the B-H and the protic nature of the N-H coupled with the overall exothermicity of the reaction.[3,4] The dehydrogenation even occurs spontaneously at elevated temperature (> 80 ^oC); however, it is not selective and forms a range of BN coupled products.[5]

The BN coupled products have potential uses in their own right; one product is polyaminoborane $(H_2B{\cdot}NH_2)_n$, which has possible uses as novel polymers.[6] The BN

unit is an isostere of C-C, and so these polymers are equivalent to polyolefins. Polyolefins are manufactured on a vast scale (~110 million tonnes per year)[7] and are used throughout industry and society. Another dehydrogenation product is polyborazylene which has potential use as a precursor to thermally stable and chemically resistant hexagonal boron nitride for polyborazylene.[8–10] Hexagonal boron nitride is of interest for use in future nanoelectronics as a support for graphene.[11]

In the next two chapters, I will focus on the dehydrogenative polymerisation of monomethyl amine-borane ($H_3B{\cdot}NMeH_2$). $H_3B{\cdot}NMeH_2$ is first dehydrogenated to form the transient amino-borane ($H_2B{=}NMeH$), that then rapidly undergoes head-to-tail polymerisation to form polymethylaminoborane $(H_2B{\cdot}NMeH)_n$.[8,12] This two-step process (Scheme 3.1) is distinct from the polymerisation of olefins, in which the alkene monomer is stable and the precursor for the polymers. Mechanistic investigations are complicated because two potentially interacting processes (dehydrogenation and polymerisation) must be understood and harnessed for a controlled polymerisation. Trimethylborazine, $(HBNMe)_3$, is the most commonly seen side product that signals an unselective dehydropolymerisation of $H_3B{\cdot}NMeH_2$ and is formed with overall two equivalents of H_2 lost per monomer.



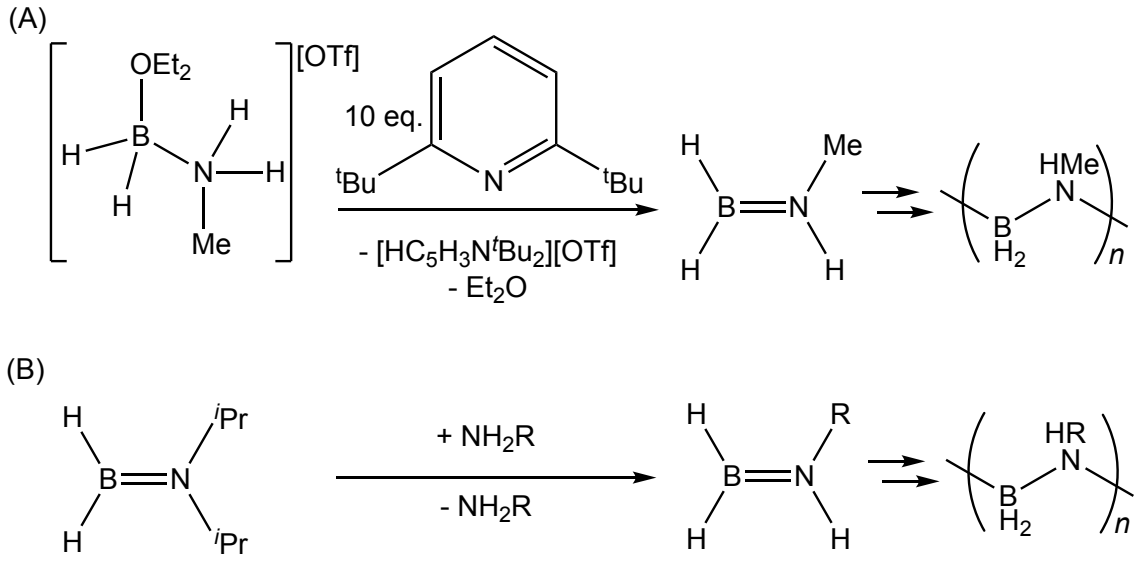
Scheme 3.1 Dehydropolymerisation of $H_3B{\cdot}NMeH_2$ consists of a dehydrogenation to a transient monomer ($H_2B{=}NMeH$) and a subsequent polymerisation to form $(H_2B{\cdot}NMeH)_n$. The main side product that signals an unselective process is $(HBNMe)_3$.

3.1.2 Polymer characterisation

Polyaminoboranes are generally characterised by ^{11}B NMR spectroscopy and by gel permeation chromatography (GPC). The ^{11}B NMR spectrum of $(H_2B{\cdot}NMeH)_n$ shows a distinctive broad peak at −6.8 ppm.[1] The GPC data enables values for M_n and $Đ$ to be determined: where M_n is the number average molecular weight of the polymer and $Đ$ is the dispersity - a measure of the homogeneity of the polymer produced. GPC analysis of polyaminoboranes is typically carried out using a refractive index (RI) detector and measured relative to polystyrene standards. Notably, determination of molecular weight of $(H_2B{\cdot}NMeH)_n$ by using GPC with a RI detector calibrated to polystyrene standards have recently been compared to dynamic light scattering and DOSY methods and show that the RI/polystyrene standards measured values could be an overestimate by a factor of approximately 5-10.[13,14] However the GPC/RI combination is the most common found in laboratories.

3.1.3 Catalyst-free routes to polyaminoboranes

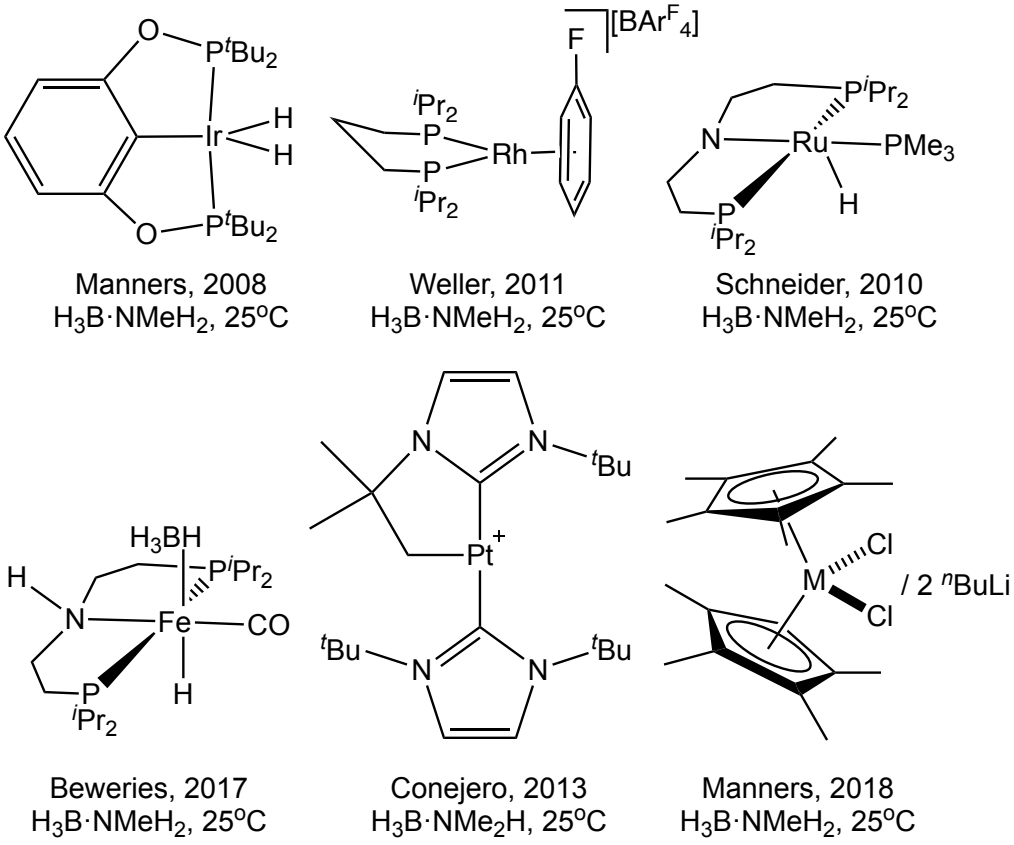
Thermal dehydrogenation of amine-boranes occurs above 80 °C and leads to an unselective mixture of trimethylborazine, polyaminoborane and short chain cyclic units such as trimethylborazane, $(HBNMeH)_3$.[5] The mixture of products vary with the temperature and duration of heating, but has not been reported to be selective for one product. Despite the lack of selectively for thermal dehydrogenation some relatively selective catalyst-free routes to polyaminoboranes have been developed. Manners produced polyaminoborane by deprotonation of amine-boronium cations $[MeH_2N{\cdot}BH_2(OEt_2)]^+$ using 2,6-ditertbutylpyridine which generated transient $H_2B{=}NMeH$ (Scheme 3.2 (A)).[12] This amino-borane then rapidly underwent head-to-tail polymerisation to give $(H_2B{\cdot}NMeH)_n$, with M_n < 5,000 g mol^{-1} and $Đ$ could not be determined. Alcaraz synthesised a range of polyaminoboranes (for example $(H_2B{\cdot}N(C_3H_5)H)_n$) by use of $^iPr_2N{=}BH_2$ to provide BH_2 moiety to primary amines (NRH_2) through amine metathesis at -40 °C, forming $H_2B{=}NRH$ and N^iPr_2H in situ (Scheme 3.2 (B)).[15] The amino-borane monomers then rapidly polymerised, again likely by head-to-tail nucleophilic polymerisation (see section 3.1.11).[16] By this method $(H_2B{\cdot}NMeH)_n$ was prepared with M_n = 20,000 g mol^{-1} and $Đ$ = 10.2. In order to produce polyaminoboranes with more controlled molecular weights and dispersities, different routes are needed and thus homogeneous transition metal catalysis has received significant attention.



Scheme 3.2 Catalyst free synthesis of polyaminoboranes. **(A)** Deprotonation of boronium cations. **(B)** Amine exchange with $H_2B{=}N^iPr_2$.

3.1.4 Catalysed routes to polyaminoboranes

High molecular weight polyaminoborane (M_n > 50,000 $gmol^{-1}$) was first prepared by catalytic dehydropolymerisation of $H_3B{\cdot}NMeH_2$ using **IrH_2(POCOP-^{t}Bu)** (POCOP-^{t}Bu=κ^3-1,3-$(OP^tBu_2)_2C_6H_3$) by Manners (Scheme 3.3).[1,17] Prior to this work Heinekey and Goldberg had also investigated the reactivity of **IrH_2(POCOP-^{t}Bu)** with $H_3B{\cdot}NMeH_2$ at lower concentrations (0.5 vs 10 M) of $H_3B{\cdot}NMeH_2$ which had given low molecular weight oligomers of $(H_2B{\cdot}NMeH)_n$ (n = 4-48 by ESI-MS).[18,19] A wide range of catalysts for dehydropolymerisation have since been developed, of both homogeneous and heterogeneous nature.[6] Within the next two chapters I will report on homogeneous catalysts for the dehydropolymerisation of $H_3B{\cdot}NMeH_2$, so this introduction shall focus on such systems. Exemplar dehydropolymerisation systems are presented in Scheme 3.3.

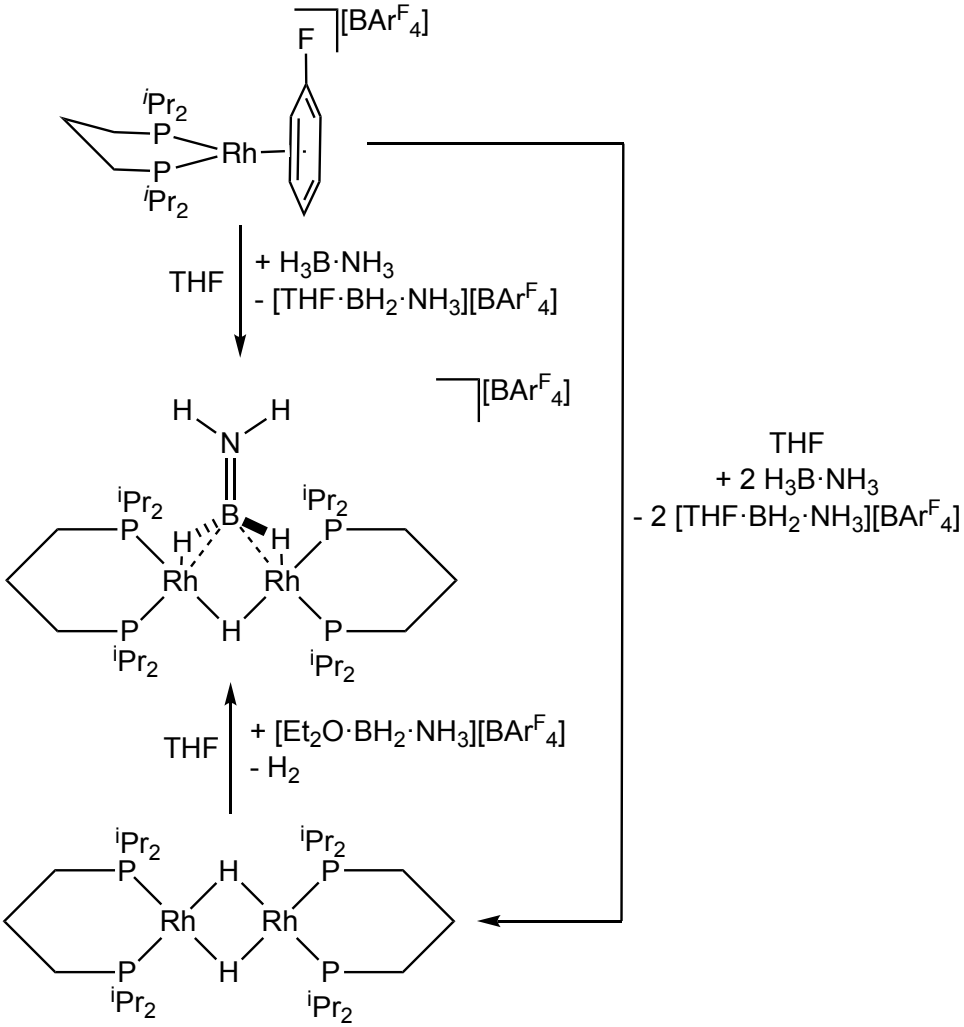


Scheme 3.3 Example catalysts and conditions for amine-borane dehydropolymerisation.[1,20–24]

3.1.5 {Rh(chelating diphosphine)} catalysts for dehydropolymerisation.

Within the group there has been a focus on cationic **[Rh(bisphosphine)]$^+$** systems for dehydropolymerisation.[6] By using **[Rh(^{i}Pr$_2$P(CH$_2$)$_n$P^{i}Pr$_2$)(C$_6$H$_5$F)][BAr$^F_4$]** (n=2-5) pre-catalysts it was demonstrated that σ-complexes of amine-boranes, **[Rh(^{i}Pr$_2$P(CH$_2$)$_n$P^{i}Pr$_2$)(H$_3$B·NMeH$_2$)][BAr$^F_4$]** are the first formed species in the dehydropolymerisation, and using the $H_3B{\cdot}NMe_3$ allowed some of these to be isolated.[25–27] Bite angle effects were probed, and it was found that if n<3 (in 1,2-$C_6H_4F_2$ solvent), then these σ-amine-borane complexes would not form, and the dehydropolymerisation was not observed.[20] If n≥3 then σ-amine-borane complexes would form, and the dehydropolymerisation of $H_3B{\cdot}NMeH_2$ would occur selectively to

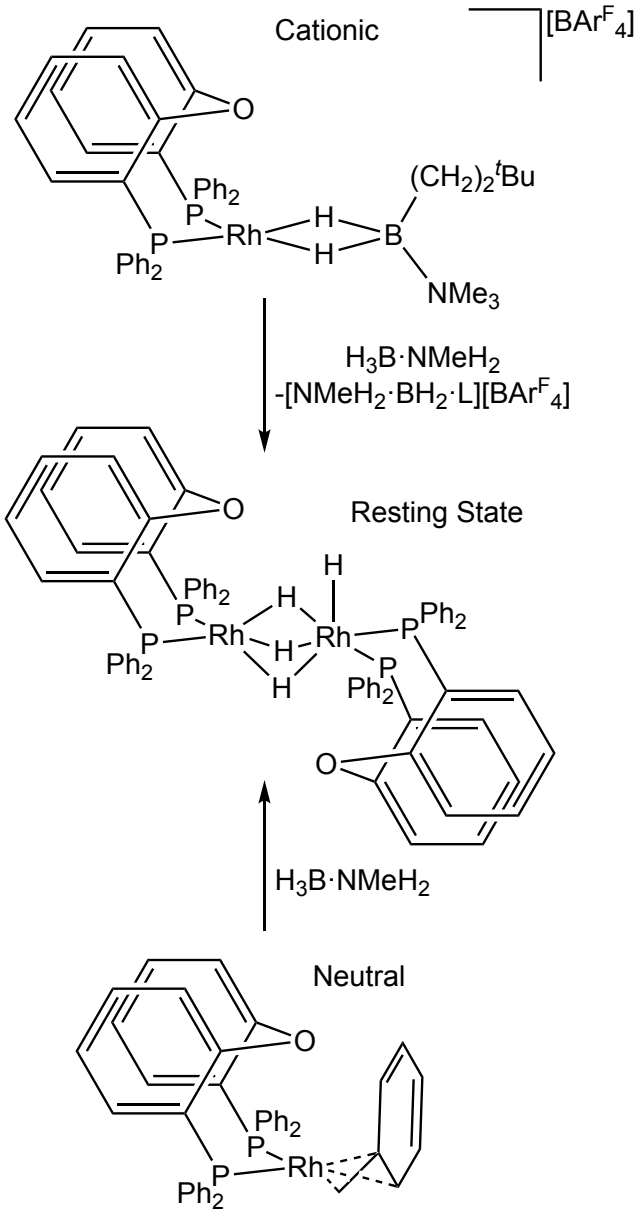
give polymer which was characterised by GPC (for n=3, 0.2 mol% loading, M_n = 77,700 g mol^{-1} Đ = 2.2). ^{31}P NMR spectra of the reaction mixture showed a mixture of species, and the identity of the active catalyst was not definitively determined. However, reaction of **[Rh(*i*Pr$_2$P(CH$_2$)$_3$P*i*Pr$_2$)(C$_6$H$_5$F)][BAr$^F_4$]** with a slight excess of $H_3B{\cdot}NH_3$ gave the bimetallic with a bridging amino-borane **[Rh$_2$(*i*Pr$_2$P(CH$_2$)$_3$P*i*Pr$_2$)$_2$(μ-H)(μ-H$_2$B=NH$_2$)][BAr$^F_4$]** cleanly (Scheme 3.4) and one equivalent per dimer of the boronium cation [THF·BH$_2$·NH$_3$][BAr$^F_4$]. Clues to the formation of this unusual species come from addition of [Et$_2$O·BH$_2$·NH$_3$][BAr$^F_4$] to the bridging hydride dimer **Rh$_2$(*i*Pr$_2$P(CH$_2$)$_3$P*i*Pr$_2$)$_2$(μ-H)$_2$** (Scheme 3.4). This lead to the rapid formation of **[Rh$_2$(*i*Pr$_2$P(CH$_2$)$_3$P*i*Pr$_2$)$_2$(μ-H)(μ-H$_2$B=NH$_2$)][BAr$^F_4$]** suggesting this bridging hydride dimer may be important to the formation of **[Rh$_2$(*i*Pr$_2$P(CH$_2$)$_3$P*i*Pr$_2$)$_2$(μ-H)(μ-H$_2$B=NH$_2$)][BAr$^F_4$]**. Additionally, the closely related complex **[Rh$_2$(*i*Pr$_2$P(CH$_2$)$_3$P*i*Pr$_2$)$_2$(μ-H)(μ-H$_2$B=NMeH)][BAr$^F_4$]** was seen as the only complex present at the end of catalysis for dehydropolymerisation with $H_3B{\cdot}NMeH_2$. These results also indicate the importance of the formation of boronium in the activation of these cationic catalysts.



Scheme 3.4 Reaction of **[Rh(*i*Pr$_2$P(CH$_2$)$_3$P*i*Pr$_2$)(C$_6$H$_5$F)][BAr$^F_4$]** with $H_3B{\cdot}NH_3$ to form **[Rh$_2$(*i*Pr$_2$P(CH$_2$)$_3$P*i*Pr$_2$)$_2$(μ-H)(μ-H$_2$B=NH$_2$)][BAr$^F_4$]** and one equivalent of the boronium cation [THF·BH_2·NH_3][BAr$^F_4$] indicates the importance of the formation of boronium in the activation of cationic catalysts. The rapid reaction of **Rh$_2$(*i*Pr$_2$P(CH$_2$)$_3$P*i*Pr$_2$)$_2$(μ-H)$_2$** with boronium to form **[Rh$_2$(*i*Pr$_2$P(CH$_2$)$_3$P*i*Pr$_2$)$_2$(μ-H)(μ-H$_2$B=NH$_2$)][BAr$^F_4$]** shows bridging neutral hydrides are closely related species.

Careful speciation studies using **[Rh(DPEphos-Ph)(H$_2$B·NMe$_3$(CH$_2$)$_2$*t*Bu)][BAr$^F_4$]** (DPEPhos-Ph = Bis[(2-diphenylphosphino)phenyl]ether) in catalysis enabled a detailed understanding of the activation of these cationic systems to eventually give a bridging dimer neutral hydride resting state (**[Rh(DPEphos-Ph)H$_2$]$_2$**) along with an equivalent of boronium ([$H_2B(NMeH_2)_2$][BAr$^F_4$]) (Scheme 3.5).[28,29] It was noted that the addition of amine to the catalytic mixture promoted these activation processes

removing induction periods which were observed in the absence of amine. The neutral complex **Rh(DPEphos-Ph)Benzyl** also generates **[Rh(DPEphos-Ph)H_2]$_2$** as the resting state of catalysis with no boronium formed. Taken with the work on **[Rh(^{i}Pr$_2$P(CH$_2$)$_n$P^{i}Pr$_2$)(C_6H_5F)][BAr$^F_4$]** these results suggest the importance of the formation of neutral hydride complexes in the dehydropolymerisation of amine-boranes. Additionally, these results show the formation of concomitant boronium occurs generally in these cationic systems. With the **[Rh(DPEphos-Ph)($H_2BNMe_3(CH_2)_2{}^t$Bu)][BAr$^F_4$]** system, the degree of polymerisation (as measured by M_n) of polymer produced decreased as the catalyst loading increased, thus allowing for control of the polymer produced. For example M_n = 6,400 g mol^{-1} at 1 mol% catalyst loading and M_n = 34,900 gmol^{-1} at 0.2 mol%. No change in degree of polymerisation was observed on changing the catalyst loading of the neutral system using **Rh(DPEphos-Ph)Benzyl**, which interestingly forms no boronium. This signals the potential role of boronium in chain length control. The variation in degree of polymerisation with catalyst loading has enabled insight into the mechanism of polymerisation of $H_2B{=}NMeH$ and is discussed further in section **3.1.12**.



Scheme 3.5 Pre-catalysts and resting state of **{Rh(DPEPhos-Ph)}** type systems for dehydropolymerisation of amine-boranes.

3.1.6 Further late transition metal catalysts for dehydropolymerisation

Schneider has reported catalysts with the cooperative PNHP ligand $HN((CH_2)_2P^iPr_2)$ (L3). **$RuH_2(PMe_3)(NH((CH_2)_2P^iPr_2)_2)$** catalysed the dehydropolymerisation of $H_3B{\cdot}NMeH_2$ to produce polyaminoborane of M_n = 191,100 g mol^{-1} and $Đ$ = 1.9.[17] Careful experimental and computational work using the pre-catalysts

$RuH(PMe_3)(N(CH_2)_2P^iPr_2)_2$) and **$RuH_2(PMe_3)(NH((CH_2)_2P^iPr_2)_2)$** demonstrated they underwent cooperative ligand assisted mechanisms (for more detail see Section 3.1.11). Modifications of the ligand structure with a methyl group on the backbone nitrogen, **$RuH_2(PMe_3)(NMe((CH_2)_2P^iPr_2)_2)$**, resulted in a decrease in rate by two orders of magnitude highlighting the efficiency of the cooperative ligand assisted mechanism.[17,21] Another late transition metal system is Conejero's **$[Pt(I^tBu')(I^tBu)][BAr_4^F]$** (where I^tBu is the N-heterocyclic carbene ligand 1,3-di-*tert*-butylimidazol-2-ylidene, and I^tBu′ denotes the cyclometalated I^tBu ligand, Scheme 3.3) which could effectively dehydrocouple $H_3B{\cdot}NMe_2H$ to form the square dimer $(H_2B{\cdot}NMe_2)_2$.[23] Although polymer formation using a primary amine-borane has not been investigated with this system it provided the first evidence for a distinctive type of mechanism for dehydrogenation of amine-boranes which will be discussed in Section 3.1.11.

3.1.7 Iron based catalysts for dehydropolymerisation

A number of Fe based systems for dehydropolymerisation of amine-boranes have also been developed. The work by Schneider on **$FeH(CO)(NR((CH_2)_2P^iPr_2)_2)$** and by Beweries on the related complex **$FeH(BH_4)(CO)(NR((CH_2)_2P^iPr_2)_2)$** has further demonstrated the versatility of coopertative PNHP ligands.[22,30] Using **$FeH(BH_4)(CO)(NH(CH_2CH_2P\mathit{i}Pr_2)_2)$** for the dehydropolymerisation of $H_3B{\cdot}NMeH_2$ Beweries reported isolated polymer of M_n = 35,000 g mol^{-1} and Đ = 2.2. Interestingly, Schneider reported a threefold improvement in ToN of **$FeH(CO)(NR((CH_2)_2P^iPr_2)_2)$** for $H_3B{\cdot}NH_3$ dehydropolymerisation by addition of NMe_2Et, significantly improving the efficiency of the catalyst.[30] The added amine prevents binding of BH_3 to an amido form of the ligand which quenches catalytic activity. It was proposed that BH_3 is produced

by the rearrangement of $2H_2B{=}NH_2$ to BH_3.THF and $HB(NH_2)_2$.[31] The ability of amine to promote the dehydrocoupling of amine-boranes has been noted more widely; specifically as already mentioned in removing induction periods in the activation of cationic rhodium systems.[29] Further iron-based examples for dehydropolymerisation include Baker's **$Fe(PhNCH_2CH_2NPh)(Cy_2PCH_2CH_2PCy_2)$** and Manners' photochemically activated **$[FeCp(CO)_2]_2$**.[32,33]

3.1.8 Early and mid-transition metal catalysts for dehydropolymerisation

Early and mid-transition metal catalysts for the dehydropolymerisation of amine-boranes are less numerous with Manners **$TiCl_2Cp^*_2$ /** 2 eq, ^{n}BuLi system the most thoroughly investigated.[24] When using **$TiCl_2Cp^*_2$ /** 2 eq. ^{n}BuLi for the dehydropolymerisation of $H_3B{\cdot}NMeH_2$ increasing reaction time or catalyst loading led to the isolation of polymer with a higher degree of polymerisation. Under optimum conditions (7 mol% **$TiCl_2Cp^*_2$ /** 2 eq. ^{n}BuLi, 8 h reaction time) polymer of M_n = 54,000 g mol^{-1} and $Đ$ = 1.6 was isolated. In addition, the substrate scope of dehydropoymerisation was extended to incorporate N-benzyl substituents, such as $H_3B{\cdot}NBzH_2$. Ti based system likely operate via a Ti(III) intermediate. Kawano's photolytically activated **$Mn(\eta^5\text{-}C_5H_5)(CO)_3$** and **$Cr(\eta^6\text{-}C_6H_6)(CO)_3$** complexes are further examples of early and mid-transition metal catalysts for dehydropolymerisation of amine-boranes.[34]

3.1.9 Summary of representative dehydropolymerisation catalysts

With this wide range of catalysts it is necessary to be able to compare them against key performance criteria. To analyse the materials properties of polyaminoboranes

large quantities are required so they need to be produced efficiently on scale. To assess the viability of these catalysts for large scale synthesis of polyaminoboranes, it is important to consider the scale and turnover numbers (ToN) for the literature reported dehydropolymerisations, and a representative selection of these are shown in Table 3.1. Typically these reactions are carried out on a small scale (< 1 g). ToNs generally are in the range 20-500 (Table 3.1) but can be improved by recharging (up to 1,500).[6] While the catalysts capable of higher TON (i.e. lower catalyst loadings) are suitable for increasing scale of the dehydropolymerisation this has not yet been a focus of work for any system.

Catalyst	Scale / g	ToN	M_n / g mol^{-1}	$Đ$
IrH_2(POCOP-^{t}Bu)[1]	0.25	333	55,000	2.9
[Rh(^{i}Pr$_2$P(CH$_2$)$_3$PPh$_2$)(η^6-C$_6$H$_5$F)][BAr$^F{}_4$][25,26]	0.05	500	77,000	2.2
FeH(BH$_4$)(CO)(NH(CH$_2$CH$_2$P^{i}Pr$_2$)$_2$)[22]	0.1	20	35,000	2.2
RuH$_2$(PMe$_3$)(NMe((CH$_2$)$_2$P^{i}Pr$_2$)$_2$)[21]	0.1	333	191,000	1.9
[Rh(DPEphos-Ph)(H$_2$BNMe$_3$(CH$_2$)$_2$^{t}Bu)][BAr$^F{}_4$][29]	0.05	1000	34,600	1.7
Rh(DPEphos-Ph)Benzyl[28]	1	400	15,000	2.5
TiCl$_2$Cp$^*{}_2$ / 2 x ^{n}BuLi[24]	0.150	14	54,000	1.6
H_2BNiPr_2+$NMeH_2$ (stoichiometric)[15]	1.5	-	20,000	10.2
[$MeH_2N{\cdot}BH_2(OEt_2)$][OTf]+base[16]	0.5	-	< 5,000	-[a]

Table 3.1 Selected, representative molecular weight and dispersity data for $(H_2B{\cdot}NMeH)_n$ prepared using different catalysts and methods. [a] not determined.

In the literature a wide variation of degrees of polymerisation have been reported for $(H_2B{\cdot}NMeH)_n$ which are generally measured by GPC. The M_n is seen to span from less than 5,000 g mol^{-1}, which would be short oligomeric material, up to values as high as 191,000 g mol^{-1} for polymeric material (Table 3.1). With this data in hand the following

loose M_n definitions have been established for the degree of polymerisation of $(H_2B{\cdot}NMeH)_n$:[6]

- Low molecular weight: $M_n < 5{,}000$ g mol^{-1}
- Medium molecular weight: M_n: 5,000–50,000 g mol^{-1}
- High molecular weight: M_n: 50,000–200,000 g mol^{-1}
- Very high molecular weight: $M_n > 200{,}000$ g mol^{-1}

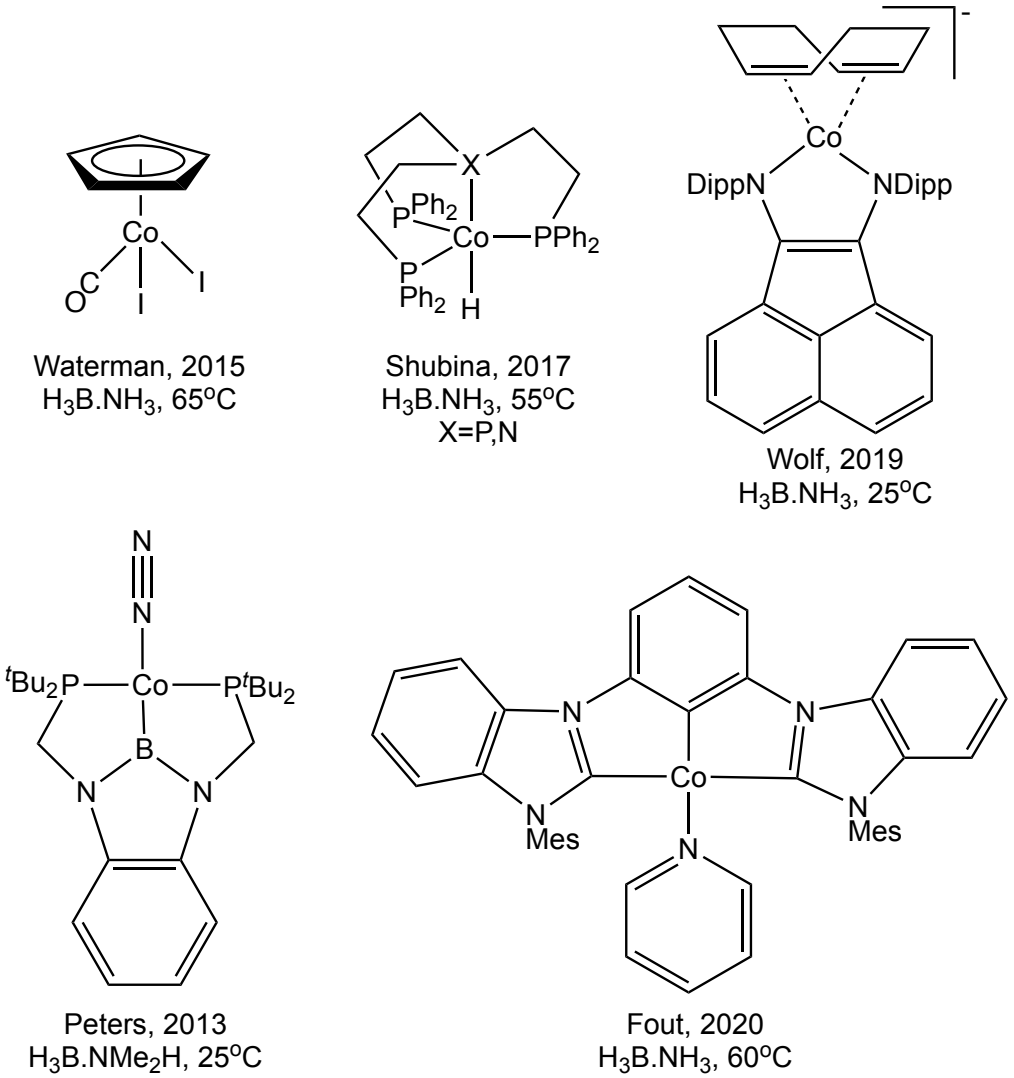
While a wide range of polymer chain lengths have been produced, chain length control within each individual catalyst has been limited. Control is so far shown most reliably with the cationic rhodium systems developed within the Weller group by varying catalyst loading.[25,28,29,35] Additionally, some progress has been made with boronium chain control. These systems are typically difficult to prepare and are highly air-sensitive making them not ideal for routine large scale polymer preparation.

3.1.10 Cobalt catalysed routes to polyaminoboranes

As described in the introduction there is significant financial and environmental motivation to move away from rhodium towards cobalt and that is the aim of the work described in this chapter. Despite the range of catalysts described above, there have only been a handful of published examples of Co complexes used for amine-borane dehydrogenation, let alone dehydropolymerisation, as shown in Scheme 3.6. These examples include a **(PBP)CoN$_2$** pincer complex (Scheme 3.6) reported by Peters, which has a meridional bis-phosphino-boryl (PBP) ligand. **(PBP)CoN$_2$** was shown to be able to dehydrocouple $H_3B{\cdot}NMe_2H$ to form the square dimer $(H_2B{\cdot}NMe_2)_2$ at room temperature.[36] Although a very interesting system, the catalyst was relatively slow with

a $ToF_{50\%}$ = 25 hr^{-1} and used at relatively high catalyst loading of 2 mol% (ToN = 50). No investigation into the dehydropolymerisation of other amine-boranes was reported using the **(PBP)CoN$_2$** system. The Cp-based cobalt complex, **CoCp(CO)I$_2$** used by Waterman was shown to be able to dehydrogenate $H_3N{\cdot}BH_3$ at 65 ^oC to give a range of products, unselectively, including borazine and borazane.[37] **CoCp(CO)I$_2$** could be used to transfer hydrogenate alkenes using $H_3N{\cdot}BH_3$ as a hydrogen source. Shubina's **CoH(E(CH$_2$CH$_2$PPh$_2$)$_3$)**(E = N and P) complexes with tripodal EP_3 ligands, dehydrogenate $H_3B{\cdot}NH_3$.[38] When E=P this dehydrogenation selectively gives $(H_2B{\cdot}NH_2)_n$, however no polymer chain length could be determined as $(H_2B{\cdot}NH_2)_n$ is formed as an insoluble precipitate. When E=N two equivalent of H_2 are produced and an unselective mixture of B-(cyclotriborazanyl)amine–borane, borazine, and polyborazylenes were obtained. While unselective this system demonstrates some variation of products produced by modification of ligand. Wolf's highly reduced diimine cobaltate complex **[K(thf)1.5{(DippBIAN)CoCOD]** (Dipp=2,6-diisopropylphenyl, BIAN=bisaryl-(imino)acenaphthene), was shown to be able to dehydrogenate a range of amine-boranes, with the focus on $H_3B{\cdot}NH_3$ but also including $H_3B{\cdot}NMeH_2$.[39] However, with $H_3B{\cdot}NMeH_2$ only short oligomers were formed of $(H_2B{\cdot}NMeH)_n$ (n=6-11) as determined by ESI-MS. Finally, the Fout group used the complex **(MesCCC)Co-py** (MesCCC = bis(2,4,6-trimethylphenyl-benzimidazol-2-ylidene)phenyl) for the dehydropolymerisation of $H_3B{\cdot}NH_3$. Stoichiometric reactions of **(MesCCC)Co-py** with $H_3B{\cdot}NMeH_2$ led to isolation of the crystallographically characterised complex **(MesCCC)CoH(NMeHBH$_3$)**, which represents an example of N-H activation to isolate a rare amidoborane species with an agostic B-H bond.[40] **(MesCCC)Co-py** was an effective catalyst for the dehydropolymerisation of $H_3N{\cdot}BH_3$ at 60 ^oC with **(MesCCC)CoH(NH$_2$BH$_3$)** shown to be the resting state of catalysis. Preliminary results

also reported activity with $H_3B{\cdot}NMeH_2$ and $H_3B{\cdot}NMe_2H$, however, M_n and $Đ$ of the polymer were not determined. Despite the number of cobalt systems developed, none have yet been shown to selectively produce high molecular weight polyaminoborane on scale.



Scheme 3.6 Example cobalt catalysts for amine-borane dehydropolymerisation.[36–40]

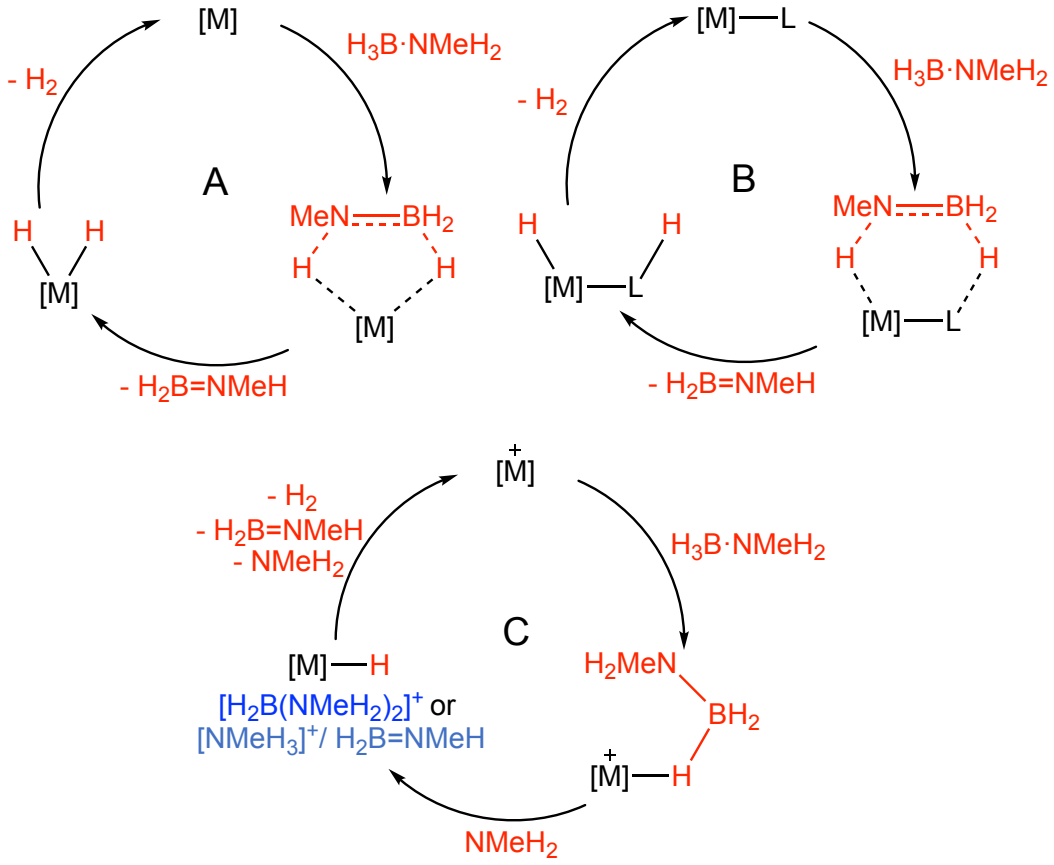
3.1.11 Mechanism for the dehydrogenation of amine-boranes

In organometallic chemistry, mechanistic understanding has enabled the optimisation of catalytic processes. Therefore elucidation of the mechanism of dehydropolymerisation is important for further refinement.[41] Most mechanistic studies

of amine-boranes have focused on the dehydrogenation rather than polymer propagation because it is more easily studied experimentally. The dehydrogenation is readily followed by measuring volume (by eudiometer - displacing water from an inverted burette) or pressure (using a 'man on the moon' type apparatus) of H_2 gas released. H_2 volume or pressure is used as it provides a proxy for how much amine-borane has been dehydrogenated and the cumulative total [H_2B=NMeH] produced. H_2 evolution is only appropriate for selective dehydropolymerisations where only one equivalent of H_2 is released. Otherwise side reactions that produce H_2 are also occurring and it is not possible to deconvolute the data into the separate processes. Data from selective dehydropolymerisation reactions have enabled kinetic profiles to be measured and the determination of reaction orders in both amine-borane and catalyst. Kinetic isotope effects have been determined by the use of selectively deuterated amine-boranes. From these data, overall mechanistic cycles have been suggested, complete with resting states and turnover limiting steps; all of on occasion have been calibrated with computational calculations.

Three principle generic types of mechanisms for dehydrogenation have been proposed and are shown in Scheme 3.7. Type (A): is an inner sphere BH/NH activation and is the most common. Type (B): a cooperative ligand assisted mechanism most frequently observed with PNP pincer based catalysts. Finally, type (C): cationic metal centre abstracts a hydride from amine-borane to form a neutral metal hydride and a boronium cation. The boronium cation is then deprotonated by the metal hydride forming hydrogen, amine, H_2B=NMeH, and regenerating the cationic metal centre. Alternatively in type (C) mechanisms the hydride abstraction could form ammonium (instead of boronium), H_2B=NMeH and a neutral metal hydride. The $[NMeH_3]^+$ is then

deprotonated by the metal hydride forming hydrogen, amine, and regenerating the cationic metal centre. For mechanisms of type A and B bond breaking/forming events could happen in any order and the dotted lines indicate the bonds that overall are made and broken.



Scheme 3.7 Mechanisms of amine-borane dehydrogenation. **(A)** Inner sphere BH/NH activation. **(B)** Cooperative ligand assisted mechanism. **(C)** Hydride abstraction/boronium deprotonation. Bond breaking/forming events could happen in any order and are not indicated by dotted lines.

Mechanism of type (B) have been proposed largely for pincer complexes such as the 'PNP' based systems of Beweries (**$FeH(BH_4)(CO)(NR((CH_2)_2P^iPr_2)_2)$**), Schenider's (**$FeH(CO)(NR((CH_2)_2P^iPr_2)_2)$**, and **$RuH(PMe_3)(N(CH_2)_2P^iPr_2)_2)$**).[21,22,30] Type (A) mechanisms have been proposed for a number of systems including Manners' **IrH_2(POCOP-^{t}Bu)** and **$TiCl_2Cp^*_2$ /** 2 eq. ^{n}BuLi systems.[17,42] Finally, type (C) mechanisms have been proposed as relevant for some cationic systems including

Conejero's **[Pt(I^{t}Bu′)(I^{t}Bu)][BAr$_4^F$]** and Weller's **[Rh(Ph$_2$P(CH$_2$)$_3$PR$_2$)-(C$_6$H$_5$F)][BAr$^F_4$]**.[23] For mechanisms of type (A) and (B), typically, N-H activation has proven turnover limiting.[6] Type (C) activation pathways are suggested for the activation of Weller's **[Rh(DPEphos-Ph)(H$_2$B·NMe$_3$(CH$_2$)$_2$^{t}Bu)][BAr$^F_4$]** and **[Rh(Ph$_2$P(CH$_2$)$_3$PR$_2$)-(C$_6$H$_5$F)][BAr$^F_4$]** systems to form the neutral bridging hydride complexes **[Rh(DPEphos-Ph)H$_2$]$_2$** and **Rh$_2$(^{i}Pr$_2$P(CH$_2$)$_3$P^{i}Pr$_2$)$_2$(μ-H)$_2$**.[25,28]

The progress of reactions is often compared in the literature using turnover frequencies (ToFs). However, due to the wide range of dehydropolymerisation conditions (concentration, H_2 pressure, temperature, solvent) and reporting methodologies (calculated for turnover to: completion, 50 % conversion, or at maximum rate), direct comparisons should be approached with caution. Despite these reservations, knowledge of reported ToFs with $H_3B{\cdot}NMeH_2$ is important for benchmarking the systems developed within this thesis, and a range have been reported: 30 h^{-1} for **FeH(CO)(NR((CH$_2$)$_2$P^{i}Pr$_2$)$_2$**,[30] 125 h^{-1} for **[Rh(DPEphos-Ph)(H$_2$BNMe$_3$(CH$_2$)$_2$^{t}Bu)][BAr$^F_4$]**,[29] 2,400 h^{-1} for **IrH$_2$(POCOP-^{t}Bu)**,[1] and 72,000 h^{-1} for **RuH(PMe$_3$)(N(CH$_2$)$_2$P^{i}Pr$_2$)$_2$)**.[17]

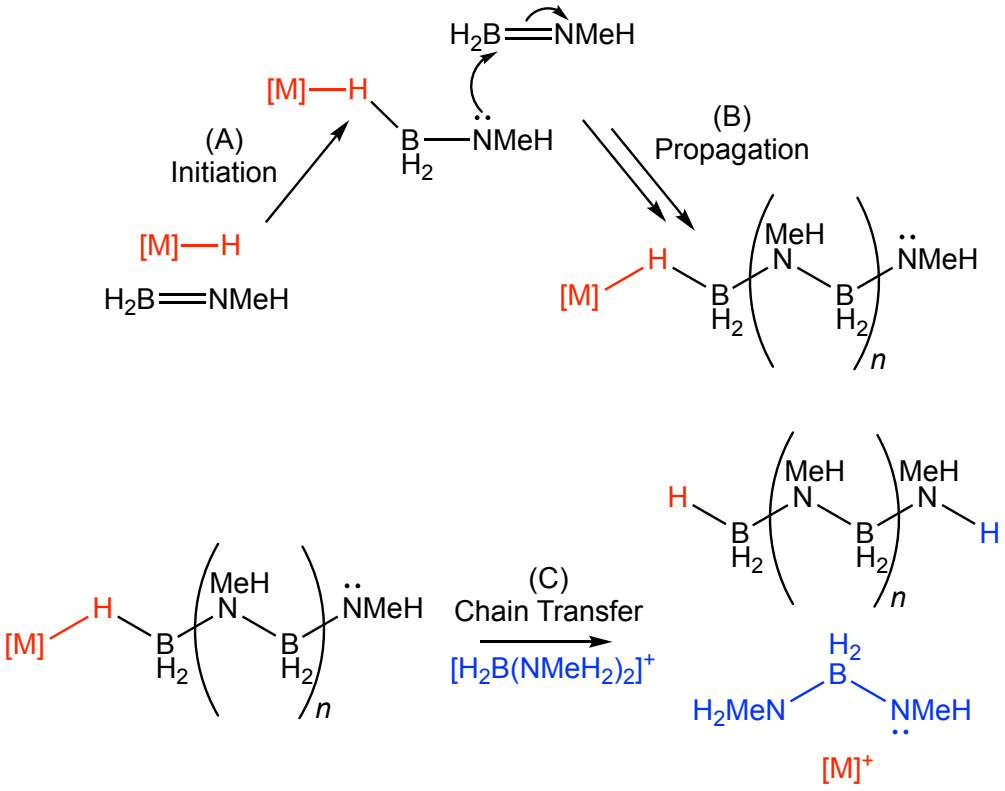
3.1.12 Mechanism for the polymerisation of amino-borane (H$_2$B=NMeH)

The mechanism of polymerisation is more challenging to investigate due to no suitable proxy being available for the absolute concentration of $H_2B{=}NMeH$ at any one point but the following details have been established. In the few computational studies polymerisation proceeds by $H_2B{=}NMeH$ undergoing nucleophilic head-to-tail propagation to form well-defined polymer $(H_2B{\cdot}NMeH)_n$ (Scheme 3.8).[35,43] This means polymerisation is initiated by nucleophilic attack of $H_2B{=}NMeH$ by a Lewis base; the

Lewis base could either be the catalyst as suggested for **IrH_2(PNONP)** or **{Rh(DPEphos-Ph)}** systems but also could be an independent nucleophile (trace amine or trace water) (Scheme 3.8 (A)).[17,35] If the catalyst is acting as the initiator it is playing a dual role involved in both dehydrogenation and polymerisation. This is followed by propagation where the nucleophilic chain end of the polymer attacks other units of $H_2B{=}NMeH$ (Scheme 3.8 (B)). Finally, chain transfer terminates the growing chain. Chain transfer is not well defined, but it is suggested that it involves boronium, $[H_2B(NMeH_2)_2]^+$, protonating the end of the growing polymer chain producing $(H_2B{\cdot}NMeH)_n$, $H_2MeN{\cdot}BH_2{\cdot}NMeH$ and a cationic metal fragment.[28] Boronium is considered a chain transfer agent (CTA) as it terminates the growing polymer chain to form $(H_2B{\cdot}NMeH)_n$ and simultaneously creates $H_2MeN{\cdot}BH_2{\cdot}NMeH$ which can be considered a new growing polymer chain (Scheme 3.8 (C)). Notably, other proton sources such as ammonium could act in an analogous way to boronium (Scheme 3.7). In this polymerisation mechanism the degree of polymerisation (χ) will be determined by the relative rates of propagation and chain transfer. The rate of propagation (R_{prop}) = k_{prop}[growing chain][$H_2B{=}NMeH$] and rate of chain transfer (R_{trans}) = k_{trans}[growing chain][CTA]:

$$X \propto \frac{\mathrm{R_{prop}}}{\mathrm{R_{trans}}} = \frac{\mathrm{k_{prop}[growing\ chain][H_2B = NMeH]}}{\mathrm{k_{trans}[growing\ chain][CTA]}} = \frac{\mathrm{k_{prop}[H_2B = NMeH]}}{\mathrm{k_{trans}[CTA]}}$$

Therefore, the resultant degree of polymerisation will vary with the ratio [$H_2B{=}NMeH$]:[CTA]. This will be explored further in Section 3.2.11.



Scheme 3.8 A proposed mechanism of polymerisation. **(A)** Initiation involves nucleophilic addition of a Lewis base to $H_2B{=}NMeH$. **(B)** Propagation is a nucleophilic head to tail polymerisation. **(C)** Chain transfer is the protonation of the growing polymer chain by a boronium which gives $(H_2BNMeH)_n$, a new growing polymer chain and regenerates a cationic catalyst.

Experimental evidence for this model of polymerisation is provided by the cationic pre-catalysts such as **[Rh(DPEphos-Ph)($H_2B{\cdot}NMe_3(CH_2)_2{}^tBu$)][$BAr^F{}_4$]** where the degree of polymerisation, as indicated by M_n, scales inversely with $[Rh]_{total}$. For example M_n = 6400 g mol^{-1} at 1 mol% catalyst loading while M_n = 34,900 $gmol^{-1}$ at 0.2 mol%.[29] In contrast with neutral pre-catalyst **Rh(DPEphos-Ph)Benzyl** varying catalyst loading did not affect the degree of polymerisation of polymer produced in either 1,2-$F_2C_6H_4$ (M_n = 15,000 g mol^{-1}) or THF (M_n = 17,000 g mol^{-1}).[28] As the neutral and cationic pre-catalysts both activate to give the same on cycle resting state (**[Rh(DPEphos-Ph)H_2]$_2$**) and only differ by the presence of concomitantly formed boronium in the cationic case. In the cationic case the relative concentration of boronium will scale with $[Rh]_{total}$ so the

inverse relationship between catalyst loading and M_n supports the role of boronium as a chain transfer agent to control the molecular weight of the polymer.

To further test this hypothesis, the neutral pre-catalyst **Rh(DPEphos-Ph)Benzyl** was doped with boronium $[H_2B(NMeH_2)_2][BAr^F{}_4]$ to see if it can act as a chain control agent and modify the degree of polymerisation. GPC analysis shows a qualitative trend in decreasing M_n with increasing concentration of $[H_2B(NMeH_2)_2][BAr^F{}_4]$, with quantitative analysis complicated by the coelution of $[BAr^F{}_4]^-$. This evidence provides strong support for the proposed polymerisation mechanism. Due to these observations and the broad agreement with observations made for cationic Rh systems more generally this polymerisation mechanism is the benchmark hypothesis used in this thesis.[28]

3.1.13 Aims of this chapter

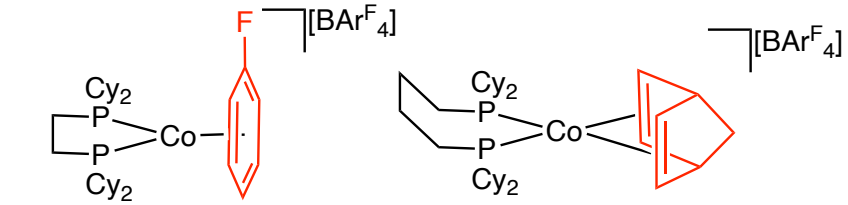
The prior work discussed above has enabled a general understanding of the fundamental processes which dictate the efficiency of dehydropolymerisation reactions. However, most of this work has been carried out on small scale, with highly air-sensitive and challenging to prepare complexes. With this mechanistic understanding in hand, attention was turned to producing robust air-stable, easy to assemble catalysts that operate at low catalyst loadings on scale, to produce polymer with chain control selectively.

There is currently a lack of understanding of properties of the polyaminoboranes; the mechanical (e.g., yield and tensile stress, casting properties), electronic and pre-ceramic properties all need further investigation in order to determine the use of these polymers.[6,8,11] These tests require large amounts of materials (> 1 g) so before they

can be carried out polyaminoborane must be produced on scale. These next two chapters will report such an advance.

3.2 Results and discussion

3.2.1 Initial Screening of cationic Co(I) catalysts for dehydropolymerisation.



[Co(L1)(η-FC$_6$H$_5$)][BAr$^F_4$] **[Co(L2)(NBD)][BAr$^F_4$]**

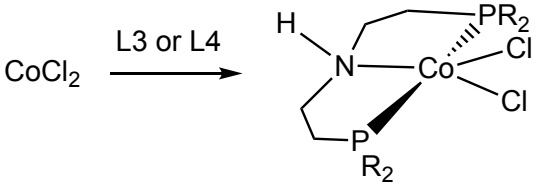
Scheme 3.9 Cationic Co(I) pre-catalysts from Chapter one.

Inspired by the previous work within the group on cationic Rh(I) pre-catalysts for the dehydropolymerisationation of amine-boranes (Section 3.1.5), the cationic Co(I) systems developed in Chapter 1 (Scheme 3.9) seemed like promising pre-catalysts for the dehydropolymerisation of amine-boranes.[20,44] **[Co(L1)(η-FC$_6$H$_5$)][BAr$^F_4$]** (5 mol%, 25 °C, 1,2-$F_2C_6H_4$, 0.22 M [$H_3B{\cdot}NMeH_2$]) (L1 = $Cy_2P(CH_2)_2PCy_2$) was screened as a precatalyst for the dehydrocoupling of $H_3B{\cdot}NMeH_2$. The reaction was monitored by ^{11}B NMR spectroscopy and no conversion of the $H_3B{\cdot}NMeH_2$ starting material observed. The addition of NH_2Me, a known amine-borane dehydropolymerisation promoter, did not initiate turnover.[29] As described in section 3.1.5 the closely related rhodium complex **[Rh(^{i}Pr$_2$P(CH$_2$)$_2$P^{i}Pr$_2$)(C$_6$H$_5$F)][BAr$^F_4$]** was also inactive for the dehydrocoupling of amine-boranes in 1,2-$F_2C_6H_4$. However, it was found that increasing the bite angle by increasing the number of carbons in the backbone encouraged both the formation of a σ-amine-borane complexes and also the

dehydropolymerisation of $H_3B{\cdot}NMeH_2$ to form $(H_2B{\cdot}NMeH_2)_n$.[20] **[Co(L2)(NBD)][BAr$^F_4$]** (L2 = $Cy_2P(CH_2)_4PCy_2$) has more carbons in the backbone; however, it decomposes upon hydrogenation in solution (section 2.2.4), so it was determined that this ligand system on cobalt was unsuitable for the dehydropolymerisation of $H_3B{\cdot}NMeH_2$.

3.2.2 Screening of Co(ligand)Cl_2 type catalysts for dehydropolymerisation

To find an appropriate ligand system for the dehydropolymerisation of $H_3B{\cdot}NMeH_2$, **Co(ligand)Cl_2** type complexes were screened, using NH_2Me as a promotor. The simple addition of a bidentate phosphine ligand to $CoCl_2$ in THF has given a wide range of literature reported isolable **Co(ligand)Cl_2** complexes.[45,46] These **Co(ligand)Cl_2** complexes are typically characterised by X-ray diffraction studies. Addition of literature known complexes **Co(DPEphos-Ph)Cl_2** or **Co(Xantphos-Ph)Cl_2** (5 mol%, 25 °C, 1,2-$F_2C_6H_4$, Xantphos-Ph = 4,5-bis(diphenylphosphino)-9,9-dimethylxanthene) to $H_3B{\cdot}NMeH_2$ (0.22 M) saw no colour change and $H_3B{\cdot}NMeH_2$ was the only species present by ^{11}B NMR spectroscopy after four hours. Subsequent addition of NH_2Me (2 M in THF, 2eq relative to [Co]) also gave no colour change and $H_3B{\cdot}NMeH_2$ was still the only species present by ^{11}B NMR spectroscopy.



$CoCl_2$(LX)
L3, R = ^{i}Pr; L4, R = Cy

Scheme 3.10 Synthesis of pre-catalysts **Co(L3)Cl_2** and **Co(L4)Cl_2**.

The purple PNHP pincer complexes **Co(L3)Cl$_2$** or **Co(L4)Cl$_2$** ($(R_2PCH_2CH_2)_2NH$; R = ^{i}Pr, L3; Cy, L4) were first reported by the Arnold group and prepared by simple addition of ligand to $CoCl_2$ (Scheme 3.10).[47] These complexes displayed broad ^{1}H and silent ^{31}P NMR spectra due to the paramagnetic metal centre. On screening **Co(L3)Cl$_2$** or **Co(L4)Cl$_2$** (5 mol%, 25 ºC, 1,2-$F_2C_6H_4$) for the dehydropolymerisation of $H_3B{\cdot}NMeH_2$ (0.22 M) by monitoring the reaction in a sealed J. Youngs NMR tube no colour change was seen and $H_3B{\cdot}NMeH_2$ was the only species present by ^{11}B NMR spectroscopy. However, on the addition of NH_2Me (2 M in THF, 2 eq. relative to [Co]) rapid bubbling was observed, and the reaction had gone to completion by the time an NMR spectrum could be collected after ~3 minutes. The ^{11}B NMR spectra showed a single broad resonance at −6.8 ppm for polyaminoborane $(H_2B{\cdot}NMeH)_n$ as the major peak (90 %), alongside a small amount of borazine (10 %). Due to this rapid pressure build-up within the sealed J. Youngs NMR tube, future reactions were carried out at lower catalyst loadings and in a 50 mL jacketed two-neck Schlenk flask connected to circulated cooling fluid to maintain a constant temperature. This was performed under a flow of Ar or connected to an eudiometer.

3.2.3 Optimisation using Co(L3)Cl$_2$ and Co(L4)Cl$_2$ pre-catalysts

The catalyst loading was reduced to 0.4 mol% from 5 mol%. Addition of **Co(L3)Cl$_2$** or **Co(L4)Cl$_2$** (0.4 mol%, 25 °C, 1,2-$F_2C_6H_4$) to $H_3B{\cdot}NMeH_2$ (0.22 M) resulted in no H_2 evolution or colour change and only $H_3B{\cdot}NMeH_2$ was observed in the ^{11}B NMR spectra. On the addition of NH_2Me (2 M in THF, 2 eq. relative to [Co]), immediate hydrogen production was observed using an eudiometer, and the solution changed from a purple to a tan colour. At the end of catalysis, an aliquot of the reaction mixture was taken for NMR spectroscopy. The ^{11}B NMR spectrum showed only $(H_2B{\cdot}NMeH)_n$

at −6.8 ppm. Due to the combination of low catalyst concentration, high concentration of substrate, and the paramagnetic Co metal centre, no clear resonances could be observed in the ^{1}H or ^{31}P NMR spectra for the catalyst. Monitoring the reaction by H_2 evolution (eudiometer) showed ~1 equivalent of H_2 per $H_3B{\cdot}NMeH_2$ had been released by the end of catalysis. Both are fast catalysts; **Co(L3)Cl₂** gives a ToF ~ 750 h^{-1}, and **Co(L4)Cl₂** is even faster with a ToF ~3,700 h^{-1}. These are ToFs to 100% conversion and yet still among the highest reported for the dehydropolymerisation of $H_3B{\cdot}NMeH_2$. The kinetic data fit no simple order in $H_3B{\cdot}NMeH_2$, and so a detailed analysis was not carried out as the focus was on optimisation of polyaminoborane production. An aliquot of the reaction mixture at the end of catalysis was interrogated by ^{11}B NMR spectroscopy which showed that polyaminoborane had formed selectively. The polymer formed was isolated by precipitation into *n*-pentane to give $(H_2B{\cdot}NMeH)_n$ (30 mg, 60% yield) as an off-white powder. The isolated polymer was analysed by GPC. The **Co(L3)Cl₂** catalyst produced polymer of M_n = 47,600 g mol^{-1} and $Đ$ = 1.5 while **Co(L4)Cl₂** catalyst produced polymer of M_n = 51,100 g mol^{-1} and $Đ$ = 1.7.

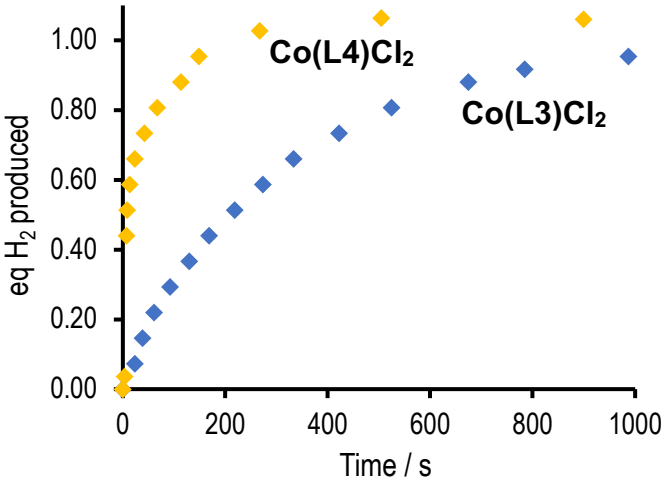


Figure 3.1 Temporal profile of H_2 realease from a dehydropolymerisation reaction with **Co(L3)Cl₂** and **Co(L4)Cl₂** (0.4 mol%, 25 °C, 1,2-$F_2C_6H_4$, 0.22 M [$H_3B{\cdot}NMeH_2$], 2 eq. NH_2Me).

If this dehydropolymerisation using **Co(L3)Cl$_2$** (^{i}Pr) or **Co(L4)Cl$_2$** (Cy) catalysts (0.4 mol%, 25 °C, 1,2-$F_2C_6H_4$, 0.22 M [$H_3B{\cdot}NMeH_2$]) was carried out under an Ar flow to constantly remove H_2 instead of under eudiometer conditions the reaction reaches completion faster (10 minutes under Ar flow vs 20 minutes eudiometer for **Co(L3)Cl$_2$**) as determined using ^{11}B NMR spectroscopy. This faster overall time to completion indicates the overall reaction rate is sensitive to hydrogen concentration in solution. This hydrogen sensitivity is a potential explanation for the complex kinetics which fit no simple order in $H_3B{\cdot}NMeH_2$. There is no notable change in the polymer produced (M_n, $Đ$ or yield) if the catalysis is performed under an Ar flow or eudiometer conditions suggesting that although H_2 may slow catalysis it does not change the fundamental speciation of the operative catalyst. However, increasing the catalyst loading had the effect of decreasing (Table 3.2) the degree of polymerisation, as measured by M_n, of the isolated polymer, while $Đ$ remains unchanged: M_n ranges from 71,000 g mol^{-1} for **Co(L4)Cl$_2$** at 0.2 mol% catalyst loading down to 22,400 g mol^{-1} at 0.8 mol%. Both **Co(L3)Cl$_2$** and **Co(L4)Cl$_2$** show similar values for the M_n of polymer produced at each catalyst loading demonstrating the reliability of this type of system. Therefore the degree of polymerisation of polymer produced (as represented by M_n) can be tuned by varying the catalysts loadings potentially enabling the production of polymer with different material or electronic properties.[6] Using catalyst loading to tune the degree of polymerisation has previously been reported for cationic rhodium systems (Section 3.1.5).[29,35] This M_n versus catalyst loading trend will be considered further in Section 3.2.12.[29,35] Reducing the catalyst loading to 0.1 mol% resulted in no dehydropolymerisation, which was assigned to the catalyst being quenched by trace impurities in either the solvent or $H_3B{\cdot}NMeH_2$.

Entry	catalyst	mol%	M_n / g mol^{-1}	$Đ$
1	**Co(L3)Cl$_2$**	0.2	66,900	1.4
2	**Co(L3)Cl$_2$**	0.4	48,000	1.4
3	**Co(L3)Cl$_2$**	0.8	33,100	1.4
4	**Co(L4)Cl$_2$**	0.2	71,000	1.5
5	**Co(L4)Cl$_2$**	0.4	51,100	1.7
6	**Co(L4)Cl$_2$**	0.8	22,400	1.5

Table 3.2 Polymer characterisation using different catalysts loadings of **Co(L3)Cl$_2$** and **Co(L4)Cl$_2$** (25 °C, 1,2-$F_2C_6H_4$, 0.22 M [$H_3B{\cdot}NMeH_2$], 2 eq NH_2Me) for dehydropolymerisation.

3.2.4 THF as a solvent for dehydropolymerisation of $H_3B{\cdot}NMeH_2$

The combination of the cost of 1,2-$F_2C_6H_4$ (~60 £/L vs ~5 £/L for THF) and the limited solubility (~0.22 M) of $H_3B{\cdot}NMeH_2$ in 1,2-$F_2C_6H_4$ limits the ability to scale up the dehydropolymerisation using 1,2-$F_2C_6H_4$ as the solvent.[35] With THF, much higher $H_3B{\cdot}NMeH_2$ concentrations (10 M) have been used with the IrH_2(PONOP) system.[1] At 0.22 M [$H_3BN{\cdot}MeH_2$] in THF neither **Co(L3)Cl$_2$** or **Co(L4)Cl$_2$** (0.4 mol%, 25 °C, 2 eq. $NMeH_2$ relative to [Co]) were observed to catalyse the dehydropolymerisation of $H_3B{\cdot}NMeH_2$, with only starting material observed in the ^{11}B NMR spectrum after one hour. However, raising the concentration to 5 M [$H_3B{\cdot}NMeH_2$] enabled both **Co(L3)Cl$_2$** and **Co(L4)Cl$_2$** (0.4 mol%, 25 °C, 2 eq. $NMeH_2$ relative to [Co]) to catalyse the dehydropolymerisation, albeit at a lower rate (at 0.4 mol% reaction completion takes ~1 hr rather than ~10 mins in 1,2-$F_2C_6H_4$ for **Co(L3)Cl$_2$**). The ^{11}B NMR spectra of an aliquot taken at the end of reaction showed selective conversion cleanly to polymer. This increase in concentration (0.22 M to 5 M) means that for the same volume of solvent (5 mL), the scale had been increased from 50 mg $H_3B{\cdot}NMeH_2$ to 1.12 g. Increasing the concentration of $H_3B{\cdot}NMeH_2$ to 5 M has also scaled the absolute

concentration of pre-catalysts. For 0.4 mol% loading from [Cat] = 0.88 mM at $[H_3B{\cdot}NMeH_2]$ = 0.22 M has increased to 20 mM [Cat] at $[H_3B{\cdot}NMeH_2]$ = 5 M. Suppose that 1 mM of catalyst is quenched by impurities in the solvent, with $[H_3B{\cdot}NMeH_2]$ = 0.22 M and 0.4 mol% catalyst loading all of the catalyst (0.88 mM) would have been quenched and catalysis would not proceed. Whereas at $[H_3B{\cdot}NMeH_2]$ = 5 M and 0.4 mol% catalyst very little of the catalyst (~5%) would have been quenched by impurities in the solvent and catalysis would proceed. At $[H_3B{\cdot}NMeH_2]$ = 5 M both **Co(L3)Cl$_2$** and **Co(L4)Cl$_2$** were operative pre-catalysts to as low as 0.02 mol% loadings, but no lower. This predicts that just less than 1 mM of catalyst was quenched by impurities in the solvent consistent with no activity seen for $[H_3B{\cdot}NMeH_2]$ = 0.22 M at 0.4 mol% catalyst loading (0.88 mM). Characterisation of the isolated polymer by GPC revealed a trend for smaller M_n at higher catalyst loading while $Đ$ remains roughly constant (Table 3.3), as seen using 1,2-$F_2C_6H_4$ solvent. As M_n scales inversely with [Cat], this activity at lower catalyst loadings enables the synthesis of higher molecular weight polymer, up to 112,400 g mol^{-1} with **Co(L4)Cl$_2$** at 0.02 mol%. The GPC trace of isolated $(H_2B{\cdot}NMeH)_n$ gives one clear defined peak (Figure 3.2), confirming monomodal polymer is produced.

Entry	catalyst	mol%	Time / mins	M_n / g mol^{-1}	$Đ$
7	**Co(L3)Cl$_2$**	0.02	90	98,800	1.6
8	**Co(L3)Cl$_2$**	0.1	60	85,800	1.6
9	**Co(L3)Cl$_2$**	0.8	10	48,000	1.7
10	**Co(L4)Cl$_2$**	0.02	90	112,400	1.5
11	**Co(L4)Cl$_2$**	0.1	60	81,900	1.5
12	**Co(L4)Cl$_2$**	0.8	10	47,500	1.6
13[a]	**Co(L4)Cl$_2$**	0.02	120	74,200	1.6
14[b]	**L3/CoCl$_2$**	0.1	60	62,500	1.6

Table 3.3 Polymer characterisation using different catalysts loadings of **Co(L3)Cl$_2$** and **Co(L4)Cl$_2$** (25 °C, THF, 5 M [$H_3B{\cdot}NMeH_2$], 2 eq. NH_2Me) for dehydropolymerisation.[a] 10 g scale. [b] Catalyst formed in-situ.

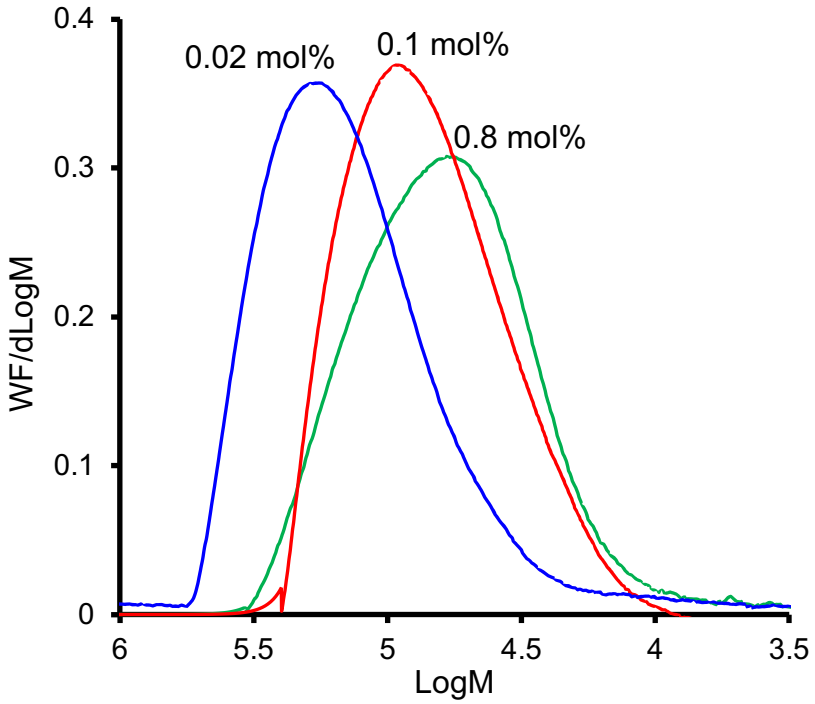


Figure 3.2 GPC traces for **Co(L3)Cl$_2$** catalysed polymerisations (25 °C, THF, 5 M [$H_3B{\cdot}NMeH_2$], 2 eq. NH_2Me) at 0.02, 0.1, 0.8 mol% catalyst loadings. One well defined peak shows monomodal polymers.

3.2.5 10 g scale dehydropolymerisation of $H_3B{\cdot}NMeH_2$ using Co(L4)Cl_2 pre-catalyst

With these new conditions in hand the polymerisation was readily scaled to 10 g using **Co(L4)Cl_2**. This was carried out in a round-bottomed flask under an N_2 flow with the polymer isolation performed open to air. The isolated polymer was an off white powder (Figure 3.3 (A)) with M_n = 74,200 g mol^{-1}, $Đ$ = 1.6 determined by GPC analysis. The ^{11}B NMR spectra of an aliquot taken at the end of catalysis still showed clean conversion to only $(H_2B{\cdot}NMeH)_n$. The only limitations to further scaling this reaction were safety concerns about the volume of H_2 gas released and the potential exotherm of the reaction due to the fast rate of dehydropolymerisation, problems which could be readily overcome by design of experiment. Additionally, it was possible to generate the catalyst in-situ from $CoCl_2$ and L3 before addition to $H_3B{\cdot}NMeH_2$/$NMeH_2$; the ^{11}B NMR spectra of a reaction aliquot taken at the end of catalysis from such in-situ preparation and it was observed that polymer was still selectively synthesised, further demonstrating the versatility of this catalyst. GPC analysis of this isolated polymer gave M_n = 62,500 g mol^{-1} and $Đ$ = 1.6, similar to that with pre-prepared catalysts.

3.2.6 Processing the $(H_2B{\cdot}NMeH)_n$ produced

When isolated the polymer is stable in air for at least one month as measured by GPC and ^{11}B NMR spectroscopy. ICP-MS determined that most of the [Co] is retained in the isolated polymer, albeit a small absolute quantity due to the low catalysts loadings used (830 ppm for a 0.4 mol% loading of **Co(L4)Cl_2**). This cobalt content was reduced (138 ppm) by rapidly passing a THF solution of $(H_2B{\cdot}NMeH)_n$ through a silica plug. Surprisingly, no degradation post purification was observed by GPC or ^{11}B NMR spectroscopy. Furthermore, this polymer could be processed to create films;

concentrated solutions (1 g mL^{-3}) of $(H_2B{\cdot}NMeH)_n$ (Table 3.3, Entry 10) in THF could be drop cast to form a brittle film of $(H_2B{\cdot}NMeH)_n$ (Figure 3.3 (B)). The ability to produce polymer on a larger scale (10 g) will enable future testing of processing methods and materials properties.

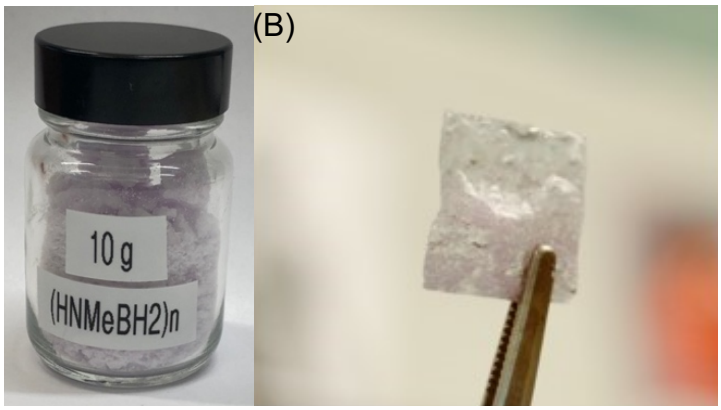


Figure 3.3 (A) 10 g of off white polymer produced under simple catalytic conditions M_n = 74,200 g mol^{-1}, $Đ$ = 1.6. **(B)** A brittle film of $(H_2B{\cdot}NMeH)_n$ produced by drop-casting from concentrated (1 g mL^{-3}) THF solution. The polymer used was produced by procedure in Table 3.3. Entry 10.

3.2.7 Mechanistic investigations

Co(L3)Cl_2 was used for a preliminary mechanistic study. However, this was complicated by the paramagnetic Co(II) centre which, when coupled with low catalyst loadings , made catalyst speciation studies by NMR spectroscopy challenging.

3.2.8 Testing for homogeneous vs heterogeneous catalysis

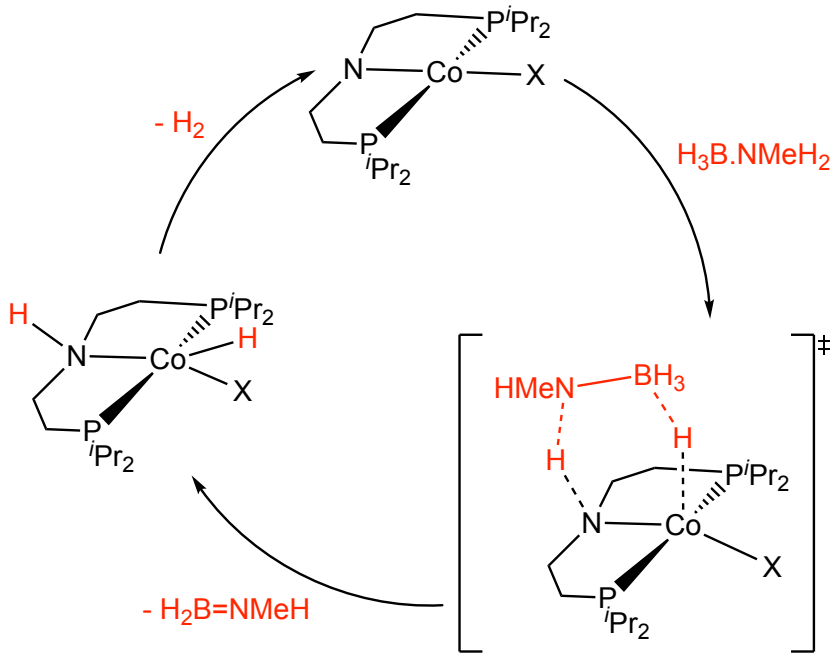
To determine if Co nanoparticles formed in-situ and catalysed the reaction, three standard tests for catalyst homogenity were performed.[48] First, sub-stoichiometric [PPh_3] (1,2-$F_2C_6H_4$, **Co(L3)Cl_2**, 0.4 mol%, 0.3 eq PPh_3 relative to [Co]) was added to the reaction mixture. No significant change in the time to completion was observed, the catalysis still proceeded to completion in less than 10 minutes. Additionally, the presence of PPh_3 did not alter the polymer recovered (M_n = 48,000 g mol^{-1}, $Đ$ = 1.4).

Sub-stoichiometric PPh_3 would be expected to stop the reaction if nanoparticles had been formed as only a fraction of the metal sites would be on the surface of the nanoparticle so these could be inhibited by less than stoichiometric amounts of phosphine. Addition of Hg (1,2-$F_2C_6H_4$, **Co(L3)Cl$_2$**, 0.4 mol%, ~1,000 eq relative to [Co]) at the start of catalysis also did not affect the time to completion, while the ^{11}B NMR spectrum of an aliquot taken at the end of catalysis showed only $(H_2B{\cdot}HMeH)_n$. The polymer was not isolated due to the contamination with Hg, thus GPC analysis could not be performed. Hg would form an amalgam with Co nanoparticles which would stop the reaction if heterogeneous.[39] Finally, a Co colloid was deliberately generated by adding 2 eq. of NMe_2 to $CoCl_2$ and $H_3B{\cdot}NMeH_2$ in the absence of ligand.[49] After an hour, there was no significant turnover, and a black magnetic precipitate assumed to be Co colloids had formed. From these results, it was concluded that the catalysis most likely operated by a homogeneous pathway.

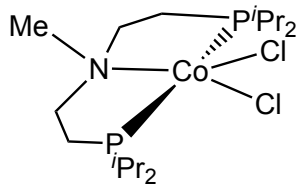
3.2.9 Suggested mechanism for amine-borane dehydrogenation

As described in the introduction cobalt catalysts are commonly found in oxidation states 0 – III inclusively. The catalyst moves between these states through a combination of classical two electron process (oxidative addition and reductive elimination) and one electron processes (disproportionation and reaction with one electron sources such as Zn). The amine-borane substrate enables the halides on the metal centre to be replaced with hydrides *via* a hydride transfer reaction. Collectively these steps give access to the complexes **Co(L3)X$_2$**, **Co(L3)X$_2$H** or **Co(L3)X** (where X=H or Cl) and are considered in more detail in Section 3.2.10.

One possible mechanism for amine-borane dehydrogenation is a cooperative ligand, constant oxidation-state, Co(II) cycle based on **Co(L3)X$_2$** type catalyst state (Scheme 3.11). Independently, Schneider and Beweries have suggested similar for **{FeL3}** based amine-borane dehydropolymerisation catalysts, as has Beller for the reduction of carboxylic acids to alcohols using **Co(L3)Cl$_2$**.[21,22,50] A ligand assisted reaction is supported by no reaction being observed when the ligand was modified to have an NMe moiety rather than an NH moiety; **CoCl$_2$(^{i}Pr$_2$PCH$_2$CH$_2$)$_2$NMe** (Scheme 3.12) did not promote the dehydropolymerisation of $H_3B{\cdot}NMeH_2$ (1,2-$F_2C_6H_4$, 0.4 mol% 2 eq NH_2Me relative to [Co]) as observed by ^{11}B NMR spectroscopy of an aliquot of the reaction mixture after 1 hour. **CoCl$_2$(^{i}Pr$_2$PCH$_2$CH$_2$)$_2$NMe** was prepared by an analogous procedure to **CoCl$_2$(L3)**, by addition of the ligand to $CoCl_2$ in THF.[47]

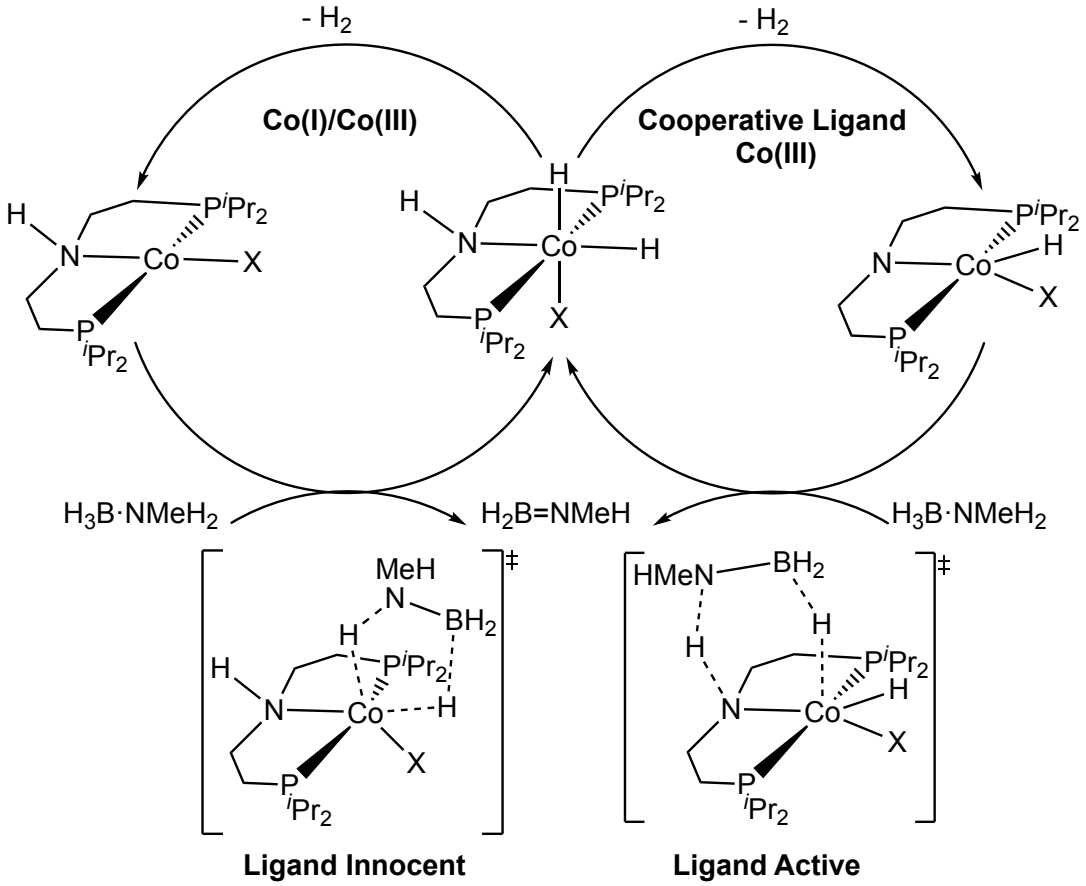


Scheme 3.11 A simplified cooperative ligand, constant oxidation-state, Co(II) cycle for dehydrogenation, with X = H or Cl.



Scheme 3.12 $CoCl_2(^iPr_2PCH_2CH_2)_2NMe$.

However, a ligand innocent Co(I)/Co(III) catalyst pathway is also possible shown in Scheme 3.13. Hydride sources are known to react with **$CoCl_2$(ligand)** complexes to form Co(I) species.[50,51] Previously reported **CoCl(L3)** undergoes reversible addition of H_2, which is consistent with the decrease in rate observed under H_2 measurement conditions.[52] Similar uncertainty between a cooperative ligand, constant oxidation-state Co(II) cycle and a Co(I)/Co(III) has been discussed recently by Beller for the reduction of carboxylic acids using **$CoCl_2$(L3)**.[50] A constant oxidation state cooperative ligand Co(III) pathway is also possible (Scheme 3.13). Notably none of these suggested mechanisms are based on the pre-catalyst **$CoCl_2$(L3)** and with the dependence on added amine and change of colour of the reaction mixture over the course of catalysis it is necessary to consider what activation processes may be occurring.



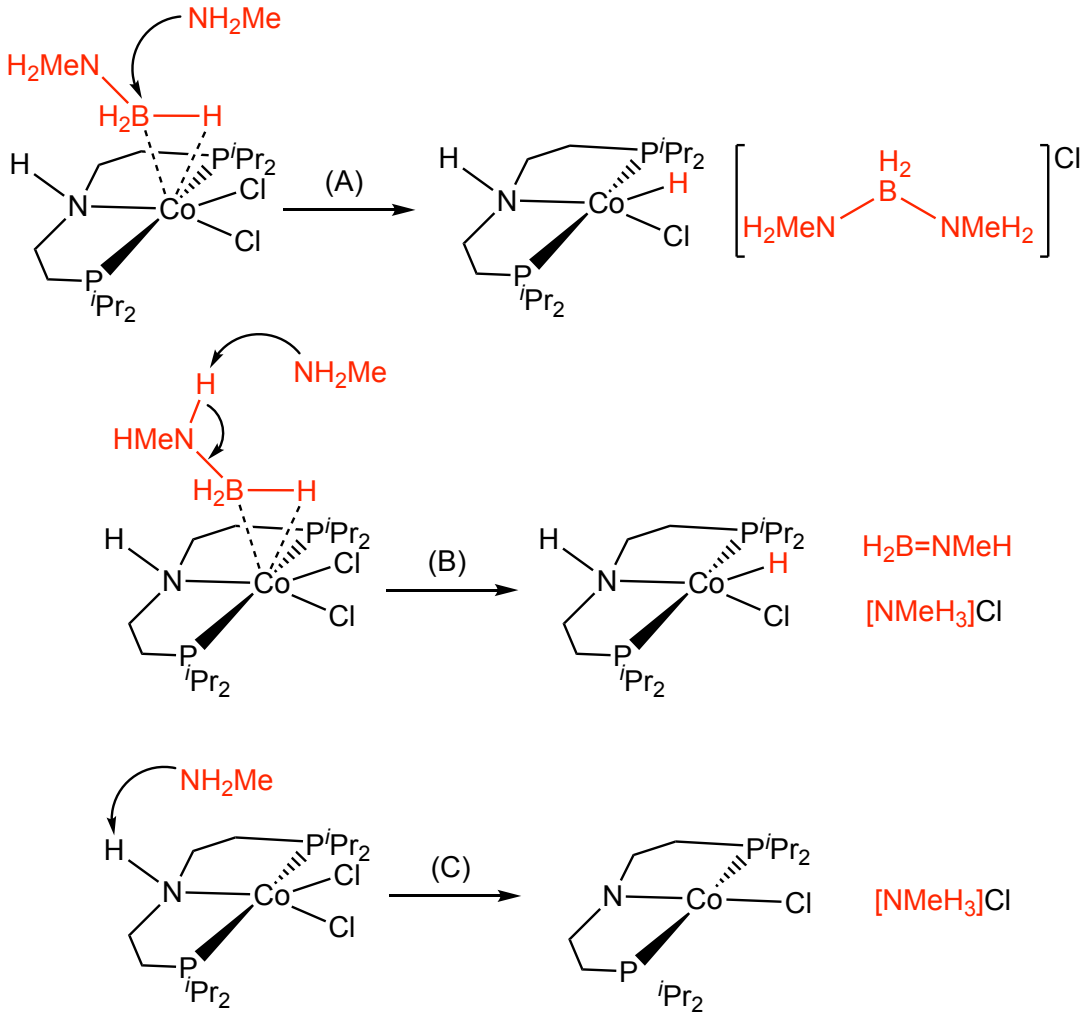
Scheme 3.13 Potential Co(I)/Co(III) catalytic cycles for dehydropolymerisation.

3.2.10 Pre-catalyst activation pathways

$NMeH_2$ is required for catalysis, and it is proposed that it promotes hydride transfer from $H_3B{\cdot}NMeH_2$, with the elimination of Cl^- to form **CoXH(L3)** (where X = H or Cl).[28] Both **CoClH(L3)** and **CoH_2(L3)** are potential on-cycle species which can be represented as **CoXH(L3)** (where X = H or Cl, Scheme 3.11 and 3.13). One activation pathway (Scheme 3.14 (A)) is *via* a hydride transfer from a σ-bound amine–borane followed by the formation of boronium, $[H_2B(NMeH_2)_2]Cl$.[23] Alternatively, the formation of $[NMeH_3]Cl$ *via* deprotonation of a σ-bound amine–borane intermediate by $NMeH_2$ and elimination of $H_2B{=}NMeH$ is also possible (Scheme 3.14 (B)).[53] Another explanation is deprotonation of the backbone NH by methylamine to yield

CoCl(^{i}Pr$_2$PCH$_2$CH$_2$)$_2$N and an equivalent of [NMeH$_3$]Cl (Scheme 3.14 (C)). However, activation by backbone deprotonation was discounted due to no reaction observed (^{1}H NMR, colour) between **CoCl$_2$(L3)** and excess H_2NMe. σ-bound amine–borane complexes are involved in two of these activation mechanisms and while no σ-bound amine–borane complexes of cobalt have been isolated, the Fout group have crystallographically characterised an agostic B-H bond in the amidoborane complex **(MesCCC)CoH(NH$_2$BH$_3$)**.[40]

In Section 3.1.12 it was described how boronium or ammonium can both potentially act as a chain transfer agent (CTA) by protonating the end of the growing nucleophilic chains. Higher concentrations of CTA will decrease the degree of polymerisation (as represented by M_n) in the dehydropolymerisation of $H_3B{\cdot}NMeH_2$. It is important to note that all of these activation pathways that invoke the monohydride **CoClH(L3)** create an equivalent of CTA in the form of either boronium or ammonium. If instead the active catalyst takes the form of the dihydride **CoH$_2$(L3)**, this would be generated by a second hydride transfer from **CoClH(L3)** (produced in Scheme 3.14) along with a second equivalent of CTA. With the paramagnetic Co making speciation studies by NMR spectroscopy difficult, working out the details of the activation processes is fundamentally challenging. However, by consideration of the relative amounts of CTA produced with different possible activation processes it is possible to predict the effect on M_n of polymer produced by different catalyst. In order to do this it is necessary to introduce Mayo plots.



Scheme 3.14 Potential activation pathways for pre-catalysts **Co(L3)Cl$_2$**. **(A)** Hydride transfer from a σ-bound amine–borane followed by the formation of boronium. **(B)** Deprotonation of a σ-bound amine–borane by $NMeH_2$ intermediate and elimination of $H_2B{=}NMeH$ and formation of $[NMeH_3]Cl$. **(C)** Deprotonation of the NH on the backbone of the ligand by $NMeH_2$ to yield **CoCl(^{i}Pr$_2$PCH$_2$CH$_2$)$_2$N** and an equivalent of $[NMeH_3]Cl$.

3.2.11 Mayo plots – understanding chain transfer agent

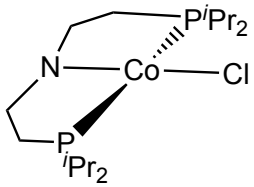
As described in Section 3.1.12 the polymerisation of $H_2B{=}NMeH$ is a nucleophilic head-to-tail propagation where chain length is controlled by chain transfer. Mayo carried out the first mechanistic study for transfer controlled polymerisations in 1943.[54,55] In this study, it was found the number average degree of polymerisation, χ_n, (M_n / mass of the repeat unit) is equal to the rate of chain propagation divided by the total rate of chain transfer. The reciprocal is the widely known Mayo equation:

$$\frac{1}{\chi_n} = \frac{R_{trans}}{R_{prop}} = \frac{[\text{growing chain}](k_{trans,0} + k_{trans}[CTA])}{k_{prop}[H_2B = NMeH][\text{growing chain}]} = \frac{1}{\chi_o} + C_{tr}\frac{[CTA]}{[M]}$$

In this equation, χ_n is the average degree of polymerisation, [M] is the monomer concentration, and [CTA] is the concentration of the chain transfer agent. The chain transfer constant, C_{tr}, is defined as the ratio k_{trans}/k_{prop}. χ_o is the number average degree of polymerisation in the absence of CTA when termination is carried out by chain transfer from monomer, solvent, or other lewis acids; $k_{trans,0}$ is the rate constant for chain transfer to those sources.

Plots of $1/\chi_n$ vs [CTA]/[M] should give a straight line known as a Mayo plot. It is essential to note that using M_n instead of χ_n will change the value of C_{tr}, but the data should still fit a straight line. Variation in the ratio [S]/[M] throughout a polymerisation potentially complicates the relationship, and the effect of a steady feed of $H_2B{=}NMeH$ during the dehydropolymerisation requires further investigation.[54] However, this equation stands as a good working model for the polymerisation of $H_2B{=}NMeH$ for this thesis.

3.2.12 Role of chain transfer agent - $CoCl(^iPr_2PCH_2CH_2)_2N$ as a probe



Scheme 3.15 **$CoCl(^iPr_2PCH_2CH_2)_2N$**.

The known Co(II) complex **$CoCl(^iPr_2PCH_2CH_2)_2N$** (Scheme 3.15) is an effective catalyst (1,2-$F_2C_6H_4$, 0.4 mol%) for the dehydropolymerisation of $H_3B{\cdot}NMeH_2$, proceeding in a similar a similar time to completion as observed for **$Co(L3)Cl_2$** without the addition of $NMeH_2$ promoter. It was observed by ^{11}B NMR spectroscopy of an aliquot of the reaction mixture at the end of dehydropolymerisation that **$CoCl(^iPr_2PCH_2CH_2)_2N$** pre-catalyst selectively forms only $(H_2B{\cdot}NMeH)_n$. The activity of **$CoCl(^iPr_2PCH_2CH_2)_2N$** for the dehydropolymerisation of $H_3B{\cdot}NMeH_2$ supports a

cooperative ligand mechanism as this deprotonation of the ligand had no significant effect on the catalytic behaviour. This suggests the ligand is readily reprotonated during dehydropolymerisation. No longer requiring $NMeH_2$ for activation supports this species being close to the catalytic cycle with the active catalyst of the form **Co(L3)HCl** (X = Cl in Scheme 3.11 and 3.13). An alternative explanation is that the presence of a new vacant coordination sight allows a second hydride transfer to occur rapidly without need for amine promoter. Either way this catalyst must be able to activate rapidly without the presence of $NMeH_2$. The isolated polymer produced from this reaction has a higher degree of polymerisation (M_n = 76,100 g mol^{-1}, $Đ$ = 1.5) than obtained for any catalyst loading with **Co(L3)Cl$_2$** suggesting a lower concentration of CTA (boronium or ammonium).[51] This observation, coupled with the variation of M_n with catalyst loading (Section 3.2.3), allowed the mechanism to be probed further using Mayo plots. Dehydropolymerisations were performed at 0.2, 0.4 and 0.8 mol% catalysts loadings for **CoCl$_2$(L3)** and at 0.4 mol% for **CoCl(^{i}Pr$_2$PCH$_2$CH$_2$)$_2$N**.

If the active catalyst takes the form **CoClH(L3)** (so X = Cl in Scheme 3.11 or 3.13), then one Cl^- has been replaced from each equivalent of **CoCl$_2$(L3)** pre-catalyst to get on cycle and one equivalent of CTA has been produced (ammonium or boronium) it follows that: [CTA] = [Pre-Catalyst]. **CoCl(^{i}Pr$_2$PCH$_2$CH$_2$)$_2$N** does not require Cl^- loss to get on cycle and so [CTA] is at best very low (approximately 0 M). A Mayo plot has been constructed (Figure 3.4) from the three catalyst loadings of **CoCl$_2$(L3)** (for catalysis in 1,2-$F_2C_6H_4$), and the line of best fit is extrapolated to [CTA]/[$H_3B.NMeH_2$] = 0. Noteworthy is that M_n obtained with **CoCl(^{i}Pr$_2$PCH$_2$CH$_2$)$_2$N** (orange circle), fits well to the trend line therefore, this is an activation pathway which fits the available data.

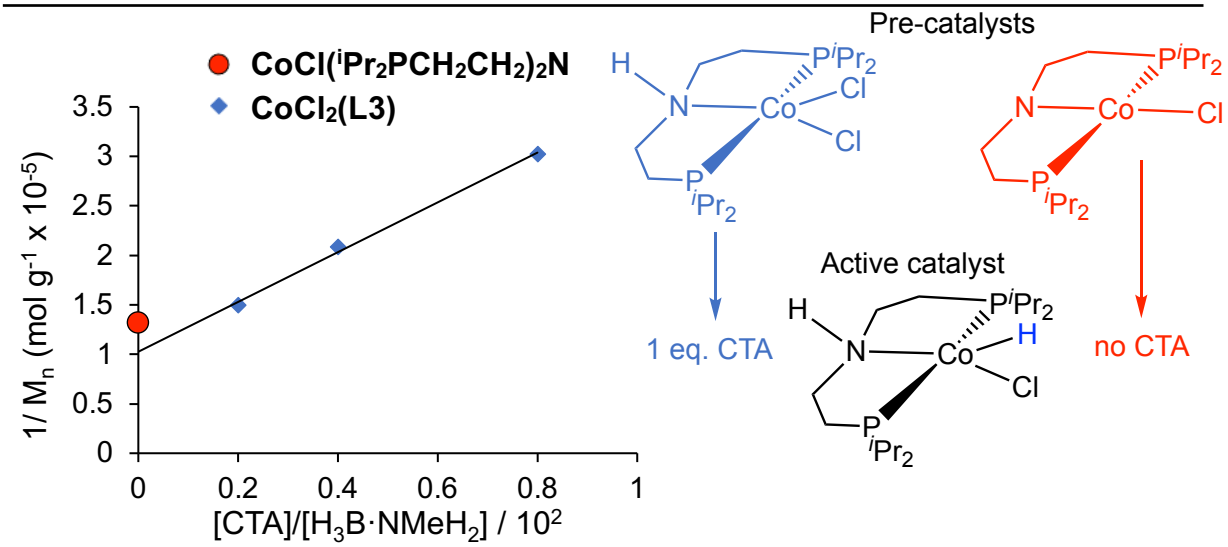


Figure 3.4 Mayo plots ($1/M_n$ vs [CTA]/[$H_3B.NMeH_2$]) for the activation processes shown schematically. Dehydropolymerisation were carried out at 0.2, 0.4 and 0.8 mol% for **$CoCl_2$(L3)** and at 0.4 mol% for **CoCl(^{i}Pr$_2$PCH$_2$CH$_2$)$_2$N**. **$CoCl_2$(L3)** activates to a **CoClH(L3)** type species producing 1 eq. of CTA (so 0.2, 0.4 and 0.8 mol%). **CoCl(^{i}Pr$_2$PCH$_2$CH$_2$)$_2$N** also activates to a **CoClH(L3)** type species so 0 eq. of CTA.

If instead the active catalyst takes the form **CoH_2(L3)** (so X = H in Scheme 3.11 or 3.13), 2 eq. of CTA are produced per Co therefore [CTA] = 2[Pre-Cat] (0.4, 0.8 and 1.6 mol%). For **CoCl(^{i}Pr$_2$PCH$_2$CH$_2$)$_2$N** one equivalent of boronium will now be generated ([CTA] = [Pre-Cat]). A Mayo plot for this activation pathway is plotted in Figure 3.5 with the line of best fit to the three different catalysts loadings, and it can be seen that the point for **CoCl(^{i}Pr$_2$PCH$_2$CH$_2$)$_2$N** (orange circle) also fits the trend line therefore this activation pathway also fits the available data. Activation of the pre-catalyst to active catalysts either of the form **CoClH(L3)** or **CoH_2(L3)** both fit the available data and it cannot yet be determined if the active catalyst has a Cl^- bound directly to the metal centre.

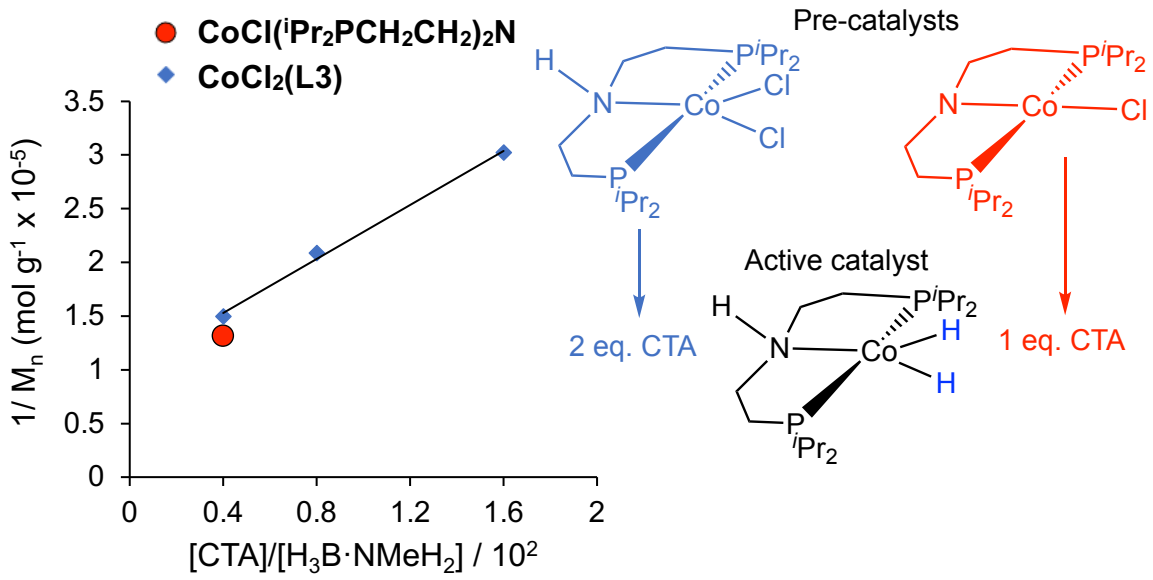
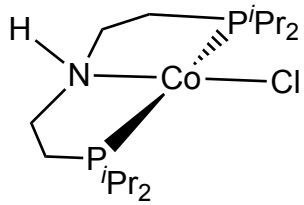


Figure 3.5 Mayo plots ($1/M_n$ vs [CTA]/[$H_3B.NMeH_2$]) for the activation processes shown schematically. Dehydropolymerisation were carried out at 0.2, 0.4 and 0.8 mol% for **$CoCl_2$(L3)** and at 0.4 mol% for **CoCl(^{i}Pr$_2$PCH$_2$CH$_2$)$_2$N**. **$CoCl_2$(L3)** activates to a **CoH_2(L3)** type species producing 2 eq. of CTA (so 0.4, 0.8 and 1.6 mol%). **CoCl(^{i}Pr$_2$PCH$_2$CH$_2$)$_2$N** also activates to a **CoH_2(L3)** type species so 1 eq. of CTA (0.4 mol%).

3.2.13 Role of chain transfer agent - CoCl(L3) as a probe



Scheme 3.16 CoCl(L3).

In order to gain more information about the activation, the literature known compound Co(I) complex **CoCl(L3)** was prepared (Scheme 3.16).[51] When **CoCl(L3)** was used as a precatalyst for the dehydropolymerisation (1,2-$F_2C_6H_4$, 0.4 mol%) it proceeded in a similar time scale to those previously reported (~ 5 minutes). The polymer produced by **CoCl(L3)** had a similar degree of polymerisation (M_n = 42,900 g mol^{-1}, Table 3.4) to **$CoCl_2$(L3)** (1,2-$F_2C_6H_4$, 0.4 mol%, 48,000 g mol^{-1}, $Đ$ = 1.5) but significantly lower than

for **CoCl(^{i}Pr$_2$PCH$_2$CH$_2$)$_2$N** (1,2-$F_2C_6H_4$, 0.4 mol%, 76,100 g mol^{-1}). These data suggest **CoCl(L3)** produces a similar concentration of CTA (boronium or ammonium) to **CoCl$_2$(L3**) but significantly more than **CoCl(^{i}Pr$_2$PCH$_2$CH$_2$)$_2$N**. This data is rationalised by both **CoCl(L3)** and **CoCl$_2$(L3**) losing one Cl^- from the metal centre by a hydride transfer and forming one unit of CTA. Meanwhile, **CoCl(^{i}Pr$_2$PCH$_2$CH$_2$)$_2$N** forms no CTA. This would mean both **CoCl$_2$(L3)** and **CoCl(^{i}Pr$_2$PCH$_2$CH$_2$)$_2$N** produce a **CoHCl(L3)** type system while **CoCl(L3)** gives **CoH$_3$(L3)**. Mayo plots are constructured for all possible cases in Figure 3.6. In plot (A) all complexes are assumed to activate to give **CoH$_3$(L3)** type systems, while the point for **CoCl(^{i}Pr$_2$PCH$_2$CH$_2$)$_2$N** fits the trend line for the three **CoCl$_2$(L3)** data points **CoCl(L3)** does not. In (B) all complexes are assumed to activate to give a **CoHCl(L3)** type system, and **CoCl(L3)** again does not fit the trend line. However, in (C), **CoCl$_2$(L3)** and **CoCl(^{i}Pr$_2$PCH$_2$CH$_2$)$_2$N** give a **CoHCl(L3)** type system while **CoCl(L3)** gives **CoH$_3$(L3,)** and this fits well with the available data.

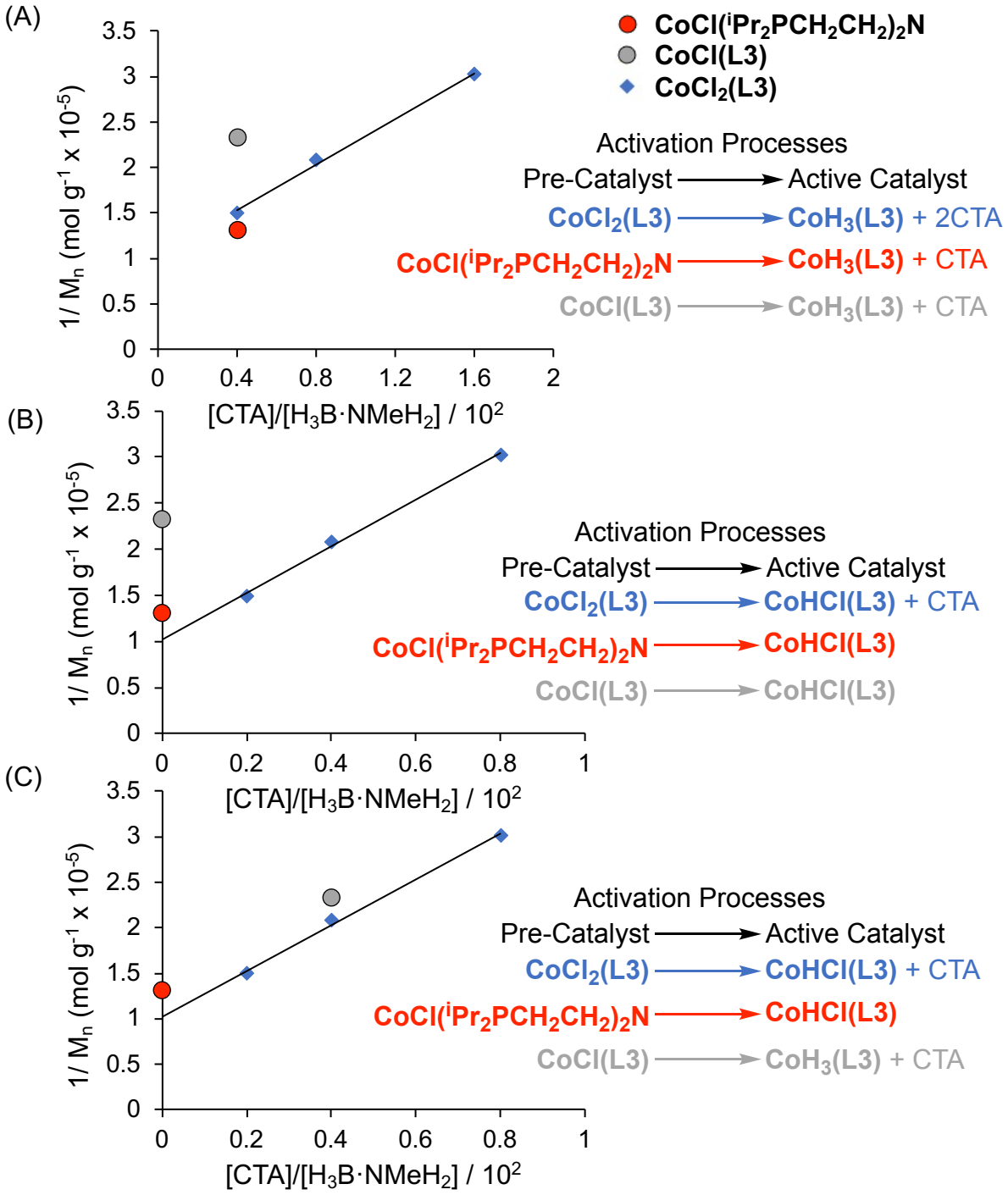


Figure 3.6 Mayo plots ($1/M_n$ vs [CTA]/[$H_3B.NMeH_2$]) for different activation processes. Dehydropolymerisation were carried out at 0.2, 0.4 and 0.8 mol% for **$CoCl_2$(L3)** and at 0.4 mol% for both **CoCl(^{i}Pr$_2$PCH$_2$CH$_2$)$_2$N** and **CoCl(L3)**. In plot, A, all complexes are assumed to activate to give **CoH_3(L3)** type systems, while the point for **CoCl(^{i}Pr$_2$PCH$_2$CH$_2$)$_2$N** fits the trend line for the three **$CoCl_2$(L3)** data points **CoCl(L3)** does not. In B, all complexes are assumed to activate to give a **CoHCl(L3)** type system, and **CoCl(L3)** again does not fit the trend line. In C, **$CoCl_2$(L3)** and **CoCl(^{i}Pr$_2$PCH$_2$CH$_2$)$_2$N** give a **CoHCl(L3)** type system while **CoCl(L3)** gives **CoH_3(L3,)** and this fits well with the available data.

Entry	catalyst	mol%	M_n / g mol^{-1}	$Đ$
15	**CoCl(^{i}Pr$_2$PCH$_2$CH$_2$)$_2$N**	0.4	76,100	1.4
16	**CoCl(L3)**	0.4	42,900	1.5

Table 3.4 Polymer characterisation using different pre-catalyst for dehydropolymerisation (25 °C, THF, 5 M [$H_3B{\cdot}NMeH_2$], 2 eq. NH_2Me, 0.4 mol%).

From the preceding mechanistic consideration it is tentatively suggested that both **CoCl$_2$(L3**) and **CoCl(^{i}Pr$_2$PCH$_2$CH$_2$)$_2$N** undergo a cooperative ligand, constant oxidation-state, Co(II) cycle for dehydrogenation, with a **CoClH(L3)** type active catalyst (Scheme 3.11, L = Cl). Whereas the Co(I) complex, **CoCl(L3)**, undergoes a distinct mechanism with no Cl^- left on the metal centre, possibly centred around the previously reported complex **CoH$_3$(L3)** (Scheme 3.13, X=H).[52] As shown in Scheme 3.13 the **CoCl(L3)** system could be undergoing either a constant oxidation state corporative ligand or variable oxidation state Co(I)/Co(III) pathway. It is important to note that although the role of chain transfer agent has enabled the general form of activation and catalyst structure to be determined, the sequence and relative barriers in the steps of the catalytic cycle have not been determined.

3.3 Conclusions

This chapter provides a scalable and efficient synthesis of polyaminoboranes that uses a simple pre-catalyst with chain control for the degree of polymersiation by varying catalyst loading. The ability to interrogate the materials properties of polyaminoboranes and therefore their potential applications rests on the ability to produce them on scale. These **Co(L3)Cl$_2$** and **Co(L4)Cl$_2$** systems represents a significant step towards convenient on-scale synthesis of polyaminoboranes. This work formed the basis of a chemical communication.[56]

There is still much to be learned about the mechanism for the dehydrogenation and subsequent polymerisation; the paramagnetic Co(II) centre results in challenging mechanistic studies. Therefore the next chapter will report on a simple diamagnetic **{Rh(L3)}** system for the dehydropolymerisation of $H_3B{\cdot}NMeH_2$ where speciation and mechanistic data will be readily collected.

3.4 References

(1) Staubitz, A.; Presa Soto, A.; Manners, I. *Angew. Chemie Int. Ed.* **2008**, *47* (33), 6212–6215.
(2) Kumar, A.; Bhatti, T. M.; Goldman, A. S. *Chem. Rev.* **2017**, *117* (19), 12357–12384.
(3) Staubitz, A.; Besora, M.; Harvey, J. N.; Manners, I. *Inorg. Chem.* **2008**, *47* (13), 5910–5918.
(4) Rossin, A.; Peruzzini, M. *Chem. Rev.* **2016**, *116* (15), 8848–8872.
(5) Bowden, M. E.; Brown, I. W. M.; Gainsford, G. J.; Wong, H. *Inorganica Chim. Acta* **2008**, *361* (7), 2147–2153.
(6) Colebatch, A. L.; Weller, A. S. *Chem. - A Eur. J.* **2019**, *25* (6), 1379–1390.
(7) Why Polyolefins Are The Polymers To Watch | Wood Mackenzie https://www.woodmac.com/news/opinion/why-polyolefins-are-the-polymers-to-watch/ (accessed Sep 18, 2021).
(8) Staubitz, A.; Robertson, A. P. M.; Manners, I. *Chem. Rev.* **2010**, *110* (7), 4079–4124.
(9) Robertson, A. P. M.; Haddow, M. F.; Manners, I. *Inorg. Chem.* **2012**, *51* (15), 8254–8264.
(10) Jaska, C. A.; Temple, K.; Lough, A. J.; Manners, I. *Chem. Commun.* **2001**, *7* (11), 962–963.
(11) Wang, X.; Hooper, T. N.; Kumar, A.; Priest, I. K.; Sheng, Y.; Samuels, T. O. M.; Wang, S.; Robertson, A. W.; Pacios, M.; Bhaskaran, H.; Weller, A. S.; Warner, J. H. *CrystEngComm* **2017**, *19* (2), 285–294.
(12) Metters, O. J.; Chapman, A. M.; Robertson, A. P. M.; Woodall, C. H.; Gates, P. J.; Wass, D. F.; Manners, I. *Chem. Commun.* **2014**, *50* (81), 12146–12149.
(13) Resendiz-Lara, D. A.; Whittell, G. R.; Leitao, E. M.; Manners, I. *Macromolecules* **2019**, *52* (18), 7052–7064.
(14) Trose, M.; Reiß, M.; Reiß, F.; Anke, F.; Spannenberg, A.; Boye, S.; Lederer, A.; Arndt, P.; Beweries, T. *Dalt. Trans.* **2018**, *47* (37), 12858–12862.
(15) De Albuquerque Pinheiro, C. A.; Roiland, C.; Jehan, P.; Alcaraz, G. *Angew. Chemie Int. Ed.* **2018**, *57* (6), 1519–1522.
(16) Marquardt, C.; Jurca, T.; Schwan, K.-C.; Stauber, A.; Virovets, A. V.; Whittell, G. R.; Manners, I.; Scheer, M. *Angew. Chemie Int. Ed.* **2015**, *54* (46), 13782–13786.
(17) Staubitz, A.; Sloan, M. E.; Robertson, A. P. M.; Friedrich, A.; Schneider, S.; Gates, P. J.; Günne, J. S. auf der; Manners, I. *J. Am. Chem. Soc.* **2010**, *132* (38), 13332–13345.
(18) Melanie C. Denney; Vincent Pons; Travis J. Hebden; D. Michael Heinekey, * and; Goldberg*, K. I. *J. Am. Chem. Soc.* **2006**, *128* (37), 12048–12049.
(19) Dietrich, B. L.; Goldberg, K. I.; Heinekey, D. M.; Autrey, T.; Linehan, J. C. *Inorg. Chem.* **2008**, *47* (19), 8583–8585.
(20) Dallanegra, R.; Robertson, A. P. M.; Chaplin, A. B.; Manners, I.; Weller, A. S. *Chem. Commun.* **2011**, *47* (13), 3763–3765.
(21) Marziale, A. N.; Friedrich, A.; Klopsch, I.; Drees, M.; Celinski, V. R.; Schmedt auf der Günne, J.; Schneider, S. *J. Am. Chem. Soc.* **2013**, *135* (36), 13342–13355.
(22) Anke, F.; Han, D.; Klahn, M.; Spannenberg, A.; Beweries, T. *Dalt. Trans.* **2017**,

46 (21), 6843–6847.
(23) Roselló-Merino, M.; López-Serrano, J.; Conejero, S. *J. Am. Chem. Soc.* **2013**, *135* (30), 10910–10913.
(24) Jurca, T.; Dellermann, T.; Stubbs, N. E.; Resendiz-Lara, D. A.; Whittell, G. R.; Manners, I. *Chem. Sci.* **2018**, *9* (13), 3360–3366.
(25) Kumar, A.; Beattie, N. A.; Pike, S. D.; Macgregor, S. A.; Weller, A. S. *Angew. Chemie Int. Ed.* **2016**, *55* (23), 6651–6656.
(26) Dallanegra, R.; Robertson, A. P. M.; Chaplin, A. B.; Manners, I.; Weller, A. S. *Chem. Commun.* **2011**, *47* (13), 3763.
(27) Colebatch, A. L.; McKay, A. I.; Beattie, N. A.; Macgregor, S. A.; Weller, A. S. *Eur. J. Inorg. Chem.* **2017**, *2017* (38–39), 4533–4540.
(28) Ryan, D. E.; Andrea, K. A.; Race, J. J.; Boyd, T. M.; Lloyd-Jones, G. C.; Weller, A. S. *ACS Catal.* **2020**, *10* (14), 7443–7448.
(29) Adams, G. M.; Ryan, D. E.; Beattie, N. A.; McKay, A. I.; Lloyd-Jones, G. C.; Weller, A. S. *ACS Catal.* **2019**, *9* (4), 3657–3666.
(30) Glüer, A.; Förster, M.; Celinski, V. R.; Schmedt Auf Der Günne, J.; Holthausen, M. C.; Schneider, S. *ACS Catal.* **2015**, *5* (12), 7214–7217.
(31) Malakar, T.; Bhunya, S.; Paul, A. *Chem. – A Eur. J.* **2015**, *21* (17), 6340–6345.
(32) Vance, J. R.; Robertson, A. P. M.; Lee, K.; Manners, I. *Chem. – A Eur. J.* **2011**, *17* (15), 4099–4103.
(33) Baker, R. T.; Gordon, J. C.; Hamilton, C. W.; Henson, N. J.; Lin, P.-H.; Maguire, S.; Murugesu, M.; Scott, B. L.; Smythe, N. C. *J. Am. Chem. Soc.* **2012**, *134* (12), 5598–5609.
(34) Kakizawa, T.; Kawano, Y.; Naganeyama, K.; Shimoi, M. *Chem. Lett.* **2011**, *40* (2), 171–173.
(35) Adams, G. M.; Colebatch, A. L.; Skornia, J. T.; McKay, A. I.; Johnson, H. C.; Lloyd−Jones, G. C.; Macgregor, S. A.; Beattie, N. A.; Weller, A. S. *J. Am. Chem. Soc.* **2018**, *140* (4), 1481–1495.
(36) Lin, T.-P.; Peters, J. C. *J. Am. Chem. Soc.* **2013**, *135* (41), 15310–15313.
(37) Pagano, J. K.; Stelmach, J. P. W.; Waterman, R. *Dalt. Trans.* **2015**, *44* (27), 12074–12077.
(38) Todisco, S.; Luconi, L.; Giambastiani, G.; Rossin, A.; Peruzzini, M.; Golub, I. E.; Filippov, O. A.; Belkova, N. V; Shubina, E. S. *Inorg. Chem.* **2017**, *56* (8), 4296–4307.
(39) Maier, T. M.; Sandl, S.; Shenderovich, I. G.; Jacobi von Wangelin, A.; Weigand, J. J.; Wolf, R. *Chem. – A Eur. J.* **2019**, *25* (1), 238–245.
(40) Nugent, J. W.; García-Melchor, M.; Fout, A. R. *Organometallics* **2020**, *39* (15), 2917–2927.
(41) Park, Y.; Kim, Y.; Chang, S. *Chem. Rev.* **2017**, *117* (13), 9247–9301.
(42) Sloan, M. E.; Staubitz, A.; Clark, T. J.; Russell, C. A.; Lloyd-Jones, G. C.; Manners, I. *J. Am. Chem. Soc.* **2010**, *132* (11), 3831–3841.
(43) Bhunya, S.; Malakar, T.; Paul, A. *Chem. Commun.* **2014**, *50* (44), 5919–5922.
(44) Boyd, T. M.; Tegner, B. E.; Tizzard, G. J.; Martínez-Martínez, A. J.; Neale, S. E.; Hayward, M. A.; Coles, S. J.; Macgregor, S. A.; Weller, A. S. *Angew. Chemie Int. Ed.* **2020**, *59* (15), 6177–6181.
(45) Chomitz, W. A.; Mickenberg, S. F.; Arnold, J. *Inorg. Chem.* **2008**, *47 VN-r* (1), 373–380.
(46) Nurseiit, A.; Janabel, J.; Gudun, K. A.; Kassymbek, A.; Segizbayev, M.; Seilkhanov, T. M.; Khalimon, A. Y. *ChemCatChem* **2019**, *11* (2), 790–798.

(47) Rozenel, S. S.; Kerr, J. B.; Arnold, J. *Dalt. Trans.* **2011**, *40* (40), 10397.
(48) Widegren, J. A.; Finke, R. G. *J. Mol. Catal. A Chem.* **2003**, *198* (1–2), 317–341.
(49) Dai, H.; Guan, H. *ACS Catal.* **2018**, *8* (10), 9125–9130.
(50) unge, K.; Wendt, B.; ingolani, A.; Spannenberg, A.; Wei, Z.; Jiao, H.; Beller, M.; Wendt, B.; Spannenberg, D. A.; Wei, Z.; Jiao, D.; Beller, M.; Cingolani, A. *Chem. Eur.J* **2018**, *24*, 1046–1052.
(51) Rozenel, S. S.; Padilla, R.; Arnold, J. *Inorg. Chem.* **2013**, *52* (19), 11544–11550.
(52) Rozenel, S. S.; Padilla, R.; Camp, C.; Arnold, J. *Chem. Commun.* **2014**, *50* (20), 2612–2614.
(53) Spearing-Ewyn, E. A. K.; Beattie, N. A.; Colebatch, A. L.; Martinez-Martinez, A. J.; Docker, A.; Boyd, T. M.; Baillie, G.; Reed, R.; Macgregor, S. A.; Weller, A. S. *Dalt. Trans.* **2019**, *48* (39), 14724–14736.
(54) Donald, M. K.; Bon, S. A. F. *Polym. Chem.* **2020**, *11* (26), 4281–4289.
(55) Mayo, F. R. *J. Am. Chem. Soc.* **1943**, *65* (12), 2324–2329.
(56) Boyd, T. M.; Andrea, K. A.; Baston, K.; Johnson, A.; Ryan, D. E.; Weller, A. S. *Chem. Commun.* **2020**, *56* (3), 482–485.

Chapter 4: A simple robust rhodium-based catalyst system for the controlled dehydropolymerisation of $H_3B{\cdot}NMeH_2$ on the gram-scale

The work in this chapter was carried out in collaboration with Dr Claire Brodie. I have indicated throughout the work which was performed specifically by Dr Claire Brodie, which is the synthesis of **Rh(L3)H_2Cl**, **Rh(L3)H_3**, **[Rh(HN((CH$_2$)$_2$PPh$_2$)$_2$)NBD]Cl**, and the speciation experiments. Besides these points the work was performed by myself, additionally I performed all X-ray structural analysis. Claire deserves a further acknowledgment and thanks for the general help and discussion within the rest of the work in the chapter.

4.1 Introduction

The last chapter discussed the efficiency of the **$CoCl_2$(L3)** system for the dehydropolymerisation of $H_3B{\cdot}NMeH_2$. However, limited mechanistic information could be determined due to the paramagnetic, open shell, electronic state of the cobalt. Furthermore, the cobalt pre-catalysts were highly air-sensitive, which meant their use required careful manipulation. In order to gain more insight into the mechanism of the dehydropolymerisation and to move towards potentially air-stable pre-catalysts it was decided to turn to rhodium based pre-catalysts. As a 4d metal, Rh is nearly always diamagnetic and generally occupies the oxidation states Rh(I) and Rh(III). Naturally-occurring rhodium is composed of only one stable isotope, ^{103}Rh. This isotope has spin ½, and coupling to it from the phosphines or other ligands bound to the metal provides much useful spectroscopic information. This coupled with the extensive research into previous Rh based catalysts for dehydropolymerisation of amine boranes, much of

which was performed in the Weller group, provided motivation to investigate **{Rh(L3)}** type systems.[1–4] In this chapter, the 18e$^-$ complex **[Rh(L3)NBD]Cl** will be shown to be an efficient pre-catalyst for amine-borane dehydropolymerisation.

4.2 Results and discussion

4.2.1 Attempted synthesis of Rh(L3)Cl

To develop an analogous system to **$CoCl_2$(L3)**, a rhodium chloride pre-catalyst was targeted. While there are no known synthetic routes to Rh(II) chloride complexes, the Rh(I) complex **Rh(L3)Cl** was a feasible initial synthetic target. Preparation of this complex was attempted by addition of L3 to **$((COD)RhCl)_2$** or **$((COE)RhCl)_2$** in THF, CH_2Cl_2 or 1,2-$C_6H_4F_2$; in all cases this led to decomposition with a large number (>10) signals observed in the resulting ^{31}P NMR spectra. This decomposition was assigned to the neutral Rh(I) complex being able to activate solvent possibly aided by the cooperative ligand giving access to a range of decomposition pathways. Solvent activation by neutral Rh(I) complexes is widely reported in the literature.[5–7]

4.2.2 Synthesis and characterisation of [Rh(L3)NBD]Cl

While attempting to prepare **Rh(L3)Cl** the NBD complex **[Rh(L3)NBD]Cl** was isolated. **[Rh(L3)NBD]Cl** was prepared by simple addition of L3 (10 wt% in THF) to **$((NBD)RhCl)_2$** in THF solution overnight at 20 ^{o}C. From this solution **[Rh(L3)NBD]Cl** precipitated as an orange crystalline solid in 90% yield, 0.5 g scale (Figure 4.1). Crystals suitable for X-ray diffraction were grown from diffusion of *n*-pentane into a CH_2Cl_2 solution of **[Rh(L3)NBD]Cl**.

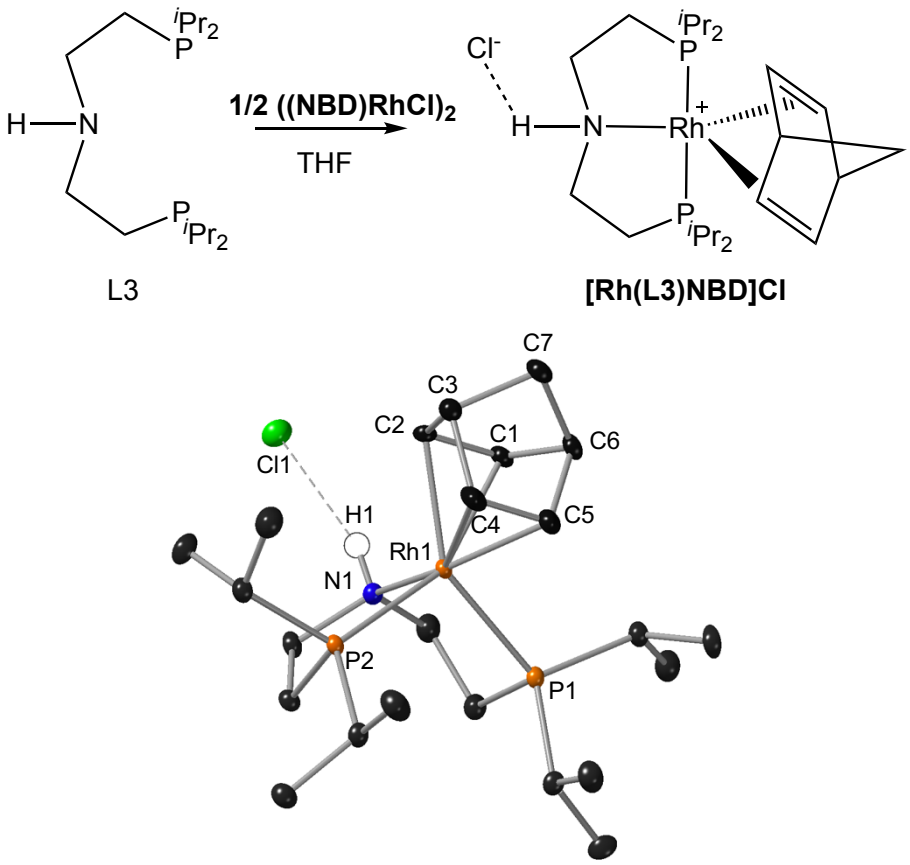


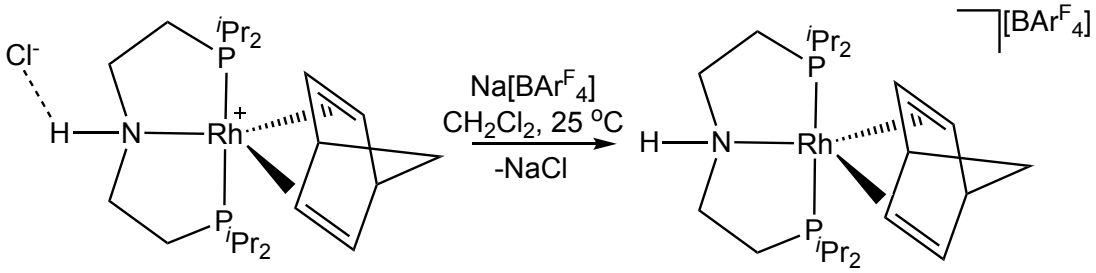
Figure 4.1 Synthesis of **[Rh(L3)NBD]Cl** (top). Molecular structure of **[Rh(L3)NBD]Cl** (bottom). Thermal ellipsoids set at 50 % and only the located hydrogen H1 on N1 is shown. A hydrogen bond is seen between N1-H1 with a bond distance 2.32(2) Å. Selected bond lengths (Å) and angles (°): Rh1-P1 2.3945(5), Rh1-P2 2.3359(5), Rh1-N1 2.1380(17), Rh1-C1 2.1305(19), Rh1-C2 2.1479(18), Rh1-C4 2.190(2), Rh1-C5 2.183(2), C1-C2 1.419(3), C4-C5 1.396(3), H1-Cl1 2.32(2), P2-Rh1-P1 103.875(18), N1-Rh1-P1 83.21(5) and N1-R1-P2 84.13(5).

The solid state structure revealed a trigonal bipyramidal Rh(I) centre, with a facially coordinated κ^3-HPNP ligand. Hydrogen bonding between Cl^- and backbone NH groups (2.32(2) Å, sum of van der Waals radii = 3.02 Å[8]) could also be observed. The solid state structure was otherwise unremarkable and solved satisfactorily with an R_1 = 2.19% (Figure 4.1). In the $^{31}P\{^1H\}$ NMR spectrum (CD_2Cl_2) a single resonance at 48.0 ppm (d, $^1J_{RhP}$ = 124 Hz) for the chemically equivalent phosphines was observed. In the ^1H NMR spectrum the N-H group is observed downfield shifted at 6.99 ppm, showing

that the N-H···Cl^- hydrogen bond is retained in CD_2Cl_2 solution. Given the solid-state structure the observation of a single broad alkene resonance (3.66 ppm, 4H), and a single bridging methylene (1.12 ppm, 2H) suggests the NBD ligand undergoes a fluxional process, likely rotation, at 298 K.

4.2.3 Synthesis and characterisation of [Rh(L3)NBD][BAr^F_4]

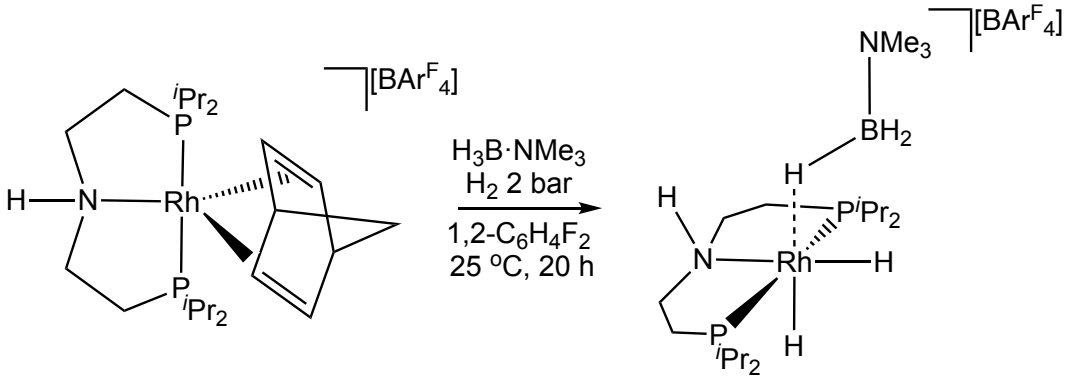
[Rh(L3)NBD]Cl provides a useful synthetic starting point for preparing cationic rhodium complexes with potential in the dehydropolymerisation of amine-boranes. Addition of Na[BAr^F_4] to **[Rh(L3)NBD]Cl** in CH_2Cl_2 led to the formation of **[Rh(L3)NBD][BAr^F_4]** (Scheme 4.1). The resultant solution was filtered to remove NaCl and crystals were isolated (87% yield) by diffusion of pentane into CH_2Cl_2 solutions of **[Rh(L3)NBD][BAr^F_4]**. The crystals were observed to be habitually twinned and a satisfactory solid state structure could not be determined by X-ray crystallographic studies. The only significant difference in the NMR spectroscopic data for **[Rh(L3)NBD][BAr^F_4]** relative to **[Rh(L3)NBD]Cl** is that in the ^{1}H NMR spectrum the signal for the backbone amine NH group is now observed at 2.75 ppm (compared with 6.99 ppm) which is consistent with the absence of a NH···Cl^- hydrogen bond.



Scheme 4.1 Synthesis of **[Rh(L3)NBD][BAr^F_4]**.

4.2.4 Synthesis and characterisation of $[Rh(L3)H_2(H_3B{\cdot}NMe_3)][BAr^F{}_4]$

Hydrogenation of bound NBD ligands, in the presence of amine-boranes, such as $H_3B{\cdot}NMe_3$, has been a route to the synthesis of σ-amine-borane complexes, so this reaction was attempted with **$[Rh(L3)NBD][BAr^F{}_4]$** (Scheme 4.2).[2] In a J. Youngs ampoule, **$[Rh(L3)NBD][BAr^F{}_4]$** and $H_3B{\cdot}NMe_3$ were dissolved in 1,2-$F_2C_6H_4$ solvent. The resultant solution was freeze-pump-thaw degassed and charged with H_2 gas (2 bar). The reaction was stirred at room temperature for 20 h under H_2 during which the solution changed colour from yellow to colourless. At this point the solution was freeze-pump-thaw degassed and an Ar atmosphere (1 bar) added. The complex **$[Rh(L3)H_2(H_3B{\cdot}NMe_3)][BAr^F{}_4]$** was isolated as a crystalline material by diffusion of pentane into the resultant solution, in 76% yield. These crystals were suitable for single crystal X-ray diffraction and the solid state structure is shown in Figure 4.2.



Scheme 4.2 Synthesis of **$[Rh(L3)H_2(H_3B{\cdot}NMe_3)][BAr^F{}_4]$**.

Examination of the solid state structure of **$[Rh(L3)H_2(H_3B{\cdot}NMe_3)][BAr^F{}_4]$** shows an octahedral coordination environment around Rh. L3 is coordinated in a *mer* fashion to the rhodium centre and the backbone NH group is syn to the σ-bound amine-borane. The hydrides bound to the metal, the BH_3 moiety and backbone NH group protons

could all be located in the Fourier difference map and were refined independently. The Rh1-H1C distance is suggestive of a bonding interaction at 1.84(3) Å and the H1C-B1 distance is 1.46(6) Å which is elongated with respect to the other BH bonds (1.13(3) Å). The Rh1-H1C-B1 angle is obtuse at 128(2)°. The Rh1–B1 distance of 2.753(3) Å is longer than the sum of the covalent radii (r_c) of rhodium and boron (r_c(Rh) = 1.42 Å, r_c(B) = 0.84 Å),[8] however it is shorter than the sum of their van der Waals radii (r_v; r_v(Rh) = 2.44 Å; r_v(B) = 1.91 Å).[9] Together, these data suggest the borane component binds to the metal through a bridging hydride in an η^1 fashion. Similar geometries have been reported for **[Rh(XantPhos-Ph)H_2($H_3B{\cdot}NMe_3$)][BAr^F_4]** (Rh1-B1 = 2.783(6) Å, XantPhos-Ph = 4,5-bis(diphenylphosphino)-9,9-dimethylxanthene) and **[Rh(XantPhos-*i*Pr)H_2($H_3B{\cdot}NMe_3$)][BAr^F_4]** (Rh1-B1 = 2.759(6) Å, XantPhos-Ph = 4,5-bis(diisopropyl phosphino)-9,9-dimethylxanthene).[2,10]

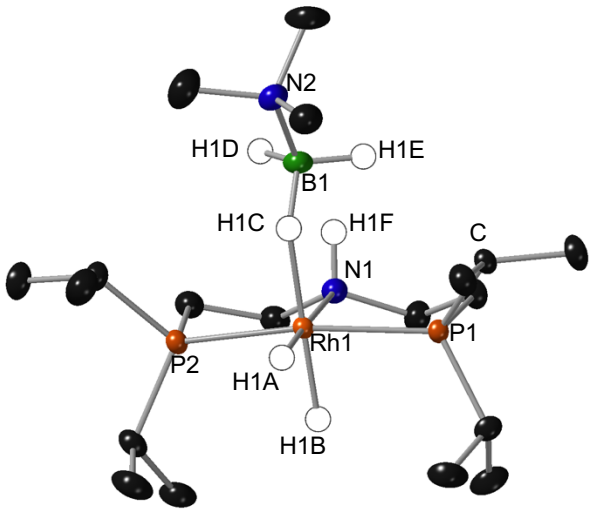


Figure 4.2 Solid-state structure of **[Rh(L3)H_2($H_3B{\cdot}NMe_3$)][BAr^F_4]**. Thermal ellipsoids set at 50 %, the $[BAr^F_4]^-$ anion removed for clarity and only the located hydrogen atoms shown. Selected bond lengths (Å) and angles (°): Rh1-P1 2.2824(7), Rh1-P2 2.2773(7), Rh1-N1 2.200(2), Rh1-H1A 1.56(4), Rh1-H1B 1.59(4), Rh1-H1C 1.84(3), Rh1-B1 2.753(3), B1-H1C 1.46(6), B1-H1D 1.13(3), B1-H1E 1.13(3), P1-Rh-P2 165.59(3), P1-Rh1-N1 85.12(6), P2-Rh1-N1 85.16(6), and Rh1-H1C-B1 128(2).

In CD_2Cl_2 at 298 K the $^{31}P\{^1H\}$ NMR spectrum of **$[Rh(L3)H_2(H_3B{\cdot}NMe_3)][BAr^F{}_4]$** showed a single resonance at 73.25 ppm (d, $^1J_{RhP}$ = 110 Hz). Two resonances were observed in the ^{11}B NMR spectrum; one at -6.6 ppm for the $[BAr^F{}_4]^-$ anion and another broad singlet at -11.4 ppm for the σ-bound $H_3B{\cdot}NMe_3$. In the hydride region of the ^1H NMR spectrum a broad multiplet was observed at -1.08 ppm and a broad singlet at -17.33 ppm. The signal at -1.08 sharpened to a singlet upon ^{11}B decoupling; this signal integrated to 3H with respect to the $BAr^F{}_4$ protons and ligand. These data suggest the signal at -1.08 ppm is due the protons on the borane of the amine-borane and that they are fluxional via rapid site exchange on the NMR timescale at room temperature. The signal at -17.33 ppm did not sharpen significantly on ^{11}B decoupling and integrated to 2H, this was assigned to the two metal bound hydrides which are again fluxional at room temperature. Further ^1H NMR spectra were collected at 290 K, 280 K and then every 5 K down to 195 K. In these it was observed that the signal at -17.33 ppm gradually became broader and separated into two separate signals of integral 1H each (Figure 4.3). At 195 K these were observed as two sharp signals at -16.21 and -18.49 ppm and this suggests that the fluxional process no longer occurs at this temperature. For these data line shape analysis was carried out using Topspin to determine rates of exchange.[11] From these rates of exchange an Eyring analysis was carried out and the kinetic parameters for this exchange process were found to be $\Delta H^{\ddagger}$ = 57.7(13) kJ mol^{-1} and $\Delta S^{\ddagger}$ = +43(5) J $K^{-1}mol^{-1}$ for this fluxional process. These data are consistent with a dissociative mechanism in which the $H_3B{\cdot}NMe_3$ ligand dissociates from the metal and coordinates on the other side via the intermediate **$[RhL3(H)_2]^+$** (Figure 4.3 (C)). The activation parameters obtained are within error to those reported for the

fluxional process in $[Rh(Xantphos\text{-}^{i}Pr)H_2(H_3B{\cdot}NMe_3)]^+$ of $\Delta H^{\ddagger}$ = 59(4) kJ mol^{-1} and $\Delta S^{\ddagger}$ = +37(15) J K^{-1} mol^{-1}.[2]

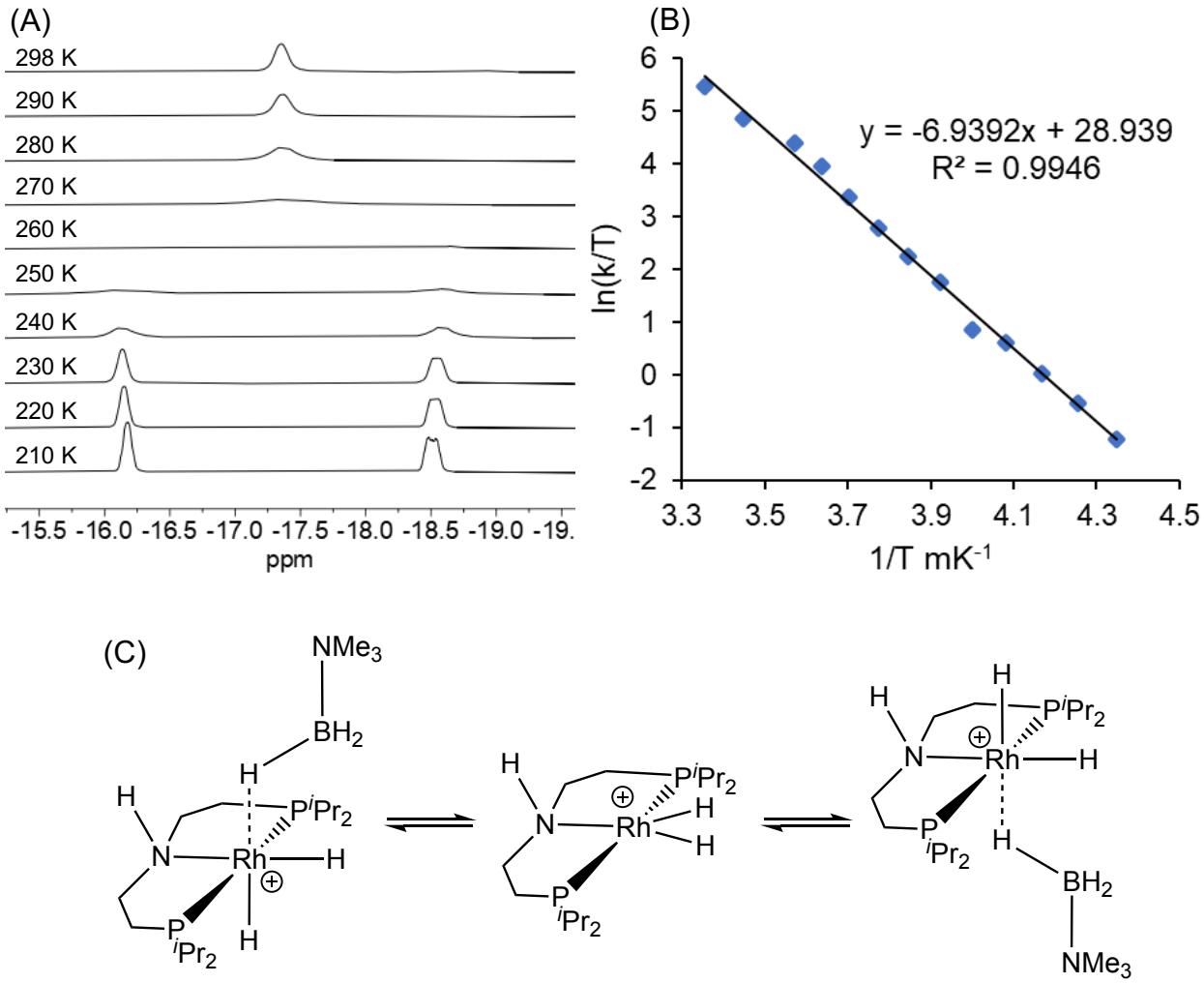


Figure 4.3 (A) Hydride region of ^{1}H NMR spectra at a range of temperatures shows fluxionality of hydrides. **(B)** Eyring analysis using kinetic parameters determined from linewidth data using topspin led to the calculation of $\Delta H^{\ddagger}$ = 57.7(13) kJ mol^{-1} and $\Delta S^{\ddagger}$ = +43(5) J K^{-1}mol^{-1}. **(C)** These parameters indicate a dissociative exchange process.

4.2.5 Use of $[Rh(L3)NBD]Cl$, $[Rh(L3)H_2(H_3B{\cdot}NMe_3)][BAr^F{}_4]$ and $[Rh(L3)NBD][BAr^F{}_4]$ for the dehydropolymerisation of $H_3B{\cdot}NMeH_2$ in 1,2-$C_6H_4F_2$

With these three complexes prepared investigation turned to their activity as pre-catalysts for the dehydrocoupling of amine-boranes. The kinetics of dehydrogenation

are readily followed by measuring H_2 volume (by eudiometer - displacing water from an inverted burette). H_2 volume is used as it provides a convenient proxy for how much amine-borane has been dehydrogenated and the total [$H_2B{=}NMeH$] produced. **[Rh(L3)NBD]Cl**, **[Rh(L3)H_2($H_3B{\cdot}NMe_3$)][BAr^F_4]** or **[Rh(L3)NBD][BAr^F_4]** (1 mol%, 1,2-$F_2C_6H_4$, 20 °C) were added to $H_3B{\cdot}NMeH_2$ (0.22 M) in a 50 mL jacketed two-neck Schlenk flask connected to circulated cooling fluid to maintain a constant temperature (20 °C) while connected to an eudiometer. The kinetic traces from the eudiometer data are shown in Figure 4.4. The activity of both **[Rh(L3)NBD]Cl** and **[Rh(L3)NBD][BAr^F_4]** is somewhat surprising as they are both saturated 18e$^-$ complexes. An initial induction period was seen for all systems, but was shortest for **[Rh(L3)H_2($H_3B{\cdot}NMe_3$)][BAr^F_4]** (50 s) meanwhile a longer induction period (~7 min) was seen for both **[Rh(L3)NBD]Cl** and **[Rh(L3)NBD][BAr^F_4]**. This longer induction period is likely due to activation of the catalyst requiring hydrogenation or hydroboration of the bound NBD ligand. All catalysts evolved ~1 eq. of H_2 by the end of catalysis. None of the kinetic profiles could be fit to a simple order in substrate and so it was decided to further optimise the catalytic conditions before performing any detailed kinetic analysis.

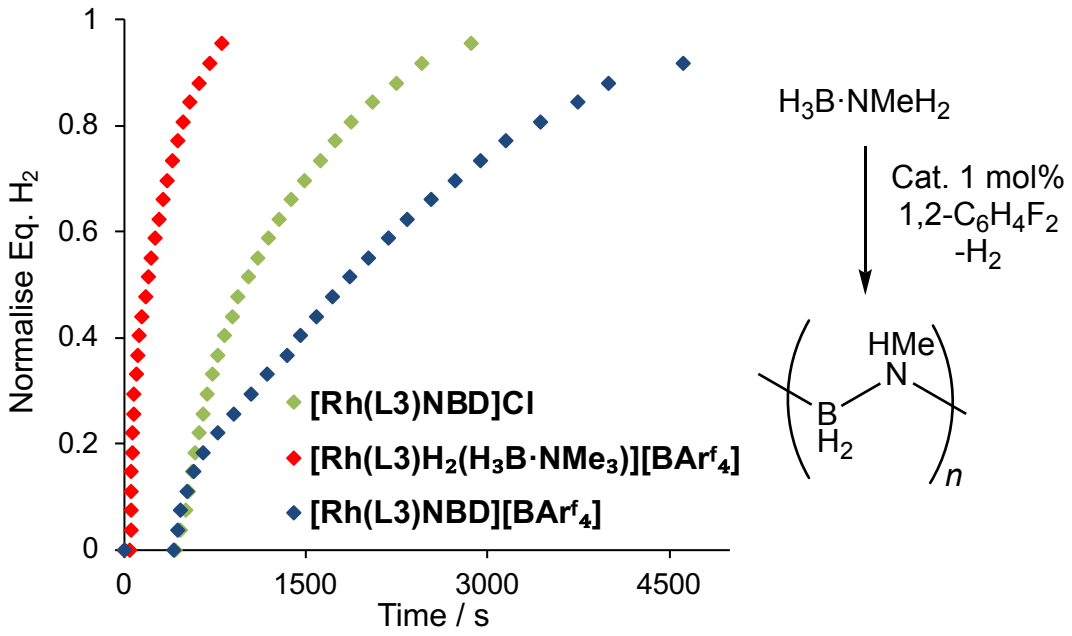


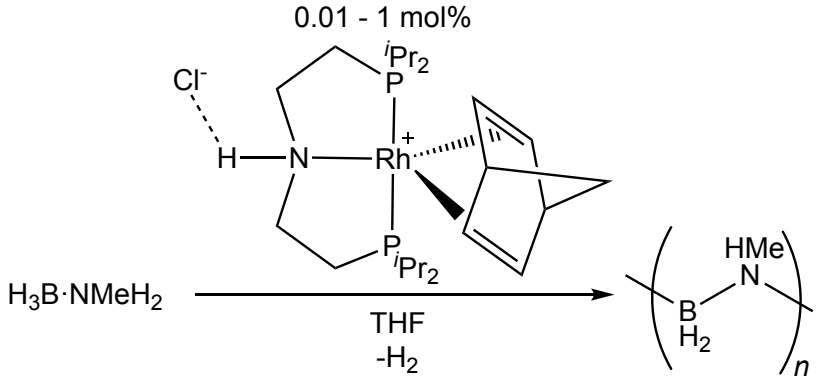
Figure 4.4 Kinetic trace for dehydropolymerisation (1 mol%, 1,2-$C_6H_4F_2$, 20 °C) of $H_3B{\cdot}NMeH_2$ (0.22 M) using **[Rh(L3)NBD]Cl**, **[Rh(L3)H_2($H_3B{\cdot}NMe_3$)][BAr^F_4]** or **[Rh(L3)NBD][BAr^F_4]** pre-catalysts.

The polymer was isolated by precipitation into *n*-pentane, and the isolated polymer characterised by ^{11}B NMR spectroscopy and GPC analysis (Table 4.1). The major signal (99%) observed in the ^{11}B NMR spectrum of all isolated material was that for polyaminoborane, at -6.3 ppm . Table 4.1 shows that the molecular weight of polymer produced by **[Rh(L3)H_2($H_3B{\cdot}NMe_3$)][BAr^F_4]** is the lowest, but all three pre-catalysts give relatively low molecular weight (< 20,000 g mol^{-1}) polymer with low dispersities. With the ability to produce polymer in hand it was decided to optimise the dehydropolymerisation reactions for large scale polymer production. In order to do this the most simply synthesised pre-catalyst, **[Rh(L3)NBD]Cl**, was screened for dehydropolymerisation at high concentration $H_3B{\cdot}NMeH_2$ in THF.

Pre-catalyst	M_n / g mol^{-1}	$Đ$
[Rh(L3)NBD]Cl	17,900	2.1
[Rh(L3)NBD][BAr$^F_4$]	19,100	1.7
[Rh(L3)H$_2$(H$_3$B·NMe$_3$)][BAr$^F_4$]	7,700	2.1

Table 4.1 $H_3B{\cdot}NMeH_2$ dehydropolymerisation polymer characterisation data using **[Rh(L3)NBD]Cl**, **[Rh(L3)NBD][BAr$^F_4$]** and **[Rh(L3)H$_2$(H$_3$B·NMe$_3$)][BAr$^F_4$]**. Dehydropolymerisation conditions: 0.22 M $H_3B{\cdot}NMeH_2$, 1,2-$C_6H_4F_2$ solvent, 20 °C. M_n and $Đ$ measured by GPC relative to polystyrene standards.

4.2.6 Use of [Rh(L3)NBD]Cl for dehydropolymerisation of $H_3B{\cdot}NMeH_2$ in THF



Scheme 4.3 [Rh(L3)NBD]Cl is an efficient catalyst for the dehydropolymerisation of $H_3B{\cdot}NMeH_2$.

The amine-borane and catalyst were combined together in an atmosphere open to air, then connected to the eudiometer prior to the addition of solvent. Typically THF is considered a poor solvent for measurement of kinetic profiles based on gas evolution by eudiometer due to the convoluting effects of solvent evaporation.[3] However, for these fast reactions at high concentration solvent evaporation was determined not to be a problem with the volume of gas realised by a control system (112 mg $H_3B.NMeH_2$, THF 2.5 ml) only 5 ml after 1 hour, this is negligible compared to the ~60 ml of gas released during a dehydropolymerisation (all taking < 40 minutes, see later). Using **[Rh(L3)NBD]Cl** (0.5 mol% **[Rh(L3)NBD]Cl**, THF, 20 °C, [$H_3B{\cdot}NMeH_2$] = 1 M) for dehydropolymerisation (Scheme 4.3) the resulting kinetic plot shows a sigmoidal

profile with three distinctive regions (Figure 4.5). The first of which is an initial induction period in which the rate gradually increases. This induction period is likely to be due to transfer hydrogenation or hydroboration of the bound NBD ligand to afford the active catalyst.[12] Over the course of the polymerisation the solution changed colour from yellow to colourless, consistent with a catalyst activation process. The second period is a linear region which lasts for the majority of catalysis. During the linear region the rate of catalysis does not change with [$H_3B{\cdot}NMeH_2$], which suggests a rate equation for catalytic turnover that is pseudo-zero order in [$H_3B{\cdot}NMeH_2$]. This order would be expected for a resting state with $H_3B{\cdot}NMeH_2$ bound to the catalyst and no further $H_3B{\cdot}NMeH_2$ added prior to the rate limiting step. The final region is a tailing off as the reaction reaches completion stopping after 1 equivalent of H_2 is produced. Zeroth order kinetics in substrate have previously been reported with Guan's **(POCOP-^{i}Pr)Fe(PMe$_2$Ph)$_2$H** (POCOP-^{i}Pr = κ^3-1,3-(OP^{i}Pr$_2$)$_2$C$_6$H$_3$) type system.[13] These kinetics were explained by an observed resting state **(POCOP-^{i}Pr)Fe(PMe$_2$Ph)(H$_3$B·NH$_3$)H** which has amine-borane bound to the metal, through a σ B-H···M interaction. These observations with **[Rh(L3)NBD]Cl** are rationalised, by the idea that when **[Rh(L3)NBD]Cl** is used as the pre-catalyst, activation occurs over the entire course of reaction giving a kinetic profile that is pseudo zero order in amine-borane, from a combination of induction, zero order and deceleration regimes. The rate for this linear regime is a k_{obs}, where $k_{obs} = k[Cat]^n$ (n is the order in [Cat]). This rate is also the maximum rate.

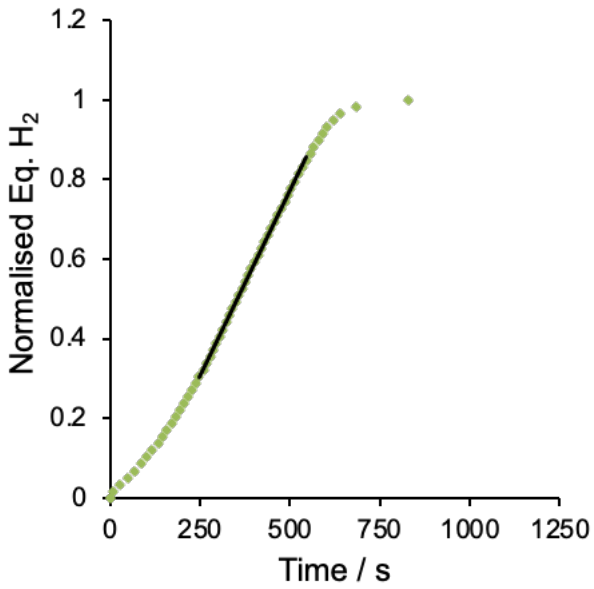


Figure 4.5 Kinetic profile determined using **[Rh(L3)NBD]Cl** as a pre-catalyst for the dehydropolymerisation (0.5 mol% **[Rh(L3)NBD]Cl**, THF, 20 °C, $[H_3B{\cdot}NMeH_2]$ = 1 M) of $H_3B{\cdot}NMeH_2$ as monitored by eudiometer. Linear region implying that the rate law is pseudo-zeroth order in $H_3B{\cdot}NMeH_2$.

After the dehydropolymerisation had reached completion an aliquot of the reaction mixture was taken for NMR spectroscopy. The major species (~98%) observed in the ^{11}B NMR spectra was $(H_2B{\cdot}NMeH)_n$ at -6.3 ppm (Figure 4.6). The side products trimethyl borazine (~1%, d 33.2 ppm (d, $^1J_{BH}$ 132 Hz)), $HB(NMeH)_2$ (~1%, 27.5 ppm (d, $^1J_{HB}$ = 127 Hz)) and a small amount (~1%) of a new unidentified species at 1.4 ppm (s, br) were also observed in the ^{11}B NMR spectrum.[14,15] Notably, no boric acid (-19.5 ppm ^{11}B NMR) was seen, which is a known product of hydrolysis of $H_3B{\cdot}NMeH_2$.[16] It was observed by GPC analysis that the isolated polymer was high molecular weight polymer at M_n = 70,800 g mol^{-1} and Đ = 1.7.

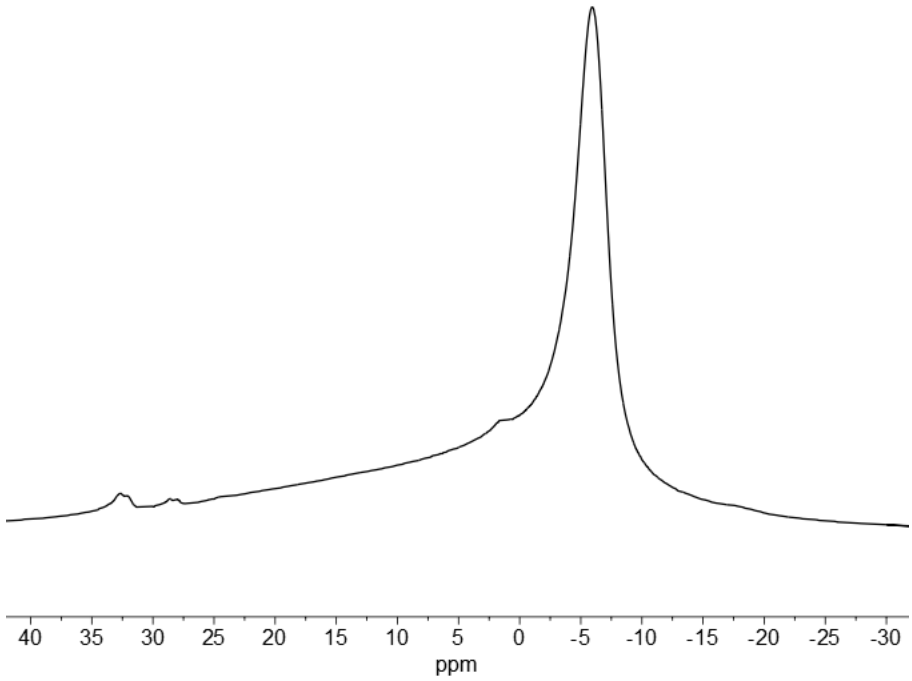


Figure 4.6 ^{11}B NMR spectrum of an aliquot of the reaction mixture showing selective production of polymer using **[Rh(L3)NBD]Cl** as a pre-catalyst for dehydropolymerisation (0.5 mol%, THF, 20 °C) of $H_3B{\cdot}NMeH_2$ (1 M).

4.2.7 Varying the concentration of $H_3B{\cdot}NMeH_2$ for dehydropolymerisation

If the reaction was recharged by addition of further solid $H_3B{\cdot}NMeH_2$ (100 eq. relative to catalyst), there was immediate dehydropolymerisation (with no induction period observed) the kinetic trace went straight to the linear kinetic regime (Figure 4.7). The lack of induction period on recharging is expected as the catalyst has already been activated in the initial dehydropolymerisation. Additionally, increasing the concentration of $H_3B{\cdot}NMeH_2$ to 1.5 M for dehydropolymerisation (0.5 mol% **[Rh(L3)NBD]Cl**, THF, 20 °C) results in no change in k_{obs} of the linear region, as expected for a reaction pseudo-zeroth order [$H_3B{\cdot}NMeH_2$] (Table 4.2). At 1.5 M [$H_3B{\cdot}NMeH_2$] a slightly shorter induction period was observed, this suggests that the

induction period has an order in $[H_3B{\cdot}NMeH_2]$ consistent with hydroboration or transfer hydrogenation of the NBD ligand. ^{11}B NMR spectra of aliquots of the reaction mixtures at the end of catalysis show selectivity has been maintained (Table 4.2). The molecular weights of isolated polymer were determined by GPC analysis to have not changed significantly (Table 4.2).

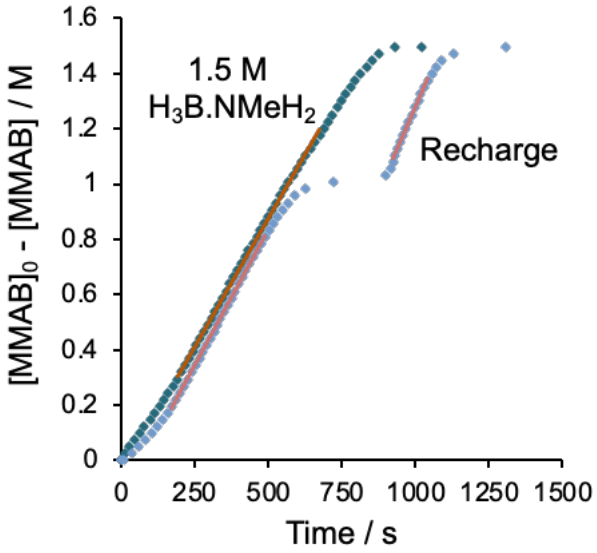


Figure 4.7 Kinetic profiles determined with **[Rh(L3)NBD]Cl** as a pre-catalyst for the dehydropolymerisation of $H_3B{\cdot}NMeH_2$. Dehydropolymerisation kinetics monitored at 1.5 M $H_3B{\cdot}NMeH_2$ (0.5 mol% **[Rh(L3)NBD]Cl**, THF, 20 °C) and also a recharging experiment (0.5 mol% **[Rh(L3)NBD]Cl**, THF, 20 °C, $[H_3B{\cdot}NMeH_2]$ = 1 M followed by another 0.5 eq. $H_3B{\cdot}NMeH_2$ relative to $[H_3B{\cdot}NMeH_2]_0$). Both showed linear regions for most of catalysis, implying a rate law zeroth order in $H_3B{\cdot}NMeH_2$.

[Rh] / mol%	Conditions	k_{obs} / mMs^{-1}	Conv. / %	Selectivity / %	M_n / g mol^{-1}	$Đ$	Yield / mg (%[d])
0.50	1.5 M $[H_3B{\cdot}NMeH_2]$	1.8(3)	99	97	80,400	1.8	43(39)
0.50	1.0 M $[H_3B{\cdot}NMeH_2]$	1.8(3)	98	99	70,800	1.7	103(89)
0.50	After Recharge[a]	2.5(3)	99	96	77,000	1.8	30(26)

Table 4.2 $H_3B{\cdot}NMeH_2$ dehydropolymerisation conditions and polymer characterisation data using [**Rh(L3)NBD]Cl** varying concentration of amine-borane and a recharging experiment. Dehydropolymerisation conditions: THF solvent, 20 °C. Conversion and selectivity measured by ^{11}B NMR spectroscopy, M_n and $Đ$ measured by GPC relative to polystyrene standards. [a]After a dehydropolymerisation run (THF solvent, 20 °C, 0.5 mol% loading, 1 M $[H_3B{\cdot}NMeH_2]$) had reached completion another 100 eq. of $H_3B{\cdot}NMeH_2$ relative to catalyst was added.

4.2.8 Effect on kinetic profile of varying catalyst loading using [Rh(L3)NBD]Cl

A reaction order in [catalyst] would give information about the mechanism of dehydropolymerisation. By varying catalyst loadings with constant initial concentration of amine-borane an order in catalyst was determined. With **[Rh(L3)NBD]Cl**, increasing the catalyst concentration led to an increase in rate. The dehydropolymerisation (THF, 20 °C, $[H_3B{\cdot}NMeH_2]$ = 1 M) was carried out at 0.25, 0.5, 0.75 and 1 mol% catalyst loadings of **[Rh(L3)NBD]Cl** and these gave k_{obs} for the pseudo-zeroth order regions of 0.99, 1.86, 2.77 and 3.67 mM s^{-1} respectively (Table 4.3). A plot of k_{obs} against [cat] fitted very well (R^2 = 0.9998) to a straight line which intercepted the origin (Figure 4.8), which suggests first order in [**[Rh(L3)NBD]Cl**]. This implies one equivalent of catalyst is involved in getting from resting state to highest energy transition state of catalysis. From this plot a k can be determined of 0.369(3) s^{-1} for a rate law of the form rate = k[**[Rh(L3)NBD]Cl**]^1[$H_3B{\cdot}NMeH_2$]^0**.** This k gives ToF = 1,300 h^{-1} for any point in the zero order regime, which is faster than with the equivalent **$Co(L3)Cl_2$** complex (ToF = 750 h^{-1}) but slower than with **$Co(L4)Cl_2$** (ToF = 3,700 h^{-1}). Notably, all of these values are among the highest reported for the dehydropolymerisation of $H_3B{\cdot}NMeH_2$. The only higher reported values are ToF_{max} = 72,000 h^{-1} for **$RuH(PMe_3)(N(CH_2)_2P^iPr_2)_2$)** and ToF_{max} = 2,400 h^{-1} for **IrH_2(POCOP-^{t}Bu)**.[17,18] First order in [catalyst] is distinct from that observed with the **{Rh(DPEphos}** system which was observed to be half order in catalyst.[3,19] This order in catalyst was due to the bridging hydride resting state **$[Rh(DPEphos\text{-}Ph)H_2]_2$** which undergoes a rapid endergonic equilibrium with two monomers within the catalytic cycle.

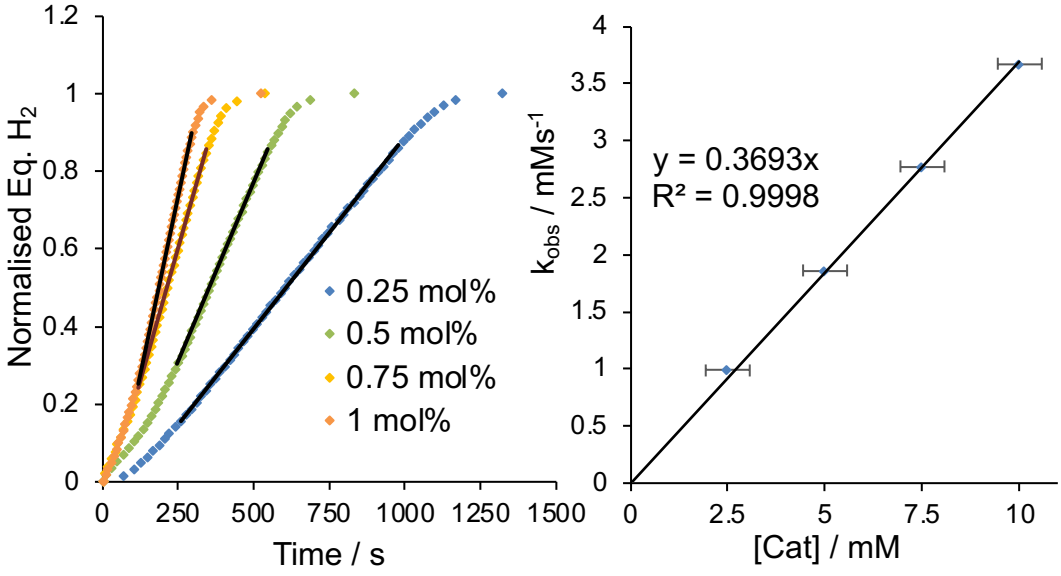


Figure 4.8 Kinetic profile determined using **[Rh(L3)NBD]Cl** at a range of catalysts loadings (0.25, 0.5, 0.75 and 1 mol%) as a pre-catalyst for the dehydropolymerisation (THF, 20 °C) of $H_3B{\cdot}NMeH_2$ (1 M) as monitored by eudiometer. Rate determined from the gradient of the linear region and plotted against catalyst loading to give a straight line and 1st order in catalyst with a rate constant k_{obs} = 0.369(3) s^{-1}.

^{11}B NMR spectra of aliquots of the reaction mixture at the end of catalysis show that these catalyst promote complete conversion with high selectivity. The resulting polymer was precipitated into *n*-pentane. GPC analysis of the isolated polymer showed no significant change in M_n or $Đ$ (Table 4.3) of polymer produced unlike that observed for **$CoCl_2$(L3)**. This absence of significant variation of M_n with catalyst loading is considered further in section 4.2.30.

[Rh] / mol%	Eq. H_2 evolved	k_{obs} / mMs^{-1}	Conv. / %	Selectivity / %	M_n / g mol^{-1}	$Đ$	Yield / mg (%[d])
0.25	1.0	0.9(3)	97	97	74,600	1.8	107(97)
0.50	1.0	1.9(3)	98	99	70,800	1.6	103(89)
0.75	1.0	2.8(3)	100	95	70,200	1.6	106(89)
1.00	1.0	3.7(3)	100	95	71,200	1.6	114(93)

Table 4.3 $H_3B{\cdot}NMeH_2$ dehydropolymerisation conditions and polymer characterisation data using **[Rh(L3)NBD]Cl** at various catalytic loadings. Dehydropolymerisation conditions: 1.0 M $H_3B{\cdot}NMeH_2$ (112 mg), THF solvent, 293 K under hydrogen evolution conditions. Conversion and selectivity measured by ^{11}B NMR spectroscopy, M_n and $Đ$ measured by GPC relative to polystyrene standards.

4.2.9 Synthesis and characterisation of [Rh(HN((CH₂)₂PPh₂)₂)NBD]Cl

To widen the phosphine scope, investigation into the more stable phenyl phosphine **$HN((CH_2)_2PPh_2)_2$** for dehydropolymerisation was targeted. **[Rh(HN((CH₂)₂PPh₂)₂)NBD]Cl** was isolated and characterised by Dr Claire Brodie. The complex **[Rh(HN((CH₂)₂PPh₂)₂)NBD]Cl** was prepared by an analogous procedure to **[Rh(L3)NBD]Cl**. For **[Rh(HN((CH₂)₂PPh₂)₂)NBD]Cl** the solid state structure revealed a trigonal bipyramidal Rh(I) centre, with hydrogen bonding between Cl^- and backbone NH groups (2.28(5) Å) (Figure 4.9). In the ^{31}P NMR spectrum (CD_2Cl_2) a single resonance at 38.8 ppm (d, $^1J_{RhP}$ = 132 Hz) for the chemically equivalent phosphines was observed. In the ^1H NMR spectrum the N–H group is observed at 7.90 ppm, showing the N–H···Cl^- hydrogen bond is retained in CD_2Cl_2 solution. There is a single broad alkene resonance (3.64 ppm, 4H), and a single bridging methylene (0.91 ppm, 2H) suggesting the NBD ligand readily rotates at 298 K. These data are all consistent with **[Rh(L3)NBD]Cl**.

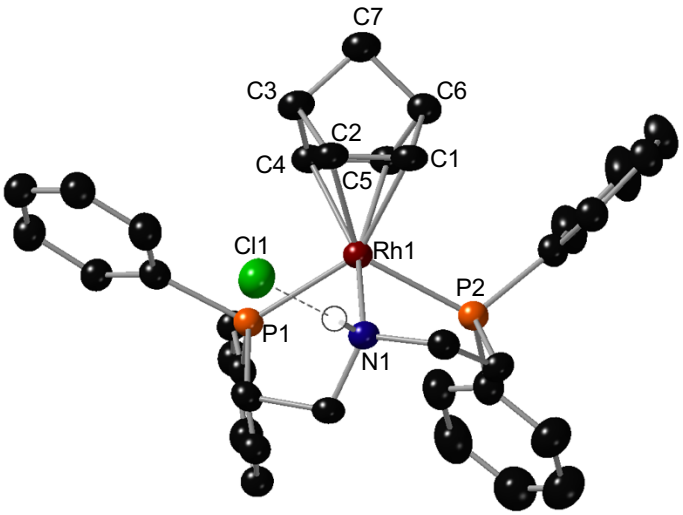


Figure 4.9 Molecular structure of **[Rh(HN((CH₂)₂PPh₂)₂) NBD]Cl**. Thermal ellipsoids set at 50 % and only the hydrogen H1 on N1 is shown. Selected bond lengths (Å) and angles (°): Rh1-P1 2.3091(11), Rh1-P2 2.3519(12), Rh1-N1 2.128(3), Rh1-C1 2.157(4), Rh1-C2 2.167(4), Rh1-C4 2.177(4), Rh1-C5 2.179(4), C1-C2 1.399(7), C4-C5 1.390(7), H1-Cl1 2.28(5), P2-Rh1-P1 114.62(4), N1-R1-P1 83.33(10) and N1-Rh1-P2 81.43(11).

4.2.10 Dehydropolymerisation of $H_3B{\cdot}NMeH_2$ using Rh(HN((CH₂)₂PPh₂)₂)NBD]Cl

The use of **[Rh(HN((CH₂)₂PPh₂)₂)NBD]Cl** as a catalyst for dehydropolymerisation was then investigated. Using **[Rh(HN((CH₂)₂PPh₂)₂)NBD]Cl** (1 mol%, THF, 20 °C, $[H_3B{\cdot}NMeH_2]$ = 1 M) as a pre-catalyst led to the formation of a insoluble black precipitate and free phosphine could be seen in the $^{31}P\{^1H\}$ NMR spectrum, so it was determined nanoparticles had formed. With this complex dehydrogenation was 9 times slower (k_{obs} = 3.7(3) mMs^{-1} vs k_{obs} = 0.4(3) mMs^{-1}). In the ^{11}B NMR spectra of an aliquot of the reaction mixture it was observed the dehydropolymerisation was now only 50% selective for $(H_2B{\cdot}NMeH)_n$ (Figure 4.10), significantly lower than with **[Rh(L3)NBD]Cl**. Significant amounts of side products $HB(NMeH)_2$ (30 %) and the unidentified peak at 1.4 ppm (20 %) were observed in the ^{11}B NMR spectra. In contrast,

with **[Rh(L3)NBD]Cl** as the pre-catalyst the reaction mixture was a clear solution and polyaminoborane was produced selectively. This points to quite a different process occurring when nanoparticles form providing evidence for homogeneous catalysis with **[Rh(L3)NBD]Cl**.

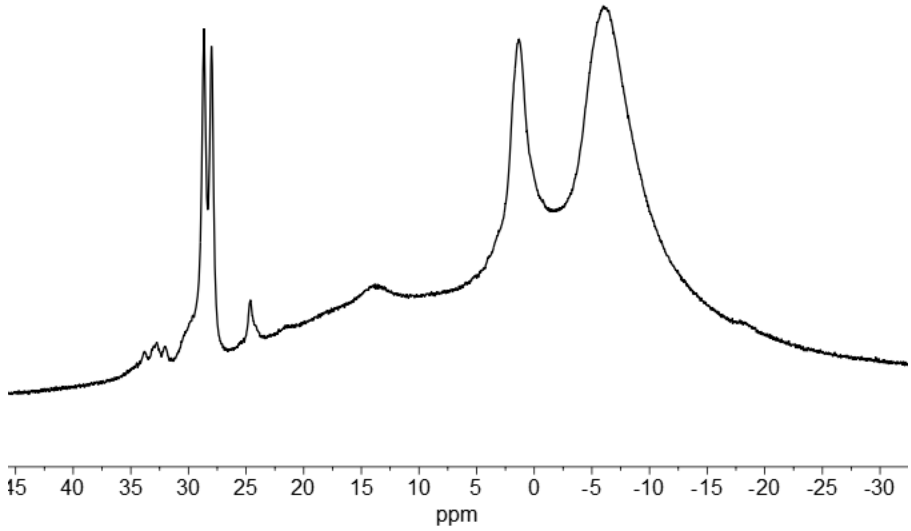


Figure 4.10 ^{11}B NMR spectrum showing poor selectivety for dehydropolymerisation using **[Rh(HN((CH$_2$)$_2$PPh$_2$)$_2$)NBD]Cl** as a pre-catalyst.

4.2.11 Testing for homogeneous vs heterogeneous catalysis

In light of the above results, the standard tests for a homogenous catalyst were performed using **[Rh(L3)NBD]Cl**.[20] Addition of Hg (100 eq.) before the start of dehydropolymerisation (0.5 mol%, THF, 20 ^oC, $[H_3B{\cdot}NMeH_2]$ = 1 M) had no significant effect on the rate of catalysis in the linear region but had small effect on the shape of the induction period (Figure 4.11). Hg could form an amalgam with Rh nanoparticles which would stop the reaction if it were operating *via* a heterogeneous catalyst.[12] This induction period is not yet fully understood.

Addition of 0.3 eq. of PMe_3 after 250 s of dehydropolymerisation (0.5 mol%, THF, 20 ^oC, $[H_3B{\cdot}NMeH_2]$ = 1 M) slightly slowed the rate of dehydropolymerisation but the reaction still went to completion (Figure 4.11). Sub-stoichiometric PMe_3 would be expected to stop the reaction if nanoparticles had been formed as only a fraction of the metal sites will be on the surface of the nanoparticle so these could be inhibited by less than stoichiometric amounts of phosphine. Notably there is no longer a linear region (zero order in amine-borane) in the kinetic profile in the presence of PMe_3. This suggests that the PMe_3 reversibly coordinates and resultantly the kinetic profile is no longer zero-order in $H_3B{\cdot}NMeH_2$ as PMe_3 competes with amine-borane for metal coordination. Taken together these tests suggest **[Rh(L3)NBD]Cl** is operating by a homogeneous mechanistic pathway.

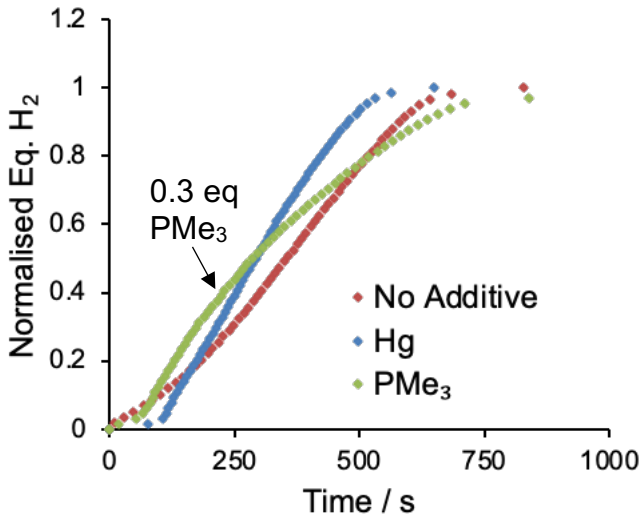


Figure 4.11 Kinetic profile determined using **[Rh(L3)NBD]Cl** as a pre-catalyst for the dehydropolymerisation (0.5 mol%, THF, 20 ^oC, $[H_3B{\cdot}NMeH_2]$ = 1 M) of $H_3B{\cdot}NMeH_2$ as monitored by eudiometer. Addition of Hg was not seen to slow catalysis. Sub-stoichiometric PMe_3 slowed catalysis only slightly. Both of these results support catalysis by a homogeneous catalyst.

4.2.12 Investigating sensitivity to hydrogen and water

If water (30 eq. relative to $[H_3B{\cdot}NMeH_2]$ i.e. a 30 fold excess) was added to the dehydropolymerisation, extremely rapid evolution of 3 eq. of H_2 was observed, reaching completion in only 10 seconds. In an aliquot of the reaction mixture only a broad peak at 19.5 ppm for $B(OH)_3$ was seen in the ^{11}B NMR spectra.[16] This provides evidence that hydrolysis is not happening to a significant extent under the standard conditions as under normal dehydropolymerisation conditions, only 1 eq. of H_2 was evolved and no $B(OH)_3$ seen in the ^{11}B NMR spectra.

Hydrogen pressure has been reported to both change the rate of catalysis and the polymer produced by the dehydropolymerisation of amine-boranes for some,[19] but not all catalyst systems.[2] This H_2 inhibition was seen when using **Co(L3)Cl$_2$** as a pre-catalyst for amine-borane dehydropolymerisation.[21] To investigate the effect of H_2 upon this system the dehydropolymerisation (0.5 mol%, THF, 20 ^oC, $[H_3B{\cdot}NMeH_2]$ = 1 M) was carried out with the reaction vessel initially open to air, or under an argon or hydrogen atmosphere. Dehydropolymerisation under either argon or hydrogen proceeded at the same rate suggesting that this system is not inhibited by hydrogen pressure (Figure 4.12). The fact the reaction rate is unchanged by H_2 pressure also suggests that hydroboration not hydrogenation of the NBD ligand is responsible for activation of **[Rh(L3)NBD]Cl** to **Rh(L3)H$_3$**. With the reaction vessel initially open to air there was a longer, more pronounced zeroth order period and the rate of reaction was faster, this was assigned to an increased concentration of trace H_2O present quenching any BH_3 that forms during the course of the dehydropolymerisation. BH_3 is known generally to inhibit dehydropolymerisation.[19] For example, the addition of NMe_2Et to

catalytic mixtures using **FeH(CO)(NR((CH$_2$)$_2$P^{i}Pr$_2$)$_2$)** for $H_3B{\cdot}NH_3$ dehydropolymerisation resulted in a threefold increase in ToN, due to the amine reacting with free BH_3 and preventing it from quenching the catalyst.[22] With **FeH(CO)(NR((CH$_2$)$_2$P^{i}Pr$_2$)$_2$)** BH_3 reduced catalytic activity by binding to the backbone amine forming an inactive borohydride complex. Further evidence for the importance of H_2O concentration is provided by repeating the dehydropolymerisation using rigorously dried THF from stills (5 ppm water from stills vs 30 ppm from SPS used throughout the rest of this chapter – water concentrations measured by Karl Fischer titration). Under these conditions the induction period is more pronounced but the catalysis ultimately attains the same maximum rate (Figure 4.12). Taken together these data suggest that water serves two key roles within this catalytic system (1) water has a role in activation of the catalyst (2) once the catalyst is on cycle, water reacts with any free BH_3 preventing it from quenching some of the catalyst and hence reducing its activity. However, the exact details of these processes have yet to be fully determined and are the focus of ongoing work. Furthermore, these changes do result in changes to degree of polymerisation of isolated polymer (Table 4.4), showing that understanding the exact cause of these changes is important in controlling the molecular weight of polymer produced and as such an important area for future work. One thing these results do indicate is that the polymerisation is relatively air-tolerant and so it was repeated in a vial open to air. The ^{11}B NMR of this sample showed selectivity and conversion for polymer had been maintained and the GPC analysis showed no significant change in the M_n of polymer produced compared to that measured with an eudiometer initially open to air. Therefore, this is an air-tolerant

polymerisation with polymer produced selectively open to air in a practical and easily performed polymerisation.

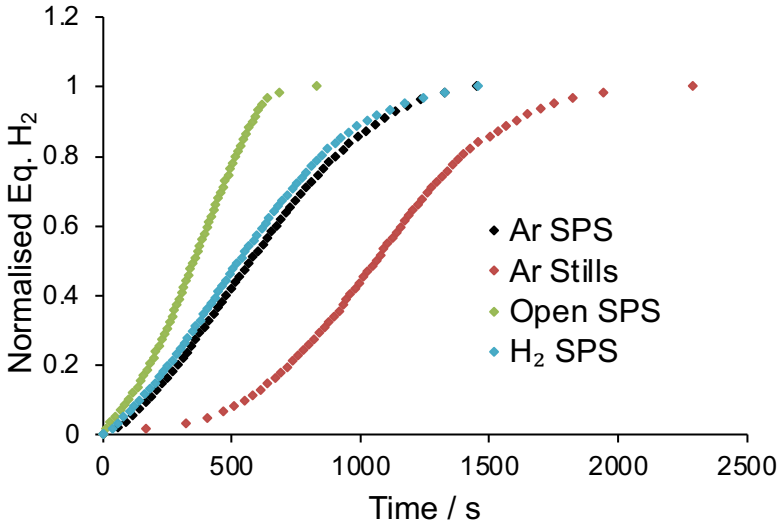


Figure 4.12 Kinetic profile determined using **[Rh(L3)NBD]Cl** as a pre-catalyst for the dehydropolymerisation (0.5 mol%, THF, 20 °C) of $H_3B{\cdot}NMeH_2$ (1 M) as monitored by eudiometer. Changing from catalysis open to air to under argon led to a gradual decrease in rate throughout the catalysis, assigned to free BH_3 quenching some of the active catalyst. Changing the atmosphere from Ar to H_2 has no effect on profile, suggesting no H_2 inhibition. Changing from SPS THF to extra dry still THF increased the induction period, showing water must have a role in catalyst activation.

Initial Atmos.	Conv. / %	Selectivity / %	M_n / g mol^{-1}	$Đ$	Yield / mg (%)
Ar (eudiometer)	99	98	73,200	1.8	55(51)
Ar (eudiometer)[a]	98	97	45,600	1.6	55(51)
Air (eudiometer)	98	99	70,800	1.6	103(96)
Air (open vial)	100	99	68,500	1.7	205(89)
H_2 (eudiometer)	99	98	47,800	1.6	49(45)

Table 4.4 Effect of initial reaction atmosphere on dehydropolymerisation of $H_3B{\cdot}NMeH_2$ using **[Rh(L3)NBD]Cl**. Typical dehydropolymerisation hydrogen evolution conditions (1M $H_3B{\cdot}NMeH_2$ in THF and 0.5 mol% **[Rh(L3)NBD]Cl**). Conversion and selectivity measured by ^{11}B NMR spectroscopy, M_n and $Đ$ measured by GPC relative to polystyrene standards. [a] Rigorously dried stills THF ([H_2O] = 5 ppm).

4.2.13 Attempted synthesis of [Rh(MeN((CH$_2$)$_2$)P^{i}Pr$_2$)NBD]Cl

Using **MeN((CH$_2$)$_2$)P^{i}Pr$_2$** which is the equivalent to ligand L3 with a methyl on the N, enables investigation into whether the proton on the backbone N is important to a ligand cooperative mechanism.[23] Adding **MeN((CH$_2$)$_2$)P^{i}Pr$_2$** to **((NBD)RhCl)$_2$** led to decomposition, with a number of peaks (>10) seen in the $^{31}P\{^1H\}$ NMR spectra. This decomposition occurred in a range of solvents (THF, CH_2Cl_2, 1,2-$C_6H_4F_2$). The decomposition is suggested to occur due to the absence of hydrogen bonding between the NH and Cl^-. This hydrogen bonding appears to stabilise **[Rh(L3)NBD]Cl** over a putative unstable complex **Rh(L3)Cl**. Here it is suggested that the complex **Rh(MeN((CH$_2$)$_2$)P^{i}Pr$_2$)Cl** first forms. This would be a 16 electron neutral Rh(I) complex and likely unstable with respect to solvent activation. Therefore, it was not possible to investigate the importance of the NH on the backbone through use of the methylated ligand.

4.2.14 Effect on kinetic profile of varying temperature using [Rh(L3)NBD]Cl

Monitoring the rate the of dehydropolymerisation (0.5 mol%, THF, $[H_3B{\cdot}NMeH_2]$ = 1 M) using **[Rh(L3)NBD]Cl** at various temperatures enabled an Eyring analysis to be carried out. Kinetic profiles were measured every 5 ^oC over the temperature range 15 - 30 ^oC (Table 4.5). At lower temperatures (10 ^oC) the reaction mixture appeared viscous and no longer gave a satisfactory temporal profile. Higher temperatures were not investigated due to concerns of solvent evaporation influencing the kinetic measurements made using an eudiometer. The rate determined from the gradient of the linear region and k_{obs}=rate/[Cat]. An Eyring (ln(k/T) vs 1/T) plot is shown in Figure

4.13. The Eyring analysis gives $\Delta H^{\ddagger}$ = 16.4(6) kcal mol^{-1}, $\Delta S^{\ddagger}$ = -5(2) $calK^{-1}mol^{-1}$ $\Delta G^{\ddagger}_{293K}$ = 17.7(12) kcal mol^{-1}. This value for $\Delta S^{\ddagger}$ is relatively modest suggesting neither an associative or dissociative process. This is consistent with a mechanism which has amine-borane already bound to the metal complex in the resting state of catalysis. ^{11}B NMR spectra of aliquots of the reaction mixtures at the end of catalysis show selectivity has been maintained (Table 4.5). The molecular weights of isolated polymer were determined by GPC analysis to have not changed significantly (Table 4.5).

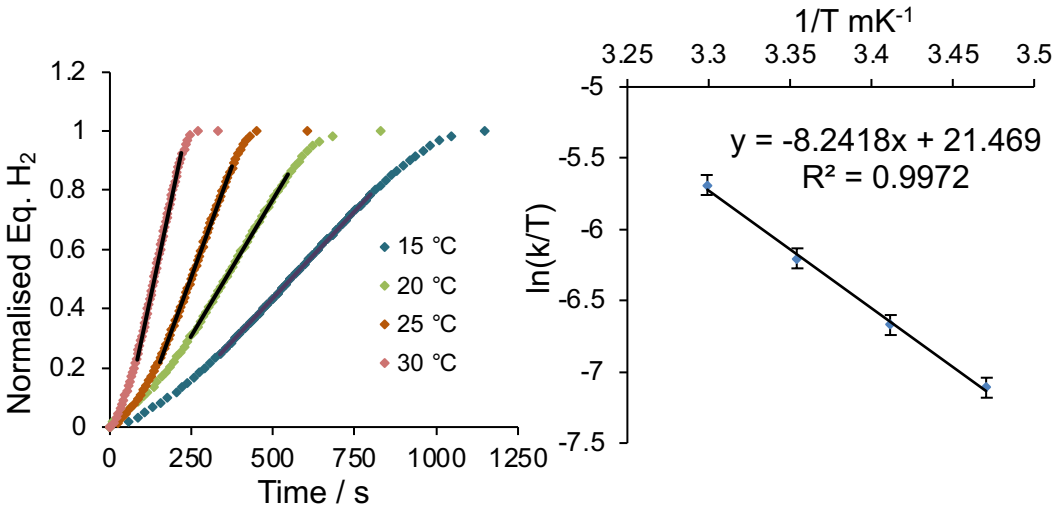


Figure 4.13 Kinetic profile determined using **[Rh(L3)NBD]Cl** (0.5 mol%) as a pre-catalyst for the dehydropolymerisation (THF) of $H_3B{\cdot}NMeH_2$ (1 M) as monitored by eudiometer. The kinetic profile was measured at 15, 20, 25 and 30 °C. The rate determined from the gradient of the linear region and k_{obs}=rate/[Cat]. Both Arrenius (bottom left, ln(rate) vs 1/T) and Eyring (bottom right, ln(k/T) vs 1/T) plots were made and from them the following parameters determined $\Delta G^{\ddagger}_{293K}$ = 17.7(12) kcal mol^{-1}, $\Delta H^{\ddagger}$ = 16.4(6) kcal mol^{-1} and $\Delta S^{\ddagger}$ = -5(2) $calK^{-1}mol^{-1}$.

Temp. / K	Eq. H_2 Evolved	k_{obs} / mMs^{-1}	Conv. / %	Selectivity / %	M_n / g mol^{-1}	$Đ$	Yield / mg (%)
288	1.0	1.1(3)	100	91	81,800	1.5	62(58)
293	1.0	1.9(3)	98	99	70,800	1.6	103(96)
298	1.0	3.0(3)	100	95	71,100	1.7	51(48)
303	1.0	5.1(3)	100	96	75,300	1.5	72(67)

Table 4.5 $H_3B{\cdot}NMeH_2$ dehydropolymerisation conditions and polymer characterisation data using **[Rh(L3)NBD]Cl** at various temperatures. Typical dehydropolymerisation hydrogen evolution conditions (1M $H_3B{\cdot}NMeH_2$ (112 mg) in THF and 0.5 mol% **[Rh(L3)NBD]Cl)**. Conversion and selectivity measured by ^{11}B NMR spectroscopy, M_n and $Đ$ measured by GPC relative to polystyrene standards.

4.2.15 Speciation study on [Rh(L3)NBD]Cl

The speciation study was led by Dr Claire Brodie. Due to a combination of the short time to completion (reaching completion in ~5 minutes) and the large volume of hydrogen evolved, speciation studies could not be carried out within an NMR tube at room temperature. To circumvent this, speciation experiments were performed by using a 50 mL jacketed two-neck Schlenk flask under standard conditions (1 mol% **[Rh(L3)NBD]Cl**, THF, 20 °C, $[H_3B{\cdot}NMeH_2]$ = 1 M) at room temperature, and aliquots of the reaction were taken periodically, placed into NMR tubes and frozen in liquid N_2 to thermally quench the reaction. The NMR tubes were then thawed inside the spectrometer which was pre-cooled to 185 K where ^{11}B, ^{31}P and ^{1}H NMR spectra could be collected. If the samples were warmed to room temperature catalysis restarted.

For speciation experiments the highest catalyst loading regularly employed in catalysis (1 mol%) was chosen, as this would give the best signal to noise in the resulting NMR spectra. Using the sampling methodology outlined above **[Rh(L3)NBD]Cl** (1 mol%) was used as a pre-catalyst for the dehydropolymerisation (THF, 20 °C) of $H_3B{\cdot}NMeH_2$

(1 M). Speciation of the reaction was followed over time by $^{31}P\{^1H\}$, ^1H and ^{11}B NMR spectroscopy. The results from this speciation experiment are shown in Figure 4.14.

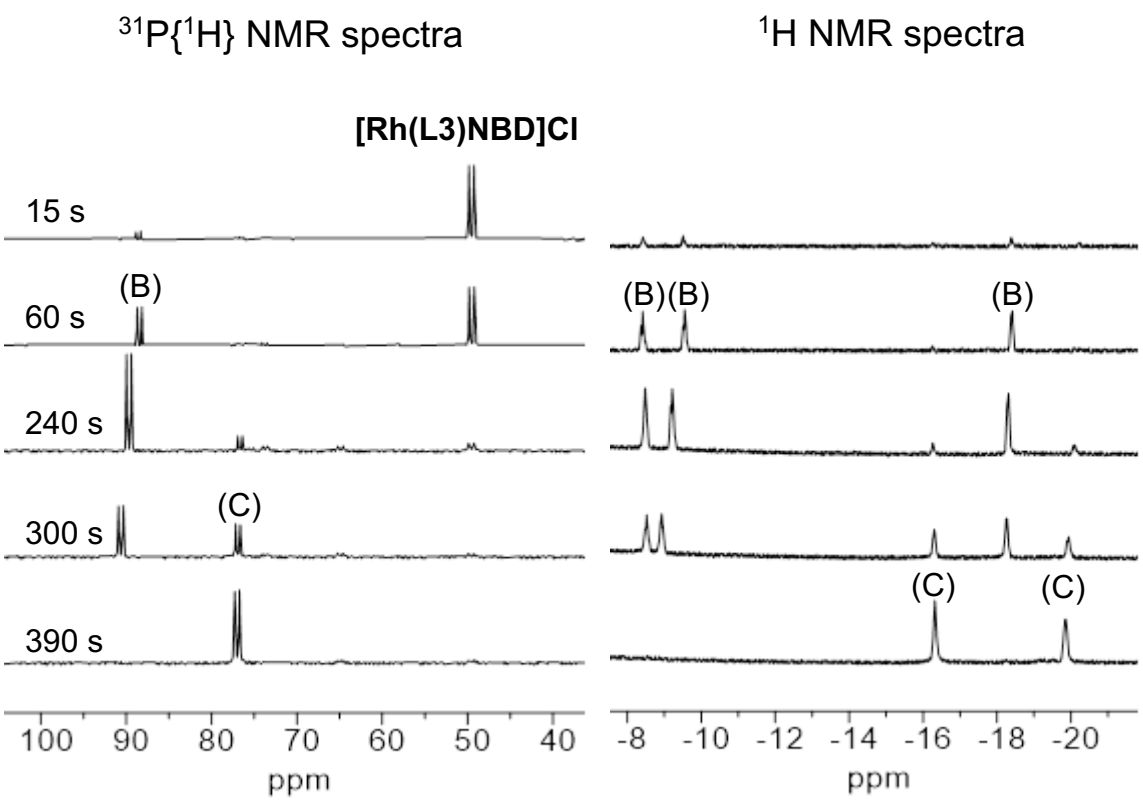
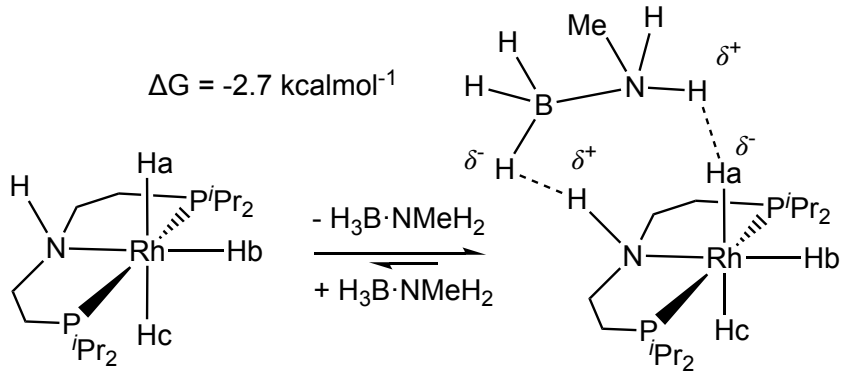


Figure 4.14 NMR speciation data for the dehydropolymerisation (THF, 20 °C) of $H_3B{\cdot}NMeH_2$ (1 M) using pre-catalyst **[Rh(L3)NBD]Cl** (1 mol%). Spectra collected at 185 K of aliquots of the reaction frozen after specified reaction times.

The $^{31}P\{^1H\}$ NMR spectrum 15 s into the dehydropolymerisation consists of largely (95%) the starting material **[Rh(L3)NBD]Cl**, which is observed at 49.5 ppm (d, J = 123 Hz). The presence of residual **[Rh(L3)NBD]Cl** likely explains the induction period observed. As the reaction proceeds **[Rh(L3)NBD]Cl** transforms to a new species (B) observed as a single environment at ~90 ppm (d, J = 115 Hz), which becomes the major species present (~85% after 240 s) and persists until the very late stages of catalysis. This suggests (B) is the resting state of the catalyst. In the ^1H NMR spectra three new hydride resonances appear simultaneous to the resonance in the $^{31}P\{^1H\}$.

The resonances were observed at -8.5, -9.5 and -18.4 ppm in a 1:1:1 ratio of integrals, suggesting (B) has three hydrides bound to the metal centre. These hydride peaks increase in intensity in proportion with the ^{31}P NMR resonance for (B). Integration of these signals with respect to the complex ligand was challenging as the ligands signals were obscured by those for the amine-borane and polymer. These data suggest (B) is a neutral trihydride complex, suggested to be **Rh(L3)H_3**. This is in agreement with previous research highlighting the importance of neutral hydride resting states in Rh catalysed amine-borane dehydropolymerisations.[3] Notably the hydride resonance at -9.5 ppm shifts downfield near the end of the dehydropolymerisation to -8.9 ppm (300 s), while the other resonances are not significantly shifted. This shift is seen only towards the end of catalysis suggesting (B) exists as one species for most of the catalysis. A potential explanation of this downfield shift is the binding of $H_3B{\cdot}NMeH_2$ to form **Rh(L3)H_3($H_3B{\cdot}NMeH_2$)**. In this complex the $H_3B{\cdot}NMeH_2$ is held in place through non-classical $^{\delta-}H\cdots H^{\delta+}$ interactions. This must be a fast equilibrium as the ^1H NMR spectrum shows a frequency average of the bound and unbound species. This binding was investigated computationally (Section 4.2.26, collaborators in Macgregor group) and the binding interaction was found to be thermodynamically favoured to the separate components by approximately 2.7 kcal mol^{-1}. Significantly it was predicted that the chemical shift of the hydride resonance at -8.9 ppm would shift upfield by 1.2 ppm on binding $H_3B{\cdot}NMeH_2$ (0.8 ppm measured experimentally). The difference in hydride chemical shifts between **Rh(L3)H_3($H_3B{\cdot}NMeH_2$)** and **Rh(L3)H_3** are compared in Figure 4.15. The close agreement between the calculated and experimental values strongly support the resting state of catalysis being **Rh(L3)H_3($H_3B{\cdot}NMeH_2$)**. A resting state of the form **Rh(L3)H_3($H_3B{\cdot}NMeH_2$)** would be consistent with the pseudo-zeroth

order in amine-borane kinetics as amine-borane is bound to the complex prior to the resting state. It is also consistent with the small $\Delta S^{\ddagger}$ obtained in the Eyring analysis for neither an associative or dissociative process.

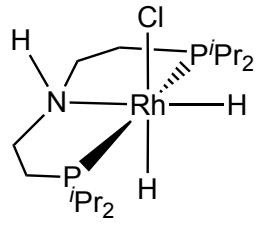


	^{1}H NMR (ppm) Observed	Calculated
Ha	-8.53	-7.45
Hb	-18.24	-17.41
Hc	-8.83	-7.95

	^{1}H NMR (ppm) Observed	Calculated
Ha	-8.42	-7.04
Hb	-18.39	-16.95
Hc	-9.52	-9.12

Figure 4.15 Resting state of catalysis when **[Rh(L3)NBD]Cl** as a pre-catalyst and a comparison of the computationally calculated and experimental NMR spectroscopic data.

At the end of catalysis a new species (C) was observed in the $^{31}P\{^1H\}$ NMR spectrum at 77.0 ppm (d, J = 112 Hz). After catalysis had reached completion (C) was the only species present in the $^{31}P\{^1H\}$ NMR spectrum. In the ^{1}H NMR spectrum two broad hydride peaks were observed at -16.3 ppm and -19.8 ppm with a 1:1 ratio of integrals, suggesting two hydrides bound to a single metal centre. Integration of these signals with respect to the complex ligand was challenging as the ligand signals were obscured by those for the amine-borane and polymer. The NMR data available for (C) is consistent with the complex **Rh(L3)H_2Cl** (Scheme 4.4), which was subsequently isolated to confirm this assignment.



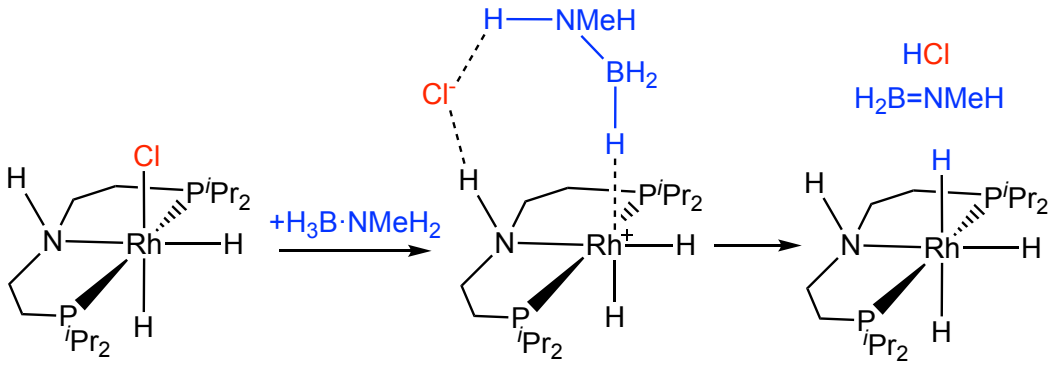
Scheme 4.4 $Rh(L3)H_2Cl$ is the speciation seen at the end of dehydropolymerisation using **[Rh(L3)NBD]Cl**.

4.2.16 Activation pathway for [Rh(L3)NBD]Cl to $Rh(L3)H_3(H_3B{\cdot}NMeH_2)$

In the speciation above it was observed that **[Rh(L3)NBD]Cl** is gradually activated to **$Rh(L3)H_3(H_3B{\cdot}NMeH_2)$**. This activation could occur by either hydrogenation or hydroboration of the bound NBD ligand to from **$Rh(L3)H_2Cl$** which then rapidly reacts onwards to form **$Rh(L3)H_3$** and concomitant boronium formation as described in the next section. At the current point the mechanism of activation is unknown.

4.2.17 Activation pathway for $Rh(L3)H_2Cl$ to $Rh(L3)H_3$

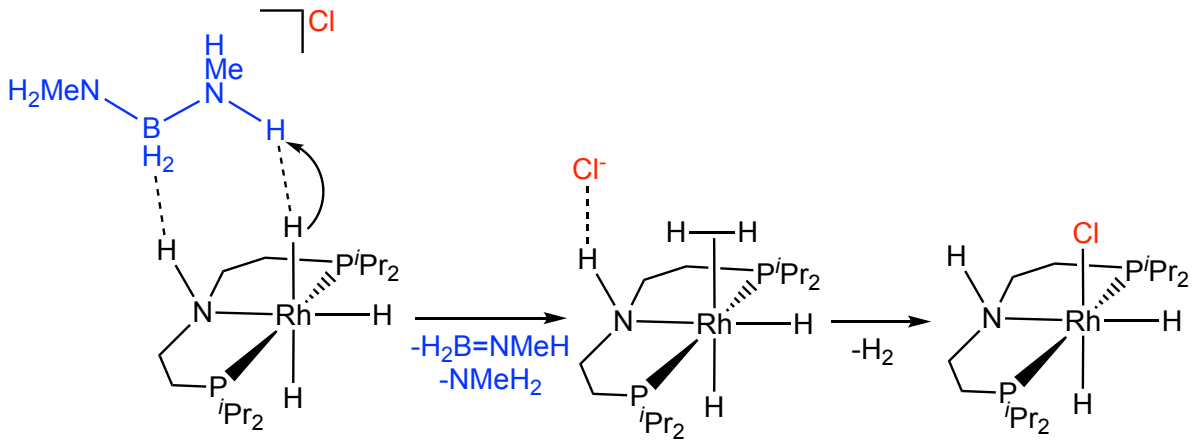
The conversion of **$Rh(L3)H_2Cl$** to **$Rh(L3)H_3$** is suggested to occur by coordination of $H_3B{\cdot}NMeH_2$ to form a σ-bound amine–borane intermediate (Scheme 4.5). The putative σ-bound amine–borane intermediate could contain a Cl^- hydrogen bound to the NH group on both the backbone and the bound amine-borane. It is suggested that hydrogen bonding between the NH of the amine-borane and the Cl assists with Cl^- dissociation from the metal. A hydride transfer then occurs to form **$Rh(L3)H_3$** with elimination of HCl and $H_2B{=}NMeH$. In the presence of trace amine $[NMeH_3]Cl$ (that arises from B-B bond cleavage) rapidly forms.[3] $H_2B{=}NMeH$ and $[NMeH_3]Cl$ likely combine to form boronium chloride, $[H_2B(NMeH_2)_2]Cl$.[15] As shown in Section 3.2.4 boronium can act as a chain transfer agent to control the M_n of polymer produced.



Scheme 4.5 Activation pathway for **Rh(L3)H_2Cl** to **Rh(L3)H_3**.

4.2.18 Formation of Rh(L3)H_2Cl at the end of catalysis

At the end of catalysis **Rh(L3)H_2Cl** was observed to be the only species present in the speciation studies**.** It is suggested that one of the **Rh(L3)H_3** hydrides deprotonates a unit of boronium to form a dihydrogen dihydride complex. Boronium and is likely directed to react selectively on the same face as the NH due to non-classical $H^{\delta+}\cdots^{\delta-}H$ interactions similar to the those suggested to coordinate $H_3B{\cdot}NMeH_2$ in **Rh(L3)H_3($H_3B{\cdot}NMeH_2$)**. This is followed by rapid loss of H_2, and Cl^- binds to the metal centre to form **Rh(L3)H_2Cl** (Scheme 4.6). Cl^- will also be directed selectively to the same face as the NH due to hydrogen bonding to this amine functionality. Protonation of rhodium trihydride complexes to form dihydrogen dihydrides is known in the literature.[24]



Scheme 4.6 Reformation of **Rh(L3)H_2Cl** at the end of catalysis.

4.2.19 Synthesis of Rh(L3)H_2Cl

To confirm the structure of the species seen at the end of catalysis, **Rh(L3)H_2Cl** was isolated and characterised by Dr Claire Brodie. **Rh(L3)H_2Cl** was prepared by addition of L3 to **[Rh(COD)Cl]$_2$** in 1,2-$C_6H_4F_2$ solvent followed by immediate freeze-pump-thaw degassing the reaction mixture and exposure to H_2 (4 bar). The reaction was then stirred for 48 h under H_2, before isolation of the product as a powder by removal of solvent in *vacuo* and washing with *n*-pentane at -78 °C. Crystals suitable for X-ray diffraction were grown through concentration of a dilute solution of **Rh(L3)H_2Cl** in a 1:3 mixture of 1,2-$F_2C_6H_4$/pentane and a satisfactory solid state structure was obtained by single crystal X-ray diffraction - R_1 = 2.94 % (Figure 4.16). In the crystal structure it was observed that the NH and Cl are both on the same face, i.e. they are placed *syn* relative to each other.

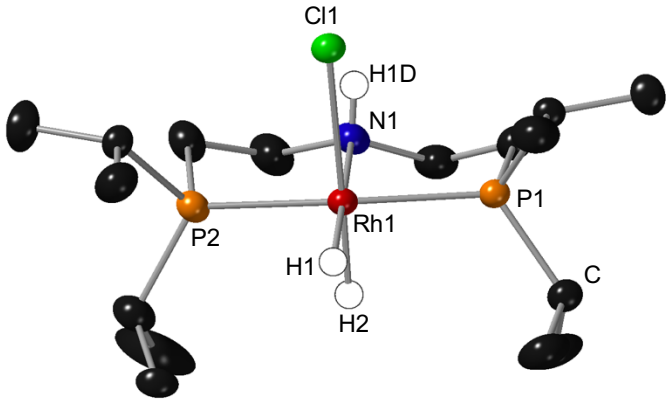


Figure 4.16 Molecular structure of **Rh(L3)H_2Cl**. Thermal ellipsoids set at 50 % and only the located hydrogens are shown. Selected bond lengths (Å) and angles (°): Rh1-Cl1 2.5033(8), Rh1-P1 2.3945(5), Rh1-P2 2.2716(9), Rh1-N1 2.2732(9), Rh1-H1 1.76(4), Rh1-H2 1.50(4), P2-Rh1-P1 167.87(3)), N1-Rh1-P1 83.82(8) and N1-R1-P2 84.79(8).

The $^{31}P\{^{1}H\}$ NMR spectra (THF-d_8) showed a single resonance at 75.7 ppm (d, $^{1}J_{RhP}$ = 115 Hz), consistent with that seen in the speciation at the end of catalysis. In the ^{1}H NMR spectrum two hydride resonances could be observed -16.3 ppm and -19.8 ppm, again these are consistent with that seen at the end of speciation experiments. Together this NMR spectroscopic data confirms **Rh(L3)H_2Cl** is the species present at the end of catalysis. The resonance at -16.3 ppm (trans to Cl) was observed as an apparent pentet ($^{1}J_{RhH} \approx {}^{2}J_{PH} \approx {}^{2}J_{HH} \approx$ 15.5 Hz) which simplified to an apparent triplet on ^{31}P decoupling (Figure 4.17). The resonance at -19.8 ppm (trans to N) was observed as a multiplet with coupling to ^{103}Rh, ^{31}P and ^{1}H. This simplified to a doublet of doublets ($^{1}J_{RhH}$ = 28.1 Hz and $^{2}J_{HH}$ = 10.0 Hz) upon ^{31}P decoupling. At 185 K the coupling in the hydride resonances could be seen most clearly so this is shown in Figure 4.17. Such **{RhH_2Cl}** type complexes are known in the literature and typically in the ^{1}H NMR spectra hydride resonances are observed at approximately -17 and -20 ppm, with coupling to ^{103}Rh, ^{31}P and ^{1}H observed.[25,26] A ^{1}H-^{1}H NOESY spectrum showed no

correlation between the backbone NH and any hydride resonances, while correlation could be seen between the resonance at -16.3 ppm and backbone CH protons presumably on the opposite face to the NH. This again is consistent with the Cl^- being on the same face of the metal as the backbone NH, which is consistent with the solid state structure.

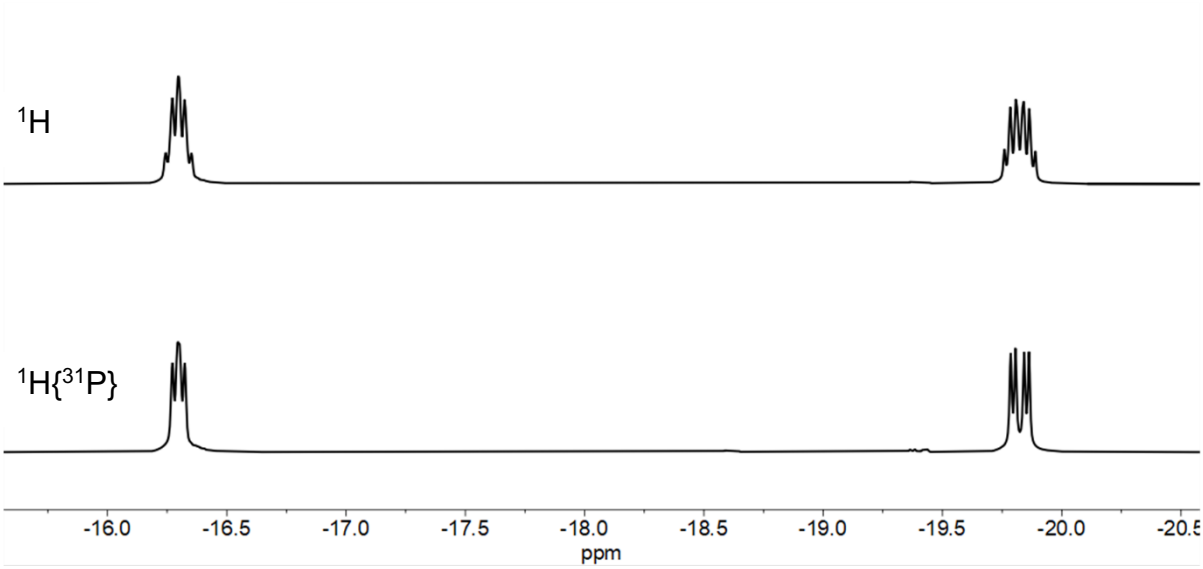


Figure 4.17 ^1H NMR and $^1H\{^{31}P\}$ spectra (THF-d_8, 500 MHz, 185K) of hydride region of **Rh(L3)H_2Cl**.

The direct hydrogenation of **[Rh(L3)NBD]Cl** could feasibly produce **Rh(L3)H_2Cl.** However, when **[Rh(L3)NBD]Cl** was placed in a hydrogen atmosphere (4 bar) directly, the reaction required heating at 70 ^oC for 1 week to consume all of the starting material as monitored by $^{31}P\{^1H\}$ NMR spectroscopy. Furthermore, significant amounts of a black precipitate (Rh metal) formed and only low yields of less than 50% were obtained. These are significantly forcing conditions and suggest that activation of **[Rh(L3)NBD]Cl** in the early stages of dehydropolymerisation does not occur via a simple hydrogenation during catalysis at room temperature and pressure and thus implicates amine-borane in its generation.

4.2.20 In-situ generation of Rh(L3)H_3

With the resting state of catalysis suggested to be **Rh(L3)H_3($H_3B{\cdot}NMeH_2$)**, by the speciation study, the closely related species **Rh(L3)H_3** was generated in-situ to help confirm this assignment. This work was led by Dr Claire Brodie. **Rh(L3)H_2Cl** and KO^{t}Bu were added to a J. Youngs tap NMR tube in THF-d_8. The resulting orange solution was freeze-pump-thaw degassed and hydrogen (2 bar) was added. The reaction was stirred by end-over-end inversion of the NMR tube for 1 hr to yield a pale yellow solution that was characterised by NMR spectroscopy. The $^{31}P\{^1H\}$ NMR spectrum revealed a doublet at 91.6 ppm (d, J = 115 Hz) as the only species present. In the ^1H NMR spectrum three hydride resonances could be identified at -8.41, -8.69 and -18.30 ppm in a 1:1:1 ratio. These resonances integrate to 1H with respect to the ligand. The hydrides at -8.41 and -8.69 ppm both appeared as apparent pentet of doublets from coupling to ^{103}Rh, ^{31}P and ^1H. These resonances simplified to a triplet of doublets upon ^{31}P decoupling (Figure 4.18). These pentent of doublets are suggested to be caused by similar coupling to all ^{103}Rh, ^{31}P and $^1H_{trans}$ and a smaller coupling to $^1H_{cis}$. For the resonance at -8.41 ppm $^1J_{RhH} \approx {}^2J_{PH} \approx {}^2J_{HHtrans} \approx 19.6$ Hz and $^2J_{HHcis} = 6.0$ Hz; while the resonance at -8.69 ppm $^1J_{RhH} \approx {}^2J_{PH} \approx {}^2J_{HHtrans} \approx 18.8$ Hz and $^2J_{HHcis} = 6.2$ Hz. The hydride resonance at -18.30 ppm displayed a complex coupling pattern which simplified to a doublet of triplets upon ^{31}P decoupling. The doublet of triplets is explained by a $^1J_{RhH} = 23.3$ Hz and a smaller coupling to the cis hydrides of $^2J_{HHcis} = 6.0$ Hz. A 1H-1H NOESY showed a correlation between the backbone NH and the hydride resonance at -8.41 ppm suggesting this is the proton *syn* to the NH. This NMR spectroscopic evidence provides a convincing picture that **Rh(L3)H_3** has been generated. These data compare closely to those for the resting state observed in the

speciation experiments and support an assignment of the resting state to **Rh(L3)H_3($H_3B{\cdot}NMeH_2$)**. This complex could not be isolated as removal of solvent led to the loss of hydrogen.

4.2.21 Formation of Rh(L3)H_2Cl by reaction of Rh(L3)H_3 with boronium

Addition of **Rh(L3)H_3** to $[BH_2(NMeH_2)_2][Cl]$ resulted in rapid gas evolution and by NMR spectroscopy of the resultant solution it was observed that **Rh(L3)H_2Cl** had formed quantitatively. For the majority of catalysis the concentration of boronium is significantly lower than that of $H_3B{\cdot}NMeH_2$ therefore any **Rh(L3)H_2Cl** that forms will rapidly react with $H_3B{\cdot}NMeH_2$ to regenerate **Rh(L3)H_3**. This supports the role of boronium in protonating the **Rh(L3)H_3** at the end of catalysis to give **Rh(L3)H_2Cl**.

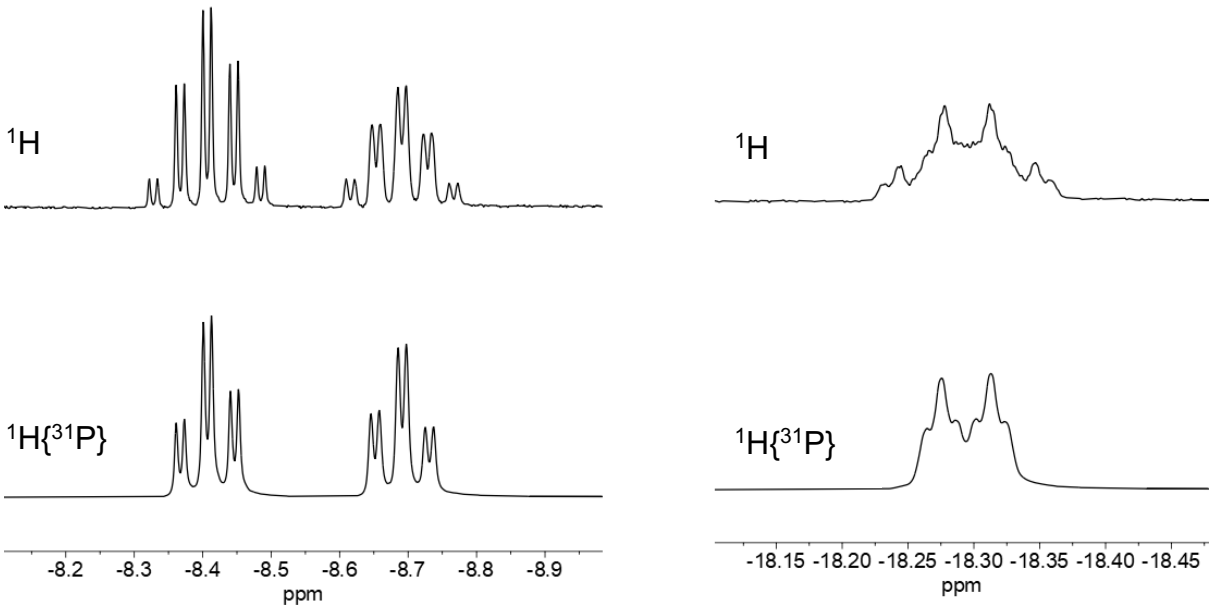


Figure 4.18 ^{1}H NMR and ^{1}H{^{31}P} spectra (THF-d_8, 500 MHz, 298 K) of hydride region under a H_2 atmosphere (2 bar) of **Rh(L3)H_3**.

4.2.22 Kinetic profile of dehydropolymerisation of $H_3B{\cdot}NMeH_2$ using Rh(L3)H_2Cl

Using **Rh(L3)H_2Cl** as a pre-catalyst for dehydropolymerisation (0.5 mol%, THF, 20 ^oC, [$H_3B{\cdot}NMeH_2$] = 1 M) no induction period was seen and the catalysis proceeded immediately to a short period of faster catalysis (burst phase) before settling to a linear region – i.e. zero-order in amine-borane (Figure 4.19). The linear region was at a slightly higher rate than for **[Rh(L3)NBD]Cl** (2.7(2) and 1.9(2) mM s^{-1} respectively) and there was more pronounced deceleration at the end of the reaction. Furthermore, the rate following the recharge with fresh substrate with **[Rh(L3)NBD]Cl** (Section 4.2.7) is similar of the rate determined for the same catalyst loading with **Rh(L3)H_2Cl** (2.4(2) and 2.7(2) mM s^{-1} respectively). These data combined with the speciation experiment showing **[Rh(L3)NBD]Cl** present until late stages of catalysis provide strong evidence for the difference in rates observed between **Rh(L3)H_2Cl** and **[Rh(L3)NBD]Cl** being due to the induction effects observed with **[Rh(L3)NBD]Cl**. ^{11}B NMR spectra of aliquots of the reaction mixture at the end of catalysis show selectivity for polyaminoborane has been maintained by a peak at -6.3 ppm in the ^{11}B NMR spectra (Table 4.6). The molecular weight of isolated polymer was determined by GPC analysis to have M_n = 71,000 g mol^{-1} and $Đ$ = 1.6, similar to that seen with **[Rh(L3)NBD]Cl**.

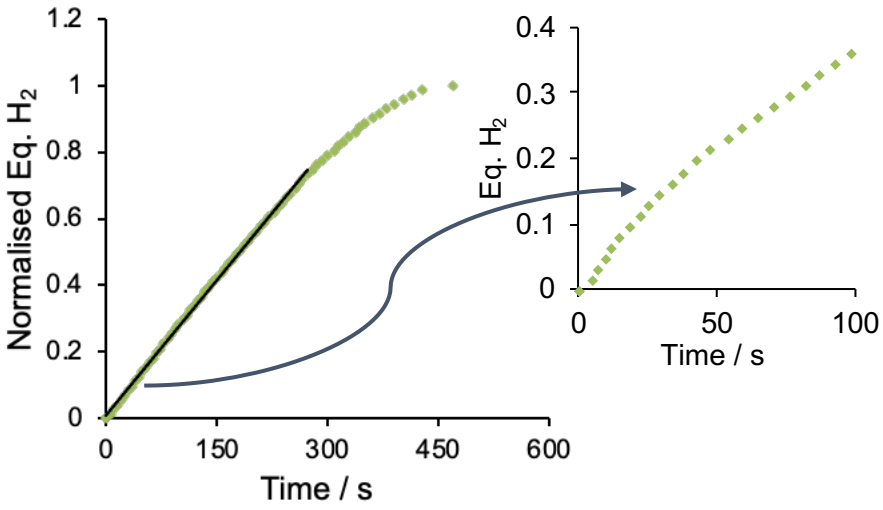


Figure 4.19 Kinetic profile determined using **Rh(L3)H_2Cl** as a pre-catalyst for the dehydropolymerisation (0.5 mol%, THF, 20 °C) of $H_3B{\cdot}NMeH_2$ (1 M) as monitored by eudiometer. Linear region suggesting that the rate law is zeroth order in $H_3B{\cdot}NMeH_2$.

4.2.23 Effect on kinetic profile of varying catalyst loading using Rh(L3)H_2Cl

For **Rh(L3)H_2Cl** increasing catalyst concentration increased the rate of reaction but qualitatively the rate for 0.25 mol% seemed significantly lower than the other observed values. In all cases a burst phase was observed at the start of catalysis. The dehydropolymerisation (THF, 20 °C, [$H_3B{\cdot}NMeH_2$] = 1 M) was carried out at 0.25, 0.5, 0.75 and 1 mol% catalyst loadings of **Rh(L3)H_2Cl** and these gave rates of 0.6(2), 2.7(2), 4.6(2) and 6.9(2) mMs^{-1} respectively (Table 4.7). A plot of rate against [Cat] fitted well to a straight line (R^2 = 0.9981) but this did not go through the origin (Figure 4.20). The trend line intercepts with the x axis at 1.8 mM. This intercept can be explained by a small amount (~1.8 mM) of catalyst being quenched out by impurities in the solvent or substrate of the reaction. This constant quantity quenched would disproportionately affect low catalyst loadings where it is a larger proportion of the total amount of catalyst. This quenching of catalyst could also explain the burst phase seen

at the start of catalysis where the concentration of catalyst is higher and a linear region is reached once all impurity has been processed. ^{11}B NMR spectra of aliquots of the reaction mixture at the end of catalysis show selectivity has been maintained (Table 4.6). Varying the catalyst loading for dehydropolymerisation (THF, 20 °C, $[H_3B{\cdot}NMeH_2]$ = 1 M) seemed to have some increase in scatter in the M_n of polymer produced (Table 4.6).

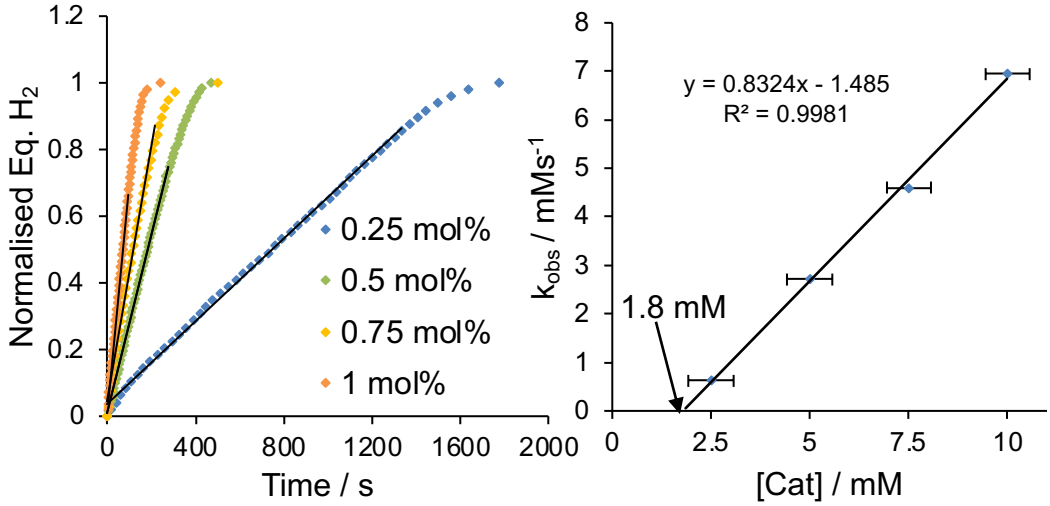


Figure 4.20 Kinetic profile determined using **Rh(L3)H_2Cl** at a range of catalysts loadings (0.25, 0.5, 0.75 and 1 mol%) as a pre-catalyst for the dehydropolymerisation (THF, 20 °C) of $H_3B{\cdot}NMeH_2$ (1 M) as monitored by eudiometer. Rate determined from the gradient of the linear region and plotted against catalyst loading to give a straight line and 1st order in catalyst with a rate constant k_{obs} = 0.83(3) s^{-1}.

[Rh] / mol%	Eq. H_2 evolved	k_{obs} / mMs^{-1}	Conv. / %	Selectivity / %	M_n / g mol^{-1}	$Đ$	Yield / mg (%)
0.25	1.0	0.6(3)	100	93	50,900	1.9	55(51)
0.50	1.0	2.7(3)	100	94	71,000	1.6	91(85)
0.75	1.0	4.6(3)	100	92	70,900	1.6	44(40)
1.00	1.0	6.9(3)	100	83	49,000	1.7	60(56)
0.25[a]	1.0	0.6(3)	100	96	61,900	1.8	60(56)

Table 4.6 $H_3B{\cdot}NMeH_2$ dehydropolymerisation conditions and polymer characterisation data using **Rh(L3)H_2Cl** at various catalytic loadings. Typical dehydropolymerisation hydrogen evolution conditions with 1M $H_3B{\cdot}NMeH_2$ (112 mg) in THF and 0.5 mol% **Rh(L3)H_2Cl**; Conversion and selectivity measured by ^{11}B NMR spectroscopy, M_n and $Đ$ measured by GPC relative to polystyrene standards. [a]Using **Rh(L3)H_2Cl** with initial 0.125 mol% cat. loading, and additional 0.125 mol% **Rh(L3)H_2Cl** added after 350 s.

To test this hypothesis that catalyst is being quenched a catalytic run (THF, 20 °C, $[H_3B{\cdot}NMeH_2]$ = 1 M) was carried out at 0.125 mol% and a small amount of H_2 was released (0.15 eq.) before dehydropolymerisation stopped, supporting all the catalyst having been quenched by impurities (Figure 4.21). Addition of a further 0.125 mol% of catalyst to the reaction mixture (0.25 mol% total) led to dehydropolymerisation at a rate which was within error of that measured for catalysis at 0.25 mol% catalyst loading (0.7(2) and 0.6(2) mMs^{-1} respectively). These data are consistent with a constant amount of catalyst being quenched by impurities in the solvent or substrate. Assuming that **Rh(L3)H_2Cl** deactivation occurs through reaction with one equivalent of H_2O then 0.18 mol% of catalyst quenched would predict the solvent contains ~30 ppm, which remarkably, is consistent with the measured $[H_2O]$ value of ~25 ppm for this solvent obtained from Karl Fischer titration. After adjusting catalyst concentration for the amount quenched a value for k was determined of 0.83(3) s^{-1} from the linear plot of rate vs [Cat]. This k gives an even higher ToF = 3,000 h^{-1} for any point in the zeroth

order region of catalysis. As for **[Rh(L3)NBD]Cl**, this is among the highest reported for the dehydropolymerisation of $H_3B{\cdot}NMeH_2$.

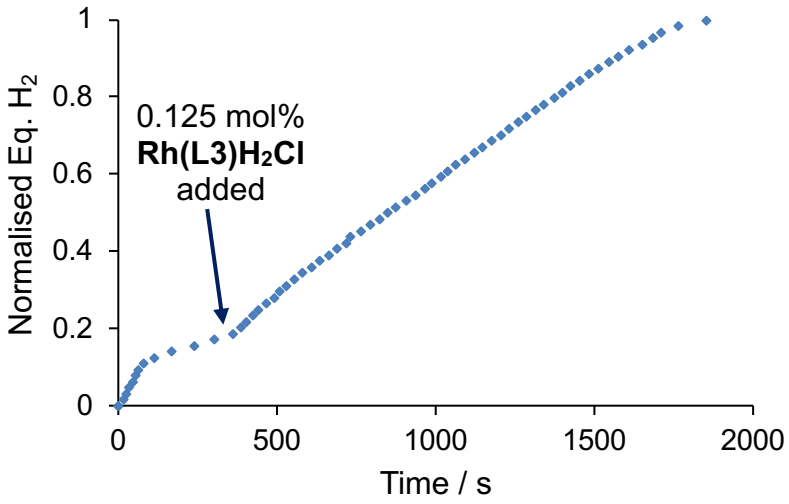


Figure 4.21 Kinetic profile determined using initially 0.125 mol% **Rh(L3)H_2Cl** before adding 0.125 mol% more catalyst as a pre-catalyst for the dehydropolymerisation (THF, 20 °C) of $H_3B{\cdot}NMeH_2$ (1 M) as monitored by eudiometer. Rate determined from the gradient of the linear region and plotted against catalyst loading to give a straight line and 1st order in catalyst with a rate constant k_{obs} = 0.83(3) s^{-1}.

4.2.24 Effect on kinetic profile of varying temperature using Rh(L3)H_2Cl

Dehydropolymerisation (0.5 mol%, THF, [$H_3B{\cdot}NMeH_2$] = 1 M) using **Rh(L3)H_2Cl** was monitored at a range of temperatures (15, 20, 25 and 30 °C). The rate determined from the gradient of the linear region (Table 4.7) and k_{obs}=rate/[Cat] with [Cat] adjusted for amount quenched by water (Section 4.2.23). An Eyring (ln(k/T) vs 1/T) plot is shown in Figure 4.22. The Eyring analysis gives $\Delta H^{\ddagger}$ = 16.0(16) kcal mol^{-1}, $\Delta S^{\ddagger}$ = -4(5) $calK^{-1}mol^{-1}$ and $\Delta G^{\ddagger}_{293K}$ = 17(3) kcal mol^{-1}. This value for $\Delta S^{\ddagger}$ is relatively modest suggesting neither an associative or dissociative process.

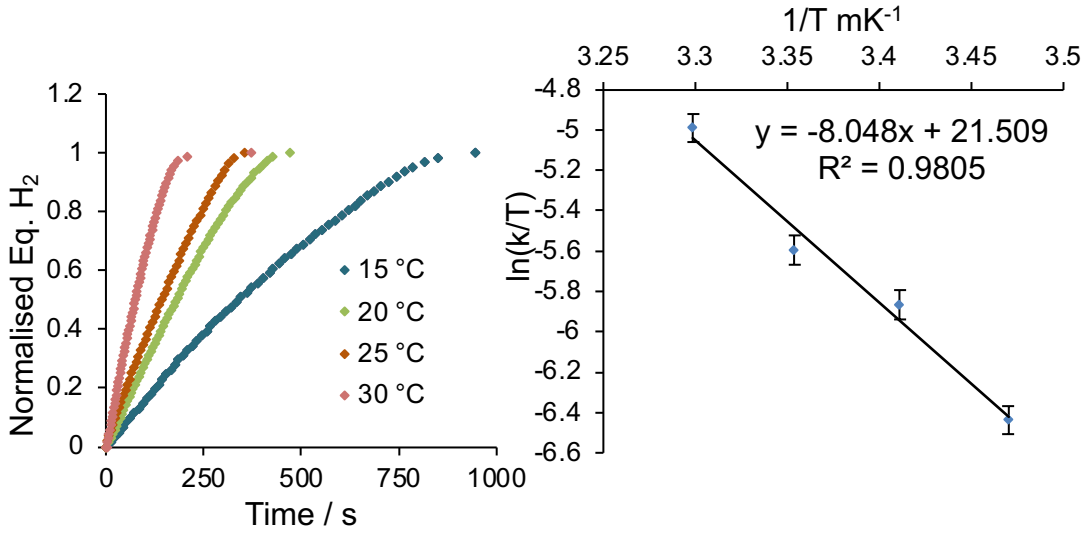


Figure 4.22 Kinetic profile determined using **Rh(L3)H_2Cl** (0.5 mol%) as a pre-catalyst for the dehydropolymerisation (THF) of $H_3B{\cdot}NMeH_2$ (1 M) as monitored by eudiometer. The kinetic profile was measured at 15, 20, 25 and 30 °C. The rate determined from the gradient of the linear region and k_{obs}=rate/[Cat] (with [Cat] adjusted for amount quenched by water (section 4.2.23). Both Arrenius (bottom left, ln(rate) vs 1/T) and Eyring (bottom right, ln(k/T) vs 1/T) plots were made and from them the following parameters determined: $\Delta G^{\ddagger}_{293K}$ = 17(3) kcal mol^{-1}, $\Delta H^{\ddagger}$ = 16.0(16) kcal mol^{-1} and $\Delta S^{\ddagger}$ = -4(5) calK^{-1}mol^{-1}.

Temp / K	Eq. H_2 Evolved	k_{obs} / mMs^{-1}	Conv. / %	Selectivity / %	M_n / gmol^{-1}	Đ	Yield / mg (%)
288	1.0	1.6(3)	100	95	81,200	1.6	65(60)
293	1.0	2.7(3)	100	94	71,000	1.6	91(85)
298	1.0	3.6(3)	100	97	74,800	1.6	60(56)
303	1.0	6.7(3)	100	96	77,800	1.5	70(65)

Table 4.7 $H_3B{\cdot}NMeH_2$ dehydropolymerisation conditions and polymer characterisation data using **Rh(L3)H_2Cl** at various temperatures. Typical dehydropolymerisation hydrogen evolution conditions with 1M $H_3B{\cdot}NMeH_2$ (112 mg) in THF_{SPS} and 0.5 mol% **Rh(L3)H_2Cl**. Conversion and selectivity measured by ^{11}B NMR spectroscopy, M_n and *Đ* measured by GPC relative to polystyrene standards.

4.2.25 Speciation Study on Rh(L3)H_2Cl

To confirm the absence of an induction period observed with **Rh(L3)H_2Cl** was due to this complex rapidly activating to the on cycle resting state a speciation study was

performed. This study used **Rh(L3)H_2Cl** (1 mol%) as a pre-catalyst for the dehydropolymerisation (THF, 20 °C) of $H_3B{\cdot}NMeH_2$ (1 M) and was led by Dr Claire Brodie. This used the same sampling method as described in Section 4.2.15. A comparison of the speciation using **Rh(L3)H_2Cl** vs **[Rh(L3)NBD]Cl** as pre-catalysts for dehydropolymerisation as followed by $^{31}P\{^1H\}$ is presented Figure 4.23. Following the reaction by $^{31}P\{^1H\}$ NMR spectroscopy it was determined that at the start of catalysis **Rh(L3)H_2Cl** was rapidly converted to ~85% **Rh(L3)H_3($H_3B{\cdot}NMeH_2$)** with ~15% **Rh(L3)H_2Cl** remaining (Figure 4.23). This rapid conversion to the resting state of catalysis would explain the immediate H_2 evolution and absence of an induction period for **Rh(L3)H_2Cl**. This ratio remained constant throughout the dehydropolymerisation. At the end of catalysis **Rh(L3)H_3($H_3B{\cdot}NMeH_2$)** was rapidly converted back to only **Rh(L3)H_2Cl**. **Rh(L3)H_2Cl** is activated to **Rh(L3)H_3($H_3B{\cdot}NMeH_2$)** much more rapidly than **[Rh(L3)NBD]Cl**. This explains the presence of an induction period for **[Rh(L3)NBD]Cl** but not **Rh(L3)H_2Cl**. Additionally, when using **Rh(L3)H_2Cl** as a pre-catalyst, a higher proportion of the resting state **Rh(L3)H_3($H_3B{\cdot}NMeH_2$)** was observed throughout catalysis. As a result of both faster activation and a higher concentration of active catalyst resting state, dehydropolymerisation using **Rh(L3)H_2Cl** pre-catalyst would be predicted to have a higher rate of turnover as observed in the kinetics.

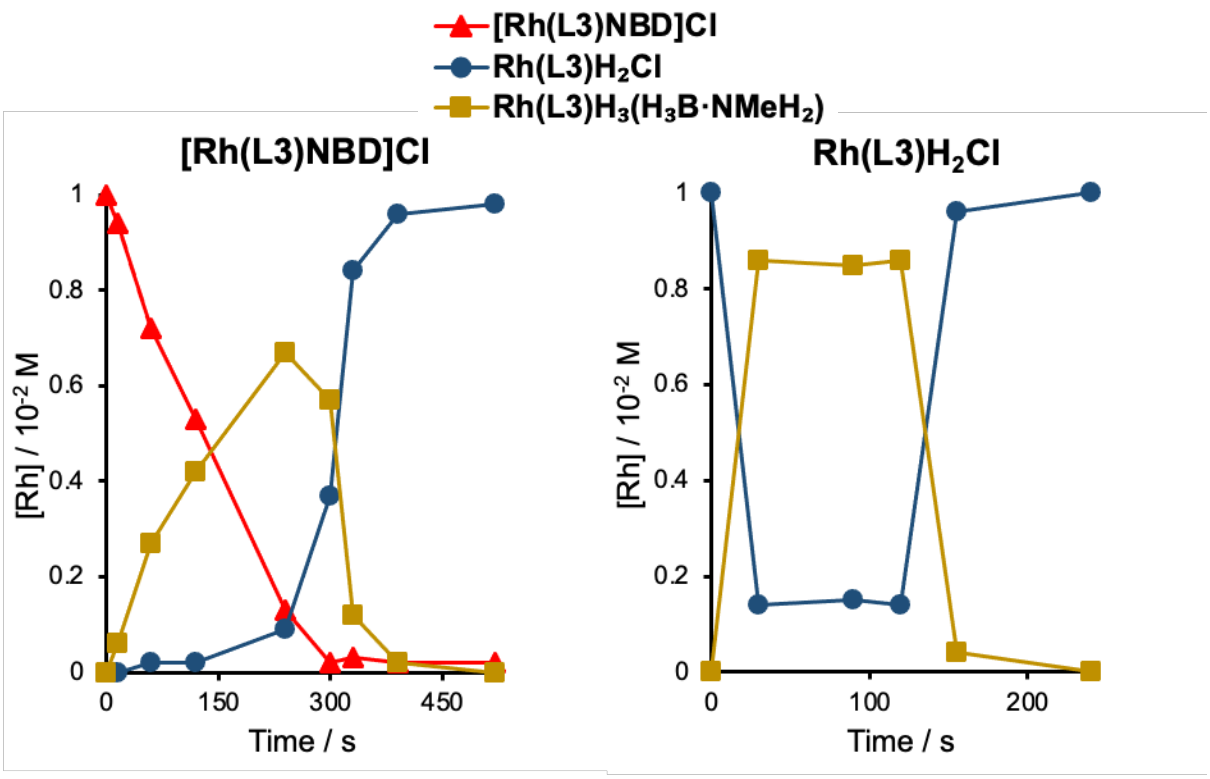
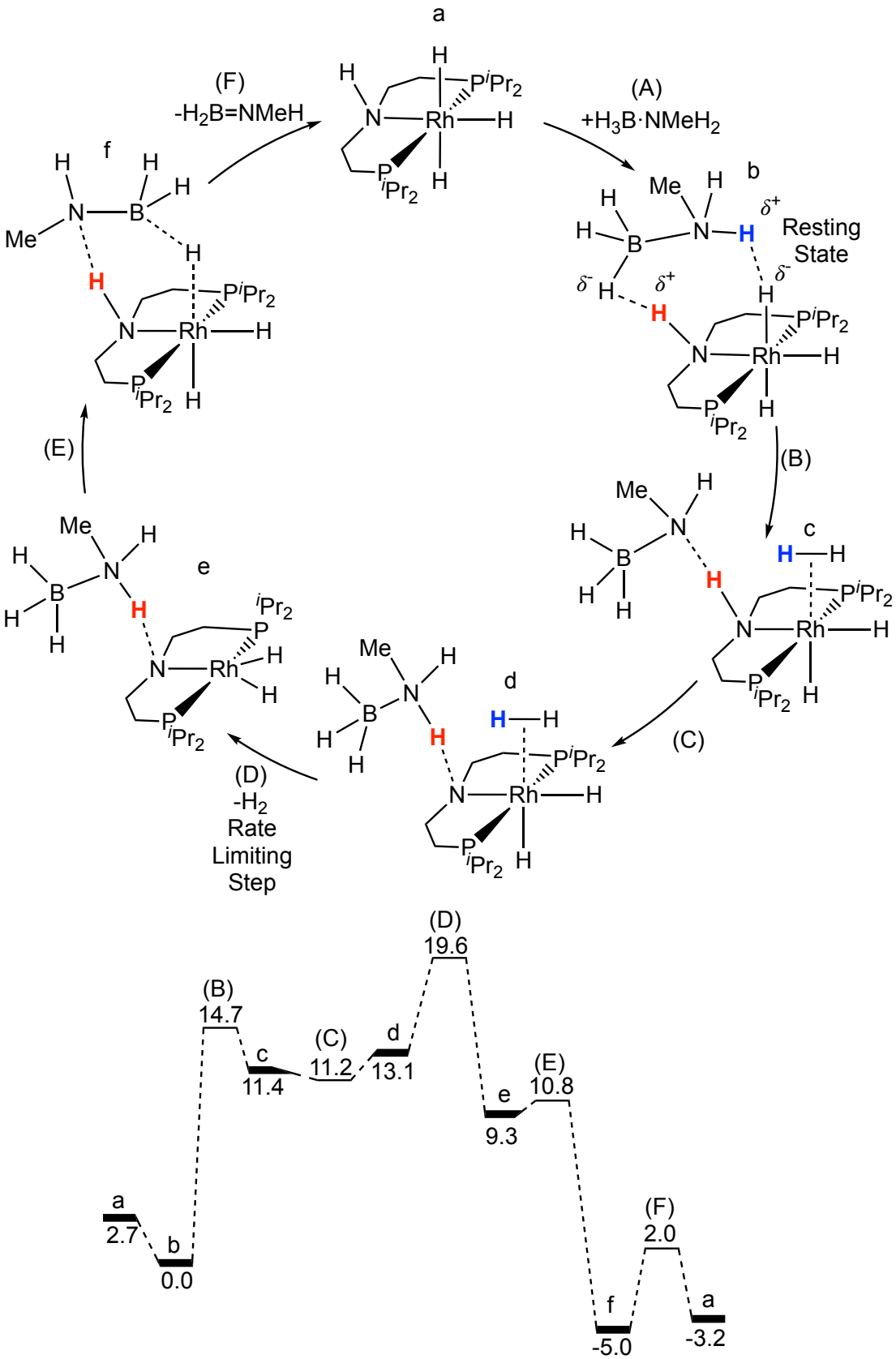


Figure 4.23 Concentrations of metal containing species in dehydropolymerisation (THF, 20 °C) of $H_3B{\cdot}NMeH_2$ (1 M) using **Rh(L3)H_2Cl** or **[Rh(L3)NBD]Cl** (1 mol%) as a pre-catalyst. The concentrations were determined by ^{31}P NMR analysis of aliquots of the reaction mixture. Lines between data points drawn to help guide the eye.

4.2.26 Computational studies

With the speciation data in hand, computational calculations were carried out to develop a suggested mechanistic pathway. These calculations were carried out by Dr Lia Sotorrios in the Macgregor group at Heriot-Watt University. The computationally optimised cycle and energetic profile are presented below in Scheme 4.7. The lowest energy structure is the experimentally observed resting state **Rh(L3)H_3($H_3B{\cdot}NMeH_2$)**. Losing H_2 in step (D) gives the highest energy transition state which is 19.6 kcal mol^{-1} above the resting state. This is within reasonable agreement with the experimentally measured $\Delta G^{\ddagger}_{293K}$ = 17(3) kcal mol^{-1} for **Rh(L3)H_2Cl** and $\Delta G^{\ddagger}_{293K}$ = 17.7(12) kcal mol^{-1}

for **[Rh(L3)NBD]Cl**. Getting from the resting state to this transition state involves pre-equilibria steps (B) and (C); prior to the turn over limiting step (D). Step (B) has the individual biggest barrier and this step is deprotonation of the amine-borane by the rhodium hydride at 14.7 kcal mol^{-1} to form a dihydrogen dihydride complex which is hydrogen bound to the deprotonated amine borane through the backbone N-H. Step (C) is a proton transfer from the ligand NH to the deprotonated amine-borane and this has no appreciable barrier. Finally, step (D) is H_2 loss with a barrier of 5.5 kcal mol^{-1}. Together steps (B), (C) and (D) will define the reaction rate. This reaction mechanism would have a rate equation for catalytic turnover that is zero order in $[H_3B{\cdot}NMeH_2]$ and first order in [Cat], as was observed in the experimentally measured kinetics. Expected KIEs for the deuterated amine-boranes $H_3B{\cdot}NMeD_2$ and $D_3B{\cdot}NMeH_2$ were calculated to be 4.5 and 1.0 respectively, and the next few sections shall compare these to experimentally measured results.



Scheme 4.7 Computationally proposed catalytic cycle and corresponding energetic profile.

4.2.27 Determination of kinetic isotope effects using [Rh(L3)NBD]Cl

Dehydropolymerisation of the deuterated amine-boranes $H_3B{\cdot}NMeD_2$ and $D_3B{\cdot}NMeH_2$ enabled the determination of kinetic isotope effects (KIE) from eudiometer kinetic measurements (Figure 4.24).[27] KIEs were determined by using the rates of the linear parts of the kinetic trace. Using **[Rh(L3)NBD]Cl** as a pre-catalyst for the dehydropolymerisation (0.5 mol%, THF, 20 °C) of $H_3B{\cdot}NMeD_2$ (1 M) gave a long induction period and a significant KIE = 2.5(3) (Table 4.8). This is a significant KIE and suggests ND bond cleavage is important to both the activation process and is included in the rate limiting step, as predicted by the computational analysis. By dehydropolymerisation (0.5 mol%, THF, 20 °C) with $D_3B{\cdot}NMeH_2$ (1 M) a KIE = 1.3(2) was determined and the rate of dehydrogenation notably slowed over the course of the dehydropolymerisation. Due to the presence of both significant tailing and an induction period it was unclear how accurate this KIE was - using **Rh(L3)H_2Cl** gave more insight.

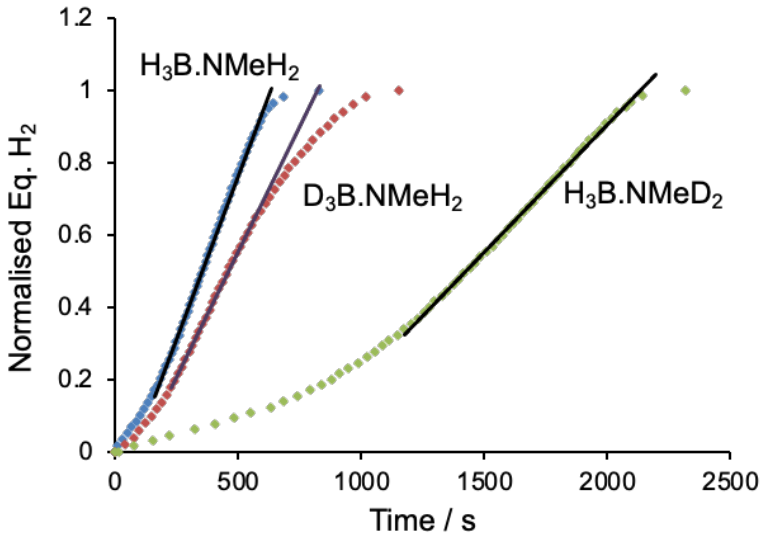


Figure 4.24 Kinetic profile determined using **[Rh(L3)NBD]Cl** as a pre-catalyst for the dehydropolymerisation (0.5 mol% **[Rh(L3)NBD]Cl**, THF, 20 °C) of $H_3B{\cdot}NMeH_2$ $H_3B{\cdot}NMeD_2$ and $D_3B{\cdot}NMeH_2$ (1 M) as monitored by eudiometer. Linear region were used to determine values for KIEs.

4.2.28 Determination of kinetic isotope effects using Rh(L3)H_2Cl

When using $H_3B.NMeD_2$ (1 M) with **Rh(L3)H_2Cl** as the pre-catalyst for dehydropolymerisation (0.5 mol%, THF, 20 ^oC,) a KIE = 2.8(3) was determined from the linear period of the kinetic trace. This KIE is significant and suggests ND bond cleavage is involved in the rate limiting step as seen in the computational calculations. The reaction profile is unremarkable, remaining linear for the vast majority of catalysis (Figure 4.25). Using $D_3B{\cdot}NMeH_2$ (1 M) for dehydropolymerisation (0.5 mol%, THF, 20 ^oC) the kinetic profile no longer has any linear regions which are zeroth order in substrate (Figure 4.25) so initial rates were used to determine a KIE = 1.0(2). With $D_3B{\cdot}NMeH_2$ the KIE was calculated to be 1.0 which is in agreement with the experimental value from initial rates, however caution is required here due to the change in reaction profile. With $H_3B{\cdot}NMeD_2$ the calculated KIE was 4.5, which is higher than the experimentally measured (2.8(3)) value but of similar magnitude and within reasonable agreement. All KIEs are compared in Table 4.8. A change in order in substrate for dehydropolymerisation of deuterated amine boranes was also reported for Schneider's **RuH_2(PMe_3)(L3)** system.[28]

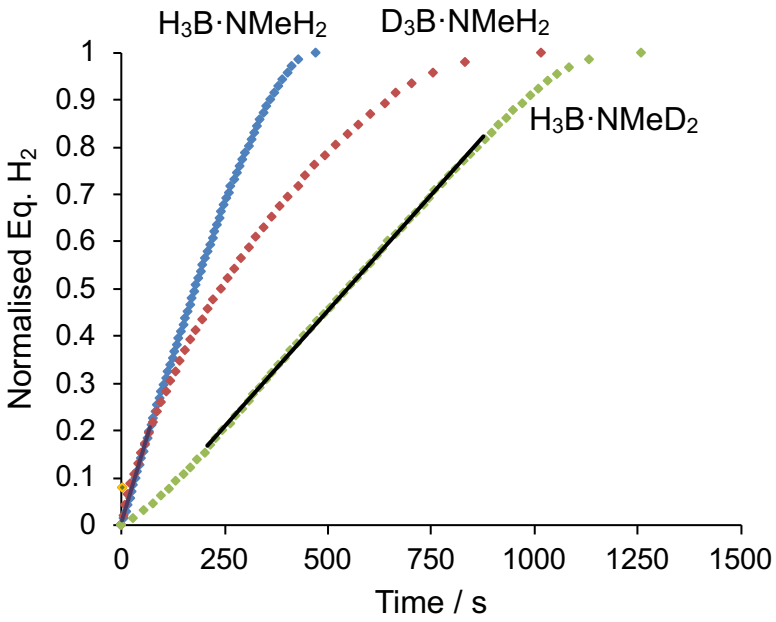


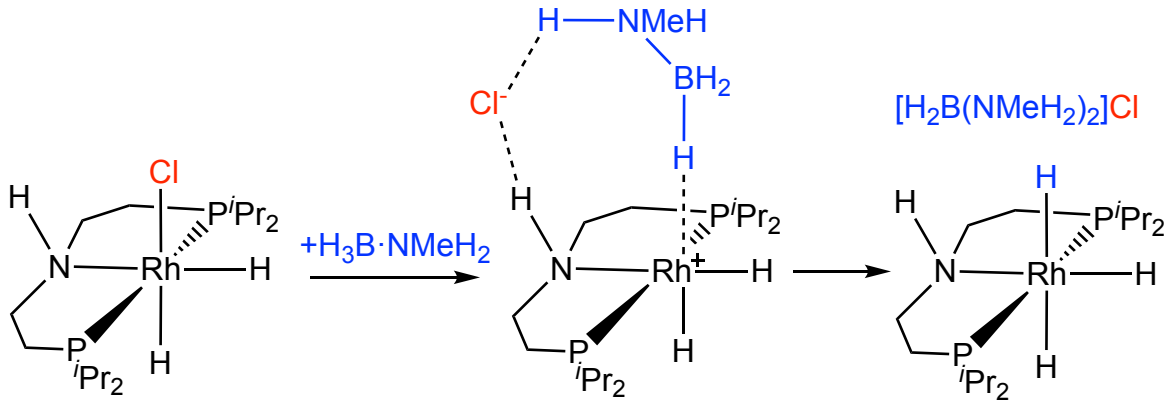
Figure 4.25 Kinetic profile determined using **Rh(L3)H_2Cl** as a pre-catalyst for the dehydropolymerisation (0.5 mol% **Rh(L3)H_2Cl**, THF, 20 °C) of $H_3B{\cdot}NMeH_2$ $H_3B{\cdot}NMeD_2$ and $D_3B{\cdot}NMeH_2$ (1 M) as monitored by eudiometer. Rate of the linear period was used for $H_3B{\cdot}NMeD_2$ while initial rates were used for $D_3B{\cdot}NMeH_2$.

Cat.	Amine-borane	Eq. H_2 evolved	k_{obs} / mMs^{-1}	KIE
[Rh(L3)NBD]Cl	$H_3B{\cdot}NMeH_2$	1.0	1.80(12)	-
[Rh(L3)NBD]Cl	$D_3B{\cdot}NMeH_2$	1.0	1.39(13)	1.3(2)
[Rh(L3)NBD]Cl	$H_3B{\cdot}NMeD_2$	1.0	0.67(5)	2.5(3)
Rh(L3)H_2Cl	$H_3B{\cdot}NMeH_2$	1.0	2.8(2)	-
Rh(L3)H_2Cl[b]	$D_3B{\cdot}NMeH_2$	1.0	2.8(2)	1.0(2)
Rh(L3)H_2Cl[b]	$H_3B{\cdot}NMeD_2$	1.0	0.72(12)	3.9(4)
Computational	$D_3B{\cdot}NMeH_2$	-	-	1.0
Computational	$H_3B{\cdot}NMeD_2$	-	-	4.5

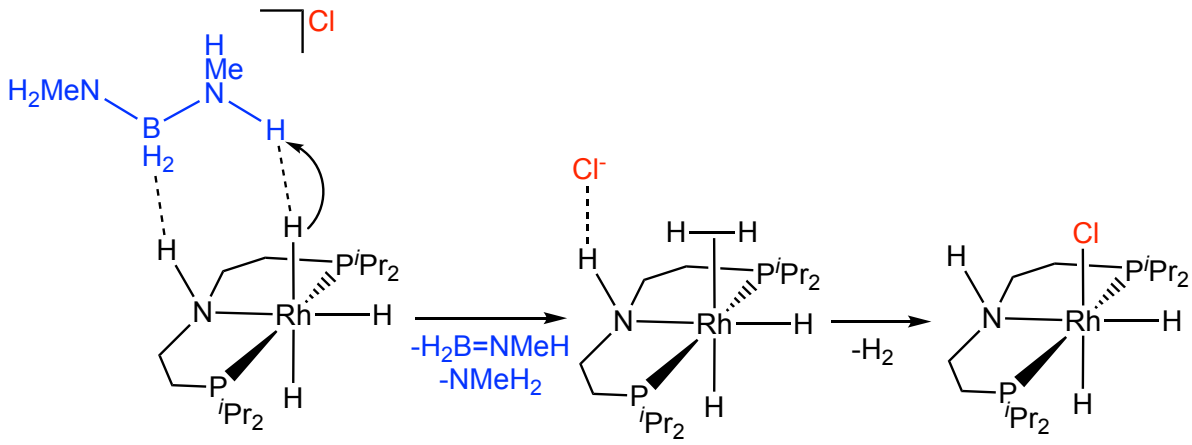
Table 4.8 Effects of isotopic substitution in $H_3B{\cdot}NMeH_2$ on kinetics of hydrogen release on dehydropolymerisation using **[Rh(L3)NBD]Cl** and **Rh(L3)H_2Cl.** Typical dehydropolymerisation hydrogen evolution conditions with 1M amine-borane in THF and 1 mol% cat. [b] calculated using initial rate.

The deviation from zeroth order in $[D_3B{\cdot}NMeH_2]$ could be explained by presence of off cycle reactions to form in active **Rh(L3)H_2Cl**. These processes were described in Section 4.2.17 and Section 4.2.18 and Schemes 4.8 and Scheme 4.9 are provided

below for clarity. First considering B-D bonds: formation of **Rh(L3)H$_3$** from **Rh(L3)H$_2$Cl** requires B-H bond cleavage, meaning a BD/BH KIE might be expected on this step. Meanwhile, returning to **Rh(L3)H$_2$Cl** from **Rh(L3)H$_3$** does not require B-H bond cleavage, so no BD/BH KIE is expected on this. A KIE on the forwards but not return reactions could result in a decreasing concentration of **Rh(L3)H$_3$** throughout the catalysis. This would mean the resting state is gradually shifting from **Rh(L3)H$_3$** to **Rh(L3)H$_2$Cl** throughout catalysis. A change in resting state throughout catalysis would explain the kinetics deviating from zeroth order in [$D_3B{\cdot}NMeH_2$] as the concentration of on cycle catalyst resting state decreased throughout catalysis decelerating the rate of reaction. Now considering N-H bonds: formation of **Rh(L3)H$_3$** from **Rh(L3)H$_2$Cl** is suggested to involve N-H transfer. Therefore a NH/ND KIE on going from **Rh(L3)H$_2$Cl** to **Rh(L3)H$_3$** might be expected. Returning to **Rh(L3)H$_2$Cl** from **Rh(L3)H$_3$** also requires N-H bond cleavage and so a notable NH/ND KIE might be expected on this step. As both conversion from **Rh(L3)H$_2$Cl** to **Rh(L3)H$_3$** and the return reaction involve NH cleavage it is suggested that dehydropolymerisation using $H_3B{\cdot}NMeD_2$ will not have a significant influence on the [**Rh(L3)H$_2$Cl**]:[**Rh(L3)H$_3$**] ratio throughout catalysis, and hence the kinetics should remain zeroth order in [$H_3B{\cdot}NMeH_2$].



Scheme 4.8 Activation pathway for **Rh(L3)H$_2$Cl** to **Rh(L3)H$_3$**



Scheme 4.9 Reformation of **Rh(L3)H_2Cl** at the end of catalysis.

To test this hypothesis speciation studies were carried in collaboration with Dr Claire Brodie using **Rh(L3)H_2Cl** as a pre-catalyst for the dehydropolymerisation (1 mol%, THF, 20 °C) of $H_3B{\cdot}NMeH_2$, $D_3B{\cdot}NMeH_2$ and $H_3B{\cdot}NMeD_2$ ([amine-borane] = 1 M) the results of which are shown in Figure 4.26. Speciation experiments were carried out by freezing aliquots of the reaction mixture then speciation determined by low temperature NMR studies as described in Section 4.2.15. It can be seen that with both $H_3B{\cdot}NMeH_2$ and $H_3B{\cdot}NMeD_2$ the concentration of **Rh(L3)H_3** remains high until the end of catalysis at which point **Rh(L3)H_2Cl** is rapidly formed, consistent with the zeroth order kinetics in substrate concentration seen (Figure 4.26). While the concentration of **Rh(L3)H_3** was observed to be higher (9.5(1) vs 8.5(1) mM) with $H_3B{\cdot}NMeD_2$ than with $H_3B{\cdot}NMeH_2$, these values are within error. This is consistent that with $H_3B{\cdot}NMeD_2$ the isotope effect on both the conversion of **Rh(L3)H_2Cl** to **Rh(L3)H_3** and the return approximately cancel resulting in little change in the concentration of on cycle resting state throughout catalysis. With $H_3B{\cdot}NMeD_2$ the concentration of **Rh(L3)H_3** decreases gradually throughout the catalysis (Figure 4.26) while the concentration of **Rh(L3)H_2Cl** increases. This is consistent with the isotope effect on conversion of **Rh(L3)H_2Cl** to

Rh(L3)H$_3$ but not the return resulting in a decrease in the concentration of on cycle resting state throughout catalysis and hence the decelerating kinetic profile observed.

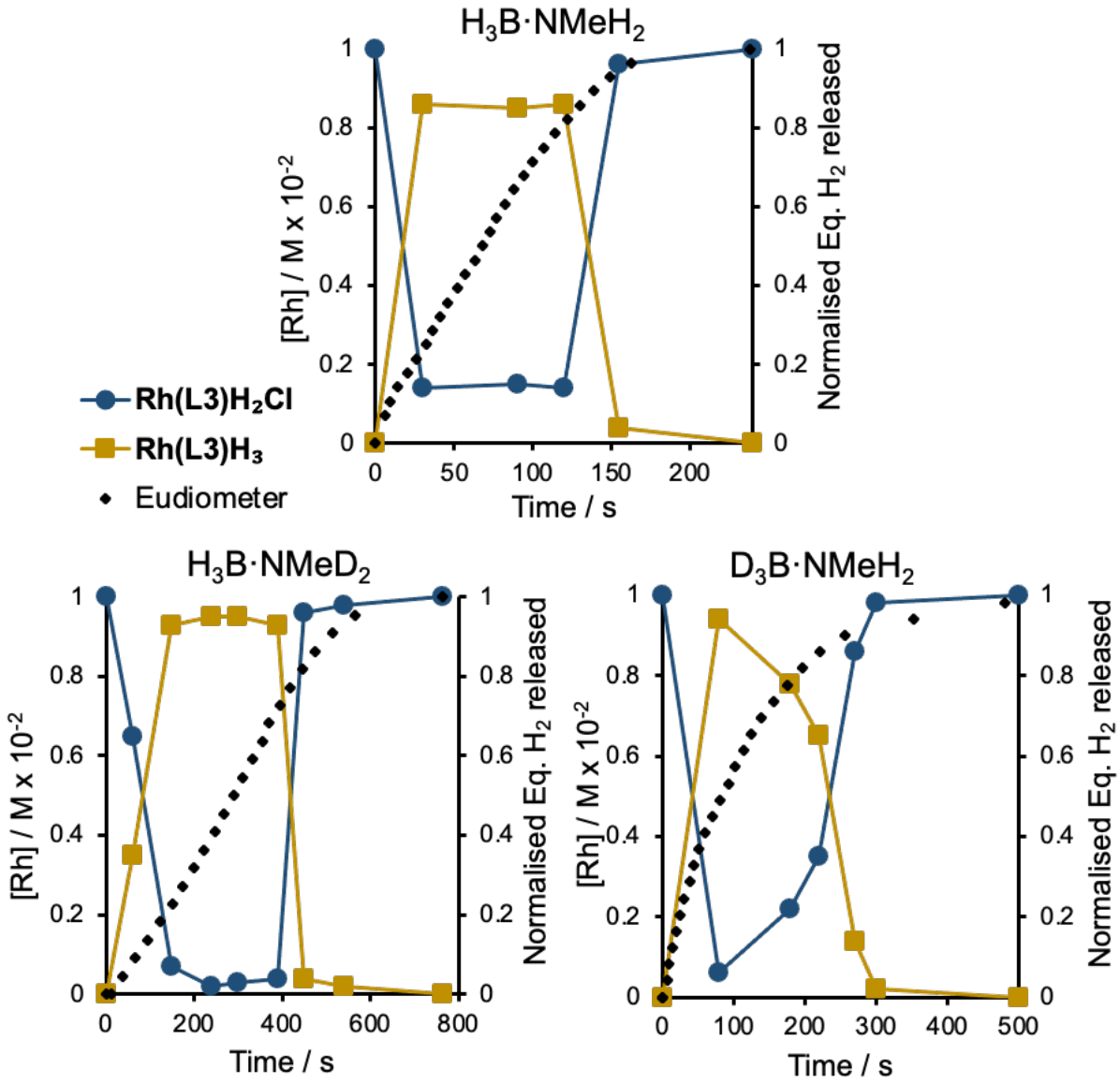
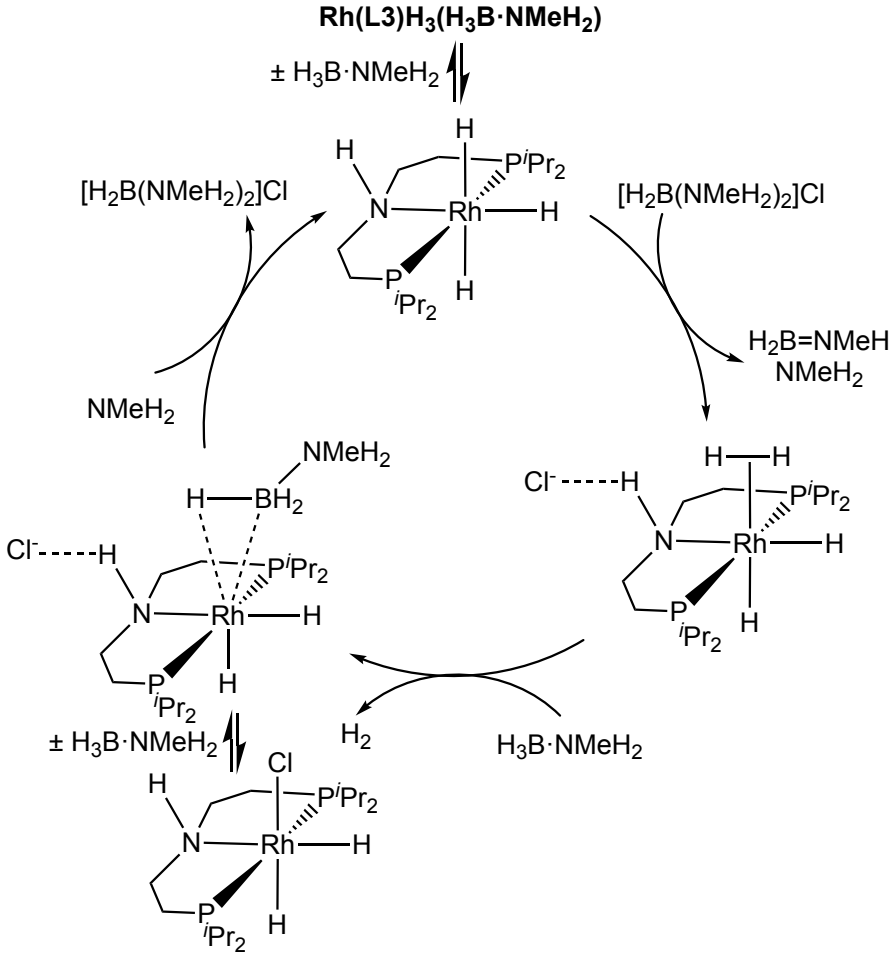


Figure 4.26 Concentrations of metal containing species in dehydropolymerisation (THF, 20 °C) of amine-borane (1 M) using **Rh(L3)H$_2$Cl** (1 mol%) as a pre-catalyst. In (A) the amine-borane is $H_3B{\cdot}NMeH_2$, in (B) $H_3B{\cdot}NMeD_2$ and in (C) $D_3B{\cdot}NMeH_2$. The concentrations were determined by ^{31}P NMR spectra of aliquots of the reaction mixture. Eudiometer data superimposed to show overall reaction progress. It was observed that the using $H_3B{\cdot}NMeH_2$ and $H_3B{\cdot}NMeD_2$ concentration of **Rh(L3)H$_3$** resting state remained high throughout the dehydropolymerisation. When dehydropolymerising $D_3B{\cdot}NMeH_2$ the concentration of **Rh(L3)H$_3$** decreased over the course of the dehydropolymerisation.

4.2.29 Alternative mechanism

These data suggest that the rate of forming **Rh(L3)H_2Cl** from **Rh(L3)H_3** and subsequent return are significant throughout catalysis as in all cases residual **Rh(L3)H_2Cl** was observed at non-negligible concentrations. Taken together these steps could suggest an alternative hydride abstraction / boronium deprotonation type mechanism for the dehydrogenation of amine-borane shown in Scheme 4.10. This mechanism would be analogous to that described in Section 3.1.11 for Conejero's **[Pt(I^{t}Bu′)(I^{t}Bu)][BAr$_4^F$]** complex.[29] Therefore it is important to consider carefully if this is the main method by which catalysis operates.



Scheme 4.10 Alternative hydride abstraction / boronium deprotonation type mechanism for the dehydrogenation of amine-borane.

With **Rh(L3)H$_3$(H$_3$B·NMeH$_2$)** as the resting state the rate law will take the form Rate = k_{obs}[**Rh(L3)H$_3$**][Boronium], if protonation from N-H is rate limiting step as the KIE studies show. [**Rh(L3)H3)**] is will be determined by the equilibrium **Rh(L3)H$_3$** + $H_3B{\cdot}NMeH_2$ ⇌ **Rh(L3)H$_3$(H$_3$B·NMeH$_2$)** and resultantly have an inverse order in [$H_3B{\cdot}NMeH_2$], unlike the pseudo-zeroth order observed. Additionally, [Cat] = [Boronium] due to boronium being generated during catalyst activation. If this cationic mechanism was dominating the kinetics we would expect the rate to be second order in [Cat], but first order was observed. Taken together these results suggest this hydride abstraction / boronium deprotonation type mechanism is not the main operative pathway of dehydropolymerisation. Instead the main operative pathway of catalysis is suggested to be the neutral cooperative pathway computationally calculated in Section 4.2.26, which agrees with all observed experimental results.

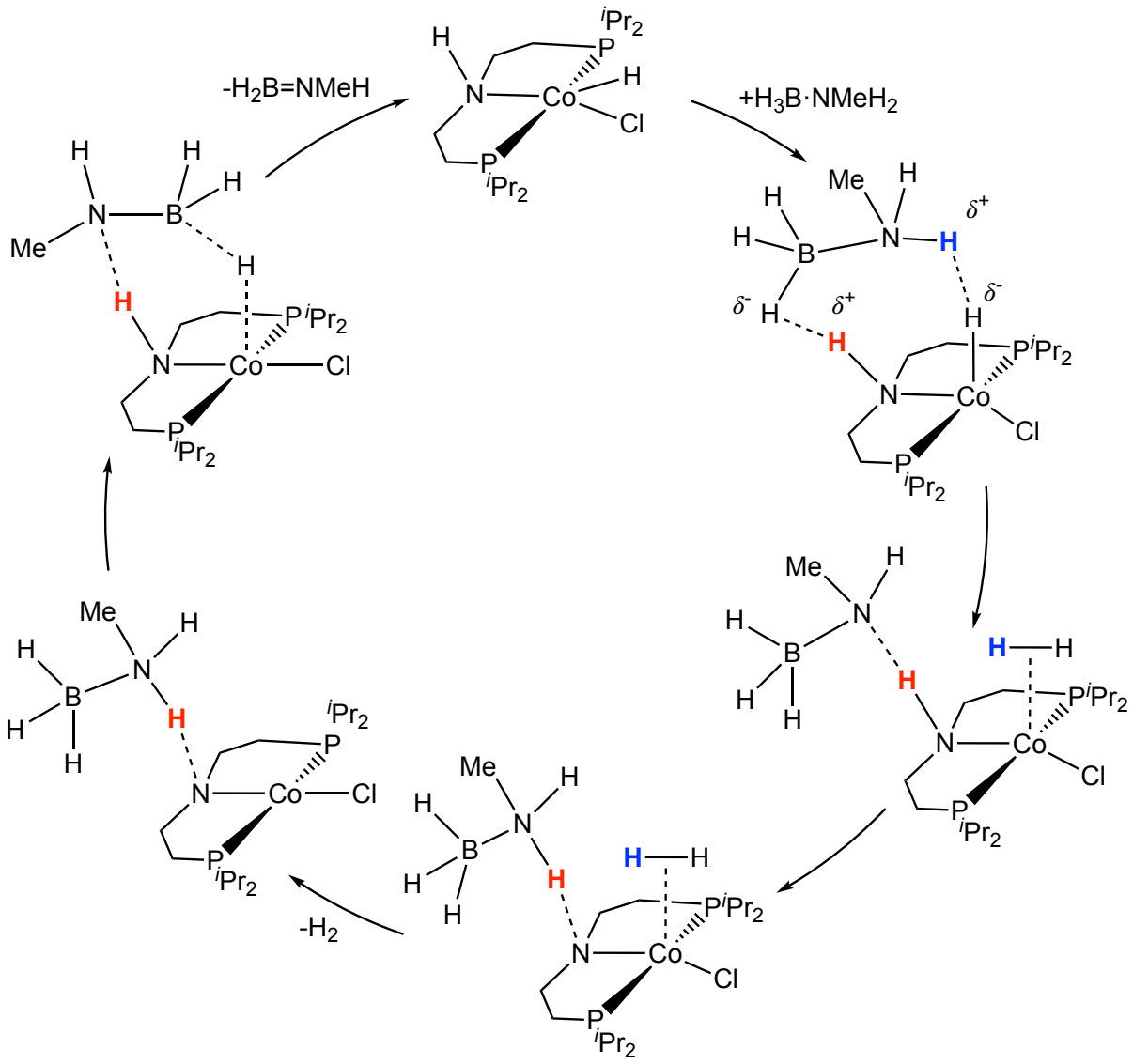
4.2.30 Variation of M_n with catalyst loading

As discussed in Sections 4.2.3 and 4.2.10 M_n of the isolated polymer does not vary with catalyst loading. This lack of variation is distinct from that observed using the cobalt system **Co(L3)Cl$_2$** and cationic rhodium systems such as **[Rh(DPEphos-Ph)(H$_2$B·NMe$_3$(CH$_2$)$_2$^{t}Bu)][BAr^F$_4$]** where the degree of polymerisation decreases with catalyst loading. A Mayo analysis (e.g. Section 3.1.12 and 3.2.11) helps provide further insight into this difference. The Mayo equation shows that the molecular weight of polymer produced should vary with the ratio [$H_2B{=}NMeH_2$]/[CTA]. Here it is assumed that [$H_2B{=}NMeH_2$] is proportional to the rate of dehydrogenation of $H_3B{\cdot}NMeH_2$. Therefore M_n ∝ (rate of dehydrogenation)/[CTA]. For dehydropolymerisation using **[Rh(L3)NBD]Cl**, the rate law for dehydrogenation was determined to take the form

k[Cat] (Section 4.2.8) Therefore, the degree of polymerisation of polymer produced should vary with the ratio $M_n \propto$ k[Cat]/[CTA]. With **Rh(L3)NBD]Cl** one equivalent of CTA (Boronium) is generated for every equivalent of catalyst resting state (Section 4.2.17) so [Cat] = [CTA] . Therefore the ratio [Cat]/[CTA] = 1 and M_n should not change with catalyst loading.

4.2.31 Further mechanistic consideration of the $CoCl_2$(L3) pre-catalyst

With this mechanistic understanding for the **[Rh(L3)NBD]Cl** in hand further consideration of the **$CoCl_2$(L3)** was warranted. Unlike when using **[Rh(L3)NBD]Cl** as a pre-catalyst, increasing the concentration of **$CoCl_2$(L3)** led to a decrease in the molecular weight of isolated polymer. Deviations from first order in catalyst would complicate the analysis in Section 4.2.30 and lead to expected variation in M_n with catalyst loading. With **$CoCl_2$(L3)** a simple rate law for the dehydrogenation could not be determined, it was clearly not a simple first order.[21] The order in catalyst could be expected to be of lower order due to the potential for a rapid endogenic dimer monomer to bridging hydride resting state,[30] or due to the observed hydrogen inhibition altering the rate law of dehydrogenation. Determining the exact cause of the variation with the cobalt system is challenging due to the low catalyst concentrations and paramagnetic nature of the complex, making speciation studies difficult. Whatever the exact cause of the deviation from first order catalysis, the impact on M_n of polymer produced is a clear decrease with increased catalyst loading.



Scheme 4.11 Potential mechanism for dehydropolymerisation of amine-borane using **$CoCl_2$(L3)** warrants further mechanistic investigation.

In Sections 3.2.11-13 considering the effect of chain transfer agent upon molecular weight of polymer produced led to **Co(L3)ClH** type catalysts being suggested to be key to the dehydropolymerisation of amine-borane using **$CoCl_2$(L3)**. If **$CoCl_2$(L3)** pre-catalyst undergoes an analogous mechanism to that proposed with **Rh(L3)NBD]Cl** the mechanism of dehydropolymerisation would be as shown in Scheme 4.11. The only difference between this and the mechanism described in Section 4.2.26 is that the coordination number around the metal centre is one lower throughout the catalytic

cycle. Further investigation into this system would be worthwhile; a combination of kinetics at high concentration in THF, isotope effects, speciation experiments (using UV-vis and EPR) and computational calculations could potentially give a complete mechanistic picture for this system.

4.2.32 Molecular weight control of $(H_2B{\cdot}NMeH)_n$ with boronium doping

In the last few sections of this thesis attention is turned to the ability to use **[Rh(L3)NBD]Cl** as a pre-catalyst to produce polymer with tuneable molecular weights and on large scale. So far in this thesis when using **[Rh(L3)NBD]Cl** as a pre-catalyst for dehydropolymerisation selective variation of the molecular weight of isolated polymer has not been demonstrated. Changing the molecular weight of the isolated polymer could potentially change its materials properties, therefore, it is important to have a simple way to control the molecular weight of polymer produced. As described in Section 3.1.12 boronium is suggested to protonate the end of a growing polymer chain and thereby act as a chain transfer agent (CTA). A higher concentration of boronium should give lower molecular weight polymers, therefore addition of boronium to catalytic mixtures was trialled to control molecular weight. Addition of $[H_2B(NMe_2H)_2]Cl$ (0.23, 0.46, 0.92 and 1.84 mol%) before the start of the polymerisation (0.5 mol% **[Rh(L3)NBD]Cl**, THF, 20 ^oC, $[H_3B{\cdot}NMeH_2]$ = 1 M) decreased the molecular weight of $(H_2B{\cdot}NMeH)_n$ of polymer produced, from M_n = 68,500 g mol^{-1} and $Đ$ = 1.7 with no boronium added to 19,300 g mol^{-1} and $Đ$ = 1.7 with 1.84 mol% added (Table 4.9). These polymerisations were carried out in vials open to air. This was carried out in collaboration with Dr Claire Brodie.

$[BH_2(NMe_2H)_2][Cl]$ / mol%	Conv. / %	Selectivity / %	M_n / g mol^{-1}	M_p / g mol^{-1}	$Đ$	Yield / mg (%)
0.00	100	97	68,500	30,400	1.7	205 (89)
0.23	100	97	58,000	47,300	1.8	203 (95)
0.46	100	96	50,300	68,000	1.6	177 (83)
0.92	100	98	37,900	85,500	1.7	196 (92)
1.84	99	98	19,300	123,100	1.8	182 (86)

Table 4.9 $H_3B{\cdot}NMeH_2$ dehydropolymerisation conditions and polymer characterisation data using **[Rh(L3)NBD]Cl** with various dopant level of $[BH_2(NMe_2H)_2][Cl]$. Typical dehydropolymerisation open conditions (1M $H_3B{\cdot}NMeH_2$ (224 mg) in THF and 0.5 mol% **[Rh(L3)NBD]Cl)**. Conversion and selectivity measured by ^{11}B NMR spectroscopy, M_n and $Đ$ measured by GPC relative to polystyrene standards.

All but the data collected for 1.84 mol% $[H_2B(NMeH_2)_2]Cl$ could be fit to a Mayo plot ($[CTA]/[H_3B{\cdot}NMeH_2]$ vs $1/M_n$, Section 3.2.11) which is shown in Figure 4.27. Note that the concentration of added boronium has been used here for simplicity, and that catalysis without any added boronium will have a concentration present from the activation processes (Section 4.2.17). The GPC trace (Figure 4.27 right) for 1.84 mol% $[H_2B(NMeH_2)_2]Cl$ boronium concentration was observed to have an elevated signal at low molecular weights (MW) (~log(MW) = 3.5) which will influence the determined M_n. This signal suggests there is a significant proportion of low molecular weight oligomers present for 1.84 mol% boronium doping. If instead the M_p values are used (the peak maximum in the chain length distribution) then all data now fits the Mayo equation (Figure 4.27). This suggests that the apparent discrepancy for the 1.84 mol% boronium doping is potentially due to the calibration of the RI detector to polystyrene standards being particularly poor at low molecular weights of polymer, altering the form of the chain length distribution. The short oligomers are potentially more rigid and could have

electrostatic interactions with the columns which may disproportionately affect the low log(MW) segments of the molecular weight distribution. These data suggest a polymerisation mechanism controlled by chain transfer with $[H_2B(NMeH_2)_2]^+$ as described in Section 3.1.12 and 3.2.11. This provides a methodology by which the molecular weight of polymer produced can be tuned by addition of boronium.

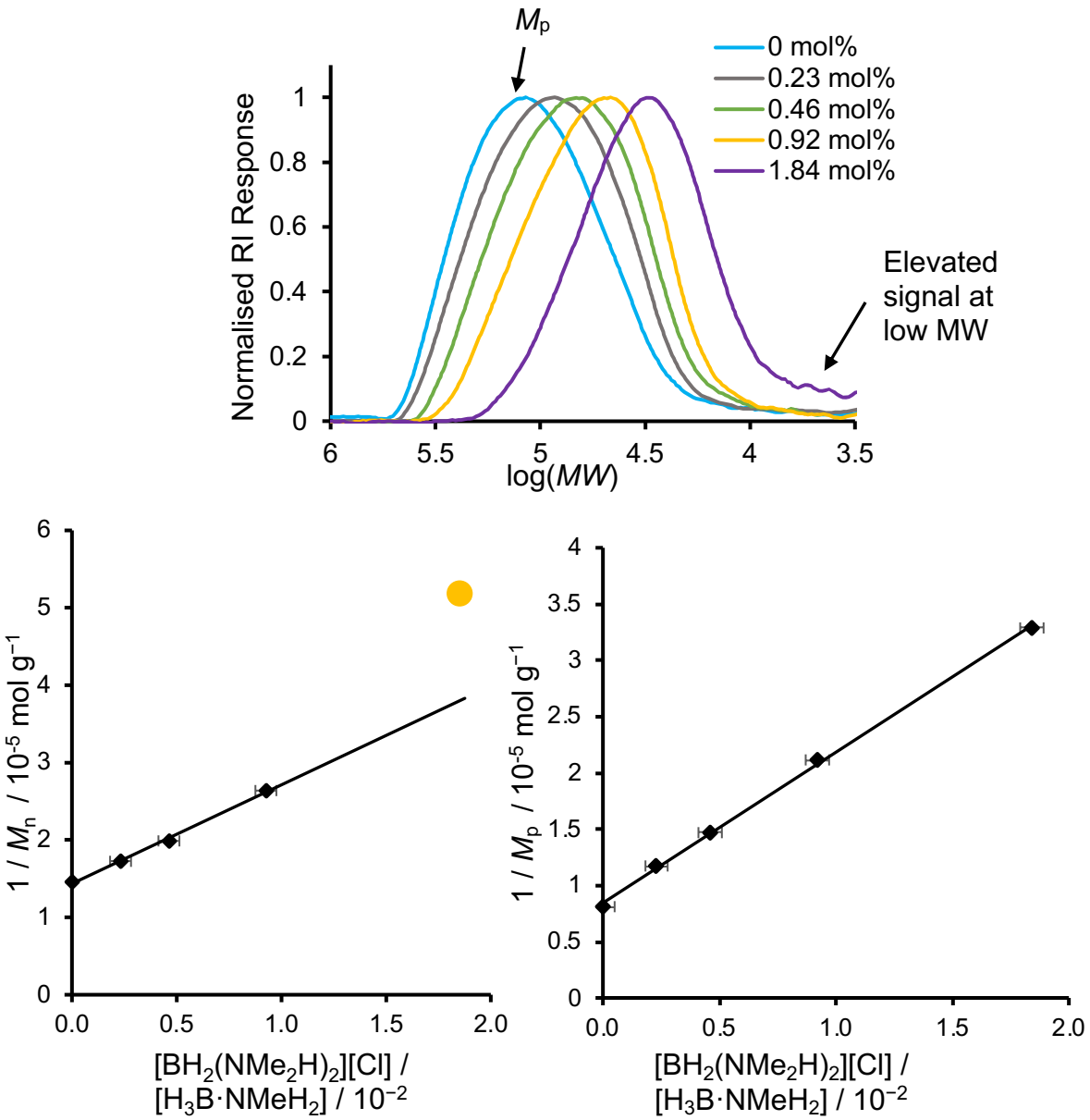


Figure 4.27 Overlayed GPC data (top) for dehydropolymerisation as described in Table 4.9. Mayo plot of for M_n data from Table 4.9 (bottom left). Mayo plot of for M_p data from Table 4.9 (bottom right).Concentration of added boronium was used for these plots.

4.2.33 10 g $H_3B{\cdot}NMeH_2$ scale dehydropolymerisation reaction

Preparing polymer on scale is important to enable the testing of the materials properties of polyaminoboranes. This was carried out in collaboration with Dr Claire Brodie. The practical conditions of air tolerance with a simple pre-catalyst meant that the polymerisation (THF, $[H_3B{\cdot}NMeH_2]$ = 5 M) was readily scaled up to 10 g at the very low catalyst loading of 0.01 mol% **[Rh(L3)NBD]Cl** (Figure 4.28).

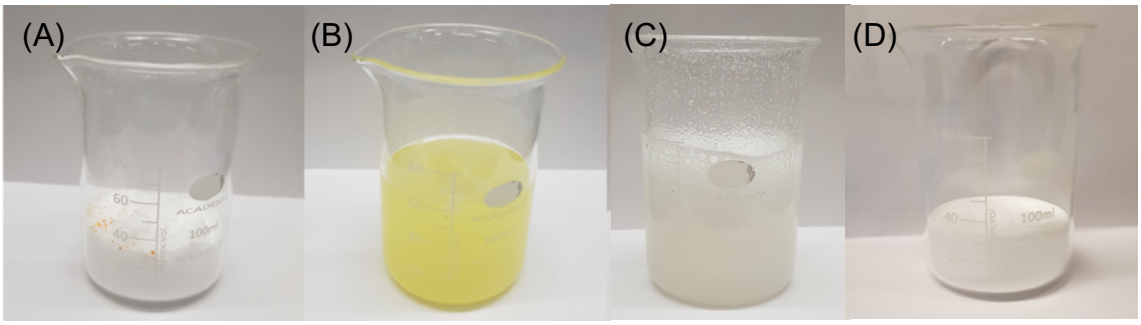


Figure 4.28 10 g scale synthesis of $(H_2B{\cdot}NMeH)_n$ by dehydropolymerisation (0.01 mol% **[Rh(L3)NBD]Cl**, 298 K, 5M $[H_3B{\cdot}NMeH_2]$ in THF (45 mL)). **(A)** 10 g $H_3B{\cdot}NMeH_2$ + 12 mg **[Rh(L3)NBD]Cl**. **(B)** induction period **(C)** productive catalysis ~10 min **(D)** isolated polymer (from precipitation with pentane).

By ^{11}B NMR spectra of an aliquot of the completed reaction it could be observed the dehydropolymerisation had 98% selectivity for the formation of $(H_2B{\cdot}NMeH)_n$ and went to near quantitative conversation (97%). This corresponds to a ToN of 10,000 which is unprecedented for amine-borane dehydropolymerisation. The next highest reported ToN is 5,000 with the **Co(L4)Cl$_2$** system reported in the last chapter.[21] With the third highest ToN = 1,000 with the **[Rh(DPEphos-Ph)(H$_2$BNMe$_3$(CH$_2$)$_2$^{t}Bu)][BAr$^F_4$]** system.[19] GPC analysis of the isolated polymer gave a slightly higher degree of polymerisation M_n = 78,800 g mol^{-1} with $Đ$ unchanged at 1.7 compared to that measured under eudiometer conditions. The process was found to be reproducible, repeating the large scale dehydropolymerisation gave only slight variation in both the

degree of polymerisation of polymer produced and the selectivity of the catalysis (Table 4.10). By providing a reasonable amount of $(H_2B{\cdot}NMeH)_n$ these large scale polymerisations enable attention to now turn to investigating the materials properties and processing of polyaminoborane, opening an exciting new chapter in polyaminoborane chemistry.

Conversion / %	Selectivity / %	M_n / g mol^{-1}	$Đ$	Yield / g (%)
92	>99	82,100	1.7	9.31(98)
97	98	78,100	1.7	9.45(99)
96	98	75,900	1.7	9.21(96)

Table 4.10 Repetitions of using pre-catalyst **[Rh(L3)NBD]Cl** to dehydropolymerise (5.0 M $H_3B{\cdot}NMeH_2$, THF) $H_3B{\cdot}NMeH_2$ on a 10 g scale. Conversion and selectivity measured by ^{11}B NMR spectroscopy, M_n and $Đ$ measured by GPC relative to polystyrene standards.

4.3 Conclusions

In this chapter I have reported on a simple controlled polymerisation of $H_3B{\cdot}NMeH_2$ to selectively form well defined polyaminoborane. This procedure can be carried out on scale using a robust catalyst. **Rh(L3)NBD]Cl** is durable pre-catalyst and polymerisation can be carried out open to air. The molecular weight of polymer produced can be controlled by doping the reaction mixture with boronium. A catalytic cycle has been determined through the combination of speciation, kinetic and computational data and this combination has given a complete mechanistic picture. The ability to prepare $(H_2B{\cdot}NMeH)_n$ on scale has enabled attention to turn to the processing of this novel material. A range of polymer processing methods are currently being employed by Dr Claire Brodie and collaborators in the Haddleton group (University of Warwick) from drop-casting, melt extrusion, and electrospray.

4.4 References

(1) Dallanegra, R.; Robertson, A. P. M.; Chaplin, A. B.; Manners, I.; Weller, A. S. *Chem. Commun.* **2011**, *47* (13), 3763–3765.
(2) Adams, G. M.; Colebatch, A. L.; Skornia, J. T.; McKay, A. I.; Johnson, H. C.; Lloyd-Jones, G. C.; Macgregor, S. A.; Beattie, N. A.; Weller, A. S. *J. Am. Chem. Soc.* **2018**, *140* (4), 1481–1495.
(3) Ryan, D. E.; Andrea, K. A.; Race, J. J.; Boyd, T. M.; Lloyd-Jones, G. C.; Weller, A. S. *ACS Catal.* **2020**, *10* (14), 7443–7448.
(4) Kumar, A.; Beattie, N. A.; Pike, S. D.; Macgregor, S. A.; Weller, A. S. *Angew. Chemie - Int. Ed.* **2016**, *55* (23), 6651–6656.
(5) Mannu, A.; Drexler, H. J.; Thede, R.; Ferro, M.; Baumann, W.; Rüger, J.; Heller, D. *J. Organomet. Chem.* **2018**, *871*, 178–184.
(6) Fennis, P. J.; Budzelaar, P. H. M.; Frijns, J. H. G.; Orpen, A. G. *J. Organomet. Chem.* **1990**, *393* (2), 287–298.
(7) Marder, T. B.; Fultz, W. C.; Calabrese, J. C.; Harlow, R. L.; Milstein, D. *J. Chem. Soc. Chem. Commun.* **1987**, No. 20, 1543–1545.
(8) Cordero, B.; Gómez, V.; Platero-Prats, A. E.; Revés, M.; Echeverría, J.; Cremades, E.; Barragán, F.; Alvarez, S. *J. Chem. Soc. Dalt. Trans.* **2008**, No. 21, 2832–2838.
(9) Alvarez, S. *Dalt. Trans.* **2013**, *42* (24), 8617–8636.
(10) Johnson, H. C.; McMullin, C. L.; Pike, S. D.; Macgregor, S. A.; Weller, A. S. *Angew. Chemie - Int. Ed.* **2013**, *52* (37), 9776–9780.
(11) Rohonczy, J. **2007**.
(12) Maier, T. M.; Sandl, S.; Shenderovich, I. G.; Jacobi von Wangelin, A.; Weigand, J. J.; Wolf, R. *Chem. - A Eur. J.* **2019**, *25* (1), 238–245.
(13) Bhattacharya, P.; Krause, J. A.; Guan, H. *J. Am. Chem. Soc.* **2014**, *136* (31), 11153–11161.
(14) Jaska, C. A.; Temple, K.; Lough, A. J.; Manners, I. *Chem. Commun.* **2001**, *7* (11), 962–963.
(15) Robertson, A. P. M.; Haddow, M. F.; Manners, I. *Inorg. Chem.* **2012**, *51* (15), 8254–8264.
(16) Dewar, M. J. S.; Jones, R. *J. Am. Chem. Soc.* **1967**, *89* (10), 2408–2410.
(17) Staubitz, A.; Presa Soto, A.; Manners, I. *Angew. Chemie Int. Ed.* **2008**, *47* (33), 6212–6215.
(18) Staubitz, A.; Sloan, M. E.; Robertson, A. P. M.; Friedrich, A.; Schneider, S.; Gates, P. J.; Günne, J. S. A. Der; Manners, I. *J. Am. Chem. Soc.* **2010**, *132* (38), 13332–13345.
(19) Adams, G. M.; Ryan, D. E.; Beattie, N. A.; McKay, A. I.; Lloyd-Jones, G. C.; Weller, A. S. *ACS Catal.* **2019**, *9* (4), 3657–3666.
(20) Widegren, J. A.; Finke, R. G. *J. Mol. Catal. A Chem.* **2003**, *198* (1–2), 317–341.
(21) Boyd, T. M.; Andrea, K. A.; Baston, K.; Johnson, A.; Ryan, D. E.; Weller, A. S. *Chem. Commun.* **2020**, *56* (3), 482–485.
(22) Glüer, A.; Förster, M.; Celinski, V. R.; Schmedt Auf Der Günne, J.; Holthausen, M. C.; Schneider, S. *ACS Catal.* **2015**, *5* (12), 7214–7217.
(23) Alig, L.; Fritz, M.; Schneider, S. *Chem. Rev.* **2019**, *119* (4), 2681–2751.
(24) Bakhmutov, V. I.; Bianchini, C.; Peruzzini, M.; Vizza, F.; Vorontsov, E. V. *Inorg.*

Chem. **2000**, *39* (8), 1655–1660.
(25) Esteruelas, M. A.; Oliván, M.; Vélez, A. *Inorg. Chem.* **2013**, *52* (9), 5339–5349.
(26) Haibach, M. C.; Wang, D. Y.; Emge, T. J.; Krogh-Jespersen, K.; Goldman, A. S. *Chem. Sci.* **2013**, *4* (9), 3683–3692.
(27) Colebatch, A. L.; Hawkey Gilder, B. W.; Whittell, G. R.; Oldroyd, N. L.; Manners, I.; Weller, A. S. *Chem. - A Eur. J.* **2018**, *24* (21), 5450–5455.
(28) Marziale, A. N.; Friedrich, A.; Klopsch, I.; Drees, M.; Celinski, V. R.; Schmedt Auf Der Günne, J.; Schneider, S. *J. Am. Chem. Soc.* **2013**, *135* (36), 13342–13355.
(29) Roselló-Merino, M.; López-Serrano, J.; Conejero, S. *J. Am. Chem. Soc.* **2013**, *135* (30), 10910–10913.
(30) Fryzuk, M. D.; Ng, J. B.; Rettig, S. J.; Huffman, J. C.; Jonas, K. *Inorg. Chem.* **1991**, *30* (10), 2437–2441.

Chapter 5: Experimental methods

5.1 General methods and chemicals

Chapter 2 and 3 are based on experimental work completed at the University of Oxford, while Chapter 4 was completed at the University of York.

5.1.1 General methods and chemicals – Chapter 2 and 3

All manipulations (unless otherwise stated) were performed under an atmosphere of argon, using standard Schlenk techniques on a dual vacuum/inlet grease-free J. Young tap manifold. All newly prepared and isolated organometallic compounds were stored in an MBraun glovebox under an atmosphere of argon. Glassware was dried in an oven at 140 °C overnight prior to use. *n*-Pentane, *n*-hexane and dichloromethane (CH_2Cl_2) were all dried using an MBraun SPS-800 solvent purification system and degassed by three freeze-pump-thaw cycles. Anhydrous tetrahydrofuran (THF) was distilled under reflux with sodium metal and benzophenone under a nitrogen atmosphere and stored over activated 3 Å molecular sieves for 24 hours before use. Deuterated dichloromethane (CD_2Cl_2) was purchased from Cambridge Isotope Laboratories Inc, dried by stirring over CaH_2 overnight before being vacuum distilled, subsequently degassed by three freeze-pump-thaw cycles and then stored over activated 3 Å molecular sieves. 1,2-difluorobenzene (1,2-$F_2C_6H_4$) and fluorobenzene (C_6H_5F) were stirred over aluminium oxide (Al_2O_3) for two hours, filtered and then stirred over CaH_2 overnight before being vacuum distilled, subsequently degassed by three freeze-pump-thaw cycles and stored over 3 Å molecular sieves. **$CoCl_2$** was purchased from Sigma-Aldrich and dried at 160 ^oC for 48 hours prior to use. Norbornadiene (bicyclo[2.2.1]hepta-2,5-diene, abbreviated as NBD) was purchased

from Sigma-Aldrich, stirred with freshly cut small pieces of sodium metal for 24 hours and then vacuum distilled, subsequently degassed by three freeze-pump-thaw cycles and store over activated 3 Å molecular sieves. The chelating phosphines 1,2-bis (dicyclohexylphosphino)ethane (dcpe, L1), and 1,4-bis(dicyclohexylphosphino)butane (dcpb, L2) were purchased from Sigma-Aldrich, stored in an MBraun glovebox under an argon atmosphere and used as received. Sodium tetrakis[3,5-bis(trifluoromethyl)phenyl]borate[1] ($Na[BAr^F_4]$, Ar^F = 3,5-$(CF_3)_2C_6H_3$) was stored in a MBraun glovebox under an argon atmosphere and used as a crystalline solid. High purity hydrogen gas (99.9%) was employed in the solid/gas and solution/gas transformations. $H_3B{\cdot}NMeH_2$ was purchased from Boron Specialities and recrystallised from Et_2O at -18 °C, except in scale-up experiments where it was used as received. PPh_3 was purchased from Sigma-Aldrich and used as received. $(^iPr_2PCH_2CH_2)_2NH$ (L3) 10 wt. % in THF was purchased from Sigma Aldrich and freeze pump thaw degassed prior to use. $(Cy_2PCH_2CH_2)_2NH$ (L4) was purchased from Sigma Aldrich and used as received. Methylamine (2 M in THF) was purchased from Sigma Aldrich and used as received. **$CoCl_2(^iPr_2PCH_2CH_2)_2NH$**,[2] **$CoCl(Cy_2PCH_2CH_2)_2NH$**,[3] **$CoCl(^iPr_2PCH_2CH_2)_2N$**,[2] **$CoCl(^iPr_2PCH_2CH_2)_2NH$**[4] and $(^iPr_2PCH_2CH_2)_2NMe$[5] were prepared by literature methods. All other chemicals were purchased from commercial sources and used as received. Elemental analyses were conducted by Mr Stephan Boyer at London Metropolitan University.

5.1.2 General methods and chemicals – Chapter 4

All manipulations, unless otherwise stated, were performed under an argon atmosphere using standard Schlenk line and glove-box techniques. Glassware was oven-dried at 130 °C overnight and flamed under vacuum prior to use. CH_2Cl_2 and

pentane were dried using a Grubbs-type solvent purification system (Innovative Technologies SPS) and degassed by three successive freeze-pump-thaw cycles. C_6D_6, CD_2Cl_2 and 1,2-$C_6H_4F_2$ (pre-treated with alumina) were dried over CaH_2, vacuum distilled, freeze-pump-thaw degassed and stored over 3 Å molecular sieves. $THF_{(Na)}$ (pre-treated over KOH) was distilled from sodium/fluorenone, freeze-pump-thaw degassed and stored over 3 Å molecular sieves. $THF_{(SPS)}$ was obtained using a Grubbs-type solvent purification system (IT SPS) and freeze-pump-thaw degassed and stored over 3 Å molecular sieves. $[Rh(NBD)Cl]_2$,[6] $H_3B{\cdot}NMeD_2$,[7] $D_3B{\cdot}NMeH_2$,[7] $[BH_2(NMe_2H)_2][Cl]$[8] and $(^iPr_2PCH_2CH_2)_2NMe$[5] were prepared by literature methods. $(^iPr_2PCH_2CH_2)_2NH$ (10% wt. solution in THF) was degassed and stored over 3 Å molecular sieves before use. Elemental microanalyses were performed by Graeme McAllister at the University of York.

5.1.3 NMR spectroscopic data – Chapter 2 and 3

Solution NMR data were collected on either a Bruker Avance III NMR spectrometer (equipped with an 11.75 T magnet) or a BrukerAvance III HD nanobay NMR spectrometer (equipped with a 9.4 T magnet) at 298 K unless otherwise stated. Variable Temperature (VT) NMR experiments at low temperatures were externally calibrated to observe the chemical-shift separation between the OH and CH_3 resonances in methanol. Non-deuterated solvents were locked to either standard external neat CD_2Cl_2 or 10% fluorobenzene in C_6D_6 samples. Residual protio solvent resonances were used as a reference for ^1H NMR spectra. A small amount of CD_2Cl_2 was added as a reference for ^2H NMR spectra. $^{31}P\{^1H\}$ NMR spectra were referenced externally to 85% H_3PO_4 (D_2O). $^{19}F\{^1H\}$ NMR spectra were referenced externally to a 1% $CFCl_3$ sample in $CHCl_3$. $^{11}B\{^1H\}$ NMR spectra were referenced externally to a 5%

$BF_3{\cdot}OEt_2$ sample in C_6D_6. All chemical shifts (d) are quoted in ppm and coupling constants (J) in Hz. In general, solution ^{19}F and ^{11}B NMR resonances for all the compounds reported are not included since they comprise of a single resonance at d -62.9 ppm and -6.5 ppm, respectively, corresponding to the $[BAr^F{}_4]^-$ anion. Magnetic susceptibility measurements were performed in CD_2Cl_2 according to the Evans NMR method.[9]

5.1.4 NMR spectroscopic data – Chapter 4

NMR spectra were recorded on a Bruker Avance III 500 MHz NMR spectrometer or a Bruker Ultra-shield 600 MHz NMR spectrometer at 298 K unless otherwise specified. Residual protio solvent was used as reference for ^1H NMR spectra in deuterated solvent samples. $^{31}P\{^1H\}$ NMR spectra were externally referenced to 85% H_3PO_4. ^1H assignments were aided by $^1H\{^{31}P\}$ experiments. All chemical shifts (δ) are quoted in ppm and coupling constants (*J*) in Hz. For NMR spectrometric samples in 1,2-$F_2C_6H_4$ solvent, ^1H NMR spectra were pre–locked to a sample of C_6D_6 (25%) and 1,2-$F_2C_6H_4$ (75%) and referenced to the centre of the downfield solvent multiplet, δ = 7.07.

5.1.5 Mass spectrometry data

Electrospray ionisation mass spectrometry (ESI-MS) was carried out using a Bruker MicroTOF instrument directly connected to a modified Innovative Technology glovebox.[10] Typical acquisition parameters were used (sample flow rate: 4 μL min^{-1}, nebuliser gas pressure: 0.4 bar, drying gas: argon at 333 K flowing at 4 L min^{-1}, capillary voltage: 4.5 kV, exit voltage: either 15 or 60 V. The spectrometer was calibrated using a mixture of tetraalkyl ammonium bromides $[N(C_nH_{2n+1})_4]Br$ (n = 2-8, 12, 16 and 18) in dichloromethane. Samples were diluted to a concentration of ca. < 1

× 10^{-6} M in the appropriate solvent (dichloromethane, 1,2-difluorobenzene) before sampling by ESI-MS.

5.1.6 Gel permeation chromatography data

At both the University of Oxford and the University of York Gel Permeation Chromatography (GPC) was performed on a Malvern Viscotek GPCmax chromatograph fitted with a reference index (RI) detector. The triple-column (plus guard column) set-up was contained within an oven (35 °C) and consisted of a porous styrene divinylbenzene copolymer with a maximum pore size of 1,500 Å. THF containing 0.1% w/w (N^nBu_4)Br was used as the eluent at a flow rate of 1.0 mL min^{-1}. Samples were dissolved in the eluent (2.0 mg mL^{-1}), filtered (0.2 μm pore size) and run immediately. The calibration was conducted using a series of monodisperse polystyrene standards (M_n = 474-476,000 $gmol^{-1}$) obtained from Sigma Aldrich.

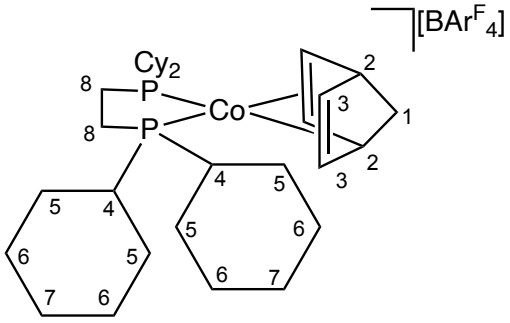
5.2 Chapter 2 experimental data

5.2.1 Synthetic procedures and characterisation data

5.2.1.1 Preparation and characterisation of [Co(L1)NBD][BAr$^F_4$]

One Schlenk flask was charged with **$CoCl_2$** (20 mg, 0.154 μmol) and another with 1,2-bis(dicyclohexylphosphino)ethane (L1, 69.5 mg, 0.154 μmol). Both solids were dissolved in tetrahydrofuran (3 mL each), and the solution containing the phosphine was added dropwise to that of **$CoCl_2$** via cannula with vigorous stirring. The resulting deep blue solution was stirred for 10 minutes before being added dropwise to a solution of $NaBAr^F_4$ (136.5 mg, 0.154 μmol) in tetrahydrofuran (5 mL), which underwent a rapid colour change to a very dark blue solution. Norbornadiene (0.2 mL) was added to the resultant solution. The reaction mixture was stirred at room temperature overnight.

One J. Youngs flask was charged with KC_8 (50 mg, 0.377 μmol) and suspended in tetrahydrofuran (3 mL). The deep blue solution was transferred onto the KC_8 suspension at -78 ^oC, allowed to warm to room temperature and stirred for 2 hours. The remaining graphite was removed by filtration of the resultant green solution, and the solvent removed under vacuum. The resultant green solid was dissolved in dichloromethane (5 mL) and stirred for 5 minutes. *n*-pentane (50 mL) was added to give a lilac suspension which was filtered via cannula. The solid was washed with *n*-pentane (3 x 5 mL), and dried *in-vacuo* (< 5 x 10^{-2} mbar, 45 min), to yield a lilac powder **[Co(L1)NBD][BAr$^F_4$]]** (140 mg, 0.10 μmol 65 % yield). Crystals suitable for X-ray diffraction study were obtained by slow diffusion of *n*-pentane (25 mL) into a solution of the lilac solid (140mg) in dichloromethane (1 ml) in a crystallisation tube fitted with a J. Young valve at room temperature. To give lilac block-like crystals (100 mg, 0.069 μmol, 45 % yield).



^{1}H NMR (400 MHz, CD_2Cl_2, 298 K): δ_H 7.72 (m, 13 H, ortho-BAr$^F_4$), 7.56 (s, 7 H, para-BAr$^F_4$), 4.26 (s, 4H, H-3) 3.91 (s, 2H, H-2), 2.40 (br, d, 4H, H-4) 2.22 (br, t, 4H, H-8), 1.95-1.60 (br, m, 24H, Cy groups), 1.55 (s, 2H, H-1) 1.5-1.15 (br, m, 24H, Cy groups)

^{31}P{^{1}H} NMR (162 MHz, CD_2Cl_2, 298 K): δ_P 61.0 (br, s)

Evans magnetic measurement of a CD_2Cl_2 sample: μ_{eff}(298 K) = 1.5(1) μB.

Magnetic measurement using SQUID magnetometer methods: 2.16 μB.

Elemental analysis found (calculated) for $C_{65}H_{68}B_1F_{24}P_2Co$: C, 54.22 (54.33); H, 4.56(4.77).

ESI-MS m/z: no parent-ion observed.

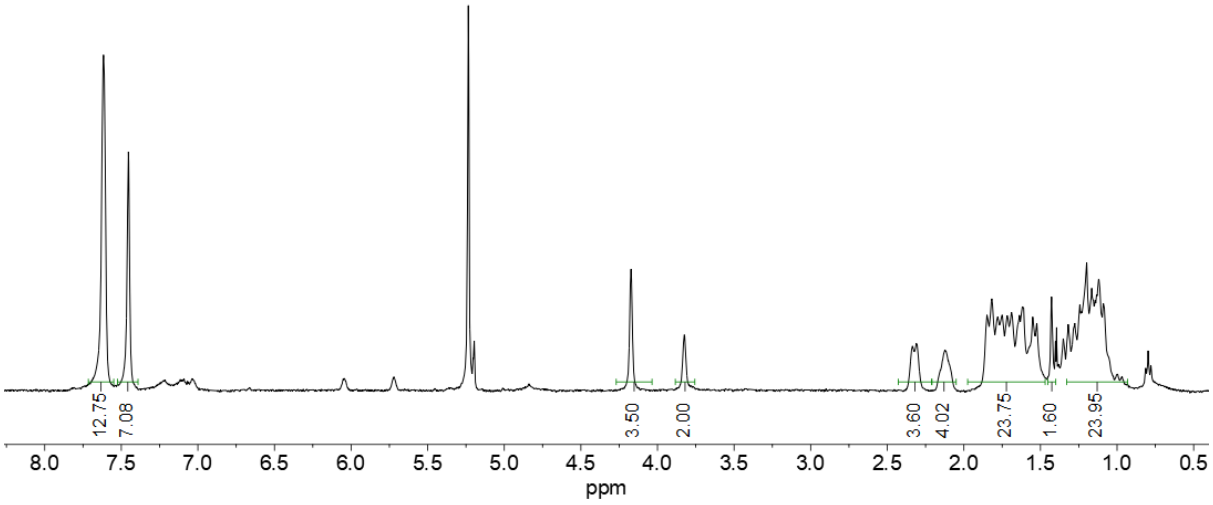


Figure 5.1 The solution ^{1}H NMR (CD_2Cl_2, 298 K, 400 MHz) spectrum of **[Co(L1)NBD][BAr$^{F}_{4}$]**

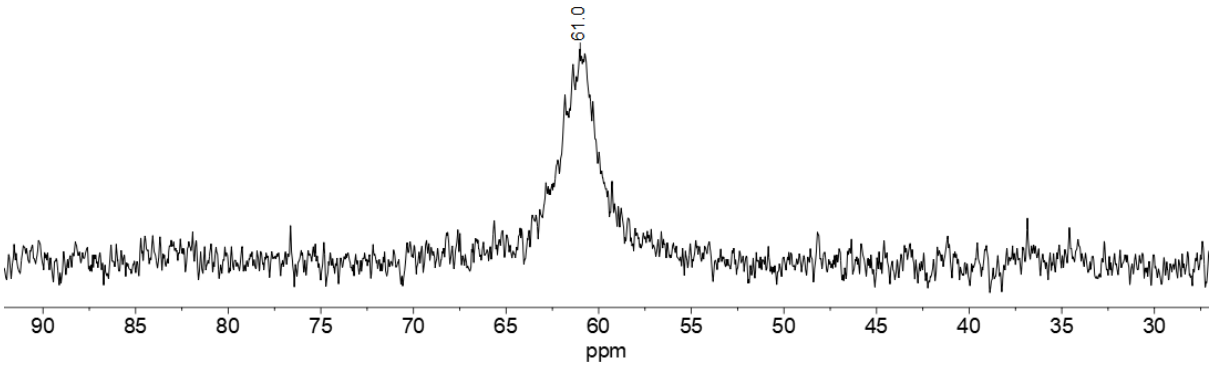
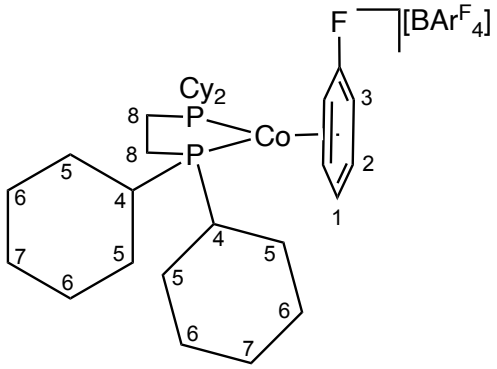


Figure 5.2 The solution $^{31}P\{^{1}H\}$ NMR (CD_2Cl_2, 298 K, 162 MHz) spectrum of **[Co(L1)NBD][BAr$^{F}_{4}$]**

5.2.1.2 Preparation and characterisation of [Co(L1)(η-FC$_6$H$_5$)][BAr$^{F}_{4}$]

One J. Youngs flask was charged with **[Co(L1)NBD][BAr$^{F}_{4}$]** (80 mg, 56 μmol) and dissolved in fluorobenzene (2 ml). The solution was freeze-pump-thaw degassed three times and refilled with H_2 (2 atm), and the solution rapidly changed from lilac to yellow. After stirring for 20 minutes, the solution was freeze-pump-thaw degassed three times and refilled with Ar (1 atm). The solution was transferred via cannula to a crystallisation tube fitted with a J. Young valve, and crystals suitable for X-ray diffraction were

obtained by slow diffusion of *n*-pentane (25 mL) into this solution at room temperature. This yielded brown plates of **[Co(L1)(η-FC$_6$H$_5$)][BAr$^F_4$]** (75 mg, 52 μmol, 90 % yield).



^{1}H NMR (400 MHz, CD_2Cl_2): δ_H 7.77 (m, 8H, ortho-BAr$^F_4$), 7.61 (m, 4H, para-BAr$^F_4$), 6.29 (s, 2H, H-3), 6.15 (s, 2H, H-2), 5.73 (s, 1H, H-1) 1.99 (t, 8H, H-4) 1.90 (s, 2H, H-8), 1.84 (br d, 2H, H-8), 1.69 (br, 14H, H-5), 1.34 (br, 18H, H-6), 1.12 (q, 4H, H-7).

^{31}P{^{1}H} NMR (162 MHz, CD_2Cl_2, 298 K): δ_P 95.5 (s)

^{19}F NMR (376 MHz, THF-d8, 23°C): δ_F -63.43 (s, 24F, BAr$^F_4$), -133.25 (s, 1F, C_6H_5F)

Evans magnetic measurement using of a CD_2Cl_2 sample: μ_{eff}(298 K) = 1.1(1) μB.

Magnetic measurement using SQUID magnetometer methods: 1.61 μB.

Elemental analysis found (calculated) for $C_{64}H_{65}B_1F_{25}P_2Co$: C, 53.22 (53.35); H, 4.46 (4.55).

ESI-MS m/z found (calculated) for C32 H53 Co F P2 [M]$^+$: 577.2937 (577.2933)

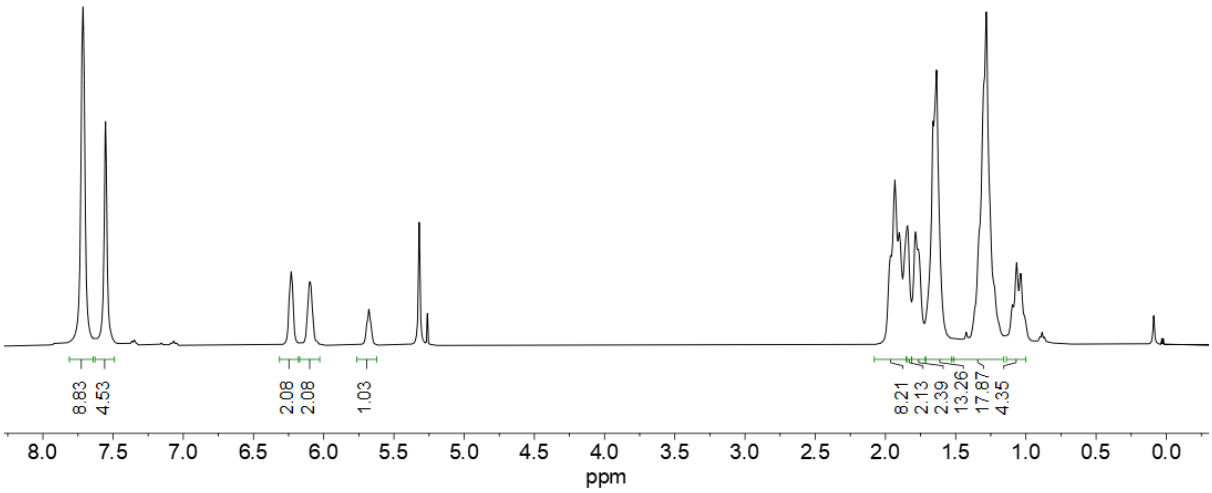


Figure 5.3 The solution ^{1}H NMR (CD_2Cl_2, 298 K, 400 MHz) spectrum of **[Co(L1)(η-FC_6H_5)][BAr^F_4]**

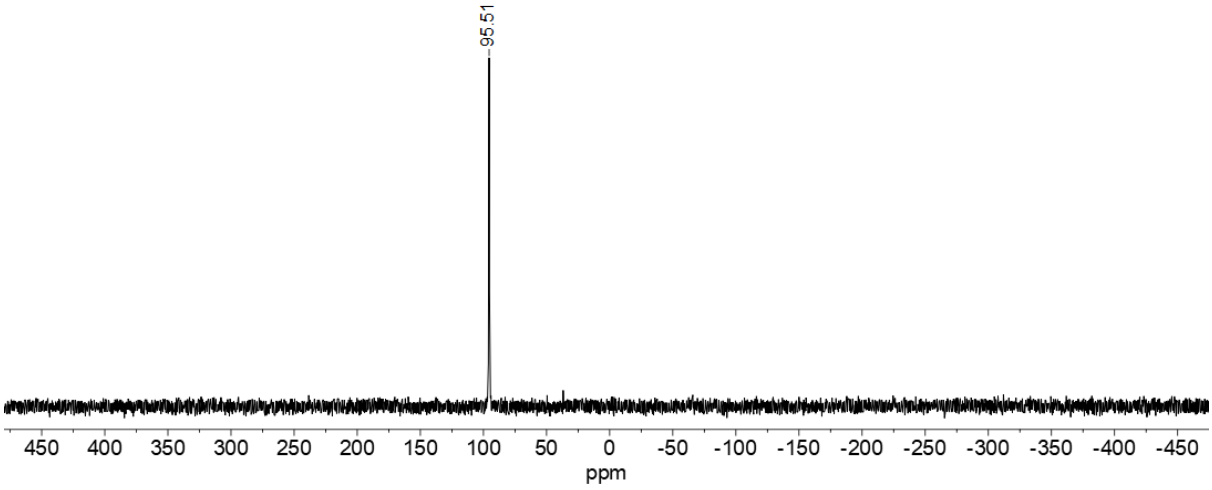


Figure 5.4 The solution $^{31}P\{^{1}H\}$ NMR (CD_2Cl_2, 298 K, 162 MHz) spectrum of **[Co(L1)(η-FC_6H_5)][BAr^F_4]**

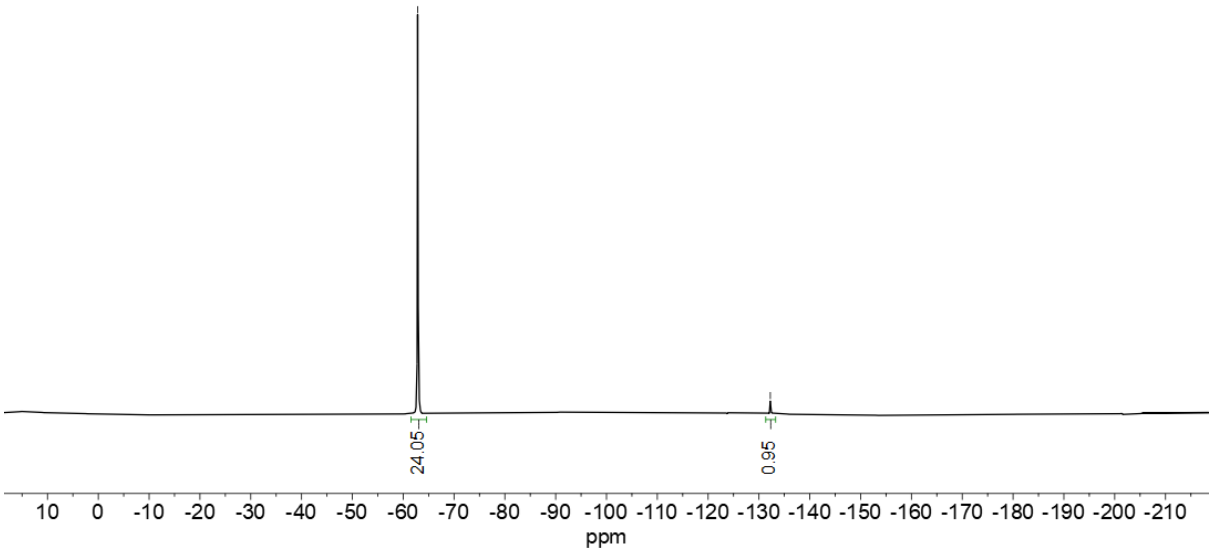


Figure 5.5 The solution $^{19}F\{^{1}H\}$ NMR (CD_2Cl_2, 298 K, 377 MHz) spectrum of **[Co(L1)(η-FC_6H_5)][BAr^F_4]**

5.2.1.3 Preparation and characterisation of [Co(L2)NBD][BAr^F_4]

One J. Youngs flask was charged with **$CoCl_2$** (20 mg, 154 μmol) and another with 1,2-bis(dicyclohexylphosphino)butane (69.5 mg, 154 μmol). Both solids were dissolved tetrahydrofuran (3 mL each), and the solution containing the phosphine was added dropwise to that of **$CoCl_2$** via cannula with vigorous stirring. The resulting deep blue solution was stirred for 10 minutes before being added dropwise to a solution of $NaBAr^F_4$ (136.5 mg, 154 μmol) in tetrahydrofuran (5 mL). Norbornadiene (0.2 mL) was added to the resultant deep blue solution and stirred at room temperature overnight.

One J. Youngs flask was charged with KC_8 (50 mg, 377 μmol) and suspended in tetrahydrofuran (3 mL). The deep blue solution was transferred onto the KC_8 suspension at -78 °C and then allowed to warm to room temperature and stirred for 2 hours. The remaining graphite was removed by filtration of the resultant green solution, and the solvent removed in vacuo. The consequent green solid was dissolved

in dichloromethane (5 mL) at -78 °C and stirred for 5 minutes. *n*-pentane (50 mL) was added to give a dark green suspension which was filtered via cannula. The solid was washed with *n*-pentane (3 x 5 mL) and dried *in-vacuo* (< 5 x 10^{-2} mbar, 45 min) to yield a dark green powder. Crystals of **[Co(L2)NBD][BAr$^{F}_{4}$]** (70 mg, 48 μmol, 31 % yield) suitable for an X-ray diffraction study were obtained by slow diffusion of *n*-pentane (25 mL) into a solution of the green solid in 1,2-difluorobenzene (1 ml).

This procedure was only successful on the provision that all solvents were freshly freeze-pump-thaw degassed, and manipulations were carried out with extreme care.

^{1}H NMR (400 MHz, THF-d_8, 298 K): δ 7.71 (m, 8H, ortho-BAr$^{F}_{4}$), 7.50 (m, 4H, para-BAr$^{F}_{4}$) cation is NMR silent.

^{31}P{^{1}H} NMR: (162 MHz, THF-d_8, 298 K): silent

Evans magnetic measurement of a CD_2Cl_2 sample: μ_{eff}(298 K) 3.2(2) μB.

Magnetic measurement using SQUID magnetometer methods: 3.14 μB

Elemental analysis found (calculated) for $C_{67}H_{72}BF_{24}P_2Co$: C, 54.89 (54.78); H, 5.08 (5.21).

ESI-MS m/z: no parent-ion observed.

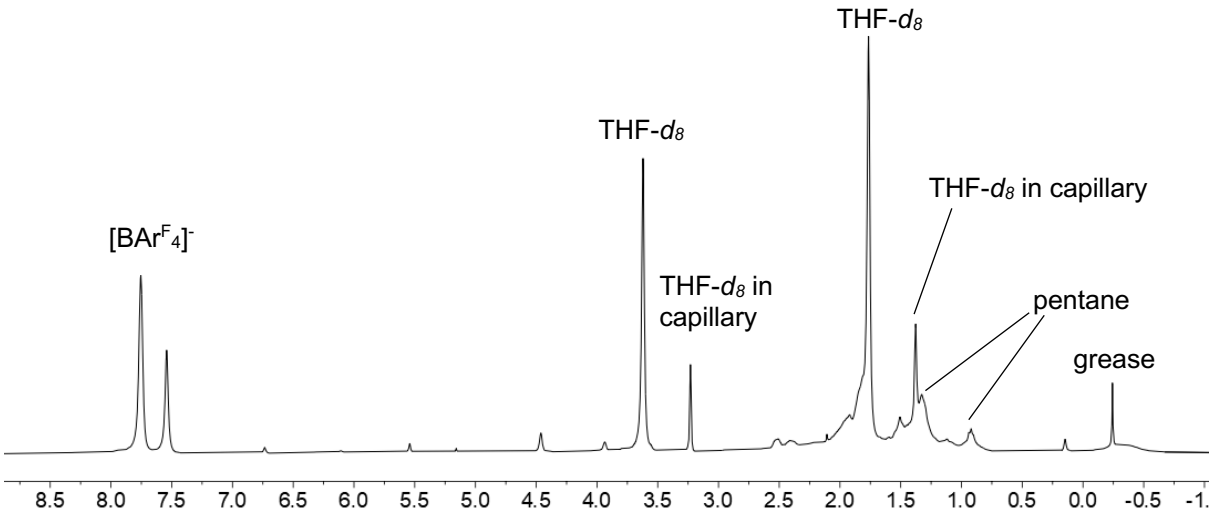


Figure 5.6 The solution ^{1}H NMR (THF-d_8, 298 K, 400 MHz) spectrum of **[Co(L2)NBD][BAr^F_4].** Collected under Evan's measurement conditions.

5.2.1.4 Preparation and characterisation of [Co(L2)NBA][BAr^F_4]

For single-crystal X-ray studies

Crystals of **[Co(L2)NBD][BAr^F_4]** (10 mg) were placed in a J. Youngs NMR tube and exposed to a hydrogen atmosphere (2 bar) for 1 h at room temperature, after which the crystals were rapidly transferred to the diffractometer, and a structure of the **[Co(L2)NBA][BAr^F_4]** could be collected.

For solid-state NMR studies

Crystals of **[Co(L2)NBD][BAr^F_4]** (45 mg) were packed in an uncapped solid-state NMR rotor inside an argon-filled glove box. The rotor was then placed in a custom-built glass J. Youngs flask[11] and exposed to a hydrogen atmosphere (2 bar) for 1 h at room temperature; after this time, the rotor was capped, and the sample immediately transferred to the NMR spectrometer.

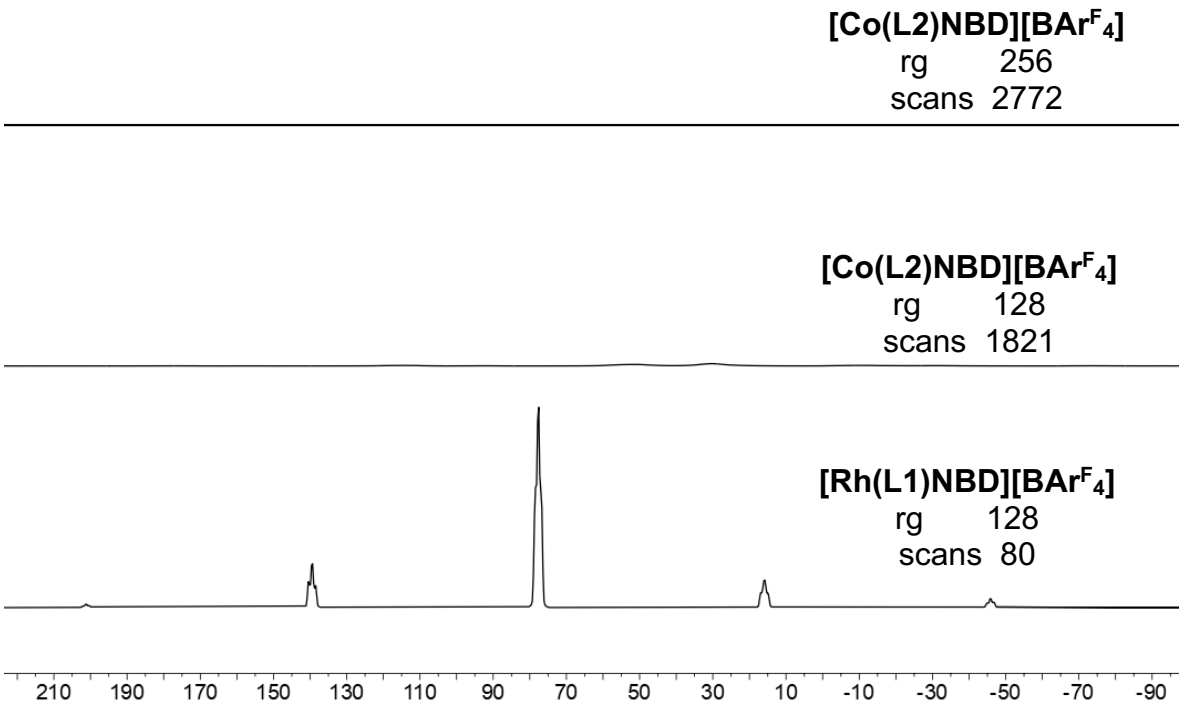


Figure 5.7 The $^{31}P\{^{1}H\}$ SSNMR (162 MHz, 298 K, 10 kHz spin rate) spectrum of **[Co(L2)NBD][BArF4], [Co(L2)NBA][BArF4]** and **[Rh(L1)NBD][BArF4].** Normalised for receiver gain and number of scans. Showing both cobalt complexes giving silent $^{31}P\{^{1}H\}$ SSNMR spectrum. Receiver gain is abbreviated to rg.

For SQUID magnetometer studies

Crystals of **[Co(L2)NBD][BArF4]** were placed within a Spectrosil® sample holder (Figure 5.13), this was exposed to a hydrogen atmosphere (2 bar) for 1 h, before sealing under vacuum and rapid transfer of the sample to the SQUID magnetometer. Magnetic measurement using SQUID magnetometer methods: 3.38 μB.

5.2.2 Crystallographic and refinement data

5.2.2.1 Crystal structure determinations

Single crystal X-ray diffraction data for all samples were collected as follows: a typical crystal was mounted on a MiTeGen Micromount using perfluoropolyether oil and cooled rapidly to the collection temperature in a stream of nitrogen gas using an Oxford Cryosystems Cryostream unit.[12] The structures of **[Co(L1)NBD][BAr$^F_4$]** and **[Co(L1)(η-FC$_6$H$_5$)][BAr$^F_4$]** were collected at the Oxford Chemical Crystallography Service from the University of Oxford, with an Agilent SuperNova diffractometer (Cu Kα radiation, λ = 1.54180 Å). **[Co(L2)NBD][BAr$^F_4$]** and **[Co(L2)NBA][BAr$^F_4$]** were collected at the National Crystallography Service, University of Southampton, Southampton, UK, using a Rigaku 007HF diffractometer equipped with Varimax confocal mirrors (Cu Kα radiation, λ = 1.54178 Å), an AFC11 goniometer, and HyPix 6000 detector.

Raw frame data were reduced using CrysAlisPro.[13] The structures were solved using SHELXT[14] and refined using full-matrix least-squares refinement on all F^2 data using the SHELXL-2018[15] using the interface OLEX2.[16] All hydrogen atoms were placed in calculated positions (riding model).

5.2.2.2 Additional comments crystal structures and refinement data

[Co(L1)NBD][BAr$^F_4$]

Four -CF_3 groups are disordered (ca. 56:44, 56:44, 53:47 51:49), and 1,2 and 1,3 equal distance geometrical and displacement parameter restraints were applied to each pair of disorder components.

[Co(L1)(η-FC_6H_5)][BAr^F_4]

Four -CF_3 groups are disordered (ca. 74:26, 69:31, 62:38 60:40), and 1,2 and 1,3 equal distance geometrical and displacement parameter restraints were applied to each pair of disorder components. The coordinated fluorobenzene is disordered over three positions (ca. 52:32:16), and 1,2 equal distance geometrical and displacement parameter restraints were applied to all disorder components.

[Co(L2)NBD][BAr^F_4]

The [BAr^F_4]$^-$ anion displays whole molecule disorder (ca. 52:48), and 1,2 and 1,3 equal distance geometrical restraints were applied to both components. Displacement parameter restraints were applied to the whole structure. One cyclohexane moiety in the asymmetric unit is disordered (ca. 65:35), and 1,2 and 1,3 equal distance geometrical restraints were applied to both components. The C4 backbone was disordered via crystallographic symmetry over two positions (50:50). Displacement parameter restraints and 1,2 and 1,3 equal distance geometrical restraints between equivalent pairs of atoms were applied to coordinated NBD.

[Co(L2)NBA][BAr^F_4]

A 1,2 equal distance geometrical restraint was applied between all secondary and tertiary C-atoms of NBA. 1,2 and 1,3 equal distance geometrical restraints were applied between all secondary C-atoms of NBA. A 1,2 equal distance geometrical restraint was applied to the disordered C4 backbone. 1,2 and 1,3 equal distance restraints were applied to the disorder components of the [BAr^F_4]$^-$ anion.

	[Co(L1)NBD][BAr$^F_4$]	[Co(L1)(ηFC$_6$H$_5$)][BAr$^F_4$]
Chemical formula	$C_{65}H_{68}BCoF_2P_2$	$C_{64}H_{65}BCoF_{25}P_2$
Formula weight	1436.87	1440.84
Temperature (K)	150	150
Crystal system	triclinic	triclinic
Space group	P-1	P-1
a (Å)	12.8234(9)	12.7272(5)
b (Å)	12.9744(8)	12.8527(5)
c (Å)	19.8379(11)	20.1804(7)
α (deg)	92.463(5)	91.965(3)
β (deg)	90.162(5)	90.053(3)
γ (deg)	96.188(5)	97.304(4)
Volume (Å^3)	3278.2(4)	3272.3(2)
Z	2	2
ρ_{calc} g/cm^3	1.456	1.462
μ/mm^{-1}	3.480	3.511
Reflections collected	24258	37212
Independent reflections	12435	37212
Restraints / parameters	537 / 957	1420 / 1080
R_{int}	0.0880	0.0928
R_1 [I > 2σ(I)]	0.0931	0.1024
wR_2 [all data]	0.2816	0.3072
GooF	1.018	1.058
Residual electron density (e Å^{-3})	1.22 / -0.56	1.52 / -0.65
CCDC no.	1967463	1967464

Table 5.1 Selected crystallographic and refinement data.

	[Co(L2)NBD][BAr$^F_4$]	[Co(L2)NBA][BAr$^F_4$]
Chemical formula	$C_{67}H_{72}BCoF_{24}P_2$	$C_{67}H_{76}BCoF_{24}P_2$
Formula weight	1464.92	1468.95
Temperature (K)	100	100
Crystal system	monoclinic	monoclinic
Space group	C2/c	C2/c
a (Å)	19.3071(2)	19.0831(3)
b (Å)	17.1586(3)	17.7975(3)
c (Å)	20.3552(2)	20.2129(3)
α (deg)	90	90
β (deg)	93.4560(10)	92.9714(12)
γ (deg)	90	90
Volume (Å^3)	6731.06(15)	6855.70(17)
Z	4	4
ρ_{calc} g/cm^3	1.446	1.423
μ/mm^{-1}	3.401	3.339
Reflections collected	38436	38479
Independent reflections	6276	6390
Restraints / parameters	1851 / 756	579 / 577
R_{int}	0.0338	0.0456
R_1 [I > 2σ(I)]	0.0609	0.0796
wR_2 [all data]	0.1772	0.2144
GooF	1.048	1.034
Residual electron density (e Å^{-3})	0.82 / -0.58	0.92 / -0.48
CCDC no.	1967534	1967533

Table 5.2 Selected crystallographic and refinement data.

5.2.2.3 Single crystal X-ray diffraction structures

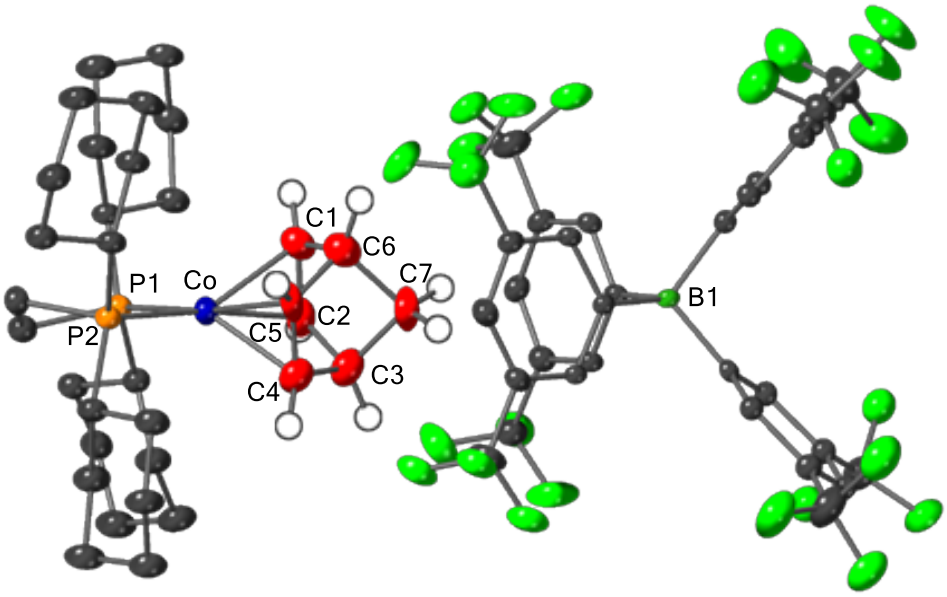


Figure 5.8 Molecular structure of **[Co(L1)NBD][BAr$^{F}_{4}$]**. Thermal ellipsoids set at 30 % and hydrogen atoms from the phosphine ligand and [BAr$^{F}_{4}$]$^{-}$ anion removed for clarity. Only the major disorder component of the [BAr$^{F}_{4}$]$^{-}$ anion is shown.

Selected bond lengths (Å) and angles (°): Co1-P1 2.226(2), Co1-P2 2.2298(19), Co1-C5 2.073(7), Co1-C2 2.091(8), Co1-C4 2.092(9), C1-C2 1.410(12), C5-C4 1.403(12), P1-Co-P2 87.48(7), CoP1P2/Co(centC1C2)(centC4C5) 22.0(2).

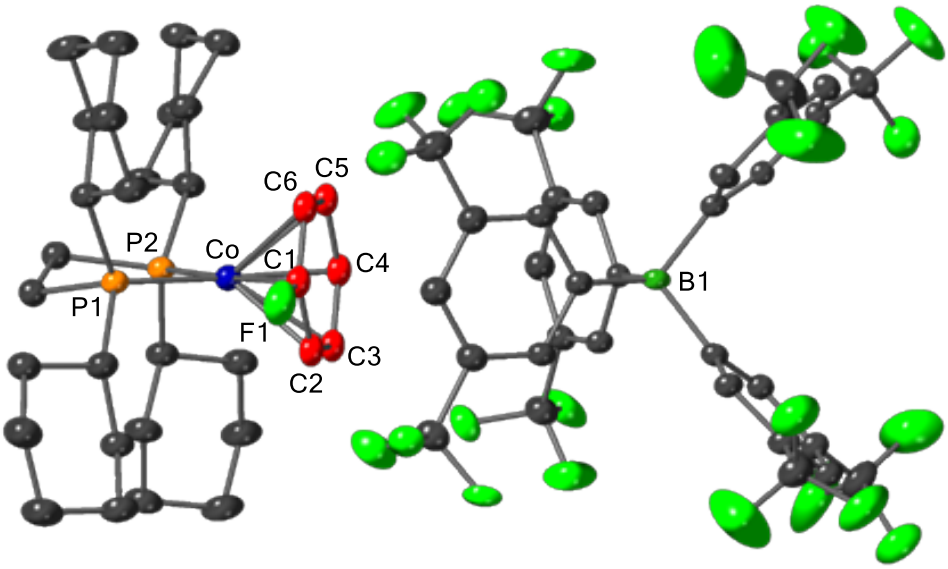


Figure 5.9 Molecular structure of **[Co(L1)(η-FC$_6$H$_5$][BAr$^{F}_{4}$]**. Thermal ellipsoids were set at 30 %, and hydrogen atoms were removed for clarity. Only the major disorder component of the [BAr$^{F}_{4}$]$^{-}$ anion is shown.

Selected bond lengths (Å) and angles (°): Co1-P1 2.1839(16), Co1-P2 2.1803(17), Co-centC1C2C3C4C5C6 1.601(5), P1-Co-P2 86.69(6).

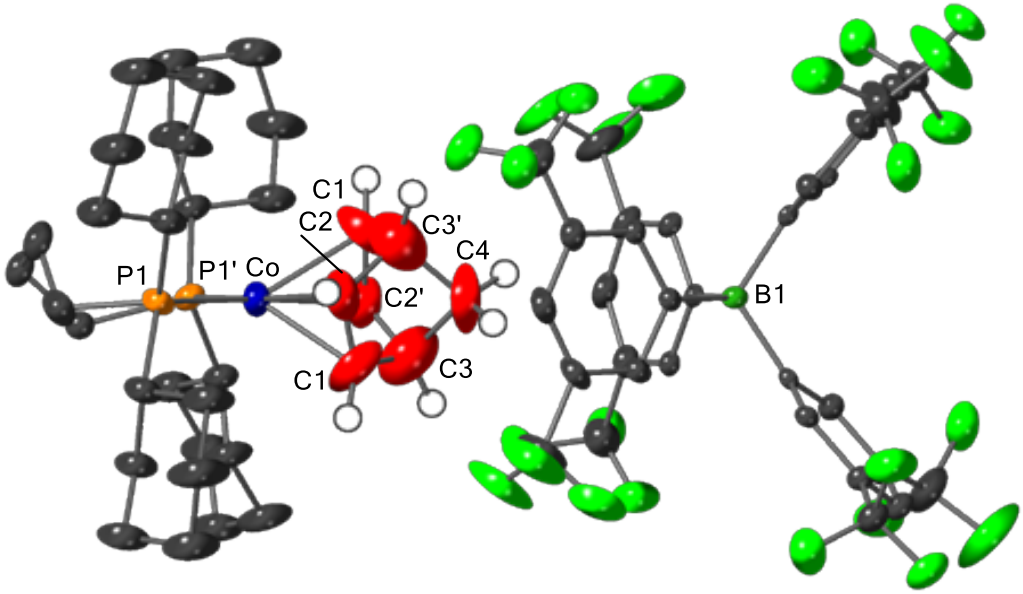


Figure 5.10 Molecular structure of **[Co(L2)NBD][BAr$^F_4$]**. Thermal ellipsoids set at 30 % and hydrogen atoms from the phosphine ligand and [BAr$^F_4$]$^-$ anion removed for clarity. Only the major disorder component of the [BAr$^F_4$]$^-$ anion is shown.

Selected bond lengths (Å) and angles (º): Co1-P1 2.2717(8), Co1-C1 2.212(6), Co1-C2 2.110(4), P1-Co-P2 103.09(4), CoP1P2/Co(centC1C2)(centC1'C2') 28.0(3).

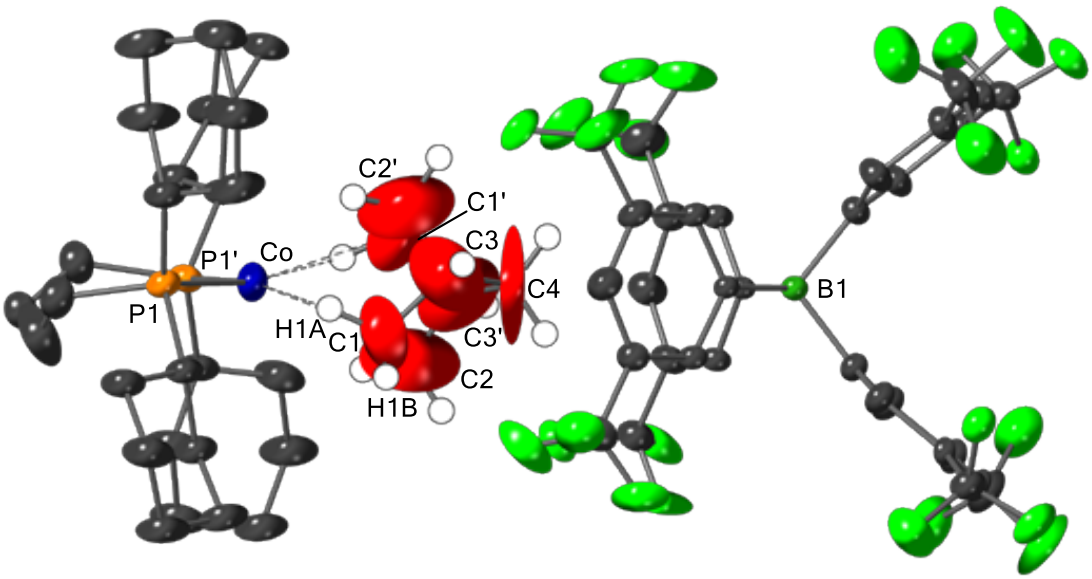


Figure 5.11 Molecular structure of **[Co(L2)NBA][BAr$^F_4$]**. Thermal ellipsoids set at 30 % and hydrogen atoms from the phosphine ligand and [BAr$^F_4$]$^-$ anion removed for clarity. Only the major disorder component of the [BAr$^F_4$]$^-$ anion on shown.

Selected bond lengths (Å) and angles (º): Co1-P1 2.232(1), Co1-C1 2.612(16), P1-Co-P2 108.94(7), CoP1P1'/CoC1C1' 39.9(8).

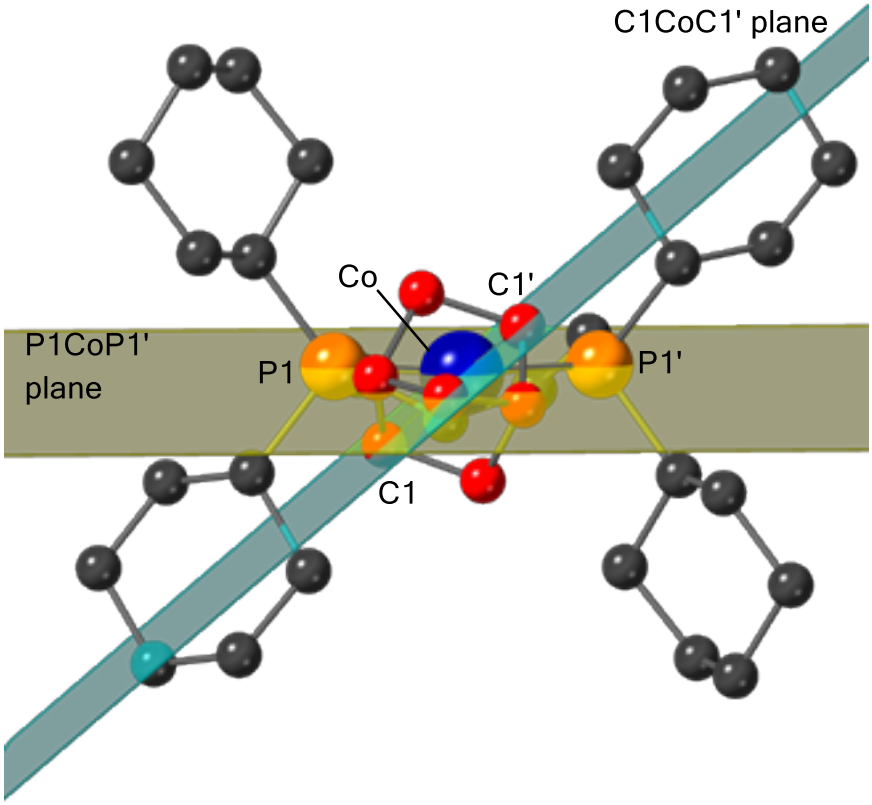


Figure 5.12 Molecular structure of **[Co(L2)NBA][BAr$^{F}_{4}$]**. Ball and stick representation used. The yellow plane is the P1CoP1' plane, and the blue plane is the C1CoC1' plane. The angle between these is used to measure how twisted away from square planar the NBA fragment is.

5.2.3 Magnetic characterisation

Zero-field cooled magnetisation data were collected as a function of temperature from samples sealed under vacuum within Spectrosil® sample holders, shown in Figure 5.13, in an applied field of 1000 Oe using an MPMS 5 Quantum Design SQUID magnetometer.

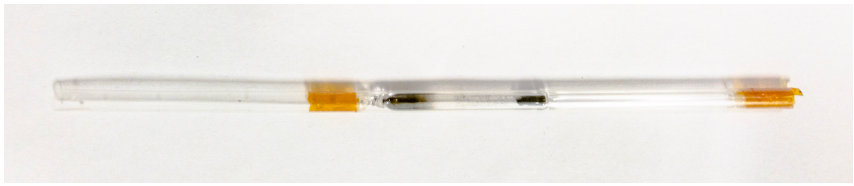


Figure 5.13 Picture of a sample holder

5.3 Chapter 3 experimental data

5.3.1 Synthesis of $CoCl_2(^iPr_2PCH_2CH_2)_2NMe$

Prepared by the analogous procedure used for **Co(L3)Cl₂** and **Co(L4)Cl₂.**[2,3] The product was isolated as a dark blue powder (80 % yield). All attempts of crystallisation were unsuccessful. ^{1}H NMR (400 MHz, CD_2Cl_2, 298 K): silent. δ ^{31}P{^{1}H} (162 MHz, CD_2Cl_2, 298 K): silent. Magnetic measurement using Evans method of a CD_2Cl_2 sample: μ_{eff} (200 K) = 4.13 μ_B (μ_{SO} = 3.88 μ_B).

5.3.2 Dehydropolymerization under open conditions

In a typical experimental set-up (e.g. 0.223 M [$H_3B{\cdot}NMeH_2$], 0.2 mol% catalyst loading), $H_3B{\cdot}NMeH_2$ (25.0 mg, 0.557 mmol) was suspended in 2.0 mL of 1,2-$F_2C_6H_4$. Double the desired amount of catalyst was weighed into a separate flask and dissolved in 1.0 mL of 1,2-$F_2C_6H_4$. The $H_3B{\cdot}NMeH_2$ containing flask was flushed with argon through an exit needle, and 0.5 mL of the catalyst solution was added to the reaction mixture quickly followed by 2 eq. of $NMeH_2$. The resultant solution was stirred for the desired reaction time at 400 rpm at room temperature. 0.5 mL of the reaction mixture was removed for NMR spectroscopy. The remaining reaction mixture was transferred to 40 mL of rapidly stirred pentane to give an off-white suspension which was isolated by filtration. The off-white solid $(H_2B{\cdot}NMeH)_n$ was dried under vacuum overnight prior to GPC analysis.

5.3.3 Dehydropolymerization under hydrogen evolution measurement conditions

In a typical experimental set-up (e.g. 0.223 M [$H_3B{\cdot}NMeH_2$], 0.4 mol% catalyst loading), $H_3B{\cdot}NMeH_2$ (25.0 mg, 0.557 mmol) was suspended in 4.0 mL of 1,2-$F_2C_6H_4$ in a jacketed two-neck Schlenk flask connected to a recirculating cooler and the temperature set at 25 °C. Double the desired amount of catalyst was weighed into a separate flask and dissolved in 2.0 mL of 1,2-$F_2C_6H_4$. The $H_3B{\cdot}NMeH_2$-containing flask was sealed off from the Ar supply and connected to a water-filled gas burette. The pre-catalyst solution was added to the reaction mixture, followed by 2 eq. $NMeH_2$ and the resultant solution was decanted into 40 mL of rapidly stirred pentane to give an off-white suspension isolated by filtration. The off-white solid $(H_2B{\cdot}NMeH)_n$ was dried under vacuum overnight prior to GPC analysis.

5.3.4 Scale-up dehydropolymerization and metal-removal procedure

In a typical experimental set-up $H_3B{\cdot}NMeH_2$ (e.g. 5 M [$H_3B{\cdot}NMeH_2$] in THF) was dissolved in THF. Double the desired amount of catalyst was weighed into a separate flask and dissolved in 1.0 mL of THF. The $H_3B{\cdot}NMeH_2$ containing flask was flushed with argon through an exit needle, and 0.5 mL of the catalyst solution was added to the reaction mixture followed by 2 eq. of $NMeH_2$. The resultant solution was stirred for the desired reaction time at 400 rpm. 0.5 mL of the reaction mixture was removed for analysis by NMR spectroscopy. The remaining reaction mixture was transferred to 40 mL of rapidly stirred pentane to give an off-white suspension which was isolated by filtration. The off-white solid $(H_2B{\cdot}NMeH)_n$ was dried under vacuum overnight prior to GPC analysis. To remove residual metal catalyst from the isolated polymer, a sample of polymer (500 mg) was dissolved in THF (50 mL) and flash filtered through a silica

plug. The solution of polymer was reduced to 5 mL and transferred to rapidly stirring pentane to give an off-white solid $(H_2B{\cdot}NMeH)_n$ was dried under vacuum overnight prior to GPC analysis.

In THF at lower absolute concentration of catalyst (e.g. 0.223 M [$H_3B{\cdot}NMeH_2$], 0.4 mol% catalyst loading) results in no reaction. This lack of activity is explained by impurities in the THF (~10 ppm H_2O) titrating out the active catalyst, resulting in reaction only at higher absolute catalysts concentrations.

5.3.5 10 g scale dehydropolymerization of $H_3B{\cdot}NMeH_2$ catalysed by $Co(L4)Cl_2$

$H_3B{\cdot}NMeH_2$ (10 g, 0.22 mol) was dissolved in THF (40 ml) under nitrogen. **$Co(L4)Cl_2$** (20 mg, 46 mmol) was separately dissolved in 5 mL of THF and transferred to the flask containing $H_3B{\cdot}NMeH_2$, followed by the addition of 2 eq. of $NMeH_2$ (50 µL). The resultant solution was stirred for 2 h under a high nitrogen flow to remove the large volume of hydrogen produced (5 L). The remaining reaction mixture was transferred to 500 mL of rapidly stirred pentane to give an off-white suspension which was isolated by filtration. The off-white solid $(H_2B{\cdot}NMeH)_n$ was dried under vacuum overnight prior to GPC analysis.

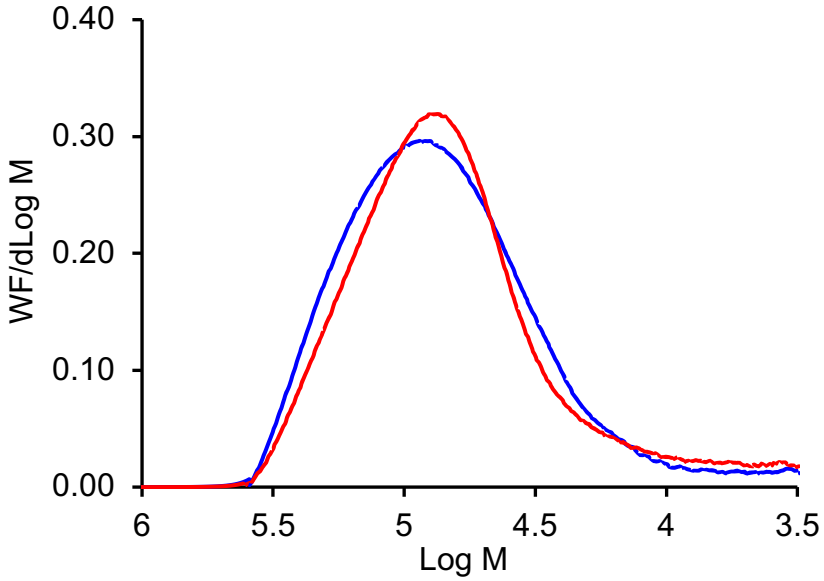


Figure 5.14 Overlaid GPC traces of $(H_2B{\cdot}NMeH)_n$ obtained using **Co(L4)Cl₂** in 1,2-$F_2C_6H_4$ at 0.4 mol% under open (red) and H_2 evolution (blue) conditions. Red trace: M_n = 51,100 gmol^{-1}; $Đ$ = 1.7. Blue trace: M_n = 51,100 gmol^{-1}; $Đ$ = 1.7.

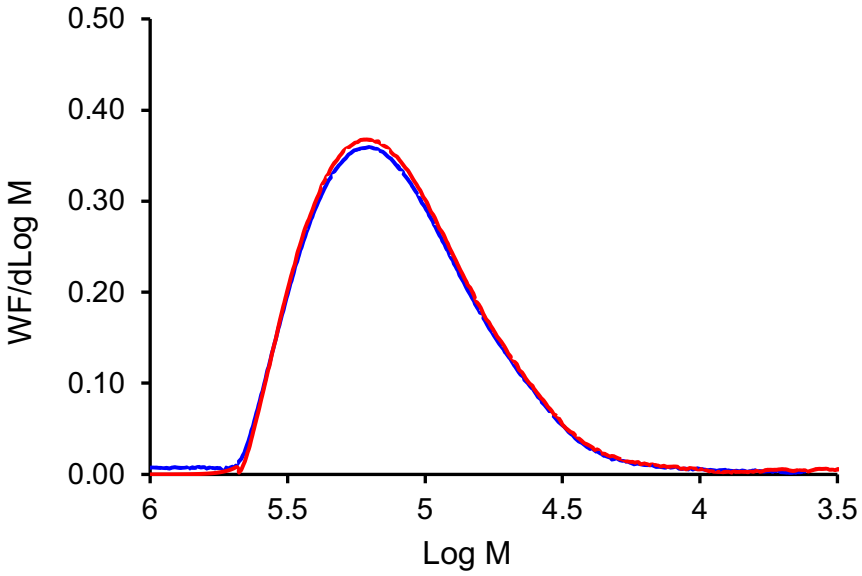


Figure 5.15 Overlaid GPC traces of $(H_2B{\cdot}NMeH)_n$ immediately after purification (blue) and after storage under air for 1 month (red). Red trace: M_n = 98,250 gmol^{-1}; $Đ$ = 1.6. Blue trace: M_n = 98,800 gmol^{-1}; $Đ$ = 1.6.

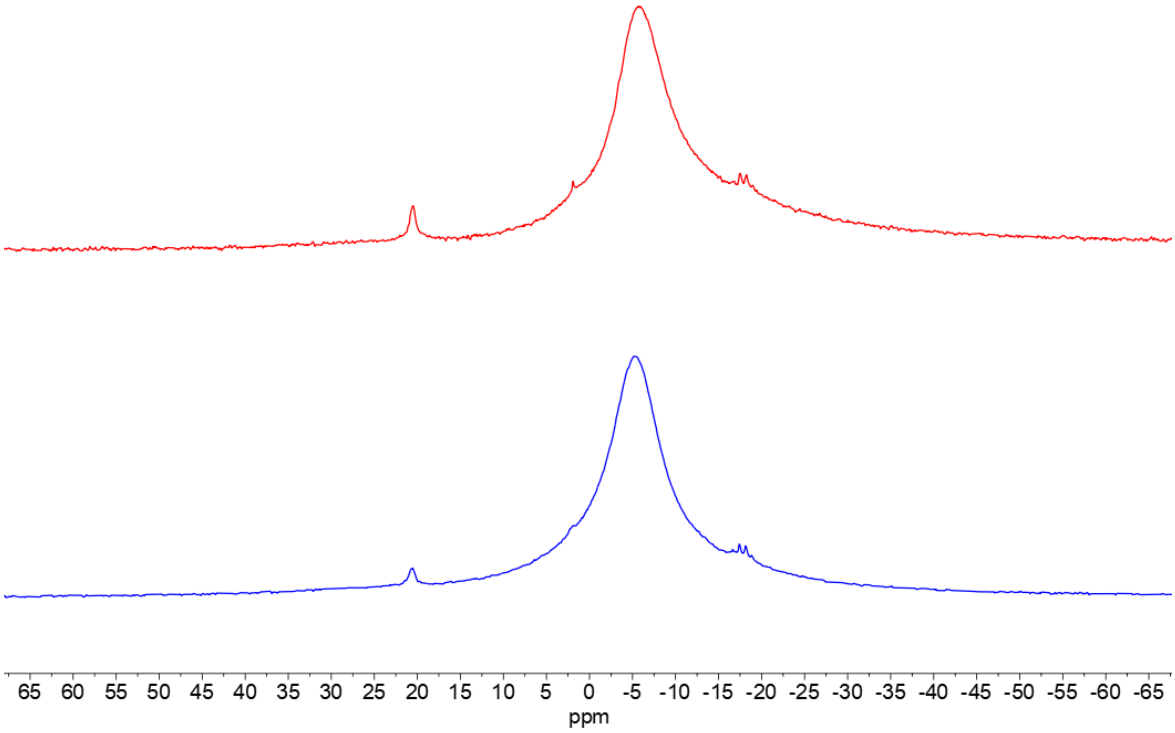


Figure 5.16 Overlaid ^{11}B NMR spectra of isolated polyaminoboranes immediately after purification (blue) and after storage under air for one month (red).

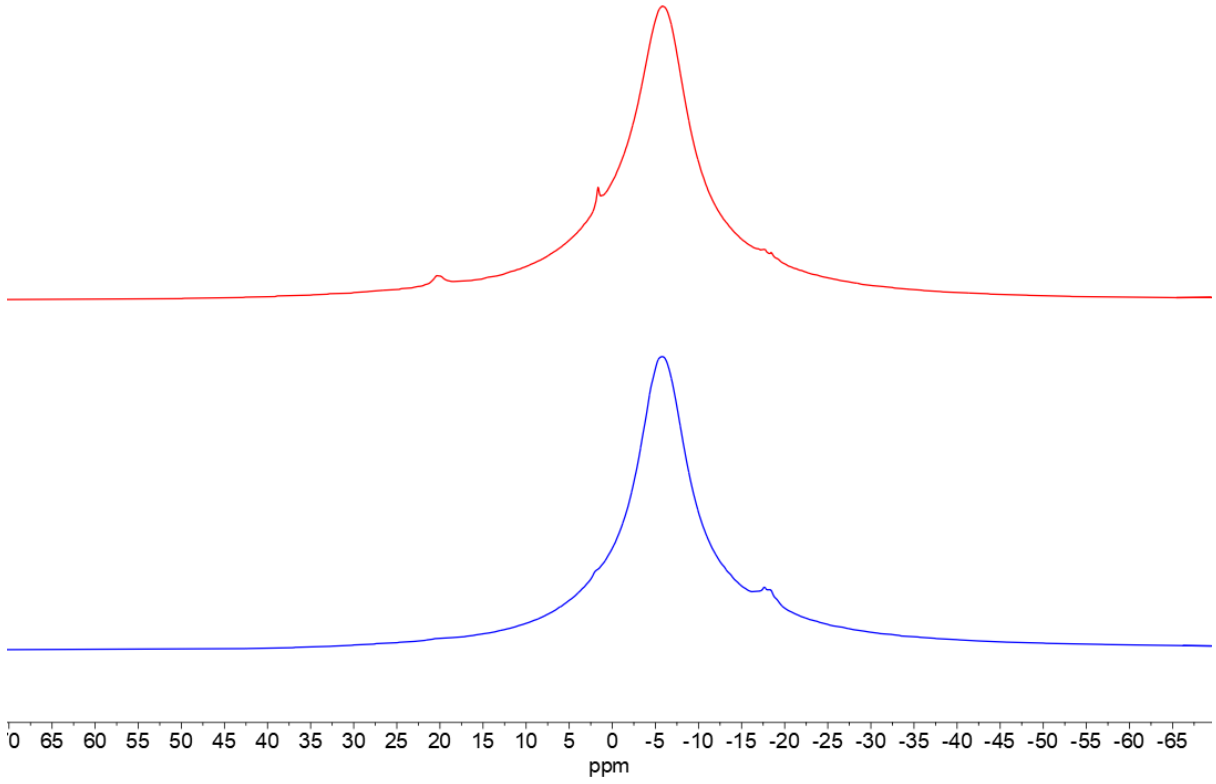


Figure 5.17 Overlaid ^{11}B NMR spectrum of isolated polyaminoboranes immediately after purification (blue) and after passing through silica to remove residual cobalt (red).

5.3.6 In situ formation of $Co(L3)Cl_2$ for the catalytic dehydropolymerisation of $H_3B{\cdot}NMeH_2$

$CoCl_2$ (3 mg) was dissolved in THF (1 ml) to which L3 (10 wt% in THF, 7 mg, 62 µL) was added and left to stir at room temperature for 1 hour. In the catalytic flask, $H_3B{\cdot}NMeH_2$ was dissolved in THF (4 ml); the flask was flushed with argon through an exit needle, and the catalyst solution was added to the reaction mixture followed by 2 equiv. of $NMeH_2$ (2 M, 25 µL). The reaction mixture was left to stir for 90 minutes. Following this, the remaining reaction mixture was transferred to 40 mL of rapidly stirring pentane to give an off-white suspension which was isolated by filtration. The off-white solid $(H_2B{\cdot}NMeH)_n$ was dried under vacuum overnight prior to GPC analysis.

5.3.7 In situ formation of colloidal cobalt nanoparticles for the dehydropolymerisation of $H_3B{\cdot}NMeH_2$

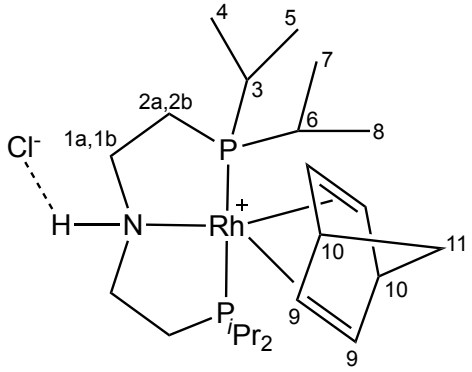
1.12 g of $H_3B{\cdot}NMeH_2$ in 4 mL of THF and 3 mg of **$CoCl_2$** in 1 mL of THF were combined in a flask resulting in a light blue solution. 2 equiv. of $NMeH_2$ (2 M, 25 µL) was then added to the flask resulting in an immediate colour change and a magnetic black precipitate. No significant turnover was observed after 1 h. After the allotted time, L3 (10 wt% in THF, 7 mg, 62 µL) was added to the reaction mixture and allowed to react for a further 2 hours upon which no additional turnover was observed.

5.4 Chapter 4: Experimental data

5.4.1 Synthesis of complexes

5.4.1.1 Synthesis of [Rh(L3)NBD]Cl

In a J. Youngs ampoule **[RhNBDCl]$_2$** (200 mg, 0.43 mmol) which was suspended in THF (5 mL). To this orange suspension L3 (10 wt% in THF, 3 mL, 0.86 mmol) was added and this resulted in an orange solution. The reaction was left to stir at room temperature for 16 hours, during which time an orange crystalline solid formed which was isolated by filtration *via* cannula. The solid was washed with *n*-pentane (3 x 5 mL) and dried *in vacuo* (< 5 x 10^{-2} mbar, 16 hrs) to yield an orange powder, **[Rh(L3)NBD]Cl** (435 mg, 0.79 mmol, 90%). Crystals suitable for X-ray diffraction study were isolated by slow diffusion of *n*-pentane (25 mL) into a solution of the orange solid (100 mg, 0.20 mmol) in CH_2Cl_2 (1 mL) at room temperature. To give orange block like crystals of **[Rh(L3)NBD]Cl** (90 mg, 0.18 mmol, 80% yield)



^{1}H NMR (600 MHz, CD_2Cl_2, 298 K): δ_H 6.99 (s, 1H, NH), 3.66 (dt, J = 3.2, 1.8 Hz, 4H, H-9), 3.50-3.47 (m, 2H H-10), 2.90 – 2.78 (m, 2H, H-3), 2.76 – 2.68 (m, 2H, H-1a), 2.33 – 2.21 (m, 2H, H-1b), 2.05 – 1.96 (m, 2H, H-2a), 1.73 (dhp, J = 7.3, 5.3 Hz, 2H, H-6), 1.61-1.57 (m, 2H, H-2b), 1.55 (overlapping dd, J = 14.5, 7.1 Hz, 12H, H-4/5), 1.22 (dd, J = 10.5, 7.0 Hz, 6H, H-7), 1.12 (t, J = 1.5 Hz, 2H, H-11), 1.06 (dd, J = 15.0, 7.4 Hz, 6H, H-8).

^{1}H NMR (500 MHz, C_6D_6, 298 K): δ_H 8.80 (s, 1H, NH), 3.71 (s, 4H, H-9), 3.18 (*pseudo*-p, J = 2.5 Hz, 2H, H-10), 2.72 (br *pseudo*-s, $v_{1/2}$ 41 Hz, 2H, H-3), 2.40 – 2.33 (br m, , $v_{1/2}$ 24 Hz, 2H, H-1a), 2.08 (br *pseudo*-s, $v_{1/2}$ 54 Hz, 2H, H-1b), 1.86 – 1.79 (br m, $v_{1/2}$ 36 Hz. 2H, H-2a), 1.39 – 1.30 (br m, $v_{1/2}$ 30 Hz, 2H, H-6), 1.25-1.18 (br m, $v_{1/2}$ 26 Hz, 12H, H-4/5), 0.99 (t, J = 1.4 Hz, 2H, H-11), 0.81 (dd, J = 11.5, 5.1 Hz, 6H, H-7), 0.65 (dd, J = 14.4, 7.4 Hz, 6H, H-8).

^{13}C{^{1}H} NMR (151 MHz, CD_2Cl_2, 298 K): δ_C 59.8 (C-11), 54.5 – 54.2 (m, C-1), 47.0 (C-10), 35.9 (d, J = 7.2 Hz, C-9), 31.3 (t, J = 3.4 Hz, C-6), 29.6 (t, J = 9.4 Hz, C-3), 27.2 (dd, J = 12.3, 4.9 Hz, C-2), 20.9 (*pseudo*-t, J = 1.3 Hz, C-5), 20.5 (*pseudo*-t, J = 3.8 Hz, C-8), 20.4 (C-4), 18.6 (*pseudo*-t, J = 2.1 Hz, C-7).

^{31}P{^{1}H} NMR (243 MHz, CD_2Cl_2, 298 K): δ_P 48.0 (d, J = 124 Hz).

^{31}P{^{1}H} NMR (203 MHz, C_6D_6, 298 K): δ_P 49.1 (d, J = 126 Hz).

Elemental analysis found (calculated) for $C_{23}H_{45}ClNP_2Rh$: C, 51.02 (51.55); H, 8.20 (8.46); N, 2.22(2.61).

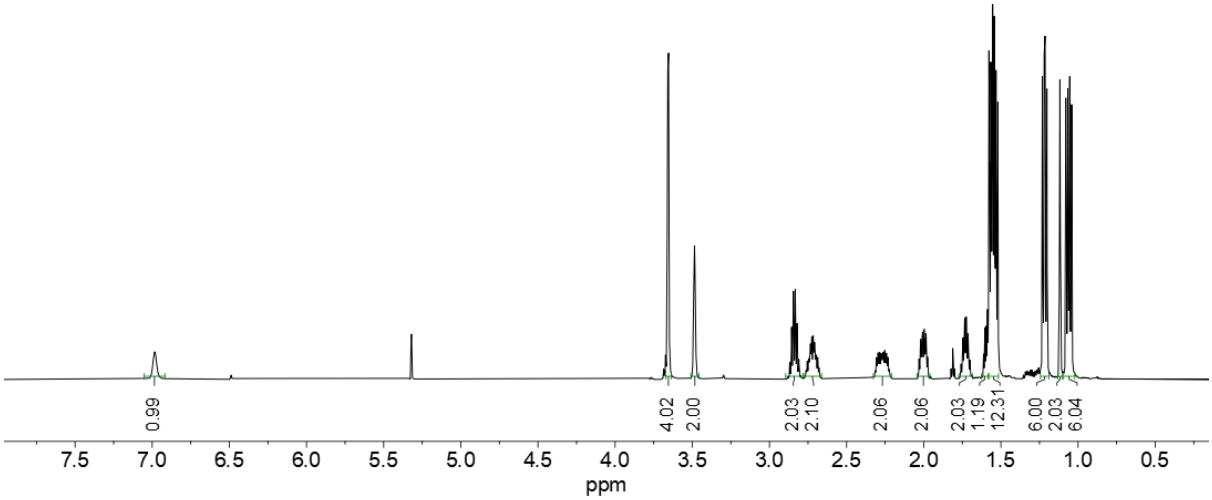


Figure 5.18 ^{1}H NMR (600 MHz, CD_2Cl_2, 298 K) spectrum of **[Rh(L3)NBD]Cl**.

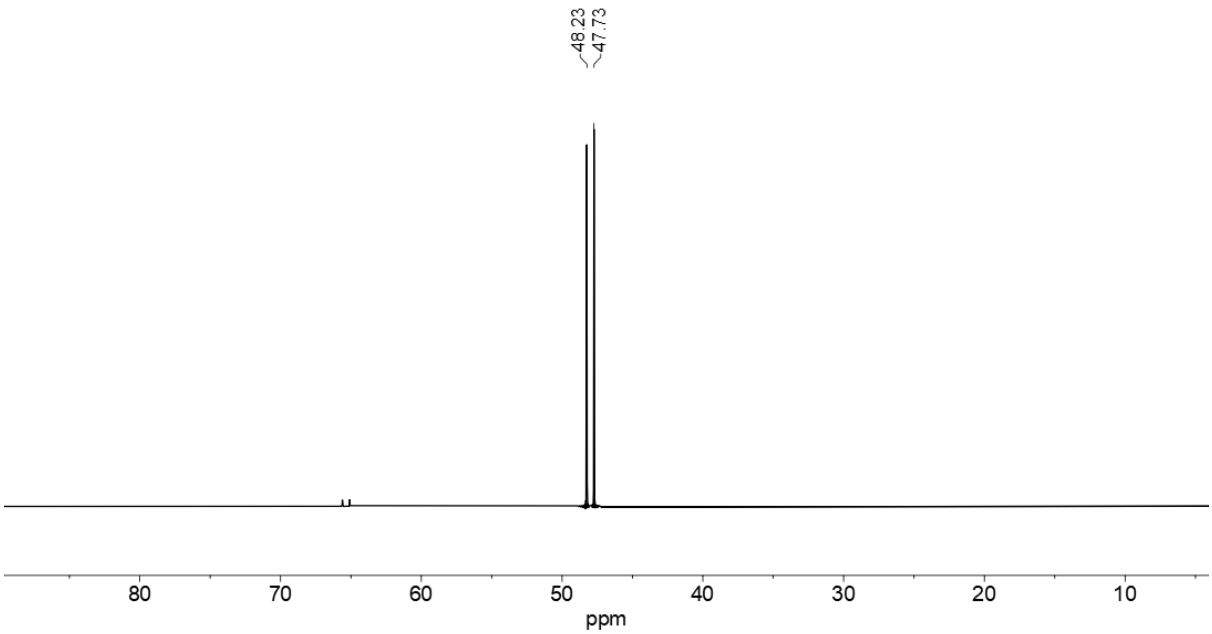


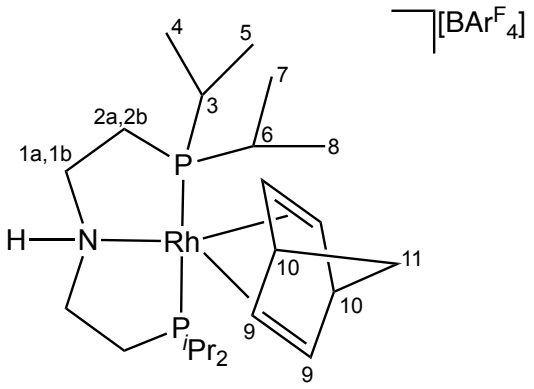
Figure 5.19 $^{31}P\{^{1}H\}$ NMR (243 MHz, CD_2Cl_2, 298 K) spectrum of **[Rh(L3)NBD]Cl**.

5.4.1.2 Synthesis of [Rh(L3)NBD][BAr$^F_4$]

An orange solution of **[Rh(L3)NBD]Cl** (200 mg, 0.19 mmol) in CH2Cl2 (5 mL), was added to an ampoule containing a suspension of Na[BAr$^F_4$] (334 mg, 0.19 mmol) in CH_2Cl_2 (5 mL). The reaction was left to stir at room temperature for 16 hours. The resultant orange solution was transferred to a crystallisation tube via cannula filter and layered with n-pentane to afford **[Rh(L3)NBD][BAr$^F_4$]** (450 mg, 0.17 mmol, 87 % yield) as block like orange crystals that were suitable for single crystal X-ray diffraction.

Or

To an ampoule containing an orange solution of **[Rh(NBD)$_2$][BAr$^F_4$]** (100 mg, 0.13 mmol) in CH_2Cl_2 (7 mL), L3 (0.92 mL, 10 % wt. soln. in THF, 0.13 mmol) was added. The reaction was left to stir at room temperature for 16 hours. The resultant orange solution was transferred to a crystallisation tube via cannula filter and layered with pentane to afford **[Rh(L3)NBD][BAr$^F_4$]** (300 mg, 0.11 mmol, 82 % yield) as block like orange crystals that were suitable for single crystal X-ray diffraction.



^{1}H NMR (600 MHz, CD_2Cl_2): δ_H 7.72 (m, 8H, [BAr$^F_4$]$^-$), 7.56 (s, 4H, [BAr$^F_4$]$^-$), 3.56 (tq, J = 3.4, 1.7 Hz, 2H, H-10), 3.37 (q, J = 2.0 Hz, 4H, H-9), 2.89 – 2.78 (m, 2H, H-3), 2.75 (s, 1H, NH), 2.75 – 2.65 (m, 2H, H-1a), 2.56 – 2.44 (m, 2H, H-1b), 1.97 – 1.89 (m, 2H, H-2b), 1.71 (heptd, J = 7.3, 4.8 Hz, 2H, H-6), 1.63 – 1.56 (m, 2H, H-2a), 1.56 (dd, J =

13.7, 7.2 Hz, 6H, H-5), 1.50 (dd, J = 13.4, 7.0 Hz, 6H, H-4), 1.25 (dd, J = 10.6, 7.0 Hz, 6H, H-8), 1.16 (t, J = 1.7 Hz, 2H, H-11), 1.09 (dd, J = 15.6, 7.5 Hz, 6H, H-7).

$^{13}C\{^{1}H\}$ NMR (151 MHz, CD_2Cl_2): δ_C 162.17 (dd, J = 99.7, 49.9 Hz), 135.22, 130.11 – 128.62 (m), 125.01 (q, J = 272.3 Hz), 118.05 – 117.72 (m), 59.74 (C-11), 55.59 (dd, J = 7.6, 5.4 Hz, C-1), 47.22 (C-10), 34.45 (C-9), 32.13 – 31.77 (m), 29.28 (t, J = 9.6 Hz, C-3), 27.98 (dd, J = 12.4, 4.4 Hz, C-2), 20.90 (C-5), 20.61 (t, J = 3.6 Hz, C-7), 20.32 (C-4), 18.33 (t, J = 2.8 Hz, C-8).

$^{31}P\{^{1}H\}$ NMR (243 MHz, CD_2Cl_2): δ_P 46.91 (d, J = 120.3 Hz).

Elemental analysis found (calculated) for $C_{55}H_{57}BF_{24}NP_2Rh$ (1363.69): C, 48.51 (48.44); H, 4.07 (4.21); N, 0.86 (1.03).

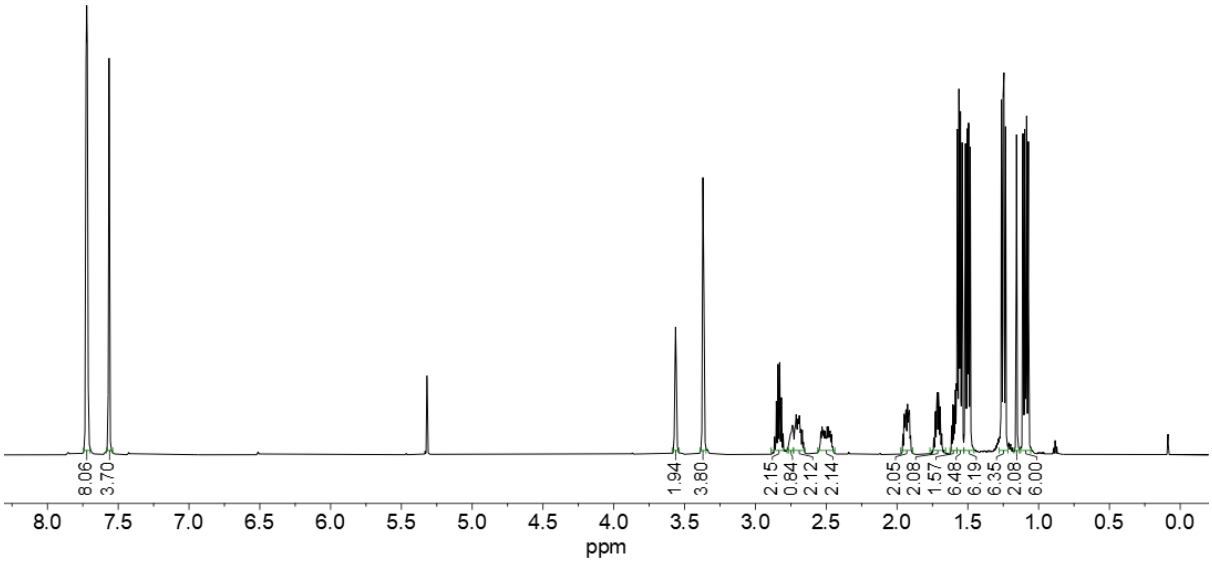


Figure 5.20 ^{1}H NMR (600 MHz, CD_2Cl_2, 298 K) spectrum of **[Rh(L3)NBD][BAr$^{F}_{4}$]**.

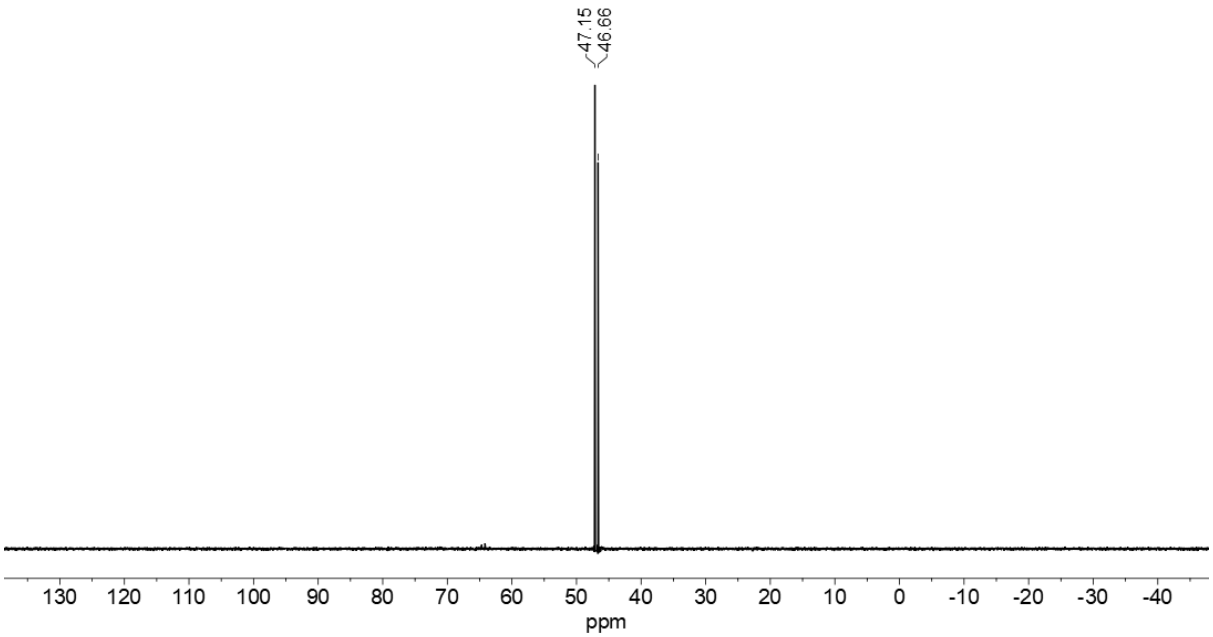
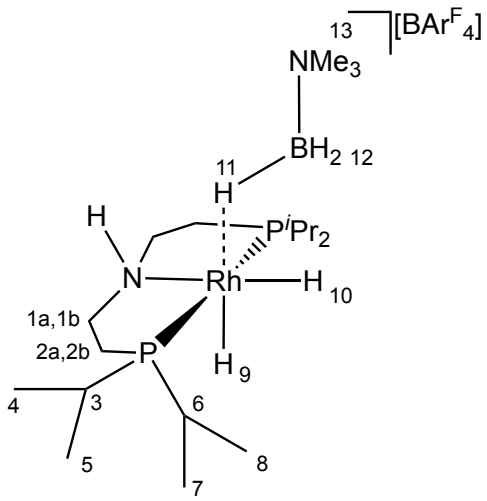


Figure 5.21 $^{31}P\{^{1}H\}$ NMR (243 MHz, CD_2Cl_2, 298 K) spectrum of **[Rh(L3)NBD][BAr$^{F}_{4}$]**.

5.4.1.3 Synthesis of [Rh(L3)H$_2$(H$_3$B·NMe$_3$)][BAr$^{F}_{4}$]

To an ampoule containing **[Rh(L3)NBD][BAr$^{F}_{4}$]** (400 mg, 0.16 mmol) and $H_3B{\cdot}NMe_3$ (25 mg, 0.27 mmol) was added 1,2-$F_2C_6H_4$ (10 mL). The solution was degassed via freeze-pump-thaw three times (<10^{-3} mbar) and before charging with H_2 gas (2 bar). The reaction was vigorously stirred at room temperature for 20 h, after which time the H_2 atmosphere was removed by freeze pump-thaw-degassing and replaced with argon. The solution was transferred via cannula filter to a recrystallisation tube and layered with pentane to afford colourless crystals of **[Rh(L3)H$_2$(H$_3$B·NMe$_3$)][BAr$^{F}_{4}$]** (297 mg, 0.12 mmol, 76% yield) which were suitable for single crystal X-ray diffraction.



^{1}H NMR (600 MHz, CD_2Cl_2): δ_H 7.73 (dt, J = 5.2, 2.4 Hz, 8H, BArF4 o-H), 7.57 (s, 4H, BArF4, p-H), 3.38 – 3.26 (m, 2H, H-1a), 2.70 (s, 1H, NH), 2.64 (s, 9H, H-13), 2.36 (dq, J = 14.6, 4.2 Hz, 2H, H-2a), 2.27 – 2.20 (m, 2H, H-6), 2.18 (dt, J = 10.7, 3.5 Hz, 2H, H-3, H-1b), 1.82 (tdt, J = 14.8, 5.9, 2.2 Hz, 2H, H-2b), 1.34 (q, J = 7.8 Hz, 6H, H-4), 1.25 (q, J = 6.4 Hz, 6H, H-5), 1.17 – 1.08 (m, 6H, H-8), 1.04 (q, J = 7.2 Hz, 6H, H-7), -1.08 (d, J = 124.7 Hz, 3H, H-11/H-12), -17.33 (s, 2H, H-9/H-10).

^{13}C{^{1}H} NMR (151 MHz, CD_2Cl_2): δ_C 162.18 (dd, J = 99.7, 49.8 Hz), 135.22, 129.61, 129.40 (dd, J = 5.8, 2.9 Hz), 129.19 (dd, J = 5.9, 2.9 Hz), 128.98, 127.72, 125.92, 125.14, 124.11, 122.31, 118.03 – 117.82 (m), 54.41 (C-13), 53.70 (C-1), 32.28 (t, J = 9.7 Hz, C-2), 29.32 (t, J = 12.1 Hz, C-3), 22.22 (C-8), 22.13 (C-4), 22.02 (t, J = 3.6 Hz, C-6), 19.25 (C-7), 16.92 (C-5).

^{31}P{^{1}H} NMR (243 MHz, CD_2Cl_2): δ_P 73.25 (d, J = 110.0 Hz).

^{11}B NMR (193 MHz, CD_2Cl_2) δ_B -6.61 (s), -11.41 (br s).

Elemental analysis found (calculated) for $C_{51}H_{63}B_2F_{24}N_2P_2Rh$ (1360.54): C, 46.28 (45.91); H, 4.83 (4.82); N, 1.95 (2.06).

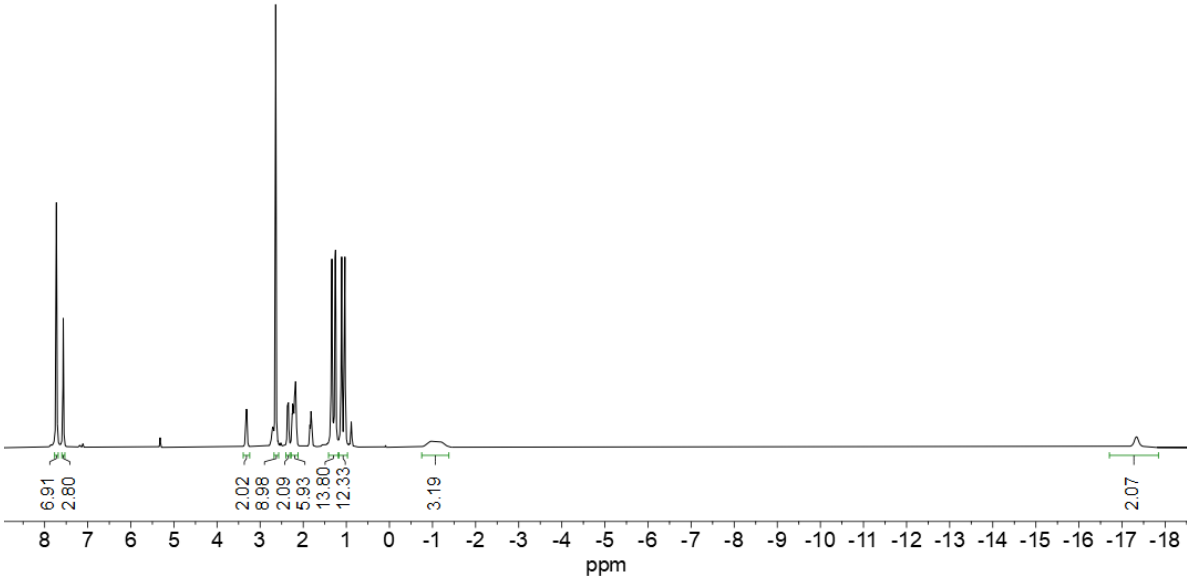


Figure 5.22 ^{1}H NMR (600 MHz, CD_2Cl_2, 298 K) spectrum of **[Rh(L3)H$_2$(H$_3$B·NMe$_3$)][BAr$^F_4$]**.

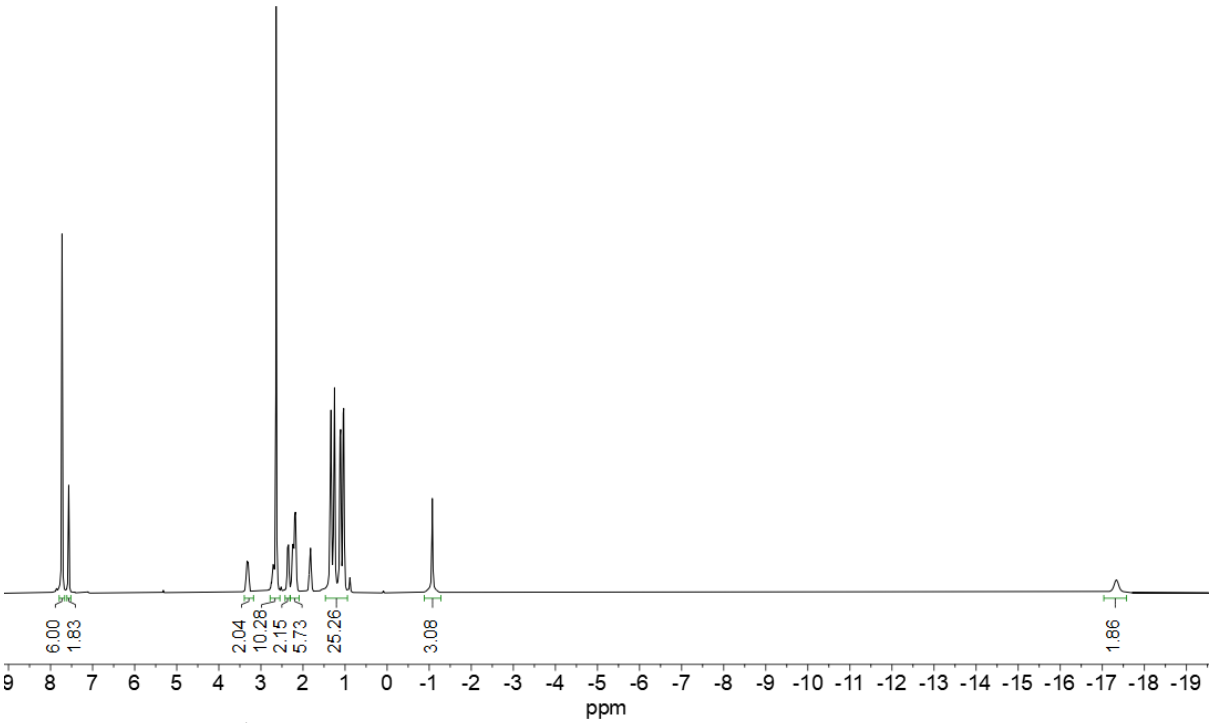


Figure 5.23 ^{1}H{11B} NMR (600 MHz, CD_2Cl_2, 298 K) spectrum of **[Rh(L3)H$_2$(H$_3$B·NMe$_3$)][BAr$^F_4$]**.

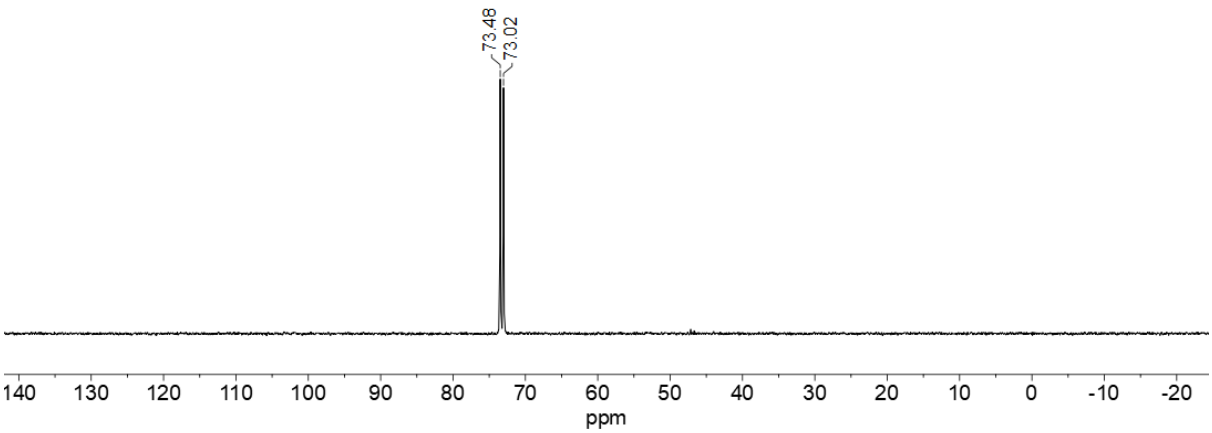


Figure 5.24 $^{31}P\{^{1}H\}$ NMR (243 MHz, CD_2Cl_2, 298 K) spectrum of **[Rh(L3)H$_2$(H$_3$B·NMe$_3$)][BAr$^F_4$]**.

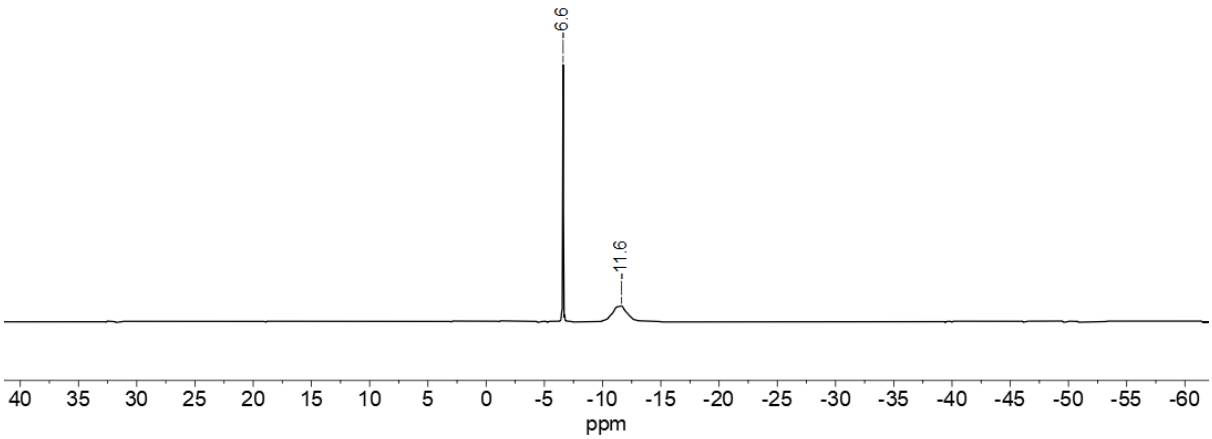


Figure 5.25 ^{11}B NMR (193 MHz, CD_2Cl_2, 298 K) spectrum of **[Rh(L3)H$_2$(H$_3$B·NMe$_3$)][BAr$^F_4$]**.

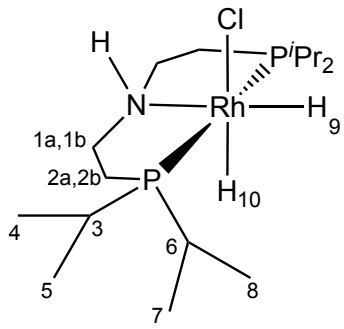
5.4.1.4 Synthesis of Rh(L3)H$_2$Cl

[Rh(COD)Cl]$_2$ (165 mg, 0.33 mmol) was added to a thick walled ampoule fitted with a rotaflow gas tight tap. To this, a solution of L3 (204 mg, 0.67 mmol) in 1,2-$C_6H_4F_2$ (5 mL) was added, to give a dark orange solution. This solution was immediately degassed by freeze-pump-thaw and the ampoule filled with hydrogen (4 bar) before sealing. The reaction mixture was then stirred at 48 hours to give a colourless solution. The hydrogen was removed by freeze-pump-thaw and replaced with an argon

atmosphere before removal of the solvent *in vacuo*. The crude solid was washed with pentane (3 × 5 mL) at -78 °C before drying under reduced pressure to yield **Rh(L3)H_2Cl** as a white powder (250 mg, 0.56 mmol, 85% yield). Crystals suitable for single crystal X-ray diffraction were grown through slow evaporation of a sample of **Rh(L3)H_2Cl** in a 1:3 mixture of 1,2-$C_6H_4F_2$:pentane.

Alternatively,

To a thick walled ampoule fitted with a rotaflow gas tight tap **[Rh(L3)NBD]Cl** (99 mg, 0.18 mmol) and 1,2-difluorobenzene (2 mL) were added. The resulting orange solution was degassed by 3 × freeze-pump-thaw and the ampoule filled with hydrogen (4 bar). The reaction was heated to 70 °C and stirred for 1 week (while monitored by ^{31}P NMR spectroscopy) to give a colourless solution. Some black insoluble solid was observed (likely rhodium(0)). The reaction vessel was cooled and the hydrogen atmosphere was removed by freeze-pump-thaw and replaced with an argon atmosphere before the reaction mixture was filtered *via* cannula. Removal of the solvent *in vacuo* from the filtrate yields a crude off-white solid, that was washed with pentane (3 × 5 mL) at -78 °C before drying under reduced pressure to yield **Rh(L3)H_2Cl** as a white powder (35 mg, 0.08 mmol, 42% yeild). NMR spectroscopic data of the solid matches those data reported above. Hydride shift assignments were aided by NOESY.



^{1}H NMR (C_6D_6, 500 MHz, 298 K): δ_H 3.58 (s, 1H, N-H), 2.99-2.89 (m, 2H, H-6), 2.79-2.59 (m, 2H, H-2a), 1.79-1.72 (overlapping m, 6H, H-3/H-2b/H-1a), 1.71-1.67 (m, 2H, H-1b), 1.57 (dd, 6H, *J* = 16.1, 7.7 Hz, H-4), 1.09 (m, 12H, H-5/H-8), 0.85 (dd, 6H, *J* = 14.1, 7.3 Hz, H-7), -15.73 - -15.84 (br m, 1H, H-9), -19.68 - -19.81 (m, 1H, H-10).

^{1}H NMR (500 MHz, THF-d_8, 298 K): δ_H 3.69 (br t, J = 15.0 Hz, N-H), 3.31-3.20 (m, 2H, H-2a), 2.70 (dhept, 2H, H-3), 2.30-2.25 (m, 2H, H-1b), 2.22-2.14 (m, 2H, H-2b), 2.13-2.06 (m, 2H, H-6), 1.92 (tdt, 2H, H-1a), 1.36 (dd, 6H, J = 16.7, 7.5 Hz, H-4/5), 1.22 (dd, J = 13.7, 6.7 Hz, H-4/5), 1.09 (dd, 6H, J = 16.0, 6.8 Hz, H-7/8), 1.04 (dd, J = 14.3, 7.0 Hz, H-7/8), -16.27- -16.38 (br *pseudo*-p, 1H, J = 15.5 Hz, H-9), -19.77- -19.90 (m, 1H, H-10).

^{13}C{^{1}H} NMR (C_6D_6, 126 MHz, 298 K): δ_C 52.7 (C-2), 32.1 (t, J = 8.4 Hz, C-1), 26.1 (*pseudo*-t, J = 11.8 Hz, C-6), 22.8 (*pseudo*-t, J = 12.1 Hz, C-3), 21.9 (C-4), 21.4 (C-8), 19.2 (C-7), 17.3 (C-5).

^{31}P{^{1}H} NMR (C_6D_6, 243 MHz, 298 K): δ_P 75.4 (d, *J* = 112 Hz).

^{31}P{^{1}H} NMR (THF-d_8, 203 MHz, 298 K): δ_P 75.7 (d, J = 115 Hz).

Elemental analysis found (calculated) for $C_{16}H_{39}ClNP_2Rh$ (445.80): C, 43.26 (43.11); H, 8.42 (8.82); N, 2.98 (3.14).

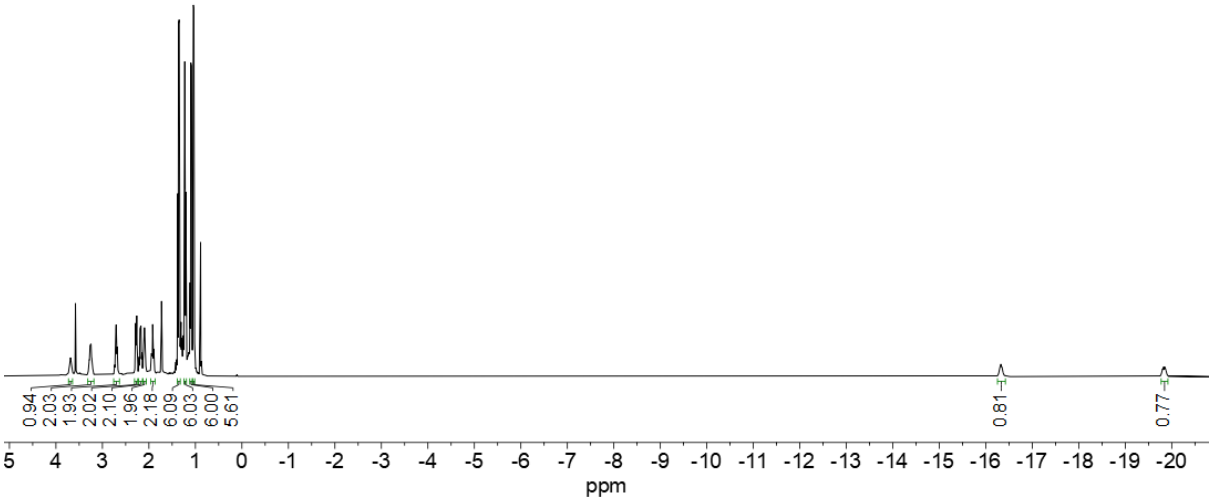


Figure 5.26 ^{1}H NMR (THF-d_8, 600 MHz, 298 K) spectrum of **Rh(L3)H$_2$Cl**.

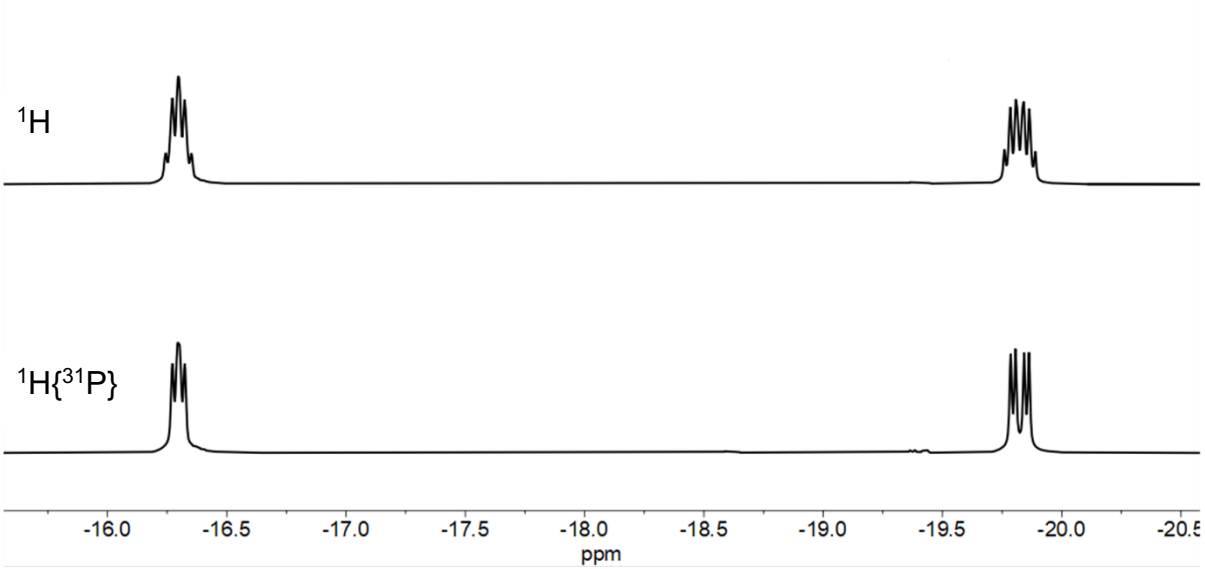


Figure 5.27 ^{1}H NMR and ^{1}H{^{31}P} spectra (THF-d_8, 500 MHz, 185K) of hydride region of **Rh(L3)H$_2$Cl**.

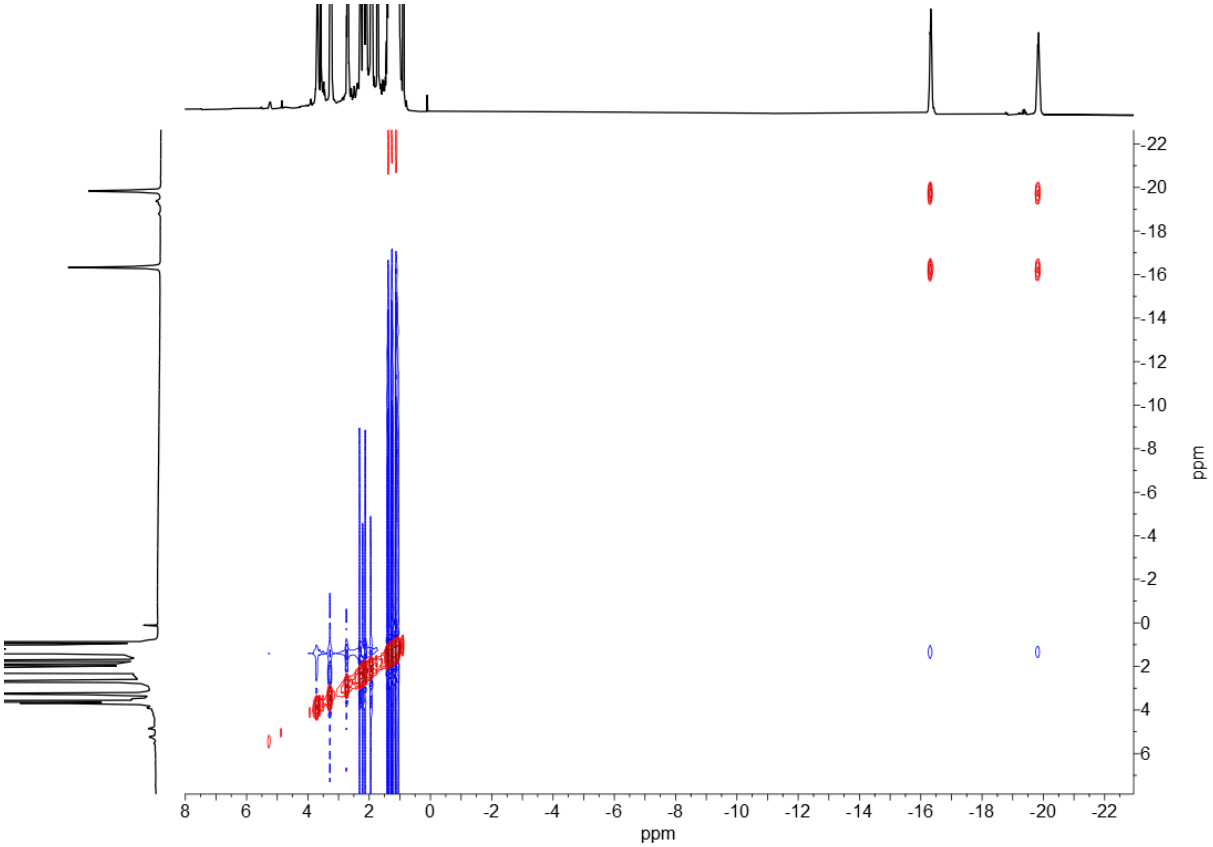


Figure 5.28 $^{1}H^{1}H$ NOESY NMR (THF-d_8, 600 MHz, 298 K) of **Rh(L3)H$_2$Cl**.

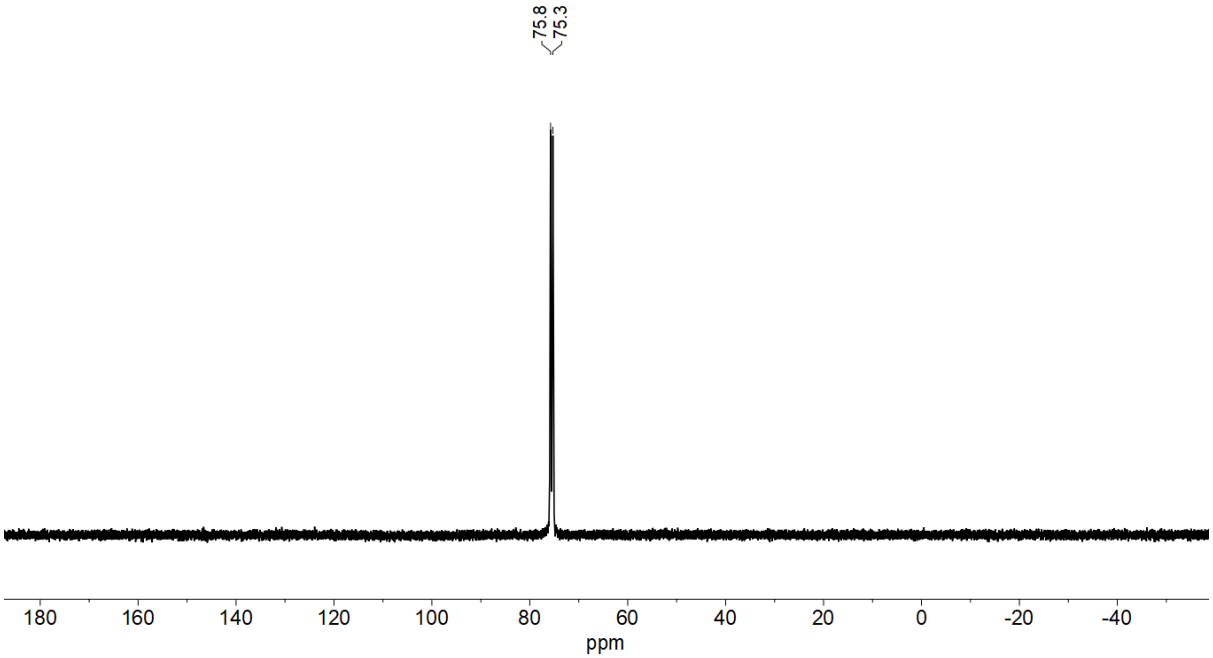
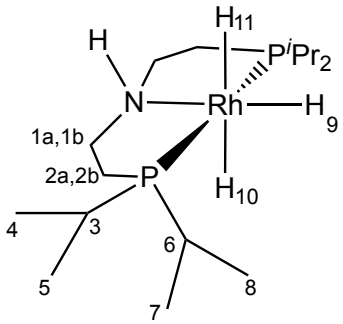


Figure 5.29 $^{31}P\{^{1}H\}$ NMR (THF-d_8, 243 MHz, 298 K) of **Rh(L3)H$_2$Cl**.

5.4.1.5 Synthesis of Rh(L3)H_3 in an NMR tube

To an NMR tube fitted with a high pressure, gas tight tap **Rh(L3)H_2Cl** (5 mg, 11.2 μmol), KO^{t}Bu (1.3 mg, 11.2 μmol) and THF-d_8 (0.5 mL) were added. The resulting deep orange solution was immediately freeze-pump-thaw degassed and the NMR tube filled with hydrogen (2 bar) while submerged in liquid nitrogen. The reaction was allowed to thaw and stirred by end-over-end inversion for 1 h to yield a pale yellow solution which was investigated by NMR spectroscopy to reveal quantitative *in situ* conversion to **Rh(L3)H_3**. Due to the instability of this complex, isolation was not possible. Hydride shift assignment was aided by NOESY.



^{1}H NMR (THF-d_8, 500 MHz, 298 K): δ_H 3.86 (s, 1H, N-H), 3.07-2.99 (m, 2H, H-1a), 2.05-1.98 (m, 4H, H-1b/H-2b), 1.92-1.84 (m, 2H, H-3), 1.82-1.74 (m, 2H, H-6), 1.63 (dt, 2H, H-2a), 1.24-1.17 (overlapping doublets, 24H, H-4/5/7/8), -8.41 (*apparent* pd, 1H, J = 19.6, 6.0 Hz, H-10), -8.69 (*apparent* pd, 1H, J = 18.8, 6.2 Hz, H-11), -18.30 (*apparent* dp, 1H, J = 23.3, 6.0 Hz, H-9).

^{13}C{^{1}H} NMR (THF-d_8, 126 MHz, 298 K): δ_C 54.4 (C-1) 30.9 (t, J = 8.1 Hz, C-2), 28.8 (t, J = 12.9 Hz, C-6), 26.6 (t, J = 12.5 Hz, C-3), 20.5, 20.4, 20.1 and 19.5 (C-4/C-5/C-7/C-8).

^{31}P{^{1}H} NMR (THF-d_8, 203 MHz, 298 K): δ_P 91.6 (d, J = 115 Hz).

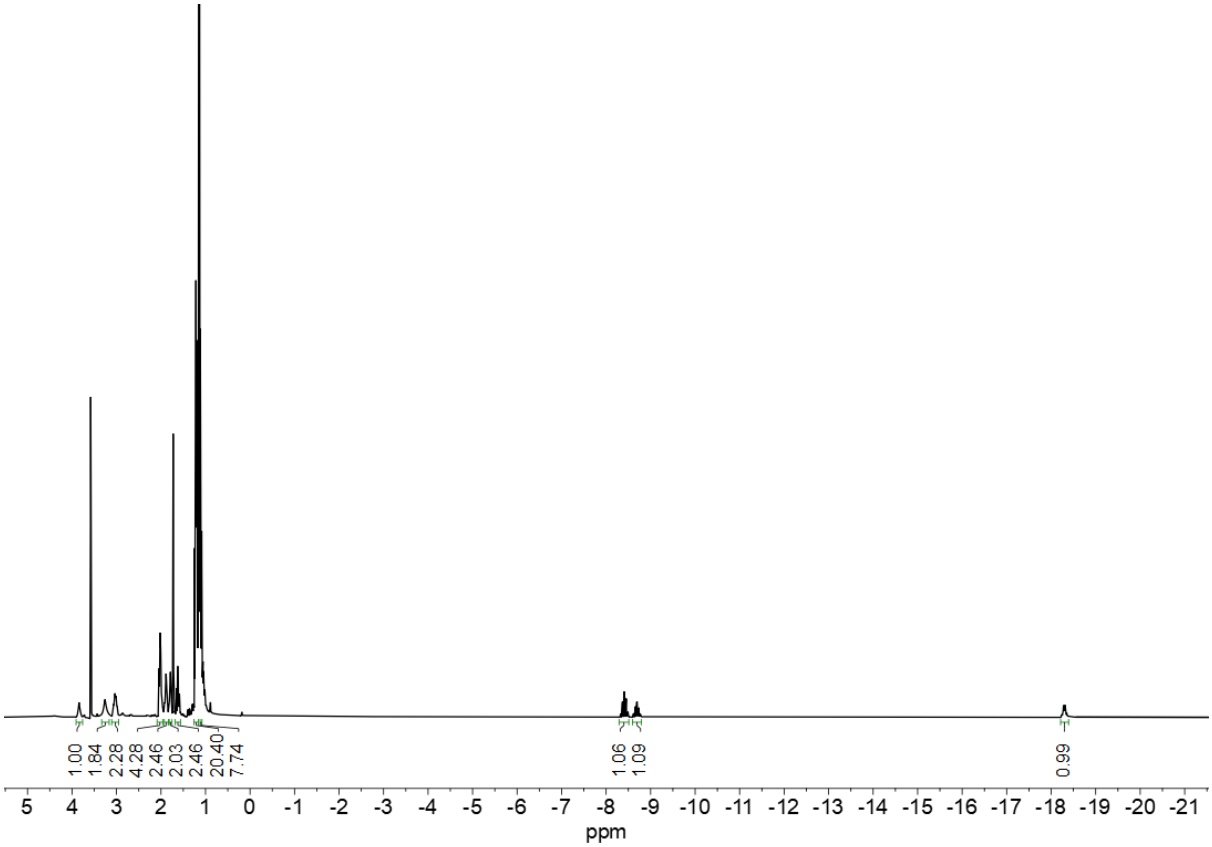


Figure 5.30 ^{1}H NMR (THF-d_8, 500 MHz, 298 K) under a H_2 atmosphere (2 bar) of **Rh(L3)H$_3$**.

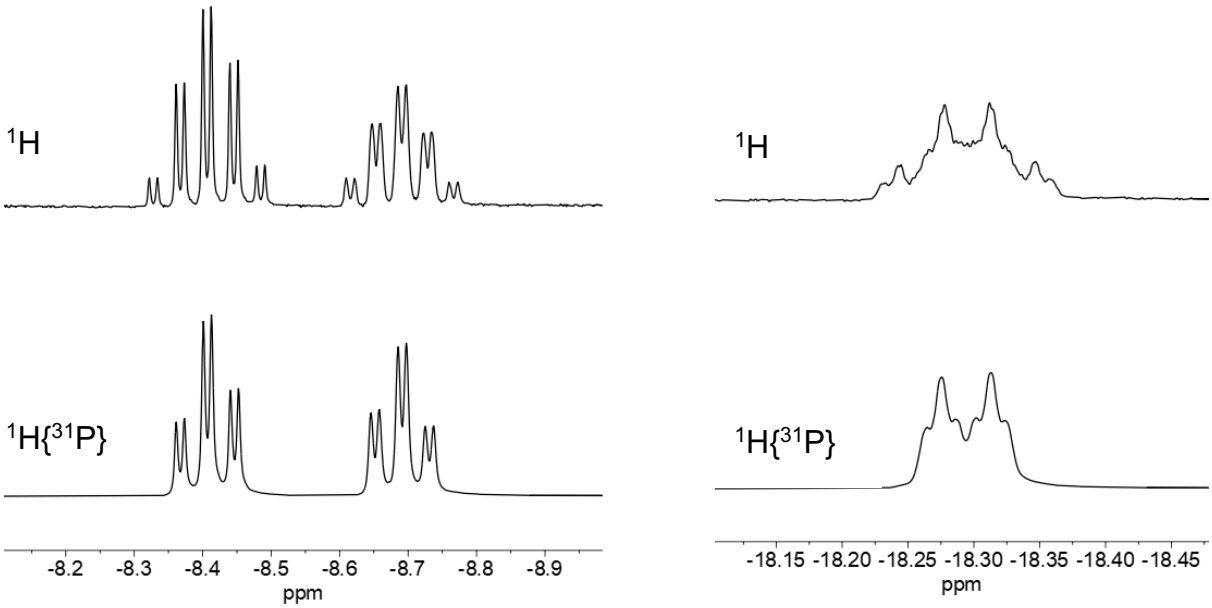


Figure 5.31 ^{1}H NMR and $^{1}H\{^{31}P\}$ spectra (THF-d_8, 500 MHz, 298 K) of hydride region under a H_2 atmosphere (2 bar) of **Rh(L3)H$_3$**.

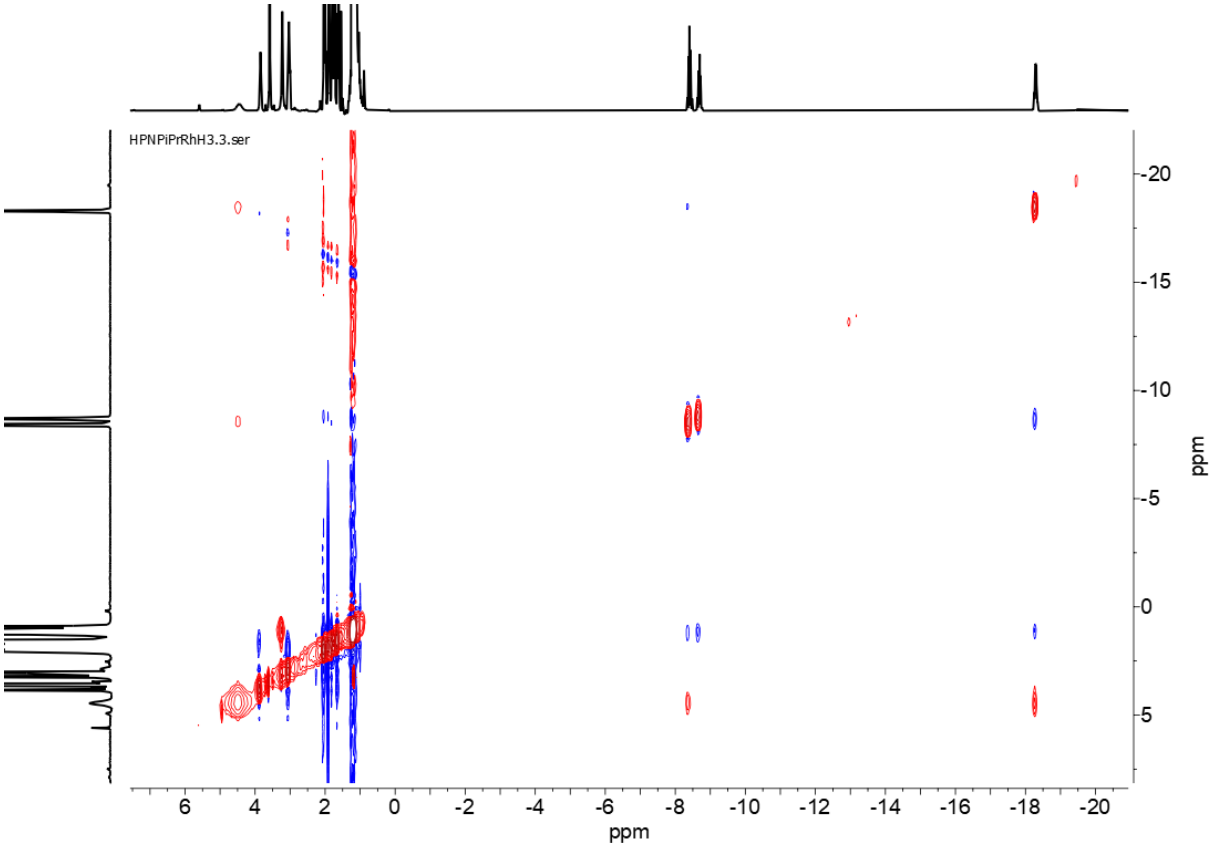


Figure 5.32 $^{1}H^{1}H$ NOESY NMR (THF-d_8, 600 MHz, 298 K) under a H_2 atmosphere (2 bar) of **Rh(L3)H$_3$**.

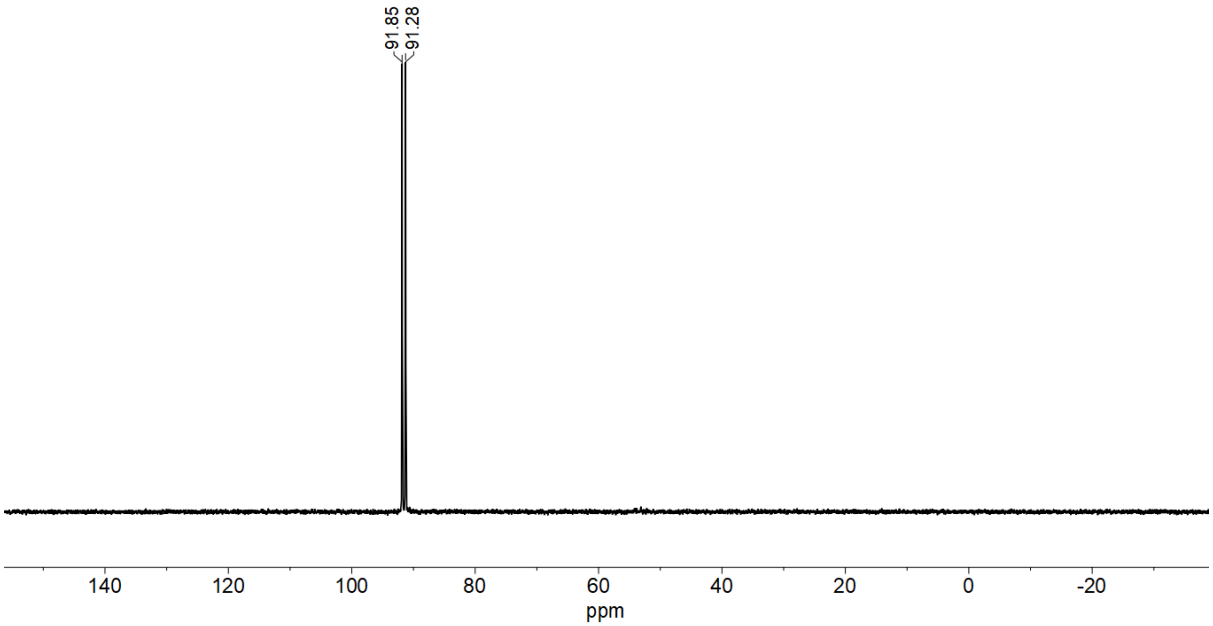
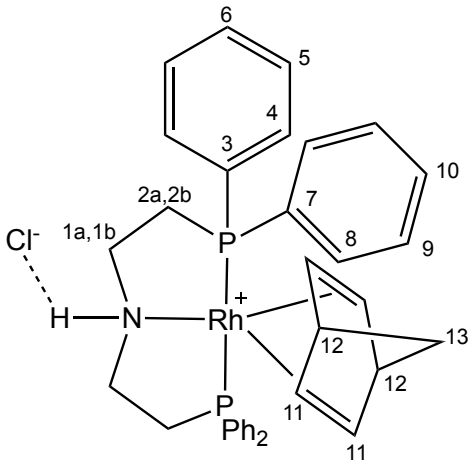


Figure 5.33 $^{31}P\{^{1}H\}$ NMR (THF-d_8, 203 MHz, 298 K) under a H_2 atmosphere (2 bar) of **Rh(L3)H$_3$**.

5.4.1.6 Synthesis of [Rh(HN((CH$_2$)$_2$PPh$_2$)$_2$)NBD]Cl

To an ampoule containing HN((CH$_2$)$_2$PPh$_2$)$_2$·HCl (201 mg, 0.44 mmol) in THF (5 mL) was added NEt$_3$ (61 µL, 0.44 mmol) and the resulting mixture allowed to stir for 10 minutes at room temperature. This solution was then transferred into an ampoule containing **[Rh(NBD)Cl]$_2$** (100 mg, 0.22 mmol) which was suspended in THF (3 mL). The reaction is left to stir at room temperature for 16 hours, during which time an orange precipitate forms which was isolated by filtration *via* cannula. The solid was washed with *n*-pentane (3 x 5 mL) and dried in vacuo (< 5 x 10^{-2} mbar, 16 hrs) to yield an orange powder, **[Rh(HN((CH$_2$)$_2$PPh$_2$)$_2$)NBD]Cl** (245 mg, 0.37 mmol, 83% yield). Crystals suitable for X-ray diffraction study were isolated by slow diffusion of *n*-pentane into a solution of the orange solid in 1,2-difluorobenzene at room temperature to give orange block-like crystals of **[Rh(HN((CH$_2$)$_2$PPh$_2$)$_2$)NBD]Cl**.



^{1}H NMR (500 MHz, CD_2Cl_2, 298 K): δ_H 7.90 (s, 1H, N-H), 7.72-7.68 (m, 4H, H-5), 7.49-7.46 (m, 4H, H-4), 7.45-7.42 (m, 2H, H-6), 7.40-7.36 (m, 2H, H-10), 7.21-7.14 (m, 8H, H-8/H-9), 3.64 (q, 4H, J = 2.0 Hz, H-11), 3.08-2.97 (m, 2H, H-1b), 2.81-2.74 (m, 2H, H-2b), 2.60 (tq, 2H, J = 3.0, 1.8 Hz, H-12), 2.48-2.41 (m, 2H, H-1a), 2.41-2.34 (m, 2H, H-2a), 0.91 (t, 2H, J = 1.3 Hz, H-13).

$^{13}C\{^1H\}$ NMR (126 MHz, CD_2Cl_2, 298 K): δ_C 140.6-139.8 (m, C-3), 135.8 (p, J = 11.1 Hz, C-7), 133.1 (t, J = 6.5 Hz, C-9), 131.5 (t, J = 5.8 Hz, C-5), 130.4 (C-10), 129.4 (C-6), 129.1 (C-4), 129.0 (C-8), 61.0 (C-13), 52.8 (t, J = 7.6 Hz, C-1), 46.7 (C-12), 43.3 (q, J = 6 Hz, C-11), 30.9 (dt, J = 22.5, 11.5 Hz, C-2).

$^{31}P\{^1H\}$ NMR (203 MHz, CD_2Cl_2, 298 K): δ_P 38.8 (d, J = 132 Hz).

Elemental analysis found (calculated) for $C_{35}H_{37}ClNP_2Rh$: C, 62.08 (62.56); H, 5.60 (5.55); N, 2.06 (2.08)

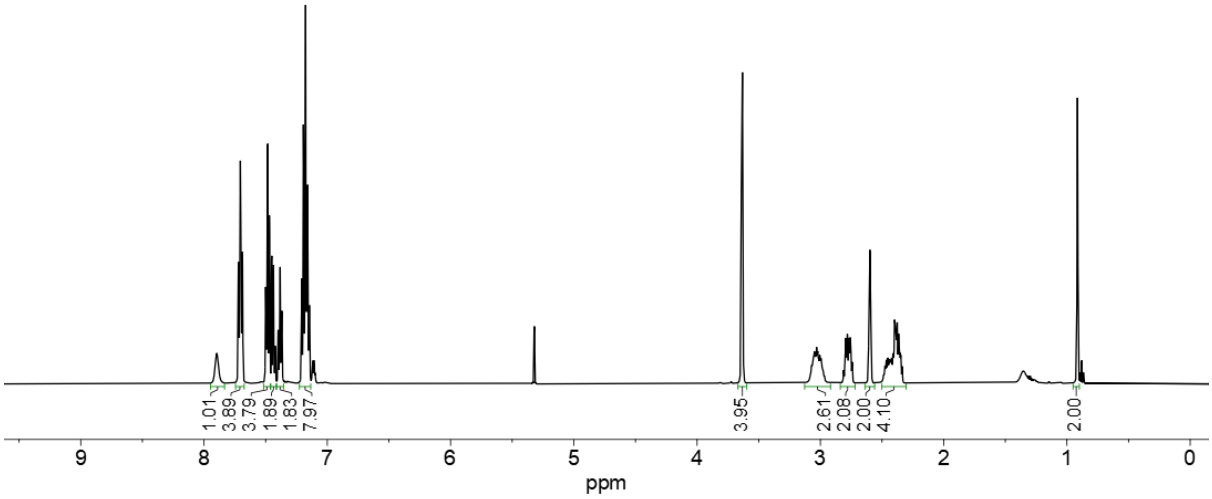


Figure 5.34 ^1H NMR (THF-d_8, 500 MHz, 298 K) spectrum of **[Rh(HN((CH$_2$)$_2$PPh$_2$)$_2$)NBD]Cl**

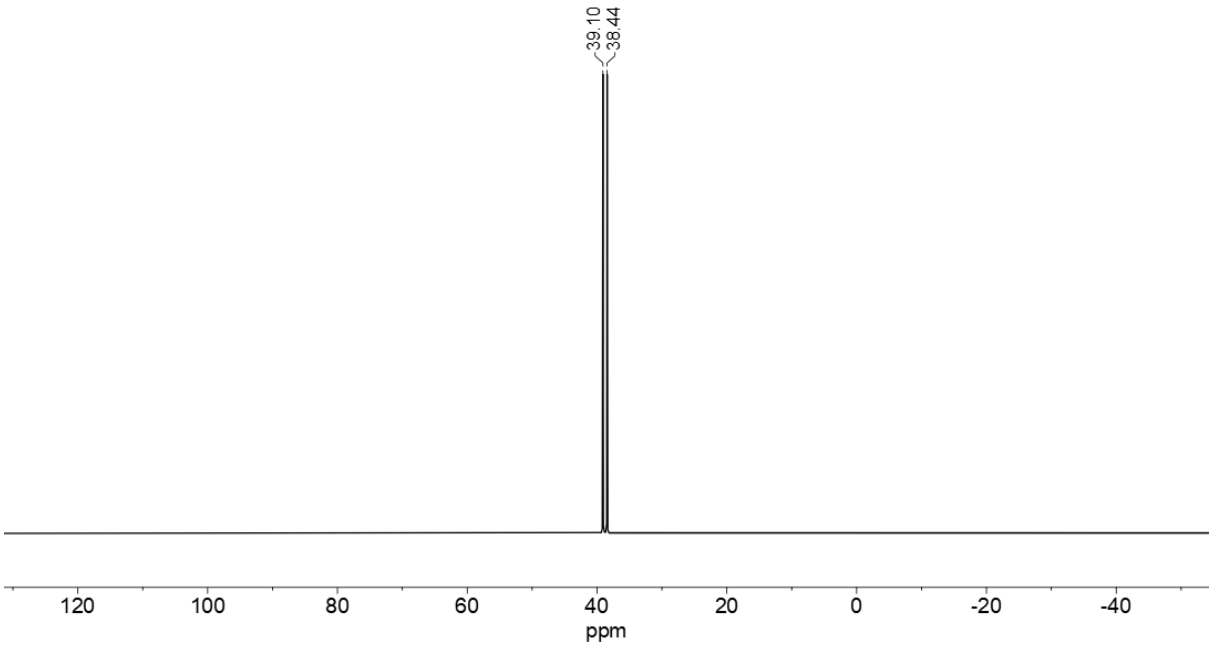


Figure 5.35 $^{31}P\{^{1}H\}$ NMR (THF-d_8, 203 MHz, 298 K) spectrum of **[Rh(HN((CH$_2$)$_2$PPh$_2$)$_2$)NBD]Cl**

5.4.2 Catalytic dehydropolymerisation of $H_3B{\cdot}NMeH_2$

5.4.2.1 Typical dehydropolymerisation procedure under hydrogen evolution measurement conditions

In a typical experiment $H_3B{\cdot}NMeH_2$ (112.0 mg, 2.49 mmol) and catalyst (i.e. **[Rh(L3)NBD]Cl** (7.0 mg, 12.5 μmol, 0.5 mol%), were placed in a jacketed two–neck Schlenk flask which was connected to a recirculating cooler and the temperature set at e.g. 20 °C. This flask was then sealed with a rubber septum and connected to a water–filled 100.0 mL gas burette. THF (2.5 mL, to give 1 M [$H_3B{\cdot}NMeH_2$] was added and the resultant solution was stirred at 400 rpm. The time taken per 1.0 mL of gas evolved was recorded, aided by videography. Upon completion of gas evolution, a 0.5 mL aliquot of the resulting solution was taken for NMR spectroscopy to determine conversion to polyaminoborane. 40.0 mL of pentane was added to the remaining reaction mixture with rapid stirring to the polymer as a white precipitate. The resulting

polymer was then isolated by filtration. The off–white to white solid $(H_2B{\cdot}NMeH)_n$ was dried under vacuum. Isolated yields of $(H_2B{\cdot}NMeH)_n$ varied from 48 - 97%.

5.4.2.2 Dehydropolymerisation procedure under open conditions in air in a vial

This reaction was carried out in a vial open to air. $H_3B{\cdot}NMeH_2$ (224 mg, 5.0 mmol) and catalyst (i.e. **[Rh(L3)NBD]Cl** (14 mg, 25 μmol)) were suspended in THF (5 mL) in a vial. The resultant solution was stirred at 400 rpm for the desired reaction time. Once gas evolution finished, a 0.5 mL aliquot of the reaction mixture was taken for NMR spectroscopy to determine selective conversion to polyaminoborane. 10.0 mL of pentane was added to the remaining reaction mixture with rapid stirring to give a suspension which was stirred for 5 minutes to allow polymer precipitation. The resulting polymer was then isolated by filtration. The off-white to white solid $(H_2B{\cdot}NMeH)_n$ (205 mg, 4.78 mmol 96%) was dried under vacuum.

5.4.2.3 10g scale dehydropolymerisation of $H_3B{\cdot}NMeH_2$

A 100 mL beaker was charged with $H_3B{\cdot}NMeH_2$ (10 g, 0.223 mol) and **[Rh(L3)NBD]Cl** (12 mg, 22 μmol *i.e*. 0.01 mol%) and THF (45 mL). The resultant solution was stirred at 500 rpm for 2 hours. Upon completion, a 0.5 mL aliquot of the resulting solution was taken for interrogation by NMR spectroscopy. The viscous reaction solution was then poured onto rapidly stirring pentane or hexanes (250 mL) to induce precipitation. The resulting white powder was isolated by gravity filtration and dried under vacuum. Isolated yields of $(H_2B{\cdot}NMeH)_n$ varied from 96 - 99%. Repeat experiments demonstrated the reliability of this system.

5.4.2.4 Dehydropolymerisation using boronium as a chain-transfer agent

These reactions were performed in vials open to air. In a typical experiment (e.g. 1 M [$H_3B{\cdot}NMeH_2$], 0.5 mol% catalyst loading), $H_3B{\cdot}NMeH_2$ (112.0 mg, 2.49 mmol), the selected amount of [$BH_2(NMeH_2)_2$][Cl] and catalyst (**[Rh(L3)NBD]Cl** (7.0 mg, 12.5 μmol)) were suspended in THF (2.5 mL) in a vial. The resultant solution was stirred at 400 rpm for the desired reaction time. Upon completion, a 0.5 mL aliquot of the reaction mixture was investigated by NMR spectroscopy. 10.0 mL of pentane was added to precipitate the polymer. The polymer was then isolated by filtration. The off-white to white solid $(H_2B{\cdot}NMeH)_n$ was dried under vacuum. Isolated yields of $(H_2B{\cdot}NMeH)_n$ varied from 86-95%.

5.4.2.5 General procedure for NMR speciation experiments

In a typical experiment, $H_3B{\cdot}NMeH_2$ (112.0 mg, 2.49 mmol) and catalyst (*e.g.* **Rh(L3)H_2Cl** (11.1 mg, 25 μmol, 1.0 mol%) or **[Rh(L3)NBD]Cl** (14.0 mg, 25 μmol, 1.0 mol%)); were placed in a jacketed two–neck Schlenk flask (connected to a recirculating cooler and the temperature set at 20 °C). THF-d_8 (2.5 mL, to give 1 M [$H_3B{\cdot}NMeH_2$]) was quickly added and the resultant solution and stirred at 400 rpm. Samples (0.5 mL) for NMR analysis were removed at the desired time points and immediately frozen in liquid nitrogen. The frozen sample was rapidly warmed and immediately placed into a pre-cooled spectrometer (185 K) for NMR spectroscopic interrogation.

Comparing the eudiometer kinetic data with the time scales from the NMR tube kinetics they were seen to be consistent . Repeating a speciation experiment using **Rh(L3)H_2Cl** and $H_3B{\cdot}NMeH_2$ provided an estimate of the error in this methodology, which was used for the rest of the experiments.

5.4.4 Crystallographic data

5.4.4.1 Crystal structure determinations

Single crystal X-ray diffraction data for all samples were collected using an Oxford Diffraction SuperNova diffractometer using an EOS CCD camera. A typical collection is as follows: a crystal was mounted on a MiTeGen Micromounts using perfluoropolyether oil and cooled rapidly to the collection temperature in a stream of nitrogen gas using an Oxford Cryosystems Cryostream unit.[12] Raw frame data were reduced using CrysAlisPro.[13] The structures were solved using SHELXT[14] and refined using full-matrix least squares refinement on all F2 data using the ShelXL-20XX[15] using the interface OLEX2.[16] Hydrogen atoms were placed in calculated positions (riding model) unless bound to N or Rh in which cause they were located in the fourier difference map and refined freely.

5.4.4.2 Crystallographic tables

	[Rh(L3)NBD]Cl	[Rh(L3)H_2(H_3B·NMe_3)][BAr^F_4]
Chemical Formula	$C_{23}H_{45}ClNP_2Rh$	$C_{54}H_{65}B_2F_{25}N_2P_2Rh$
Formula weight	535.90	1403.55
Temperature (K)	110	110
Crystal system	monoclinic	triclinic
Space group	$P2_1/n$	P-1
a (Å)	9.7559(2)	14.0877(4)
b (Å)	18.3224(3)	14.6482(6)
c (Å)	14.2052(3)	17.7890(5)
α (°)	90	108.909(3)
β (°)	100.910(2)	98.374(3)
γ (°)	90	113.017(3)
Volume (Å^3)	2493.31(9)	3035.97(19)
Z	4	2
ρ_{calc} (g cm^{-3})	1.428	1.535
μ (mm^{-1})	7.792	3.810
Reflection collected	14933	21856
Independent reflections	4752	11490
Restraints / parameters	0 / 265	158 / 842
R_{int}	0.0280	0.0309
R_1 [I > 2σ(I)]	0.0219	0.0389
wR_2 [all data]	0.0516	0.1270
GooF	1.031	0.976
Residual electron density (e Å^{-3})	0.35 / -0.52	1.16 / -0.62
CCDC no.	2115101	-

Table 5.3 Selected crystallographic and refinement data.

	$Rh(L3)H_2Cl$	**$[Rh(HN((CH_2)_2PPh_2)_2)NBD]Cl$**
Chemical Formula	$C_{16}H_{39}ClNP_2Rh$	$C_{45.5}H_{44}ClF_{3.5}NP_2Rh$
Formula weight	445.78	871.61
Temperature (K)	110	110
Crystal system	monoclinic	triclinic
Space group	$P2_1/n$	P-1
a (Å)	11.3355(3)	15.4913(4)
b (Å)	13.6491(3)	15.7569(8)
c (Å)	14.4542(3)	17.6006(6)
α (°)	90	74.470(4)
β (°)	96.9450(10)	89.483(2)
γ (°)	90	73.867(3)
Volume ($Å^3$)	2185.99(9)	3966.4(3)
Z	4	4
ρ_{calc} (g cm^{-3})	1.355	1.460
μ (mm^{-1})	8.772	5.278
Reflection collected	8168	28605
Independent reflections	4122	14986
Restraints / parameters	0 / 210	158 / 1017
R_{int}	0.0294	0.0361
R_1 [I > 2σ(I)]	0.0317	0.0588
wR_2 [all data]	0.0767	0.1700
GooF	1.033	1.066
Residual electron density (e $Å^{-3}$)	0.53 / -1.25	2.24 / -1.63
CCDC no.	2115102	-

Table 5.4 Selected crystallographic and refinement data.

5.4.4.3 Single crystal X-ray diffraction structures

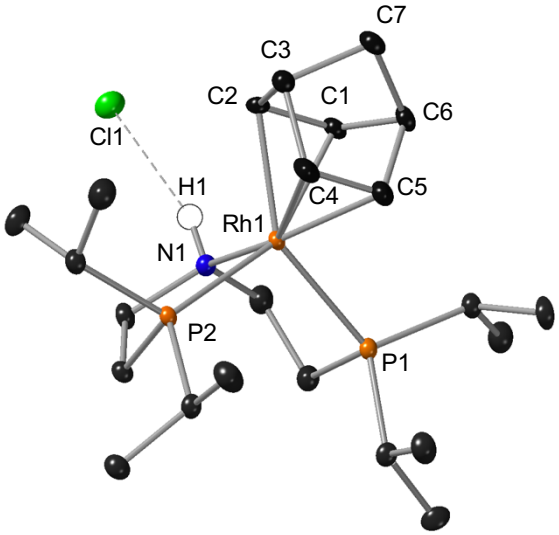


Figure 5.36 Molecular structure of **[Rh(L3)NBD]Cl**. Thermal ellipsoids set at 50 % and only the located hydrogen H1 on N1 is shown.

Selected bond lengths (Å) and angles (°): Rh1-P1 2.3945(5), Rh1-P2 2.3359(5), Rh1-N1 2.1380(17), Rh1-C1 2.1305(19), Rh1-C2 2.1479(18), Rh1-C4 2.190(2), Rh1-C5 2.183(2), C1-C2 1.419(3), C4-C5 1.396(3), H1-Cl1 2.32(2), P2-Rh1-P1 103.875(18), N1-Rh1-P1 83.21(5) and N1-R1-P2 84.13(5).

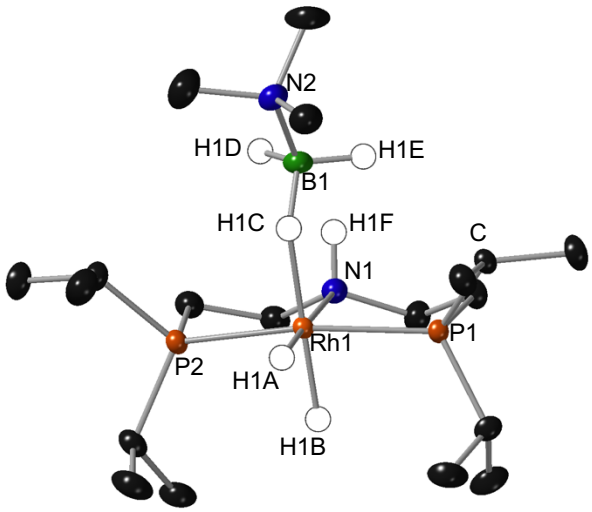


Figure 5.37 Solid-state structure of **[Rh(L3)H_2(H_3B·NMe_3)][BAr^F_4]**. Thermal ellipsoids set at 50 %, the [BAr^F_4]$^-$ anion removed for clarity and only the located hydrogen atoms shown.

Selected bond lengths (Å) and angles (°): Rh1-P1 2.2824(7), Rh1-P2 2.2773(7), Rh1-N1 2.200(2), Rh1-H1A 1.56(4), Rh1-H1B 1.59(4), Rh1-H1C 1.84(3), Rh1-B1 2.753(3), B1-H1C 1.46(6), B1-H1D 1.13(3), B1-H1E 1.13(3), P1-Rh-P2 165.59(3), P1-Rh1-N1 85.12(6), P2-Rh1-N1 85.16(6), and Rh1-H1C-B1 128(2).

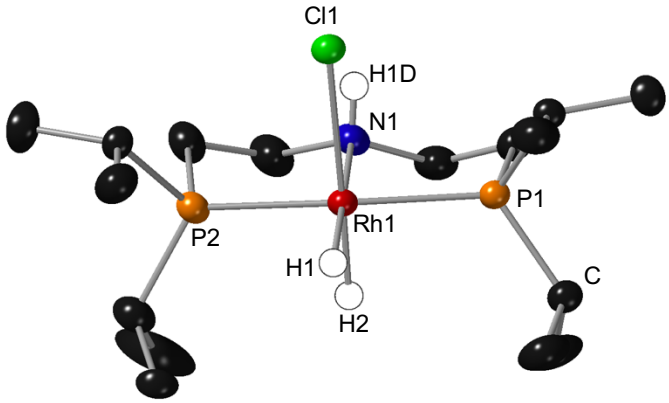


Figure 5.38 Molecular structure of **Rh(L3)H_2Cl**. Thermal ellipsoids set at 50 % and only the located hydrogens are shown.

Selected bond lengths (Å) and angles (º): Rh1-Cl1 2.5033(8), Rh1-P1 2.3945(5), Rh1-P2 2.2716(9), Rh1-N1 2.2732(9), Rh1-H1 1.76(4), Rh1-H2 1.50(4), P2-Rh1-P1 167.87(3)), N1-Rh1-P1 83.82(8) and N1-R1-P2 84.79(8).

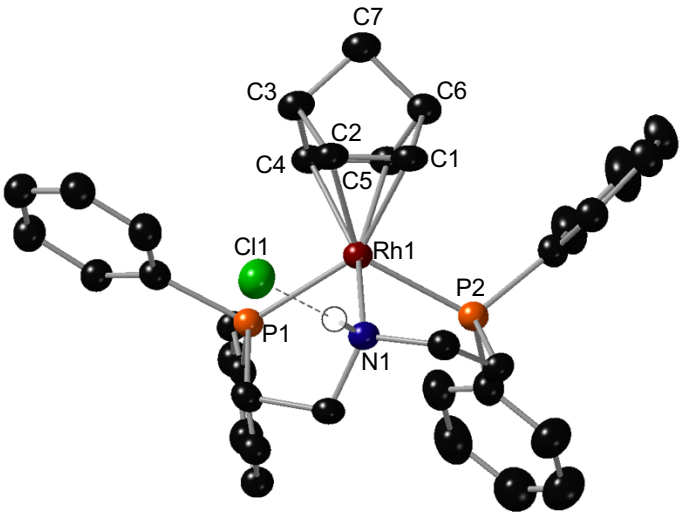


Figure 5.39 Molecular structure of **[Rh(HN((CH$_2$)$_2$PPh$_2$)$_2$)NBD]Cl**. Thermal ellipsoids set at 50 % and only the hydrogen H1 on N1 is shown.

Selected bond lengths (Å) and angles (º): Rh1-P1 2.3091(11), Rh1-P2 2.3519(12), Rh1-N1 2.128(3), Rh1-C1 2.157(4), Rh1-C2 2.167(4), Rh1-C4 2.177(4), Rh1-C5 2.179(4), C1-C2 1.399(7), C4-C5 1.390(7), H1-Cl1 2.28(5), P2-Rh1-P1 114.62(4), N1-R1-P1 83.33(10) and N1-Rh1-P2 81.43(11).

5.5 References

(1) Martínez-Martínez, A. J.; Weller, A. S. *Dalt. Trans.* **2019**, *48* (11), 3551–3554.
(2) Rozenel, S. S.; Padilla, R.; Arnold, J. *Inorg. Chem.* **2013**, *52* (19), 11544–11550.
(3) Spiegelberg, B.; Dell'Acqua, A.; Xia, T.; Spannenberg, A.; Tin, S.; Hinze, S.; de Vries, J. G. *Chem. – A Eur. J.* **2019**, *25* (33), 7820–7825.
(4) Werkmeister, S.; Junge, K.; Wendt, B.; Alberico, E.; Jiao, H.; Baumann, W.; Junge, H.; Gallou, F.; Beller, M. *Angew. Chemie Int. Ed.* **2014**, *53* (33), 8722–8726.
(5) Tamizmani, M.; Sivasankar, C. *J. Organomet. Chem.* **2017**, *845*, 82–89.
(6) Abel, E. W.; Bennett, M. A.; Wilkinson, G. .
(7) Colebatch, A. L.; Hawkey Gilder, B. W.; Whittell, G. R.; Oldroyd, N. L.; Manners, I.; Weller, A. S. *Chem. – A Eur. J.* **2018**, *24* (21), 5450–5455.
(8) Inoue, M.; Kodama, G. *Inorg. Chem.* **2002**, *7* (3), 430–433.
(9) Piguet, C. *J. Chem. Educ.* **1997**, *74* (7), 815.
(10) Lubben, A. T.; McIndoe, J. S.; Weller, A. S. *Organometallics* **2008**, *27* (13), 3303–3306.
(11) Chadwick, F. M.; McKay, A. I.; Martinez-Martinez, A. J.; Rees, N. H.; Krämer, T.; Macgregor, S. A.; Weller, A. S. *Chem. Sci.* **2017**, *8* (9), 6014–6029.
(12) Cosier, J.; Glazer, A. M. *J. Appl. Crystallogr.* **1986**, *19* (2), 105–107.
(13) Agilent (2014). CrysAlis PRO. Agilent Technologies Ltd, Yarnton, Oxfordshire, E. .
(14) Sheldrick, G. M. *Acta Crystallographica Section A: Foundations of Crystallography*. International Union of Crystallography December 21, 2008, pp 112–122.
(15) Sheldrick, G. M. *Acta Crystallogr. Sect. A Found. Crystallogr.* **2015**, *71* (1), 3–8.
(16) Dolomanov, O. V.; Bourhis, L. J.; Gildea, R. J.; Howard, J. A. K.; Puschmann, H. *J. Appl. Crystallogr.* **2009**, *42* (2), 339–341.